

Developing platforms for tissue engineering of the airways

Jopeth Ramis, M.Sc.

Thesis submitted to the University of Nottingham for the degree of Doctor of Philosophy

Abstract

Understanding airway dynamics has been under rigorous study for past decades due to its implication in health and disease, where *in vitro, in vivo* and human subjects are continuously being investigated for causation of diseased pathways. However, limitations arise as the variability in the models are unavoidable, and many factors such as cell microenvironments are usually uncontrollable. To surpass this problem, tissue engineering offers a platform to create systematically a controlled environment for the cells to grow. This discipline is used in order to observe cause-and-effect scenarios that elucidates physiological processes and pathological dysregulation within the biology of interest. A platform that allows factors to be tuned to mimic biological conditions of the airways will be truly helpful in unlocking information on how airway cells behave and respond to their environment.

In this work, the tissue engineering central dogma of cells, biomaterials and bioreactor was utilised to setup an observable environment for the cells to be studied. Specifically, airway smooth muscle and epithelial cells were cultured on biomimetic scaffolds that can be tuned mechanically and chemically. Airway smooth muscle cells cultured on stiffening scaffolds showed an asthma-like phenotype, displaying elevated marker for contractility, cell size, and proliferation capacity. For the airway epithelium, proliferation was also increased in increasing matrix stiffness, and augmenting the scaffold with a functional group similar to the native epithelium further supported its growth. Lastly, a double-chambered bioreactor was designed to support culture of the airways, in which its evaluation and performance was assessed computationally and experimentally to obtain optimum parameters for airway culture.

It is hoped that the platforms developed in this thesis for the tissue engineering of the airways will elucidate pathways on how disease processes occur without the need for *in vivo* models. Such model may be used not just on understanding of the biology of the airways, but also a platform to evaluate therapeutic options for alleviation of chronic and lethal airway diseases.

Conference proceedings

Jopeth Ramis, Dominick Shaw, Felicity Rose, Lee Buttery, and Amanda Tatler, Airway smooth muscle cell morphology and α-smooth muscle actin is modulated by substrate stiffness. Joint Respiratory Research Day 2019, May 29, 2019, Jubilee Conference Centre, Nottingham, United Kingdom

Jopeth Ramis, Dominick Shaw, Felicity Rose, Lee Buttery, and Amanda Tatler, Airway smooth muscle cell morphology and α-smooth muscle actin is modulated by substrate stiffness. Joint UK Society for Biomaterials-Tissue and Cell Engineering Society conference 2019, June 11-13, 2019, East Midlands Conference Centre, Nottingham, United Kingdom

Jopeth Ramis, Dominick Shaw, Felicity Rose, Lee Buttery, and Amanda Tatler, Airway smooth muscle cell displays asthma-like phenotype in elevated matrix stiffness. Tissue Engineering and Regenerative Medicine America Chapter conference, December 2-5, 2019, Loews Sapphire Falls Resort Universal, Orlando, Florida, United States of America.

Acknowledgements

I could not even begin to imagine if the following people in my life would not help me, I wouldn't be here finishing my PhD.

I want to thank the British Council and the Department of Science and Technology, Philippines. With the scholarship that you gave me, it made my dreams possible by supporting me financially and administratively. Thank you for choosing me as a Newton Scholar, and may you help other students as well in your pursuit towards national excellence.

To my dearest supervisors. Thank you all for your guidance on me for my whole PhD life, as I admire your patience towards my slowness in research at times and my plethora of emails when I needed help from my experiments. With you letting me experience mistakes by myself but still guiding me through the way, I have learned loads on how to become a proper scientist. I thank Prof. Felicity Rose for helping me cope when I was culture shocked in the U.K. at first. That talk with the officer for mental health and wellbeing made me calm down my depression. Also, on the technical side, I am glad that you have paved ways for collaboration on other people who has helped me with my research.

To Dr. Amanda Tatler, the supervisor that I am really glad I had, thank you for being so patient with me with the western blot and cell experiments. In the end I had a workaround it, but I have learned a lot from you and your expertise in airway biology. I felt at ease on approaching you whenever I have problems with my experiments, and I am always amazed on how you manage to be a brilliant scientist and be a great mom to your family.

Dr. Lee Buttery, the one who accepted me as his PhD student from the beginning and let me do my proposal from the start. Several universities do not want to accept my proposal, but you had faith in me in the beginning until now, and you have helped me whenever I need administrative assistance. Thank you for making time to listen to my dreams as a scientist, and now hopefully our grant will be a success to make a head start of my dream! I really thank you for making my entire PhD possible, and for making new avenues to move forward in my career.

To my friends in RMCT, especially Mahi, Hadi, Elisa, Inchirah, Francesco, Sahrish, Joshua, Amelie, Omar, Jason, Paola, Jazz, Rabea, Mat, Juniad and Conor, thanks for all the assistance on the experiments, made the lab day joyous despite the often failures.

On this subset of friends, I want to say thanks to Mahi, who has been supportive for my research and gave me valuable tips not just on the lab but on academic politics as well. To Inchirah and Elisa, whom I can always talk to when I am stressed, and all our afternoon teas where we just rant on stuff we need to rant. That usually makes my day happy and content.

To my dearest friends in the U.K., Carolina, Paola, Conrad, John, Gelo, Abby, Dalton, Ben, Federico and Alejandra, whom I always have house parties! I will truly miss you as you have drained away my weekly stress in the lab. I hope we will have more dance and food parties in the future when we meet again!

To my friends in the Philippines, the squammy group! Crizaldy, Robert, Michael, Jielyn, Riu, LP, and Jhen, for always making me laugh by messaging hilarious conversations and calling me online. My homesickness is quenched whenever I see your happiness as a group.

To ma'am Lorraine, the best boss I ever had whom I always share my dreams, and to Maurice, who is my design buddy, thanks for your support on the bioreactor! Let's go and have our fancy research after this!

To Francesco Pappalardo, my dearest friend that is closer than a brother. You have been with me from the beginning, and I am every thankful for your loyalty with me. From those late nights we had as we do crazy experiments, to the travels we had all through Europe, and the most depressing times in my life here in the U.K., you have never left me. I owe you a lot on helping me get through with this tortuous PhD life, as without a companion, I would have suffered alone in my PhD.

To my church members in FPCP, especially Pastor Popeng and Pastor Timmy, and also COR members Noel Cabigting and Dave Balino, who prayed with me to affirm my purpose in life and to go here for the sake of God's Kingdom. May God continue to bless you as you have blessed other people with your gift of service to the community.

To my family, Nanay, Tatay, Jayvee, Joshua and Louise, it has been difficult to be apart from you, more so with only a few communications due to the huge time difference. From your upbringing to me until now, you have helped me shape my life to what I am now today. Salamat po sa lahat, mahal na mahal ko po kayo!

And to whom I owe everything that I have in this life, My Lord and Saviour Jesus Christ. You have instilled in my heart a sole purpose of my being: to preach the gospel of truth and serve the poor and vulnerable people through science and medicine. From all the struggles of my life, I shall dedicate it unto your will, and I will make it possible for your Name. Praise be unto the only Son of God, who lives and reigns forever and ever! Amen!

Abbreviations

α-MEM	Alpha Minimum Essential Medium
α-SMA	Alpha smooth muscle actin
AEC	Airway epithelial cell
ASMC	Airway smooth muscle cell
ANOVA	Analysis of Variance
BSA	Bovine Serum Albumin
COPD	Chronic Obstructive Pulmonary Disease
DI	Dialysed
DMEM	Dulbecco's Modified Eagle Medium
DMSO	Dimethyl sulfoxide
DNA	Deoxyribonucleic acid
DTNB	5,5'-dithio-bis-[2-nitrobenzoic acid])
EDTA	Ethylenediaminetetraacetic acid
EGF	Epithelial growth factor
FBS	Foetal Bovine Serum
GelMA	gelatin Methacryloyl
H&E	Hematoxylin and Eosin
Hz	Hertz
IL-6	Interleukin-6
IMS	Industrial Methylated Spirit
Pa	Pascals, N/m^2
PBS	Phosphate Buffered Solution
pGSK3b	Phosphorylated Glycogen synthase kinase 3 beta
PR	Precipitated
pSMAD2	Phosphorylated Mothers against decapentaplegic homolog 2

TGF-b1	Transforming growth factor beta type 1
TIMP-1	Tissue Inhibitor Metalloproteinase type 1
TNBS	2,4,6-Trinitrobenzene-sulfonic acid
SEM	Scanning electron microscope
SD	Standard Deviation

Table of Contents

Cover Page……i

Abstract……iii

Conference Proceedings……v

Acknowledgements……vi

Abbreviations……ix

Table of Contents……xi

List of Figures……xvi

List of Tables……xx

Dedication……xxi

Chapter 1 Introduction 1

1.1Classifications of human airway cells 2

1.1.1 Expression of functional molecules of airway cells 5

1.1.2 Mechanobiology in the Lung.....8

1.1.3 Secretome-Mechanotransduction feedback signalling 9

1.2 Interactions of airway cells 12

1.2.1 The physiological airway: Major cellular roles.....12

1.2.2 Airway Cell Interactions in the Developing Airway.....15

1.2.3 The pathological airway: Dysregulation cascades 19

1.2.4 Models for understanding the airways.....23

1.3 Thesis aims.....25

Chapter 2 General Methods 28

2.1 Cell culture of primary airway smooth muscle cells……28

2.2 Passaging primary airway smooth muscle cells……28

2.3 Passaging of Calu-3 airway epithelial cell……29

2.4 Cryopreservation and resuscitation of cells....29
2.5 Metabolic assay measurements....30
2.6 DNA quantification....30
2.7 Scanning Electron Microscopy....31

Chapter 3 Development of downstream processes to improve physical and mechanical properties of methacrylated gelatin 33

3.1 Introduction....33
3.2 Materials and Methods....38
3.2.1 Syntheses of GelMA....38
3.2.1.1 Downstream processing of GelMA via precipitation method....39
3.2.1.2 Downstream processing of GelMA via dialysis method....40
3.2.2 Characterisation of synthesised GelMA....40
3.2.2.1 Morphological analysis....40
3.2.2.2 Degree of substitution assay....40
3.2.2.3 Molecular weight distribution via Gel Permeation Chromatography....41
3.2.2.4 Thermogravimetric analysis....41
3.2.3 GelMA hydrogel production....42
3.2.4 GelMA hydrogel characterisation....42
3.2.4.1 Compressive modulus determination....42
3.2.4.2 Rheological analysis....43
3.2.4.3 Swelling ratio evaluation....43
3.2.4.4 Cell culture....44
3.2.4.5 Cell viability assay....44
3.2.5 Statistical analysis....45
3.3 Results....46
3.3.1 Morphology of GelMA prepared by dialysis and precipitation....46
3.3.2 Molecular weight of GelMA....49
3.4.3 Compressive mechanical strength and swelling ratio....50
3.3.4 Rheological analysis of GelMA hydrogels....52
3.3.5 Cellular viability studies of GelMA hydrogels....56

3.4 Discussion 57

Chapter 4 Airway smooth muscle cell recapitulates asthma-like phenotype by increasing substrate stiffness 61

4.1 Introduction 61
4.2 Materials and methods 65
4.2.1 Synthesis of GelMA 65
4.2.3 Cell culture 66
4.2.4 Immunocytochemistry and morphometric analysis 66
4.2.5 Flow cytometry 67
4.2.6 Cell proliferation assay 68
4.2.7 IL-6 and TIMP-1 quantification 69
4.2.8 Statistical analysis 70
4.3 Results & Discussion 71
4.3.1 Preparation of scaffold with physiological and pathological matrix stiffness 71
4.3.2 Matrix stiffness affects the morphology and α-smooth muscle actin expression of ASMCs 72
4.3.3 Cell volume and TGF-β1 signalling is increased with matrix stiffness 75
4.3.4 Cell proliferation is increased with matrix stiffness 78
4.3.5 IL-6 and TIMP-1 is downregulated with increasing matrix stiffness 79

Chapter 5 Basal membrane biomimicry with tuneable properties for human bronchial epithelial cell culture 86

5.1 Introduction 86
5.2 Methods 90
5.2.1 Electrospinning of GelMA 90
5.2.2 Crosslinking of GelMA nanofibers 90
5.2.3 Scaffold characterisation 91
5.2.3.1 Scanning electron microscopy 91
5.2.3.2 Surface elastic modulus determination 91
5.2.3.3 Fourier Transform Infrared Spectroscopy 92
5.2.3.4 Protein diffusivity studies 92

5.2.3.5 Porosity measurements.....92
5.2.4 GelMA nanofiber functionalisation.....93
5.2.4.1 L-cysteine conjugation via EDC-NHS coupling.....93
5.2.4.2 Thiol content determination.....93
5.2.4.3 H2O2 scavenging assay.....94
5.2.5 Biocompatibility studies.....95
5.2.5.1 Cell morphology evaluation.....95
5.3 Results & Discussion 96
5.3.1 Nanofiber physical properties evaluation.....96
5.3.2 Nanofibre cysteine functionalization via EDC-NHS..... 100
5.3.3 Cell culture results 102

Chapter 6 Tissue engineering of human airway cultured in a 'novel' Taylor-Couette-Poiseuille bi-perfusion bioreactor..... 109

6.1 Introduction 109
6.2 Methods..... 114
6.2.1 Fabrication of the bioreactor..... 114
6.2.2 Flow and shear-field simulation..... 116
6.2.3 Residence time distribution analysis (RTD) 117
6.2.3 Response surface methodology – central composite design 118
6.2.4 Trachea bioreactor culture 120
6.2.5 Trachea histology..... 121
6.3 Results..... 122
6.3.1 Bioreactor flow-field simulation (velocity and vorticity) 122
6.3.2 Surface shear stress evaluation in inner cylinder 125
6.3.3 Residence time distribution analysis 128
6.3.3.1 First moment: Mean residence time.....128
6.3.3.2 Second moment: variance.....130
6.3.3.3 Peclet number.....132
6.3.3.4 Real reactor flow schemes: bypassing and tailing.....134

6.3.4 Temporal changes in trachea culture using TCP bioreactor.....137
6.4 Discussion.....141

Chapter 7 General Discussion..... 146

7.1 Key findings.....146
7.2 Current limitations.....151
7.3 Future work.....152
7.4 Final Conclusion.....153

References.....156

List of Figures

Figure 1.1. Cross-sectional isometric view of the anatomy of the lower respiratory tract. The trachea has the airway smooth muscle on the dorsal side which connects the incomplete c-ring of the cartilage. It is lined with pseudostratified ciliated epithelium. Intermittent cartilaginous plates are found within the length of bronchus, and underneath wrapped with airway smooth muscle tissue. The typical diameter of the trachea is 15-20 mm and 100-110 mm in length(Standring, 2016), (Breatnach, Abbott, & Fraser, 1984). The left primary bronchus has an anteroposterior diameter of 9.6-12.3 mm and length of 41.9-43.9 mm, while the right primary bronchus diameter is 11.9-13.8 mm with length of approximately 13.8 mm(J. W. Lee, Son, Choi, Han, & Lee, 2014). All values shown are ranges for both adult men and women. 4
Figure 1.2. Summary of potential interaction of airway cells in normal physiology via paracrine signalling, cell-cell interaction, and mechanotransduction cascades as listed in Table 2. Legend: green upward arrow – upregulation, horizontal flat arrowhead – inhibition, check symbol– enabling function 88
Figure 1.3. Tracheal ASM in relaxed and contracted state. After stimuli induction, ASMCs shorten its actin and myosin filaments resulting in contraction of the tissue and therefore reducing the luminal diameter of the trachea. Upon contraction, compressive forces are being introduced cyclically on the whole organ, thereby inducing global mechanobiological stimuli throughout airway cells..... 10
Figure 1.4. General mechanotransduction dynamics in the airways. Epithelium-induced ASM contraction coming from external stimuli such as particulates from inspired air or epithelial damage cascades throughout the airways by the release of functional molecules that act as a stimulant to the ASMCs. Cyclic contraction or relaxation of ASM due to epithelial-derived agonists affects the whole organ in which a compressive force is induced, initiating ECM production in chondrocytes that both serve as a Ca^{2+} ion reservoir for modulation of ASM activity and as a scaffold on basal epithelial cells on the interface of cartilage and epithelium, where epithelial cells differentiate further into a pseudostratified epithelium with diverse phenotypes. The cyclic compressive force also increases the ciliary beat frequency of AECs and ATP release, enhancing mucus clearance and inducing epithelial repair. 11
Figure 1.5. Signalling pathways in the developing airways. Key functional molecules are Sox9 (cartilage formation), FGF-10 (epithelial branching), and FGF-9 (ASMC differentiation). 15
Figure 1.6. Anatomy of pathologies in the bronchus. Inflammation, mucous over secretion, and hypercontractility of the ASM are few of the pathologies seen in the trachea and bronchi. 20
Figure 3.1 Process flow chart of gelatin methacryloyl synthesis and downstream processing. The following annotation are used: M-01 (mixer, gelatin), R-01 (reactor), M-02 (mixer, neutralization), F-01 (filtration) and D-01 (dryer)..... 39
Figure 1. Photomicrographs and scanning electron micrographs of (a) dialysed and (b) precipitated GelMA. Scale bar: solid = 50 µm, dashed = 5 µm..... 46
Figure 3.3 Representative thermogravimetric curves of (left) DI and (right) PR GelMA..... 48
Figure 3.4 Chromatogram and molecular weight distribution of dialysed and precipitated GelMA using gel permeation chromatography. Student's t-test shows a significant difference between number averaged molecular weight (Mn) and weighted averaged molecular weight (Mw) (***p<0.0001, n=3). Calculated polydispersity for dialysed and precipitated GelMA was 1.85±0.024 and 2.35±0.016 respectively. Error bars represent SD..... 49

Figure 3.5 (a) GelMA hydrogels from left to right: 5% DI, 5% PR, 10% DI and 10% PR. (b) Compressive modulus and (c) swelling ratio of GelMA hydrogels; error bars as standard deviations. Different concentration and downstream processing techniques show statistically significant differences via ANOVA and Tukey's post hoc test (*p < 0.05, **p < 0.01, ***p < 0.001, n≥3). Error bars represent SD. ……..50
Figure 3.6 Strain sweep of (a) 5% Dialyzed, (b) 5% Precipitated, (c) 10% Dialyzed, and (d) 10% Precipitated gelatin methacryloyl at 1 Hz and T=37°C……..52
Figure 3.7 Frequency sweep of (a) 5% Dialyzed, (b) 5% Precipitated, (c) 10% Dialyzed, and (d) 10% Precipitated gelatin methacryloyl at 0.5% strain and T=37°C. Bar graphs of the determined storage (e) and loss (f) moduli on all samples. Statistically significant differences between 5% DI and PR to 10% PR at 95% CI via ANOVA and Tukey's post hoc test (*p < 0.05, **p < 0.01, n≥3). Error bars represent SD……53
Figure 3.8 Time sweep of (a) 5% Dialyzed, (b) 5% Precipitated, (c) 10% Dialyzed, and (d) 10% Precipitated gelatin methacryloyl at 1 Hz, 0.5% Strain and T=37°C……54
Figure 3.9 Temperature sweep of (a) 5% Dialyzed, (b) 5% Precipitated, (c) 10% Dialyzed, and (d) 10% Precipitated gelatin methacryloyl at 1 Hz, 0.5% Strain, and heating rate of 2°C/min……55
Figure 3.10 Cell viability assessment of NIH 3T3 fibroblasts encapsulated in 5% DI and PR (a & b), and 10% DI and PR (c & d) GelMA at Day 1 and 4, using Live (green, Calcein-AM)-Dead (red, Ethidium homodimer) stain. Bar graph (e) showing no significant difference in cellular viabilities between culture days (Repeated measures ANOVA, p=0.1114, at least 50 cells in each 3 different regions were analysed). Scale bar = 250 µm. Error bars represent SD……56
Figure 4.1 Young's modulus of GelMA hydrogels, with normal (= 1x, 5%), ≈5.5x (10%) and 11.4x (15% wt/vol GelMA) physiological stiffness levels as compared to native trachea. 71
Figure 4.2 (a) Immunofluorescence staining of hASMCs cultured) under 1x, 6x and 12x physiological stiffness GelMA hydrogels, with control cultured on a cover slip. Cells were stained with α-smooth muscle actin (green, Alexa Fluor™ 488). Scale bar = 100 µm. Box-plot graph shown are morphometric measurement of cells: (b) Cell area (c) perimeter presented in pixel units. (d) Average fluorescence intensity of α-smooth muscle actin per cell presented as fluorescence units (integrated density). Box and whiskers plot show min to max range values obtained. No. of cells/donor analysed n ≥ 33, 3 donors, 3 technical replicates, 2 independent runs. 73
Figure 4.3 (a) Immunofluorescence staining of cell nuclei with DAPI. Scale bar = 50 µm. Nuclei morphometric analysis showing (b) Nuclei Area and (c) Nuclear Eccentricity. In nuclear eccentricity, the lower the number, the more circular the nucleus. No. of nuclei n ≥ 68, 3 donors, triplicate, 2 independent runs. 74
Figure 4.4 (a) Cell diameter increase as stiffness increases. (a) Scatter plots showing increasing density of cells in >20 um region from 1x stiffness to control. b and c) forward scatter histogram and geometric mean line plot, showing an increasing trend (a & c, *p<0.05, b, **p<0.001). c) After gating with 10 um and 20 um calibration beads, cell population were classified into 10, 20 and >20um sizes, where a trend is seen that cell diameter increase as stiffness increase (*p<0.05, **p<0.001, ***p<0.0001). N=3 biological replicates, minimum of 10,000 cells analysed per sample and serum-starved for 24 hr before analysis. 75
Figure 4.5 (a) Immunofluorescence staining of hASMCs cultured under 1x, 6x and 12x physiological stiffness GelMA hydrogels, with control cultured on a cover slip. Cells were stained with pSMAD2 (red, Alexa Fluor™ 555) and pGSK-3β (green, Alexa Fluor™ 488) (Scale bar = 100 µm). Box-plot shows average fluorescence intensity of (b) pSMAD2 and pGSK-3β (c) per cell presented as fluorescence units (integrated density). Box and whiskers plot show min to max

range values obtained. No. of cells/donor analysed n ≥ 106, 3 donors, 3 technical replicates, 2 independent runs ((*p<0.05, **p<0.001, ****p<0.00001) 77
Figure 4.6 ASMCs proliferate more on stiffer matrix. a & b) Cell cycle analysis of cells, where % S phase of cells increases as the stiffness of gel increases. Minimum of 10,000 cells analysed per sample and serum-starved for 24 hr before analysis. c & d) Relative fold increase of relative fluorescence units (RFU) and DNA content of ASMC cultured with 10% FBS from Day 0, where there is a significant increase on the rate of proliferation on Day 7 among different matrix stiffness (*p<0.05, **p<0.001, ***p<0.0001). N=3 biological replicates, 3 technical replicates, 1 independent run for cell cycle analysis and 2 independent runs for Presto Blue and PicoGreen assay; cells are seeded at 5,000 cells/cm^2. 78
Figure 4.7 Quantification of IL-6 (left) and TIMP-1 (right) in cell culture supernatant via ELISA. Data is normalised with cell number, with 3 donors, 3 technical replicates, 2 independent runs. ANOVA shows statistically significant difference between stiffness levels, with **p < 0.001. 79
Figure 5.1 Scanning electron micrograph of electrospun GelMA and the fibre alignment distribution. Scale bar = 1 um with magnification of 10,000x. The table shows the mean morphological characteristics of the produced nanofiber. 96
Figure 5.2 (a) Average from 36 force curves, triplicate samples. Two-way ANOVA shows a statistically significant difference between samples with p<0.0001. Stiffnesses recorded were as follows: 4% H_2O (296.9±67.39 kPa), 8% H_2O (602.5±97.66 kPa), 12% H_2O (933.3±66.56 kPa), with p<0.0001. (b) FTIR shows reduction of absorbance in 1670-1600 cm^{-1} spectra, confirming crosslinking of the methacrylate groups in electrospun GelMA. Legend: Yellow = uncrosslinked GelMA, Blue = 4% H_2O crosslinked, Green = 8% H_2O crosslinked, Red = 12% H_2O crosslinked. (c) Morphology of electrospun nanofibers after crosslinking in different water concentrations. 97
Figure 5.3 (a) Diffusion profile of crosslinked electrospun GelMA nanofibers. The profile shows a decreasing trend of (b) membrane thickness, (c) porosity and (d) diffusivity as stiffness increases (moderated by % H_2O in crosslinking). Legend: brown = 4% H_2O, magenta = 8% H_2O, and green = 12% H_2O. Used ANOVA with Tukey's post hoc test (p*<0.05, p**<0.01,p****<0.0001). Data shown here are from triplicate samples. 99
Figure 5.4 (a) DNTB assay for the determination of free thiol groups. Day 0 showed a significant difference in the number of thiols between samples. The figure below (a) showed positive sulfhydryl GelMA despite of EDC being absent in the reaction, which indicates absorption of L-cysteine that may lead to a false positive. (b) H_2O_2 scavenging assay, confirming the antioxidant properties of the sulfhydryl group. Time course determination of sulfhydryl compound is then performed (c) showing that GelMA nanofibers were indeed functionalised with thiol; samples without EDC did not show any reaction to DNTB, which shows desorption of L-cysteine residues. Used ANOVA with Tukey's post-hoc test (*p<0.05, **p<0.01, ***p<0.001, ****p<0.0001). 100
Figure 5.5 Presto Blue assay results after 4 days of culture of Calu-3 epithelial cells in electrospun scaffolds. (a) One-way ANOVA revealed higher metabolic activity in increasing scaffold stiffness (b) Two-way ANOVA showed significantly higher metabolic activity in the thiolated samples as compared to non-treated scaffolds, indicating an increased rate of proliferation (p*<0.01, p**<0.001, n=3 technical replicates). (c) FESEM false-coloured photomicrographs of calu-3 cells in different scaffold stiffnesses and treatment. Scale bar = 10 µm at 1,000x magnification. 102
Figure 5.6 Schematic of protein adhesion in epithelial cell secretions through disulphide bonding in L-cysteine conjugated scaffolds. 106
Figure 6.1 (Top) Numbered isometric exploded 3D assembly of the Taylor-Couette-Poiseuille bi-perfusion bioreactor. (Below) Flow imaging of the bespoke bioreactor, using aqueous solution of anisotropic stearic acid crystals perfused with phenol red after steady state conditions. 114

Figure 6.2 Photo on the operation of the bioreactor in the culture of trachea. The left diagram shows a process flow diagram on the operation during culture 120
Figure 6.3 Contour plots of the velocity profile and streamlines of vorticity in the bioreactor at r_i/r_o =0.5 (bronchus). Profile shown in radial-horizontal plane..... 122
Figure 6.4 Contour plots of the velocity profile and streamlines of vorticity in the bioreactor at r_i/r_o =0.625 (trachea). Profile shown in radial-horizontal plane. 123
Figure 6.5 3D surface maps of the shear stress at the surface of the inner cylinder with r_i/r_o =0.5 (bronchus). Average and maximum surface shear values are plotted for comparison and evaluation of factor effects. 125
Figure 6.6 3D surface maps of the shear stress at the surface of the inner cylinder with r_i/r_o =0.625 (trachea). Average and maximum surface shear values are plotted for comparison and evaluation of factor effects..... 126
Figure 6.7 Top: 3D contour plot on the mean residence time of both trachea (r_i/r_o =0.625) and bronchus (r_i/r_o =0.5). Bottom: Interaction plots showing the coupled effect of rotation rate and flow rate to the mean residence time. Legend: black – 30 rpm, red - 120 rpm. Dashed line shows 95% confidence interval..... 128
Figure 6.8 Top: 3D contour plot on the second moment of RTD (variance) of both trachea (r_i/r_o =0.625) and bronchus (r_i/r_o =0.5). Bottom: Interaction plots showing the coupled effect of rotation rate and flow rate to the resulting variance. Legend: black – 30 rpm, red - 120 rpm. Dashed line shows 95% confidence interval. 130
Figure 6.9 Top: 3D contour plot on the second moment of RTD (variance) of both trachea (r_i/r_o =0.625) and bronchus (r_i/r_o =0.5). Bottom: Interaction plots showing the coupled effect of rotation rate and flow rate to the resulting variance. Legend: black – 30 rpm, red - 120 rpm. Dashed line shows 95% confidence interval. 132
Figure 6.10 Reactor residence time distribution contour plots showing the probability of occurrence of bypassing (Top plots) and tailing (bottom plots) for trachea and bronchus mounted in the reactor. Blue region shows desired characteristics of the bioreactor, whereas the red region are the parameters which causes bypassing and tailing. 134
Figure 6.11 H&E sections of native trachea (top) and post-reactor trachea (bottom). Magnification: 4x and 20x. Scale bar = 100 µm 137
Figure 6.12 Masson's trichrome sections of trachea. Magnification: 4x and 20x. Scale bar = 100 µm. Blue staining shows collagen, red is cytoplasm and connective tissue, while black stains for nuclei..... 139
Figure 6.13 Periodic acid-Schiff base staining sections of trachea. Staining showed infiltration of fungi. Magnification: 4x and 20x. Scale bar = 100 µm 140

List of Tables

Table 1.1. Secretion of functional molecules of human airway cells……..7

Table 1.2 List of materials used in cell and tissue engineering and their corresponding hydrogel elastic modulus……35

Table 1.3. Antibodies used in the experiment……..68

Table 5.1 Factors used in electrospinning……91

Table 6.1 Process factors used in RSM……..120

To the Almighty God Jesus Christ who bestowed me this purpose and gift to bless His people

Chapter 1

Introduction

Despite their relative architectural simplicity, human airways have a profoundly important role in maintaining lung function. Upon inhalation, the airways are not only used as a pathway of air to the lungs but also 1) improve the quality of the air by humidification and heating, 2) serve as a barrier to the external environment, 3) produce mucus to aid ejection of foreign particles and bacteria through coughing, and 4) provide structural support (Pierce & Worsnop, 1999). Each of the cell types present within the airways has a crucial role in one or more of these functions of the airways. Compromise of airway function results in a variety of pathological conditions including asthma and chronic obstructive pulmonary disease (COPD), which leads to increased mortality, morbidity and reduces the quality of life of patients diagnosed with such conditions.

Efforts to resolve airway damage caused by trauma and disease has inspired researchers to engineer the tissue itself, and over the past decade, various methodologies such as bioprinting and decellularisation of airways have been employed *in vivo*. Unfortunately, however, long-term success has thus far been elusive with tissue-engineered airway constructs mostly failing in animal models (ten Hallers *et al.*, 2004). These failures have likely been caused by mechanical failure, inflammation, malacia, or stenosis (Kojima *et al.*, 2002; Olze *et al.*, 1997; Vacanti *et al.*, 1994; Wechselberger *et al.*, 2002; Weidenbecher *et al.*, 2009). The long-term viability of tissue-engineered airway constructs has been reported in dogs (Kim *et al.*, 2004) and humans (Gonfiotti *et al.*, 2014) although

controversies arose over the scientific integrity of the trials (Vogel, 2015). The direct mechanisms on why these failures occurred are still unclear. Many tissue-engineered tracheas have been reported to be similar to native airways in terms of mechanical strength, glycosaminoglycan and hydroxyproline content, matured epithelial lining and other histological aspects (Aguirre *et al.,* 2010; Gao *et al.,* 2017; Hatachi *et al.,* 2018; Kojima *et al.,* 2003). However, it has become clear that a significant dissimilarity between these engineered airways and native airways is the absence of airway smooth muscle (ASM) in the engineered constructs. Molecular and mechanical cross-talk between cells is often fundamental to tissue growth and homeostasis (Lin *et al.,* 2017; Sanchez-Esteban *et al.,* 1998; Yu *et al.,* 2016), therefore the lack of ASM cells within the engineered airways could have profound effects upon cellular functions that compromise the airway integrity.

This thesis aims to provide new insights on the mechanisms that airway cells behave on different matrix properties and their possible interaction, specifically airway smooth muscle and epithelial cells. The findings to be discussed shed light on our current understanding of the physiology and pathology of the airways, and possible repercussions on treatment and management.

1.1 Classifications of human airway cells

The human airway is composed of several different types of cell, including chondrocytes, airway smooth muscle cells (ASMC), airway epithelial cells (AEC), mesenchymal stem cells (MSC), fibroblasts, neurons, fat cells (adipocytes) and endothelial cells. For this

literature review, the focus will be on interactions between chondrocytes, ASMC, AEC and MSC.

Chondrocytes are the resident cells of cartilage and produce abundant extracellular matrix (ECM) components made up of collagens, glycosaminoglycan and proteoglycans to create hyaline cartilage (Archer & Francis-West, 2003; Fox *et al.,* 2009), which mechanically supports the overall structure of the airway. ASMCs form together with a muscular tissue with connective fibres attached to the cartilage. The smooth muscle tissue is capable of contracting the airway luminal diameter which could modulate the air resistance as it travels in and out of the lungs (Amrani & Panettieri, 2003). AECs are located on the luminal side of the airways and provide a barrier to the external environment. These cells release mucus, which traps particles, pathogens and other foreign components for ease of ejection through coughing or sneezing (Mills *et al.*, 1999). Cilia on the pseudostratified epithelium contribute to this ejection through a process called mucociliary clearance. Lung MSCs are capable of differentiating into chondrocytes, ASMCs, or AECs to replace cells and maintain airway homeostasis (Rojas *et al.,* 2005). Fig. 1.1 is a diagram illustrating the histology of the airways and the location of the cells across different tracts.

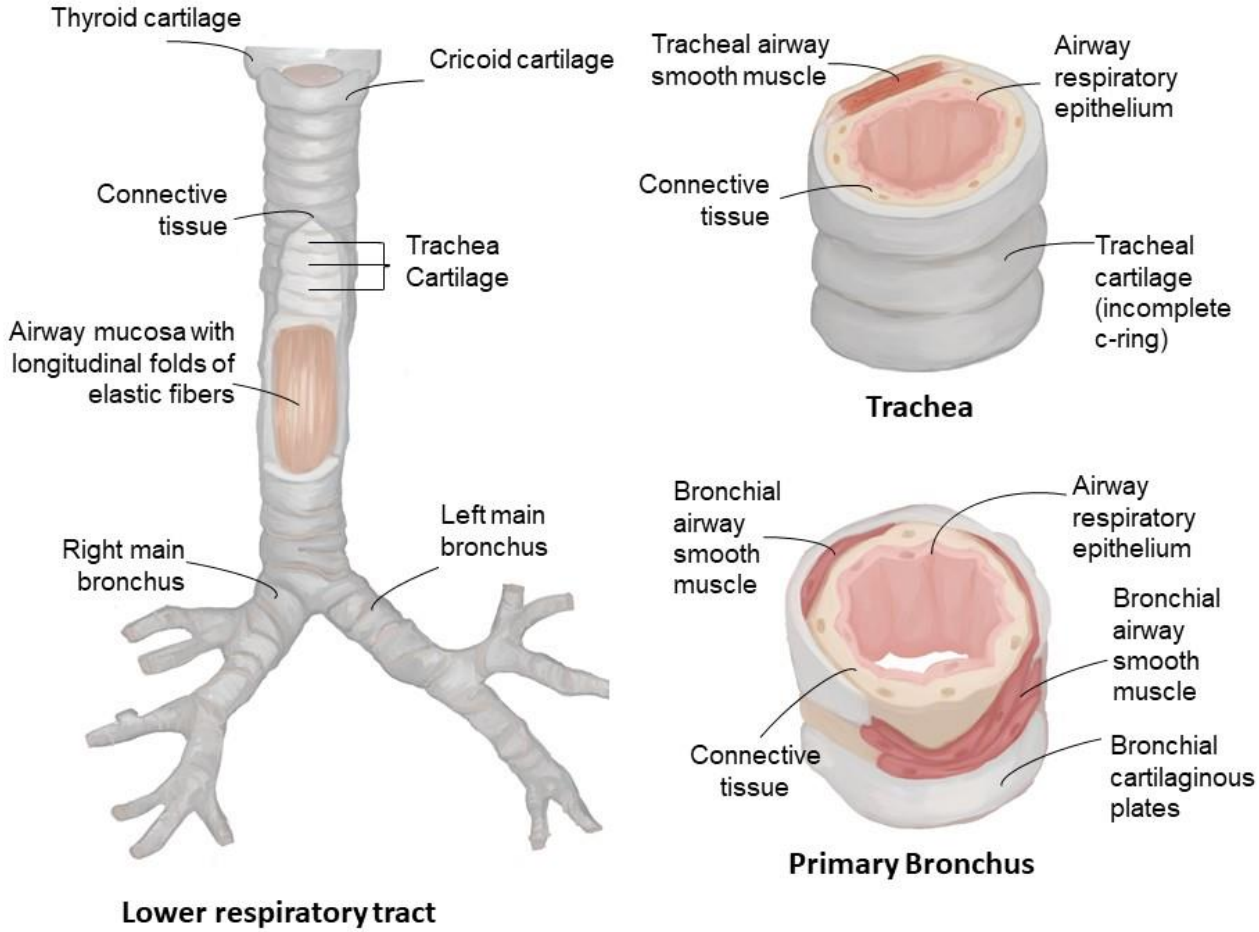


Figure 1.1. Cross-sectional isometric view of the anatomy of the lower respiratory tract. The trachea has the airway smooth muscle on the dorsal side which connects the incomplete c-ring of the cartilage. It is lined with pseudostratified ciliated epithelium. Intermittent cartilaginous plates are found within the length of bronchus, and underneath wrapped with airway smooth muscle tissue. The typical diameter of the trachea is 15-20 mm and 100-110 mm in length (Standring, 2016), (Breatnach *et al.,* 1984) . The left primary bronchus has an anteroposterior diameter of 9.6-12.3 mm and length of 41.9-43.9 mm, while the right primary bronchus diameter is 11.9-13.8 mm with length of approximately 13.8 mm (Lee *et al.,* 2014). All values shown are ranges for both adult men and women. Drawn by Francesca Tarsitano.

As with all organs and tissues interaction between each of these cells is likely to be fundamental for the maintenance of airway function and organ homeostasis. Understanding such interactions will be crucial if efforts to tissue engineer human airways are to be ultimately successful. Cell-cell interactions may occur via a combination of mechanisms including secretion of a vast array of functional molecules which can act in a paracrine

manner, and mechanobiological events where cell-cell interactions occur via transmission and detection of mechanical changes.

1.1.1 Expression of functional molecules of airway cells

A plethora of bioactive components, including growth factors and cytokines, can be released by the airway cells as described in Table 1.1 with a summary of interactions in Fig. 1.2. More detailed lists of the secretory profiles of chondrocytes (Polacek *et al.,* 2011; Polacek *et al.,* 2010; Rosenthal *et al.,* 2011), MSCs (Polacek *et al.,* 2011; Polacek *et al.,* 2010), ASMCs (Rossios *et al.,* 2017) and AECs (Hackett *et al.,* 2011) can be found elsewhere. Once released, many of these components are capable of autocrine and paracrine effects to induce either local cellular level changes or more wide-spread tissue-level changes in the airway to affect a vast array of signalling pathways that contribute to normal airway function and homeostasis.

Functional molecules released in the airways can be class clustered on their functionality. Mitogenic growth factors including epidermal growth factor (EGF), fibroblast growth factor (FGF) and Insulin growth factor (IGF) promote cellular proliferation (Barrow *et al.,* 1993; Retsch-Bogart *et al.,* 1990; Stamatiou *et al.,* 2012a). Tissue remodelling growth factors that modify the expression of extracellular matrix components include Transforming growth factor β (TGF- β), Interleukin-1β (IL-1β), vascular epithelial growth factor (VEGF) and Connective tissue growth factor (CTGF). Each of these factors is involved in wound repair and matrix remodelling pathways for maintenance of tissue homeostasis (Aizawa *et al.,* 2001; Ivkovic *et al.,* 2003; Lotz, 2001; Pufe *et al.,* 2004). Cytokines such as Interleukins act as inflammatory mediators in response to an injurious

or inflammatory stimuli or when a chronic pathological conditions arise, and they can alter the phenotype and secretions of molecules of airway cells (Govindaraju *et al.,* 2008; Jikko *et al.,* 1998; Khan, 2013; Kuperman *et al.,* 2002; Wang & Lou, 2001). Most of these functional molecules are produced by the cells comprising the airways in either homeostatic or pathological processes (see Table 1.1) and can change the function and/or phenotype of other cells.

Table 1.1 Secretion of functional molecules of human airway cells

Mesenchymal Stem Cell		Chondrocyte		Airway Smooth Muscle Cell		Airway Epithelial Cell	
Component	*Stimulant*	*Component*	*Stimulant*	*Component*	*Stimulant*	*Component*	*Stimulant*
Activin A[1,2]		Adrenomedullin[3]		Adrenomedullin[4]		Adrenomedullin[5,6]	
Angiopoietin-1[7]		Angiopoietin-like 4[8]	Hypoxia[8]	Amphiregulin[9]		Amphiregulin[10]	Cigarette smoke[10]
Angiopoietin-2[11]	Shear forces[11]	Angiopoietin-like 7[12,13]		Connective tissue growth factor [14,15]	TGF-β1[15]	Angiopoietin[5]	
Bone morphogenic protein-2[16,17] & 4[18]	Cyclic tensile strain[16], PGE_2[17]	Connective tissue growth factor[12,13,19-21]		Fibroblast growth factor-2[22]	Stem cell factor[22]	Endothelin[5,23,24]	Compression[24]
Connective tissue growth factor[12,13,19,20]		Chitinase 3-like 1[12,13,25,26]		Fibroblast growth factor-9[27]		Epidermal growth factor[5,28]	
Fibroblast growth factor-2[29,30]	Hypoxia[29], TNF-α[29]	Chitinase 3-like 2[12,13,26]		Fibroblast growth factor-10[31]	Injury[31]	Insulin growth factor-1[5,32]	
Hepatocyte growth factor[29,30]	Hypoxia[29], TNF-α[29]	Epidermal growth factor[28,33]		Interleukin-6[34,35]	Tumour necrosis factor α[35]	Interleukin-1β[36]	
Insulin growth factor-1[29,30,37,38]	Hypoxia[29], TNF-α[29]	Fibroblast growth factor-2[39]	Interleukin-1β[39]	Interleukin-8[9,40]	Interleukin-1β[40], TNF-α[40]	Interleukin-6[36,41]	Thrombin[41], Trypsin[41]
Interleukin-1[38]		Interleukin-6[42]	Fluid shear stress[42]	Nerve growth factor[43]	Interleukin-1β[43]	Interleukin -8[36,41] Nitric Oxide[44]	Thrombin[41], Trypsin[41], TNF- α[36]
Interleukin-6 [45]	Cyclic tensile strain[45], dexamethasone[45]	Nitric Oxide[46]	Interleukin-1[46]	Nitric Oxide[34]		Interleukin-11[36]	
Interleukin-7[47]		Osteomodulin[12,13]		Prostaglandin E_2[9]	Interleukin-1β[34]	Prostaglandin E_2[41]	Thrombin[41], Trypsin[41]
Interleukin-8[45]	Cyclic tensile strain[45], dexamethasone [45]	Prostaglandin E_2[33]	EGF[33]	Transforming growth factor-α[28]		Transforming growth factor-β1[36], β2[5],	
Interleukin-10[19, 20]		Transforming growth factor-α[28]		Transforming growth factor-β1[22,48]	Stem cell factor[22], Neutrophil-derived elastase[49]	Tumour necrosis factor α[36]	
Osteoprotegrin[2]		Vascular endothelial growth factor[50]		Vascular endothelial growth factor[51-53]	Angiotensin-2[52], Endothelin-1[52], TGF-β1[53], Bradykinin[51]	Vascular endothelial growth factor[9,41,54]	Thrombin[41], Trypsin[41], Hypoxia[54], TGF-β1[54], Amphiregulin[9]
Platelet-derived growth factor[55]							
Transforming growth factor-β[2,30,56]	Osteopontin[57]						
Vascular endothelial growth factor[2,29,30,37,38,58]	Hypoxia[2,29], TNF-α[29], Pigment epithelium derived factor[58]						

References: 1.Djouad *et al.,* 2010, 2. Burdon *et al.,* 2011, 3.Chosa, E. *et al.,* 2003, 4.Upton *et al.,* 2001, 5.Hackett *et al.,* 2011, 6.Martinez *et al.,* 1995, 7.Fang *et al.,* 2010, 8.Murata *et al.,* 2009, 9.Deacon & Knox, 2015, 10.Maunders *et al.,* 2007, 11.Gardner *et al.,* 2016, 12.Polacek *et al.,* 2010, 13.Polacek *et al.,* 2011, 14.Johnson *et al.,* 2006, 15.Xie *et al.,* 2005, 16.Sumanasinghe *et al.,* 2006, 17.Arikawa *et al.,* 2006, 18.Wislet-Gendebien *et al.,* 2004, 19.Omoto *et al.,* 2004, 20.Fukunaga *et al.,* 2003, 21.Huang *et al.,* 2010, 22.Oliveira *et al.,* 2016, 23.Fagan *et al.,* 2001, 24.Lan *et al.,* 2018, 25.Recklies *et al.,* 2002, 26.Hu *et al.,* 1996, 27.Coffey *et al.,* 2013, 28.Ruocco *et al.,* 1996, 29.Crisostomo *et al.,* 2008, 30.Baraniak & McDevitt 2010, 31.Volckaert *et al.,* 2011, 32.Chetty *et al.,* 2004, 33.Huh *et al.,* 2003, 34.Johnson & Knox 1997, 35.McKay *et al.,* 2000, 36.Mills *et al.,* 1999, 37.Chen *et al.,* 2008, 38.Takahashi *et al.,* 2006, 39.Chien *et al.,* 2016, 40.John *et al.,* 1998, 41.Asokananthan *et al.,* 2002, 42.Mohtai *et al.,* 1996, 43.Freund *et al.,* 2002, 44.Guo *et al.,* 1995, 45.Sumanasinghe *et al.,* 2009, 46.Stadler *et al.,* 1991, 47.Nemoto *et al.,* 2013, 48.McKay *et al.,* 1998, 49.Lee *et al.,* 2006, 50.Lingaraj *et al.,* 2010, 51.Knox *et al.,* 2001, 52.Alagappan *et al.,* 2007, 53.Wen *et al.,* 2003, 54.Boussat *et al.,* 2000, 55.Windmolders *et al.,* 2014, 56.Spees *et al.,* 2016, 57.Driver *et al.,* 2015, 58.Li *et al.,* 2016

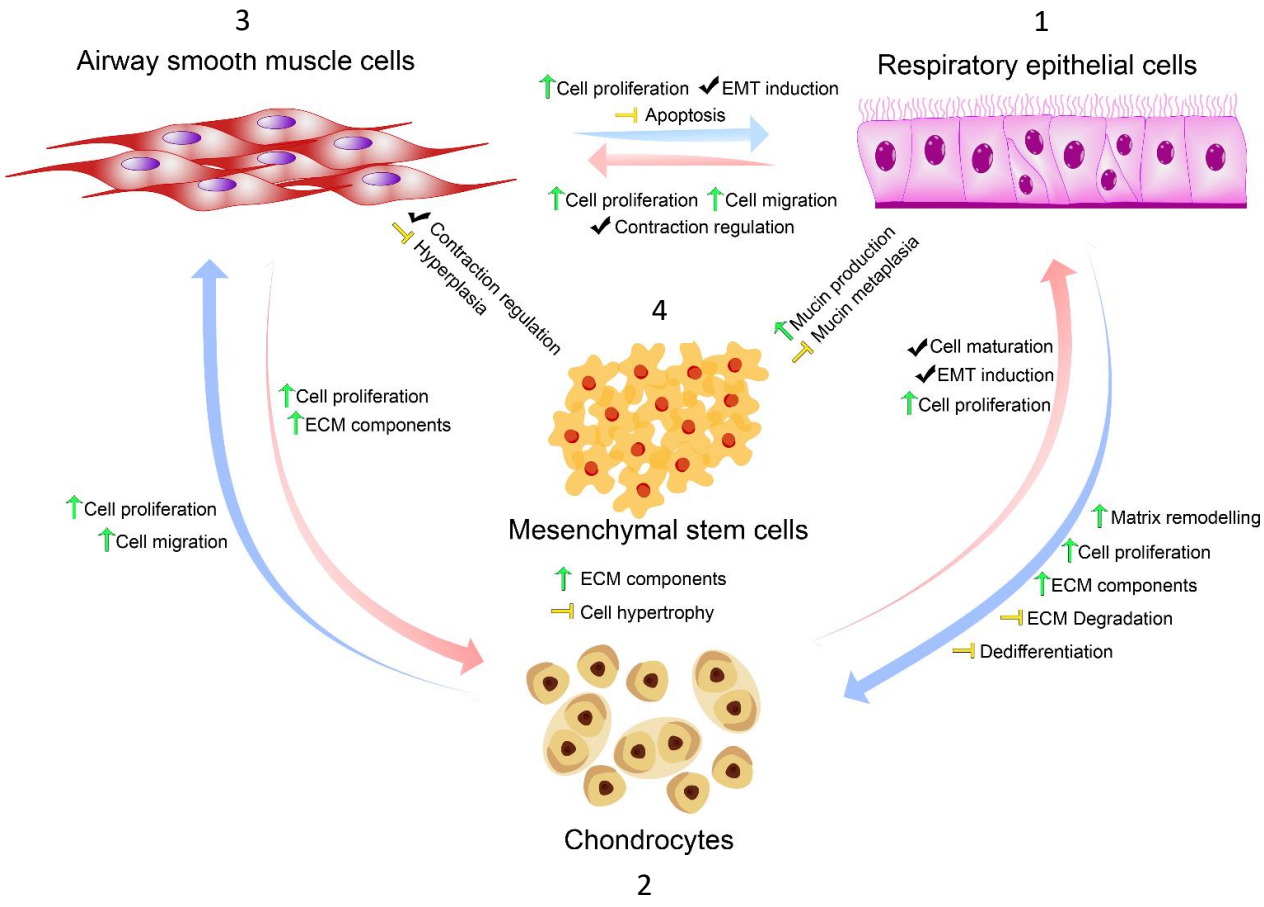


Figure 1.2. Summary of potential interaction of airway cells in normal physiology via paracrine signalling, cell-cell interaction, and mechanotransduction cascades as listed in Table 1.1. Legend: green upward arrow – upregulation, horizontal flat arrowhead – inhibition, check symbol– enabling function. Agonists secreted by the epithelium (1) contribute to proliferation and microenvironment changes in chondrocytes (2) and ASMCs (3), which a feedback system is in place. MSCs (4) also provides regulation of function in the airways.

1.1.2 Mechanobiology in the Lung

The lungs are an inherently mechanical organ, subjected to constant cycles of stretching and relaxation during breathing. An adult, on average, takes 12-20 breaths per minute during tidal breathing (Huether & McCance, 1994). The cells comprising the airways are therefore adapted to this mechanical environment and in many cases can respond biologically to it in a process known as mechanobiology. In fact, mechanical processes are critical to healthy lung development and regrowth of the lung following surgical resections

(Sanchez-Esteban *et al.,* 1998). This statement is supported by the emerging role of YAP (Yes-associated protein) and TAZ (transcriptional coactivator with PDZ-binding motif) transcription factors as mediators for mechanical stimuli. YAP/TAZ are main effectors of the Hippo pathway which ultimately affect cell growth, proliferation and inhibition of apoptosis (Mohri *et al.,* 2017). Stretching the matrix in which cells are embedded can activate YAP/TAZ, which in turn deactivates contact inhibition and thereby activate proliferation (Aragona *et al.,* 2013). Furthermore, it has recently been shown that stretch-mediated activation of TGF-β regulates macrophage function (John *et al.,* 2016), suggesting that breathing may play a crucial role in maintaining immune homeostasis in the lung.

1.1.3 Secretome-Mechanotransduction feedback signalling

There is the potential for crosstalk between mechanobiology and secretory pathways in the lung. Mechanical signals are able to influence the secretion of functional molecules in the airway, which can then contribute in a positive feedback manner to cellular and tissue-level mechanical action such as contraction and relaxation. For example, mechanical signals including stretching and contraction can cause the activation and release of TGF-β from epithelial cells and ASM cells (Jenkins *et al.,* 2006; A. E. John *et al.,* 2016; Jolly *et al.,* 2014; Tatler *et al.,* 2011). Once activated TGF-β has the potential to influence the contraction of airway cells (Goldsmith *et al.,* 2006; Zaleskas *et al.,* 2001) as well as regulating remodelling processes (Le *et al.,* 2007; McMillan *et al.,* 2005; Postma & Timens, 2006). Fig. 1.3 shows the global contraction mechanism that occurs in trachea

where airway smooth muscle tissue, upon response to an agonist, contracts or relaxes. This mechanism also occurs in bronchi, but the constriction is more pronounced as the wall integrity is weaker due to less cartilage, as well as the airway smooth muscle location that is wrapped around the bronchus tubes.

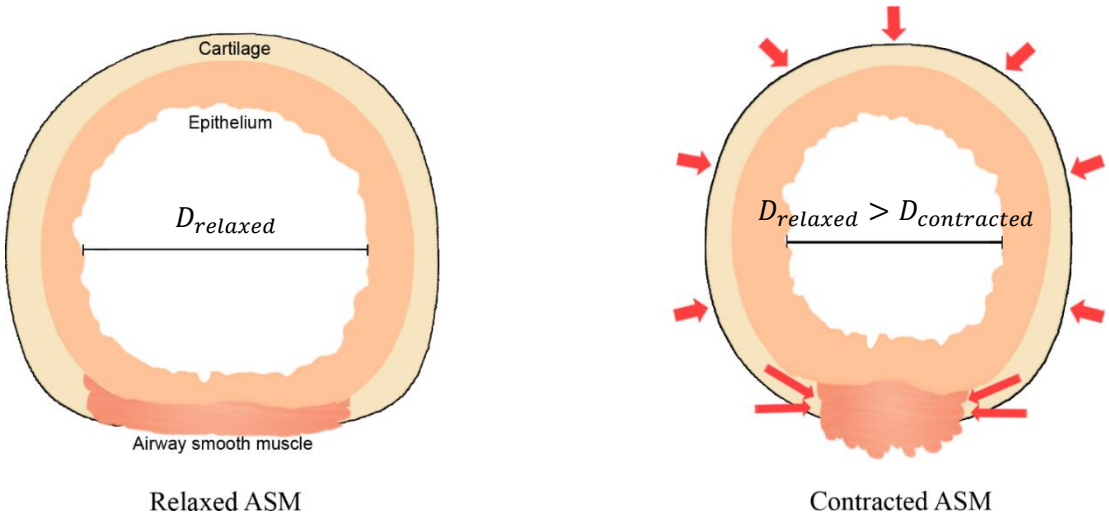


Figure 1.3. Tracheal ASM in relaxed and contracted state. After stimuli induction, ASMCs shorten actin and myosin filaments resulting in contraction of the tissue and therefore reducing the luminal diameter of the trachea. Upon contraction, compressive forces are introduced cyclically on the whole organ, thereby inducing global mechanobiological stimuli throughout airway cells.

Altered mechanical movements can then drive cells to secrete growth factors and cytokines, and so perpetuating the loop. Fig. 1.4 shows the proposed feedback loop on secretome-mechanotransduction pathways, where cellular to organ level responses are mapped with corresponding secretome and mechanobiological actions. Evidence of the feedback mechanism can be observed in the early works of Fedan's team where it has been shown *ex vivo* that the presence of cartilage and epithelium affected the contraction of the ASM (Raeburn *et al.,* 1986)' (Hay *et al.,* 1986) . Removal or denudation of cartilage and epithelium lead to the altered sensitivity of airway smooth muscle.

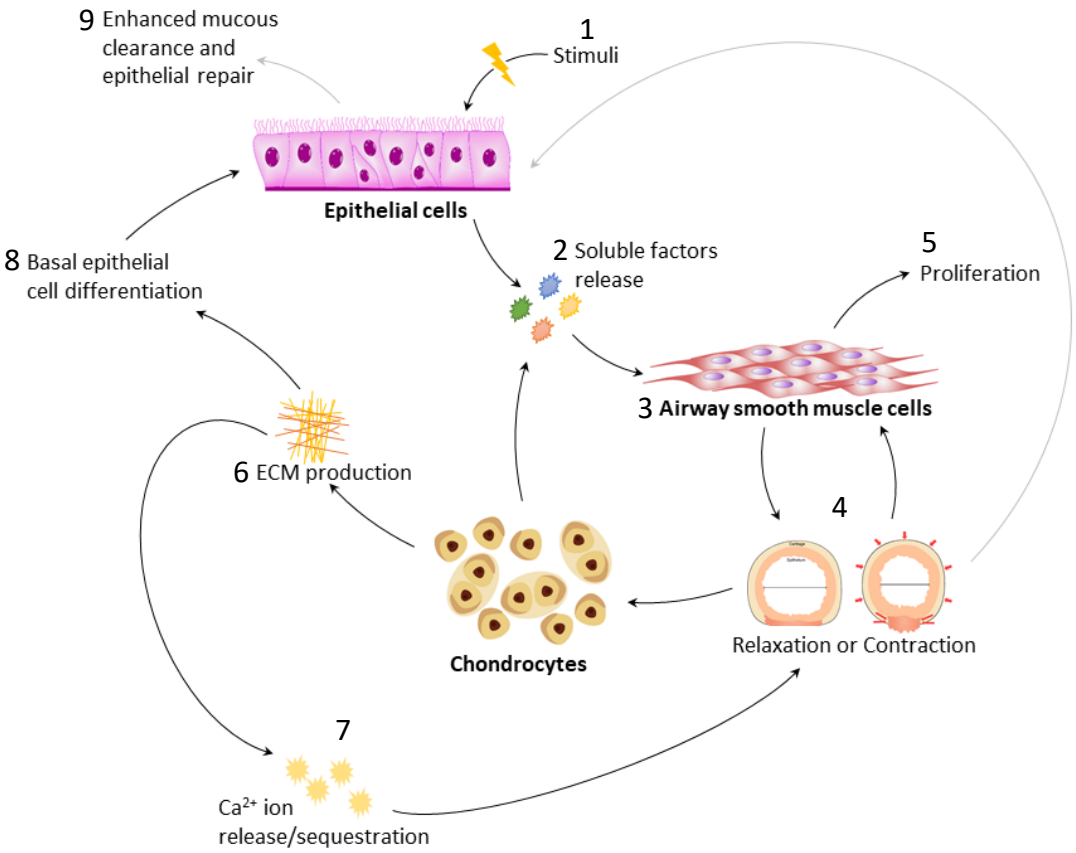


Figure 1.4. General mechanotransduction dynamics in the airways. Epithelium-induced ASM contraction coming from external stimuli (1) such as particulates from inspired air or epithelial damage cascades throughout the airways by the release of functional molecules (2) that act as a stimulant to the ASMCs (3). Cyclic contraction or relaxation of ASM (4) due to epithelial-derived agonists affects the whole organ in which a compressive force is induced. This increases the rate of proliferation of ASMCs (5), initiating ECM production in chondrocytes (6) that both serve as a Ca^{2+} ion reservoir for modulation of ASM activity (7) and as a scaffold on basal epithelial cells on the interface of cartilage and epithelium (8), where epithelial cells differentiate further into a pseudostratified epithelium with diverse phenotypes. The cyclic compressive force also increases the ciliary beat frequency of AECs and ATP release, enhancing mucus clearance and inducing epithelial repair (9).

Contraction of the airways is primarily mediated through either cellular secretions or neural control. Since AECs are exposed to the external environment conditions, it can be hypothesized that the airway epithelium is a key activator of the mechanotransduction cascade, and can release factors to induce contraction or relaxation of the airways. The

ASM then is the central biological actuator and receives signals to either contract or relax. Chondrocytes are the regulators of the process: mechanically like a hinge that translates the movement of the ASM into the whole organ, as well as metabolically through regulation of Ca^{2+} fluctuations that entirely affects the contraction of ASM. This global-scale interaction can be seen as the main regulatory pathway for organ maintenance and homeostasis.

The importance of such cellular interactions has been demonstrated *in vivo*. Mouse mutants genetically manipulated to inhibit cartilage or smooth muscle formation in the developing airways have shown the co-dependence of cartilage and smooth muscle upon growth, the important role of the cartilage on the epithelium differentiation, and that the absence of either tissue resulted in malformation of the airway (Hines *et al.,* 2013). This study highlights the necessity of understanding the interplay between cell types in the airway.

1.2 Interactions of airway cells

1.2.1 The physiological airway: major cellular roles

The cellular niche of the airways provides pathways for the homeostasis of the surrounding tissues. Structurally, the lumen of the airway is covered by AECs that are supported by the cartilage and modulated by ASMCs. In the physiological condition, it can be hypothesized that the AECs receive stimuli from the environment and provide cues for the airway dynamics; cell and tissue-level event cascades initiated by the secretome can drive multiple responses in the airways (Fig. 1.4). Growth factors secreted by AECs (Hackett *et al.*, 2011; Maunders *et al.*, 2007), ASMCs (Coffey *et al.*, 2013; Johnson *et al.*, 2006; Xie *et al.*, 2005),

and chondrocytes (Hu *et al.,* 1996; Polacek *et al.,* 2011; Polacek *et al.,* 2010; Recklies *et al.,* 2002) can act as mitogens across all cell types thereby driving cellular proliferation (Nishida *et al.,* 2002; Stamatiou *et al.,* 2012b; Weksler *et al.,* 1999), migration (Takeda *et al.,* 2009), and cell survival through protease-activated receptor-2–, AKT-, ERK-, and p38-MAPK dependent pathways (Stamatiou *et al.,* 2012a; Walker *et al.,* 1998), (Malavia *et al.,* 2009) . Several of the factors released are being induced either by other growth factors or via mechanotransduction, prompting a cascade of events to maintain cellular homeostasis (see Table 1.1 for a list of factors and known stimulant).

Apart from cellular proliferation, the integrity of the airways is also dependent on the secretion of molecules for maintenance of the extracellular environment. Acting as the mechanical framework of the airways, chondrocytes produce mechanically resilient ECM components like collagen type II and proteoglycans that are necessary for the load-bearing capacity of the airway (Archer & Francis-West, 2003; Fox *et al.,* 2009). These components can be upregulated through 1) secretome, by factors secreted by AECs (Chetty *et al.,* 2004; Fagan *et al.,* 2001; Hackett *et al.,* 2011; Mills *et al.,* 1999) and 2) mechanotransduction, by the contraction-relaxation mechanism of ASMCs that relates to TGFb activation (Tatler *et al.,* 2011). The latter mechanism might be explained by the fact that chondrocytes when subjected to cyclic compressive stress, upregulate their ECM production (Mauck *et al.,* 2000; Sanchez-Adams *et al.,* 2014). This suggests that the mechanotransduction events produced by the ASMCs can influence chondrocyte functionality. In the remodelling phase, AECs secrete several cytokines that may aid chondrocytes in their growth phase, inducing the release of matrix remodelling enzymes for tissue expansion (Aizawa *et al.,* 2001; Lotz, 2001; Pufe *et al.,* 2004). Additionally, a paracrine feedback response of EGF

from AECs to chondrocytes can trigger the release of PGE_2 (Huh *et al.,* 2003), which increases the rate of proliferation of AECs through induction of c-Jun and Three-phosphoinositide dependent protein kinase-1 (PDK1) pathways (Fan *et al.,* 2015).

Chondrocytes, in turn, regulate physiological responses of AECs and ASMCs. The maintenance of epithelial integrity is dependent upon fibroblast growth factor 2 (FGF-2) (Guzy *et al.,* 2015) , which chondrocytes secrete in response to interleukin-1β (IL-1β) (Chien *et al.,* 2016) . AECs produce IL-1β after an insult from an allergen or related stimuli (Mills *et al.,* 1999). This potential feedback loop provides an example of AECs responding to an environmental insult via secretion of mediators leading to activation of nearby chondrocytes to maintain AEC and airway homeostasis. In terms of ASMC regulation, ECM components produced by chondrocytes can serve as a reservoir of Ca^{2+} ions due to their highly negative net charge. This modulates ASM contraction (Gupta *et al.,* 1991; Raeburn *et al.,* 1986) which affect its differentiation and growth. The feedback loop between the production of cartilage ECM and ASM contraction-relaxation affects the extent of the mechanical effects (contraction and relaxation) the airway is being induced. Such effects has been investigated by Ramchandani et al. (Ramchandani *et al.,* 2000) , where the proportion of cartilage to ASM influence mechanical compliance of the airways. This interaction varies highly from developmental to maturation state of the airways (Ramchandani *et al.,* 2000).

Overall, a broad and complex interaction is seen between cell types. Fine-tuning of secretory and mechanotransduction effects initiated by resident cells in the airways are necessary for homeostasis conditions.

1.2.2 Airway Cell Interactions in the Developing Airway

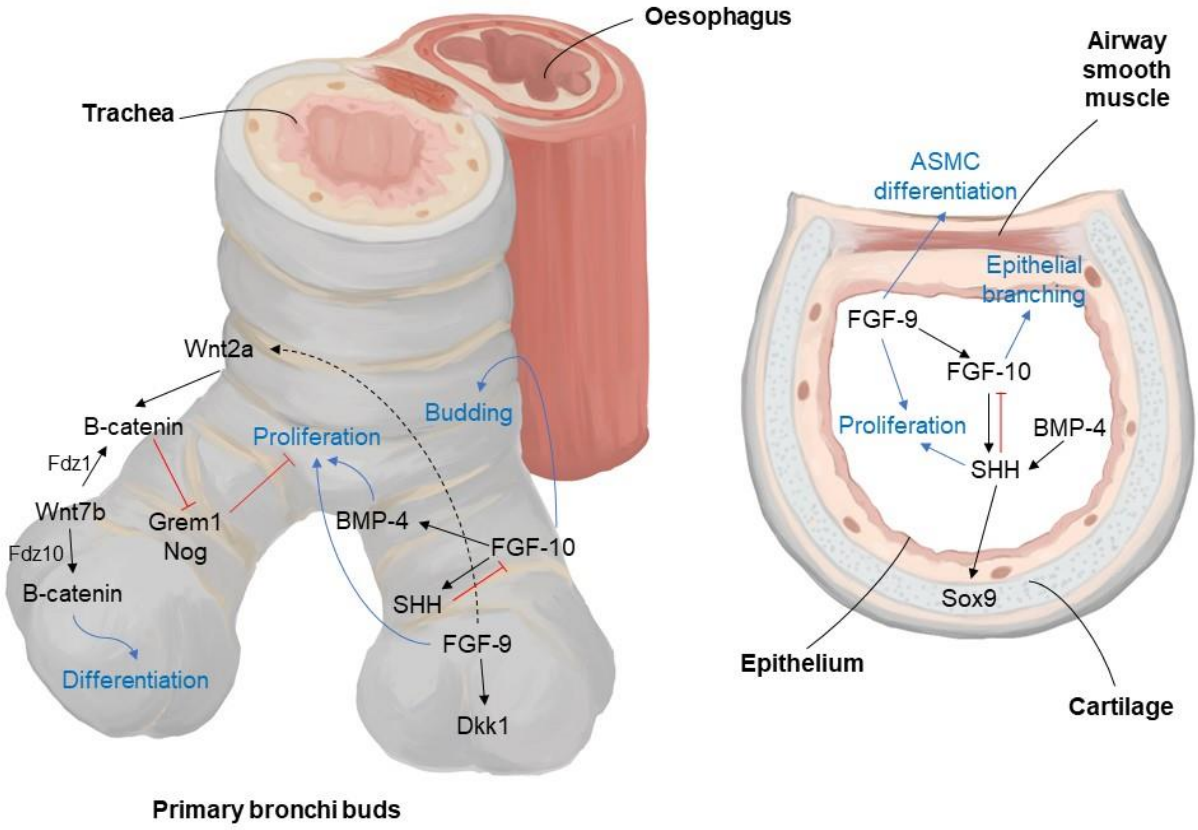


Figure 1.5. Signalling pathways in the developing airways. Key functional molecules are Sox9 (cartilage formation), FGF-10 (epithelial branching), and FGF-9 (ASMC differentiation). Drawn by Francesca Tarsitano.

Pansky outlines the overview of human airway development (Pansky, 1982). A laryngotracheal groove forms and deepens starting at week 4 of embryonic life. This part forms the primitive airways, with two bronchi buds forming at week 5. Differentiation of ASMCs starts at the end of week 7 and, a week after, the visibility of the tracheal cartilage through mesenchymal rudiments are already seen. Tracheal cartilaginous mass further develops in a cranial to caudal fashion, occurring concurrently as fibroelastic tissues between the rings and airway smooth muscle within the c-ring cartilage gap arises within

two weeks. On the other hand, cartilage development is seen at week 10 in primary bronchi and week 12 in segmental bronchi. Additionally, ASMCs aid the posterior wall formation of the larger bronchi where cartilage tissue is absent. In the trachea, the ciliated epithelium appears at week 10, and mucosal glands are seen from week 12, similarly following a craniocaudal direction (Pansky, 1982a). The bronchi, however, forms ciliated epithelium at week 12 and a week afterwards produce mucous glands (Pansky, 1982b). At week 20, the microscopic features of the trachea are visible, followed by the bronchus; both the final forms are reached post-natal (Pansky, 1982a). A general scheme on developmental signalling is shown in Fig. 1.5.

The importance of mesenchymal cells on the developing organ highlights the potentially important role of airway smooth muscle for the maturation of the airway as it is differentiated earlier than the rest of the cells. ASMCs drive the layout structure of the airways via FGF-10 (Mailleux *et al.,* 2005) signalling that is required for lung morphogenesis (Bellusci *et al.,* 1997). Airway ASM peristalsis in the prenatal environment (Jesudason *et al.,* 2006), which increases frequency towards birth (Parvez *et al.*, 2006), cues the cause of intermittent c-ring structure formation in the trachea as mechanical contraction is varied periodically across the tissue. Cartilage maturation can also be observed in co-culture of chondrocytes with ASMCs increases production of collagen II and IX by chondrocytes, increasing their pro-chondrogenic activity (Cairns *et al.*, 2010). Both cell types affect the function of each other on proliferation, differentiation, and airway biomechanics (Hines *et al.,* 2013), which in turn affect the epithelial coverage and differentiation of the airways (Shannon *et al.,* 1998).

As the ASM forms, it pushes the luminal fluid to the terminal ends of the airways by peristaltic phasic contraction (Schittny *et al.,* 2000). A rhythmic ASMC contractility is observed due to intercellular calcium wave propagation (Featherstone *et al.*, 2005). These calcium waves can then affect calcium-activated chloride channels that release chlorine ions to the adjacent AECs, stimulating the secretion of prenatal lung liquid. This is known as the fluid pump hypothesis (Jesudason, 2009), where the interaction between ASMCs and AECs via mechanotransduction and secretome pathways are highlighted as necessary to support lung development. AECs can also release nitric oxide (NO), which can act as an ASM relaxant by decreasing the Ca^{2+} oscillation on cells (Perez-Zoghbi *et al.,*2010). NO is found to be released in the bronchial and proximal bronchiolar epithelia in foetal state, suggesting its contribution to airway morphogenesis (Sherman *et al.,* 1999). Phenotypically, ASMCs that are in non-contractile state are in a proliferative state, with associated reduced expression of contractile components such as smooth muscle myosin heavy chain (sm-MHC), calponin, sm-alpha-actin, and desmin (Halayko *et al.,* 1996). A similar effect on ASMC relaxation can also be induced by PGE_2 (Lan *et al.*, 2001), which can be secreted from AECs (Barnett *et al.,* 1988). It is therefore apparent that the airway epithelium can regulate contraction of ASM (Barnes *et al.,* 1985; Barnett *et al.,* 1988; Panitch *et al.,* 1993) in early lung development. Since the epithelium is the exposed layer of the airways, stimuli coming from external sources can cause the release of agonists that regulate contraction and relaxation of ASM. It can be viewed that AECs provide the biochemical stimuli and ASMCs the mechanical stimuli.

Cartilage, on the other hand, is capable of influencing the phenotype and/or function of AECs. The absence of cartilage in the trachea has been proven to decrease basal cell density, precocious development of club cells, and decreased $KRT14^+$ cell population (a cell that has high reparative effects on the airways); all likely due to altered FGF signalling (Hines *et al.,* 2013). Chondrocytes express and release connective tissue growth factor (CTGF) (Fukunaga *et al.,* 2003; B.-L. Huang *et al.,* 2010; Omoto *et al.,* 2004; Polacek *et al.,* 2011; Polacek *et al.,* 2010) , which can induce epithelial-mesenchymal transition ((EMT) (Sonnylal *et al.,* 2013) , generating fibroblasts (Câmara & Jarai, 2010) between the layers of where AEC and chondrocyte reside. Such fibroblasts can proliferate in response to FGF (Gospodarowicz & Moran, 1975) (which chondrocytes also produce), and so in time, develop a perichondrium layer. The presence of a perichondrium in the intersection of epithelial and cartilage tissue layers could, therefore, result from the paracrine effects of the chondrocytes on the basal layer of the respiratory epithelium.

The airways also, in response to an injury, are believed to recapitulate the developmental conditions: ASMCs in onset of injury express FGF-10, a growth factor secreted from progenitor ASMCs (Mailleux *et al.,* 2005) in developing lungs, which promotes epithelial repair (Volckaert *et al.,* 2011). Results also from Hines et al. reinforce the likelihood of the cartilage as a developmental niche for airway basal cells (Hines *et al.,* 2013), supporting the epithelial regeneration pathway. The crosstalk between cells help maintain the integrity of the airways, following the same developmental pathways for whole organ homeostasis. However, in pathological conditions, signalling and biomechanics are compromised, resulting in unsynchronised overgrowth or degradation of tissues within the airways coupled with overlapping signals that perpetuate the condition.

1.2.3 The pathological airway: dysregulation cascades

The mechanobiology and signalling pathways in the airways are significantly altered in pathological conditions. Current information on the mouse and pig cystic fibrosis models show cartilage and ASM abnormalities prior to subsequent epithelial defects (Bonvin *et al.,* 2008; Meyerholz *et al.,* 2010; Pan *et al.,* 2006). Similarly, in the developing airways, epithelial defects are also seen when there are aberrations in cartilage and ASM formation (Hines *et al.,* 2013). The hypothesis on recapitulation of developmental signalling in the adult state could also be reflected to the pathogenesis in asthma: inferior mechanical properties of the cartilage (Haraguchi *et al.,* 1999b), increased ASM mass (Carroll *et al.,* 1993; Regamey *et al.,* 2008) coupled with hypercontractility (Ma *et al.,* 2002; Matsumoto *et al.,* 2007) and altered AEC phenotype which integrity is lost (Naylor, 1962). Fig. 1.6 shows the anatomy of the bronchi in normal and pathological conditions.

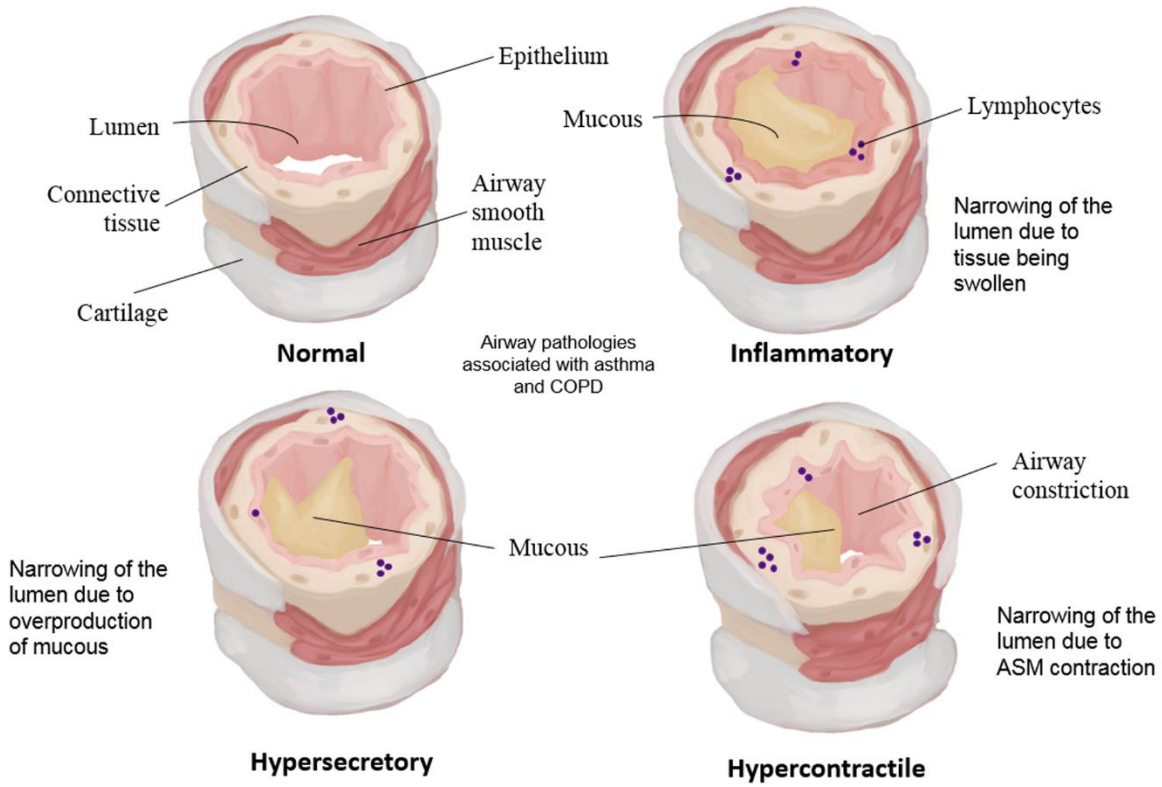


Figure 1.6. Anatomy of pathologies in the bronchus. Inflammation, mucous over secretion, and hypercontractility of the ASM are few of the pathologies seen in the trachea and bronchi. Drawn by Francesca Tarsitano.

As previously discussed, mechanical events such as the cycles of contraction and relaxation in the airways can affect the release of soluble factors, which in turn can have paracrine effects of mediator release and mechanobiology. However, excessive mechanical activity and elevated soluble factors release can arise from pathologic conditions, such as asthma, which shifts the equilibrium so that cellular responses are aberrant. These events alter the microenvironment, specifically the ECM components, and can lead to perpetuation of pathologic conditions in the airways. For example in asthma, airway remodelling is vividly seen: ASM mass is increased (Regamey *et al.*, 2008), becomes hypercontractile (Ma *et al.*, 2002) and degradation of cartilage with increased perichondral fibrosis occurs

(Haraguchi *et al.,* 1999a). This is affected by altered cross-talk between ASMCs, AECs, and chondrocytes. Asthmatic ASMCs release increased amounts of PGE_2 (Khan, 2013) that can cause delayed development of chondrocytes by the inhibition of BMP signalling (Clark *et al.,* 2009). Dedifferentiated chondrocytes express elevated levels of smooth muscle actin (Kinner & Spector, 2001), synthesises collagen type I (Marlovits *et al.,* 2004) and acquires a contractile phenotype (Kinner & Spector, 2001; Parreno *et al.,* 2016). Additionally, IL-1β, which is involved in the pathogenesis of asthma, can causes FGF-2 release from chondrocytes (Chien *et al.,* 2016), which could promote fibroblast proliferation in the perichondrium and contribute to perichondrial fibrosis in asthma (Haraguchi *et al.,* 1999a). Furthermore, since ASMC contraction can activate TGF-β (Tatler *et al.,* 2011) which is a protein crucial for ECM production and pathological remodelling of airways, it is possible that enhanced airway contraction in asthma drives structural changes within the airways.

The collateral damage brought by structural and morphological changes in ASMCs and chondrocytes relays to the airway epithelium. Amphiregulin which is secreted highly from asthmatic ASMCs causes elevated expression of VEGF, PGE_2, Cyclooxygenase-2, and CXCL8 in AECs (Deacon & Knox, 2015; Kim *et al.,* 2009), which can modulate ASMC contraction and proliferation. In addition, the mechanotransducive effect of the ASMCs can also be perpetuated by the secretion of Endothelin-1 by AECs upon compression via ASM contraction to drive further ASMC proliferation and contraction (Lan *et al.,* 2018). In chronic pathological conditions, the airway epithelium is dysfunctional (Benayoun *et al.,* 2003), and one explanation is probably due to CTGF release of ASMCs from TGF-β1 stimulation (Xie *et al.,* 2005) thru AEC secretion (Mills *et al.,* 1999). As discussed above

in interaction between AECs-chondrocytes, CTGF may play a role in epithelial-mesenchymal transition of AECs, which could also be the case in ASMC-AEC crosstalk. However, in pathologic conditions such as COPD and asthma, CTGF overexpression promotes AEC senescence (Jang *et al.*, 2017). These senescent AECs alters the phenotype of the respiratory epithelium in pathological conditions. Peribronchial fibrosis, submucosal gland hypertrophy, and mucous metaplasia are the observed changes in the epithelium (Haraguchi *et al.*, 1999a), (Chung, 2005) . Additionally, since ASMCs are highly proliferative and contractile in these conditions, it will likely affect neighbouring cells due to changes in secretory and mechanobiological processes. Exacerbated by denudation of the cartilage in several pathological conditions, renewal of epithelial integrity will be difficult without any external intervention.

There have been several attempts to regulate the pathologies in the airways: from pharmaceutical to cellular-based methods. Looking back at the developmental origins of airway growth, progenitor cells may be the key to recapitulate the regenerative capacity of the airways.

Cues coming from the secretome and cell-cell interactions provide us with a snapshot on the physiological and molecular environment that the airway cells maintain. It has been shown in this literature review that a biological event from a cell population can have a cascading effect, from secretion to mechanical action and vice versa. This complex regulation of events changes drastically from developmental to adult physiology, whereas in the pathological state these events go uncontrolled, perpetuating dysregulation across

the organ. Mapping these interactions could provide new routes of intervention methods involving major phenomena occurring in pathologic conditions of the airways, and bring hope to the success of airway regeneration through tissue engineering and regenerative medicine.

1.2.4 Models for understanding the airways

The complex interaction in the airways can be segregated by developing models of the airways. Chondrocytes, airway smooth muscle and epithelial cells can be isolated readily from primary sources and then cultured in a 2D or 3D environment. The tuning of the factors that affect growth should easily be controllable as confounding factors might not replicate what is happening *in vivo.*

Of all the models being used, the most utilised model is the 2D *in vitro* cell culture. This is due to its simplicity and easiness to perform in a standard cell culture lab. Chondrocytes and ASMCs are usually cultured in a tissue culture plastic, while for AECs it is necessary to have an air-liquid interface to induce differentiation of cells similar to *in vivo* conditions. However, the main drawback in *in vitro* cell culture is the lack of 3D structure which affects the phenotype and cellular interactions (Duval *et al.*, 2017). In addition, the stiffness of the tissue culture plastic is much stiffer than the physiological stiffness levels, disabling contraction for the airway cells (Wright *et al.,* 2013) and dedifferentiation is observed in later passages (Caron *et al.,* 2012; Hayashi *et al.,* 1998).

A workaround traditional 2D tissue culture plastic culture is by coating the wells with collagen. Contractile activity can be effectively observed as collagen hydrogels are more

compliant with the traction of ASMCs, where a change in gel area can permit estimation of the extent of contraction (Matsumoto *et al.,* 2007). For chondrocytes, cell encapsulation effectively maintains its phenotype due to the inherent structure of the lacunae, where cells are surrounded by their matrix (van Susante *et al.,* 1995). In airway epithelial cells, the collagen augments its differentiation capacity and forms a 3D organised structure (Chevillard *et al.,* 1993). Collagen has been effective in obtaining a more physiological response in comparison with 2D cultures. The major caveat of using collagen however is that the stiffness level is only limited to several kPa (Lin & Gu, 2015); most cell types in the airways grow in a much stiffer environment (Candiello *et al.*, 2007; Rains *et al.,* 1992).

Advances in biomaterials have made it possible to create more relevant models for airway cells. Several modes of biomaterial production used in culturing the airways are bioprinting (Bae *et al.,* 2018; Kaye *et al.*, 2019), electrospinning (Bridge *et al.*, 2015; Mahoney *et al.*, 2016), and decellularized airways (Macchiarini *et al.*, 2008; Zang *et al.*, 2012). One of the most famous models was the tissue-engineered trachea made by the group of Paolo Macchiarini, where his team developed an airway made from either decellularized trachea matrix (Macchiarini *et al.,* 2008) or polyethylene terephthalate-polyurethane hybrid electrospun nanofibres (Ajalloueian *et al.*, 2014). Unfortunately, most of his patients died, and the major causes of death were airway occlusion, trachea-oesophageal fistula, and discontinuous epithelial coverage of the luminal side of the trachea (Corbascio *et al.,* 2014). This has caused a backlash in the tissue engineering of the trachea. To be able to fully control the microenvironment and its effect on airway cells is a necessity in order to provide the means on creating a compliant model for studying the airways. Matrix stiffness,

extracellular matrix composition, and the culture conditions are several parameters that needed to be tuned for complementing our current understanding of the airways.

1.3 Thesis aims

The general objective of the thesis was to understand the mechanisms of airway cells in its response to the mechanical properties of the matrix, and its possible interactions with the resident cells. Specifically, the aim was to understand the behaviour of airway smooth muscle and epithelial cells on scaffolds with differing, tuneable stiffnesses. The model developed herein demonstrates the culture of airway smooth muscle cells on gelatin methacryloyl hydrogels, where the stiffness can be tuned to mimic changes in stiffness associated with the physiological and pathological conditions. By assessing morphology, proliferation, and contractile markers of the cells the model demonstrates and correlates to physiological and pathological conditions of the airways. Further development of the model shows inclusion of the airway epithelial cells, cultured directly on electrospun gelatin methacryloyl scaffolds mimicking the basal membrane also and tuned to different stiffness. Finally, a bioreactor was designed to allow culture of tissue-engineered epithelium-airway smooth muscle.

The specific objectives are presented and investigated are as follows:

- Development of a method to synthesise gelatin methacryloyl to increase further its mechanical strength for mimicking physiological and pathological conditions
- Culturing airway smooth muscle cells in gelatin methacryloyl hydrogels with stiffness representing physiological and pathological conditions, in which morphology and markers for proliferation and contraction will be assessed
- Optimising electrospinning conditions to produce gelatin methacryloyl fibres, and develop a post-modification method to tune the stiffness and the surface chemistry of the produced fibres for culture of airway epithelial cells
- Design and build a bioreactor for culturing the airways, while supporting dual media culture and an air-liquid interface

Chapter 2

General Methods

2.1 Cell culture of primary airway smooth muscle cells

Primary airway smooth muscle cells were obtained from bronchial biopsies in Nottingham City Hospital (Nottingham, U.K.). The research was approved by the University of Nottingham Ethics Committee, and patients gave written informed consents in relation to the procedure. Cryopreserved airway smooth muscle cells (ASMCs) were received at passage 4, and defrosted at the standard expansion media of DMEM High Glucose supplemented with 10% Foetal Bovine Serum, 1% L-Glutamine, 1% Penicillin/Streptomycin, and 1% Antibiotic/Antimycotic solution (All from Sigma). Cells were expanded in T-175 flask in a humidified incubator at 37°C at 5% CO_2 in air.

2.2 Passaging primary airway smooth muscle cells

After 90% confluence, cells are aspirated with media, washed with PBS, and detached with 3mL of 0.05% solution of Trypsin-EDTA (Fisher Scientific) for 5 minutes in a humidified incubator at 37°C. Expansion media of 7 mL volume is added to neutralise the trypsin, and all contents were transferred into a 20 mL centrifuge tube. Cells were pelleted by centrifuging at x300g for 5 minutes, and the supernatant was aspirated. The pellet was resuspended in expansion media, counted using a Neubauer haemocytometer, and pipetted in a T-175 flask with a cell number of 5×10^5 cells/flask. A total of 20 mL media was

placed in the flask and incubated again until 90% confluence. Passages used in the study were 5-6 for primary airway smooth muscle cells.

2.3 Passaging of Calu-3 airway epithelial cell

Calu-3 cells were cultured in α-MEM (Lonza) supplemented with 1% Antibiotic/Antimycotic solution, 1 % Sodium Pyruvate, 1 % Glutamax, and 10% Foetal Bovine Serum (Sigma) in a T-75 flask at 37°C and 5% CO2. At 80% confluence, the cells are passaged by washing the flask with PBS and immersing with trypsin-EDTA solution for 5 min for detaching the cells. The trypsin was neutralised using the culture media and the cell suspension was centrifuged at 200g for 5 min. A split ratio of 1:3 was done for every passaging with the frequency of twice a week. For viability experiments, passage 34 was used throughout the studies.

2.4 Cryopreservation and resuscitation of cells

After cells were trypsinised and centrifuged, the supernatant was removed and the cells were resuspended in 90% v/v FBS and 10% DMSO (Fisher Scientific) at a density of 5 x 10^5 cells/mL. Each 1 mL of cell suspension is transferred into a 2 mL cryovial (Fisher Scientific) and cooled at a controlled rate of 1°C/minute via storage in Mr. Frosty™ (Fisher Scientific) at -80°C Freezer overnight. The vials were then transferred in a liquid nitrogen storage tank until used for experiments.

For cell resuscitation, vials were taken off the liquid nitrogen tank and thawed in a 37°C water bath until a small chunk of ice was present. The thawed liquid was pipetted in 5 mL of expansion media, centrifuged at x300g for 5 minutes, and the supernatant removed. The

cells were resuspended in 1 mL of expansion media, plated in a T-175 flask and incubated for further use.

2.5 Metabolic assay measurements

The metabolic assay was quantified using Presto Blue™ and used according to manufacturer's instructions. Briefly, the media was aspirated and replaced with a solution containing 10% v/v Presto Blue and 90% of the fresh media used in culturing the specific cell type. Samples are then incubated at 37°C at 5% CO_2 in air for 1 hr, and the supernatant was transferred to a black-walled 96-well plate, including blank samples. Fluorescence was measured using a plate reader (Tecan Infinite Pro M200), and blank readings were subtracted from the measured units.

2.6 DNA quantification

Protocol on DNA content evaluation was done using the PicoGreen assay kit (Fisher Scientific). Cells were detached from the scaffolds or wells by treating with Accutase (Sigma) for 15 mins. Afterwards, cells were centrifuged at x300g, aspirated the supernatant, washed once with PBS, centrifuged again, and aspirated once more the supernatant. Lysis buffer was placed and the solution was pipetted several times to ensure homogenisation. The lysates were digested with 50 U/mL of RNAse under ice for 10 minutes, and then mixed with PicoGreen reagent for 5 minutes. The fluorescence intensity was measured in a plate reader, and the values were converted into µg/mL DNA using calf thymus lambda DNA as a calibration standard. Values were converted into fold change by dividing the readings into the DNA content of samples at Day 0.

2.7 Scanning Electron Microscopy

Samples were dried in a vacuum oven at 20°C overnight prior to imaging. Mounting preparation was done by placing the sample on an aluminium stub with carbon tape, then subsequently coated with iridium for 60 seconds to obtain 10 nm thickness. Images were taken using Jeol 7100 Field Emission Gun SEM, at 5 kV acceleration voltage under vacuum.

Chapter 3

Development of downstream processes to improve physical and mechanical properties of methacrylated gelatin

3.1 Introduction

The study of cell mechanobiology and increasing evidence that matrix stiffness and composition can affect both genotype and phenotype of cells has led to the considerable current interest in using matrix properties as a tool and technology in cell biology research (Tschumperlin *et al.,* 2010). Matrix remodelling is known to have profound effects on tissue physiology where a minor shift in stiffness can lead to a range of effects, including proliferation, differentiation or apoptosis of cells and can also lead to pathological states like tissue fibrosis (Schrader *et al.,* 2011; Wells, 2005).

A relatively straightforward approach to investigate the mechanobiology of cells is to culture them on polymers where stiffness can be controlled and tuned. The classes of materials that can be used are either synthetic or natural polymers. Synthetic polymers are a class of polymers synthesised from monomeric molecules, where mechanical and chemical properties can be well-defined by tuning the synthesis parameters. These class of materials usually has high mechanical strength, excellent optical properties, and biocompatibility. However, the biological inertness of synthetic polymers often hampers

their applications, as the ability of the material to be changed by cellular remodelling is more desirable to recapitulate biomimetic response. Natural polymers, on the other hand, elicits a favourable cellular response. This is because it contains chemical moieties that are recognised by enzymatic units for degradation and remodelling. But usually, natural-derived materials can be friable after extraction, and thus requiring modifications to increase the mechanical properties that fit the application. The following table (Table 3.1) is a list of materials used for cell and tissue engineering with a given range of stiffness:

Table 3.1 List of materials used in cell and tissue engineering and their corresponding hydrogel elastic modulus

Material used	Cells used	Stiffness range (Elastic Modulus)	References
Synthetic Polymers			
Polyvinyl alcohol	Chondrocytes	1.85-3.66 MPa	(Bonakdar *et al.,* 2010)
Polyethylene glycol	Vascular smooth muscle cells	2-5 MPa	(Mann *et al.,* 2001)
Polyethylene glycol diacrylate	Chondrocytes	0.055-42.9 MPa	(Nguyen *et al.,* 2012)
Poly(hydroxyl-ethyl methacrylate)	Skeletal Muscle cells	0.56-13.3 MPa	(Barnes *et al.,* 1988)
Polyacrylamide	Airway smooth muscle cells	15 kPa-5 MPa	(Denisin & Pruitt, 2016)
Natural Polymers			
Hyaluronic acid	Fibroblasts	20.7-66.3 kPa	(Jeon *et al.,* 2007)
Alginate	Mesenchymal stem cells	3-10 kPa	(LeRoux *et al.,* 1999)
Collagen	Fibroblasts	75-200 Pa	(Jin et al. 2016)
Methacrylated Chitosan	Chondrocytes	25-400 kPa	(J. Hu *et al.,* 2012)
Methacrylated gelatin	Fibroblasts	2-30 kPa	(Nichol *et al.,* 2010b)

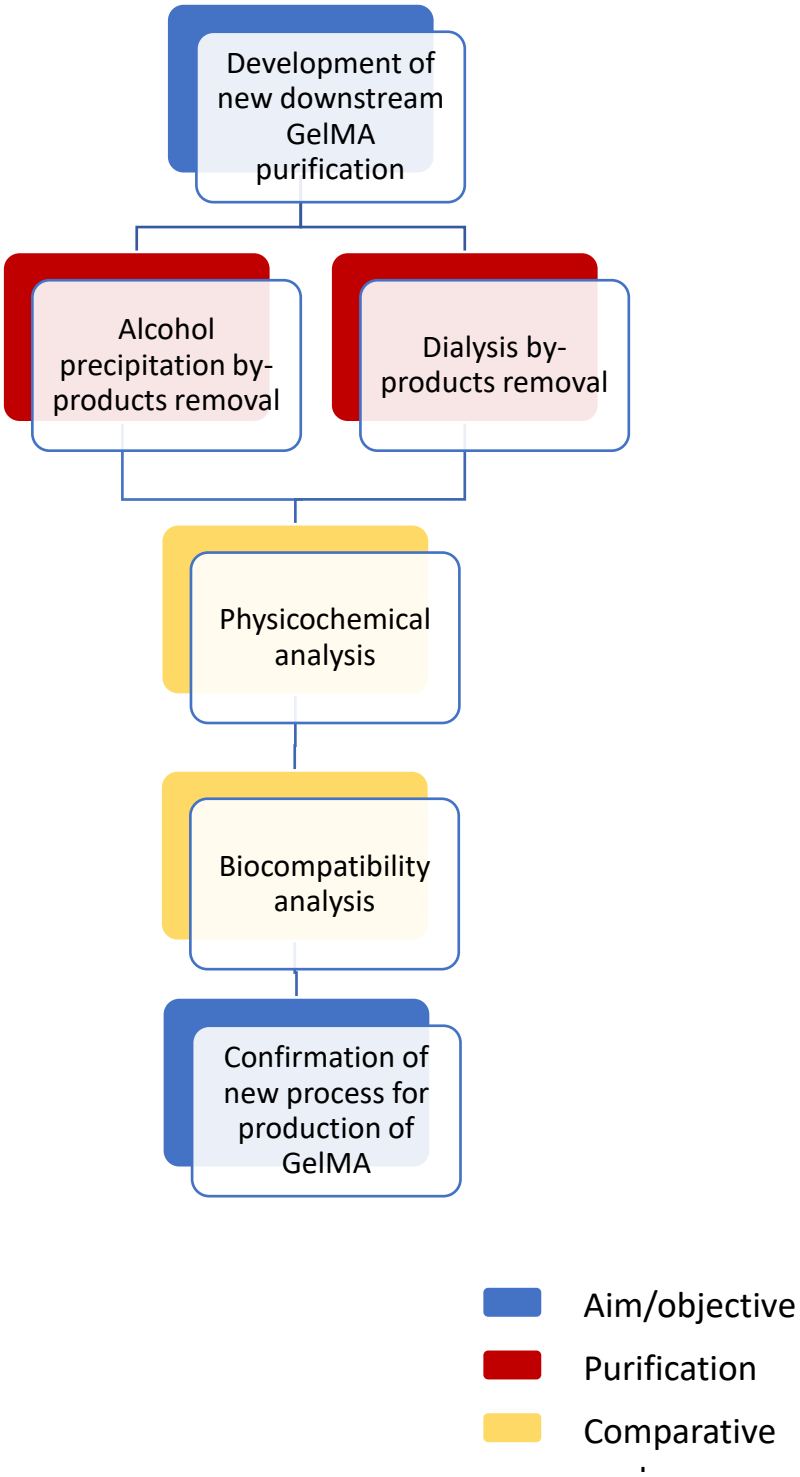
Stiffness of both polymer classes can be readily controlled by simply adjusting the concentration of the polymer, photoinitiators, and/or time of crosslinking. Synthetic polymers can achieve a higher elastic modulus which could be suitable for airway tissue

engineering, but they still do not contain moieties which could interact with integrins and matrix remodelling enzymes. Conjugation of integrin-binding motifs can improve cellular interaction, but cell-mediated matrix remodelling will still not occur due to inertness of the polymeric backbone. Turning into natural polymers, only collagen and gelatin contain both integrin-binding motifs and a backbone for cell-mediated degradation. This latter property is more desirable, because the dynamic response of cells to their environment is captured.

Collagen and gelatin are both being used in traditional cell culture methods to elicit cell attachment to tissue culture plates. However, in terms of mechanical properties, collagen can only attain modulus in the range of hundreds of pascals. Modifying the side chain of collagen by crosslinking has only increased its capacity to ~1500 Pa (Gaudet & Shreiber, 2012). The reason for such mechanical response is that the amount of material that can be placed in aqueous solutions is very low, as collagen is practically insoluble in water. Adjusting the pH can improve its solubility, but this might compromise the buffer capacity of the culture media to maintain a physiological pH. Gelatin, on the other hand, is a partially hydrolysed version of collagen and is much more soluble than collagen. The increased solubilisation of gelatin in aqueous solution permits elevated scaffold stiffness with increased solids content in the hydrogel. Modifying the gelatin side chains can improve further its mechanical properties, and the degree of modification can be adjusted to tune the stiffness of the material. The increased mechanical properties can be achieved while still having the integrin-binding motif RGD for cell interaction (Davidenko *et al.*, 2016). Additionally, since gelatin is made of partially denatured collagen, the matrix can be manipulated by cells themselves as the protein backbone is similar to the chemistries found in the airway matrix.

The matrix stiffness of GelMA, however, can only be stiffened to a few tens of kPa. As the objective of the work was to evaluate the matrix of airway cells in a wide range of mechanical properties, we aimed to increase the limit of GelMA stiffness by developing a new platform in its process of production. Currently, the method used for downstream processing uses dialysis, which can degrade gelatin by hydrolysis and so reduce the molecular weight and the resulting mechanical properties that are coupled with it. The hypothesis in this study was that by modifying the purification step to precipitation, it would improve the material's mechanical properties, make the more process more efficient in terms of time and yield, while still maintaining the biocompatibility of the material.

Chapter experimental overview



3.2 Materials and Methods

Gelatin from porcine skin (Type A, 175 bloom), methacrylic anhydride (MAA, 94%), denatured alcohol (100%), 2-hydroxy-1-(4-(hydroxyethoxy)phenyl)-2-methyl-1-propanone (Irgacure 2959), 2,4,6-Trinitrobenzene-sulfonic acid (TNBS), Dulbecco's Modified Eagle Medium (DMEM) sodium carbonate and sodium bicarbonate were all purchased from Sigma-Aldrich and used as received.

3.2.1 Syntheses of GelMA

A 10% wt/vol gelatin was prepared by dissolving gelatin in 0.25 M carbonate-bicarbonate buffer (7.95 g of Na_2CO_3 and 14.7 g $NaHCO_3$ in 1 L of deionised water) 60°C and 700 rpm. Upon complete dissolution, the pH of the solution was adjusted to 9.0 using 5.0 N NaOH, as suggested by the study of (Shirahama, *et al.*, 2016). While stirring, MAA was added at a ratio of 0.2 mL/grams gelatin at a rate of 0.5 mL/min through manual pipetting. The reaction was held in a light-free condition and minimised air uptake environment, where a narrow-necked reaction vessel was covered by aluminium foil. After 2 h of stirring, the reaction was halted by neutralising the solution into a pH of 7.4 by adding 5.0 N NaOH or 1 M $NaHCO_3$. The reaction products were processed either via conventional dialysis method, or precipitation method (Fig. 3.1), which the following sections discuss.

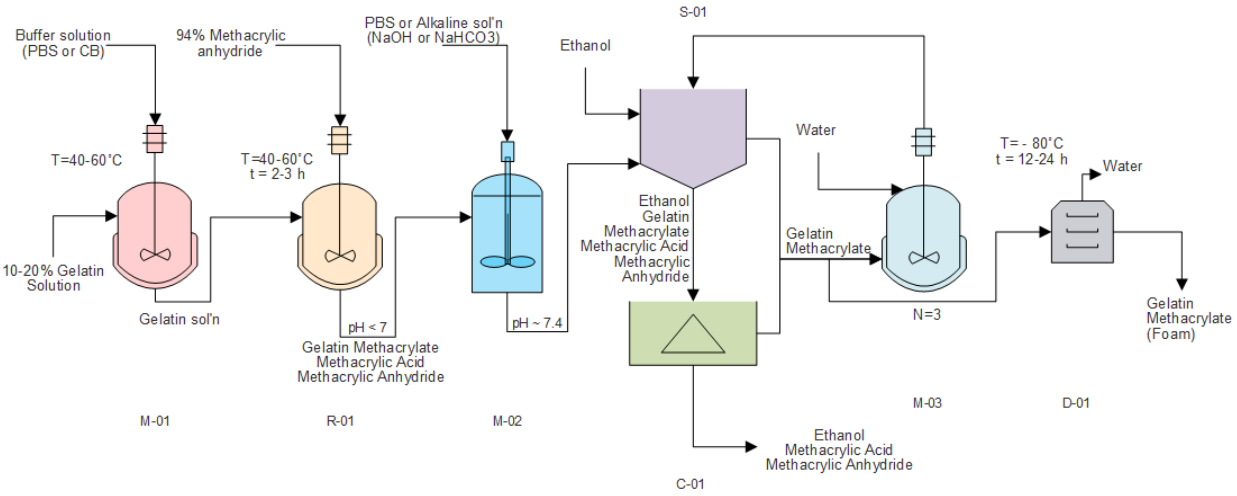


Figure 3.1 Process flow chart of gelatin methacryloyl synthesis and downstream processing. The following annotation are used: M-01 (mixer, gelatin), R-01 (reactor), M-02 (mixer, neutralization), F-01 (filtration) and D-01 (dryer)

3.2.1.1 Downstream processing of GelMA via precipitation method

The reaction liquid was precipitated readily by adding the solution dropwise in a large volume of denatured alcohol (volume of precipitating solvent: 10x the amount of reaction liquid). The precipitate was removed from the solvent via filtration and centrifugation, and was dissolved in deionised water at 60°C and 700 rpm. The resulting solution was precipitated again, and this process was repeated 3x to ensure the complete removal of the unwanted by-products and unreacted components of the reaction. The precipitated GelMA was placed with a filter cloth and applied with pressure to remove the remaining excess solvent, and then freeze-dried at -50°C for two days. The resulting product was a lump of solid material; afterwards, the freeze-dried GelMA was powdered using a coffee grinder, and was stored in a freezer at -20°C until use. This process is referred to as precipitated GelMA (PR).

3.2.1.2 Downstream processing of GelMA via dialysis method

The effluent coming from the reactor was transferred to a dialysis bag with a molecular weight cut off (MWCO) value of 12-14 kDa and suspended in a stirred vessel with deionised water at 40˚C for 7 days. The dialysis process was also kept in a light-free and minimised air uptake environment. To obtain GelMA in a water-free condition, the dialysed GelMA solution was filtered by a 0.2 µm syringe filter, and the filtered liquid was snap-frozen by immersion in liquid nitrogen and freeze-dried at -50°Cto remove excess water for 7 days. The product obtained afterwards was a white, foamy GelMA, and was stored in a freezer at -20˚C until use. The product is referred as dialysed GelMA (DI).

3.2.2 Characterisation of synthesised GelMA

3.2.2.1 Morphological analysis

Synthesised GelMA was imaged using Environmental Scanning Electron Microscopy (ESEM, FEI Quanta 650) under high vacuum mode. Dry samples were loaded unto aluminium stubs with carbon tabs to hold samples in place. Acceleration voltage used was 10 kV, and several magnification modes were used for image capture, with at least 3 varying locations as a representative image of the synthesised GelMA

3.2.2.2 Degree of substitution assay

The TNBS method was used for the determination of the degree of methacrylation in gelatin. Briefly, 15 mg of sample was dissolved in 2 mL of 4% wt/vol $NaHCO_3$ containing 0.01 M of TNBS and reacted at 40°C and 125 rpm for 3 h. A 3 mL 6.0 N HCl was added into the solution and increased the temperature to T=80°C, leaving it for 1 h to react. The

solution was then cooled to room temperature by immersing the reaction vial in a water bath, and then the solution was further diluted by adding 5 mL of distilled water. Absorbance was then measured at 345 nm using a 96-well plate reader (Infinite Pro, Tecan), and the degree of substitution (DS) from three independent, triplicate samples were calculated as follows:

$$DS = 100 \times \left(1 - \frac{A_{GelMA} - A_{blank}}{A_{Gelatin} - A_{blank}}\right) \quad (3.1)$$

3.2.2.3 Molecular weight distribution via Gel Permeation Chromatography

To analyse the molecular weight distribution of GelMA, gel permeation chromatography was used. A solution was prepared by dissolving gelatin methacryloyl in tissue culture water at a concentration of 2.5 mg/mL. Aqueous GPC was performed using a Shimadzu UPLC system adapted with RID-10A differential refractive index detector. The eluent was DPBS, which used at 35 °C with a flow rate of 1 mL/min. The instrument was fitted with three PL aquagel-OH columns. PEG/PEO standards (EasiVial) were used to calibrate the columns. The number and weight average molecular mass, as well as the polydispersity of precipitated and dialyzed GelMA, were then calculated from the chromatogram data.

3.2.2.4 Thermogravimetric analysis

GelMA DI and PR samples were analysed using a thermogravimetric analysis to determine solids content, which consists of inorganic salts coming from the buffer solution and gelatin. A gram of each sample was loaded to a metallic pan, and afterwards subjected into heating in 99.5% oxygen atmosphere at a heating rate of 20ºC min-1 between ambient temperature and 1000ºC in a Mettler Thermal analyser. Continuous records of weight loss

and temperature were analysed using the Mettler thermal analysis software, and the inorganic salts remaining at 1000ºC were determined from the % mass at the endpoint.

3.2.3 GelMA hydrogel production

The dissolving media was prepared beforehand by mixing DMEM with Irgacure 2959 (photoinitiator) at a concentration of 0.5% wt/vol, leaving the mixed solution overnight in an incubator. A 5 or 10% wt/vol of synthesised GelMA was then dissolved in DMEM with photoinitiator by magnetic stirring at T=50°C and 700 rpm. After complete dissolution, the solution was cooled at room temperature by immersion in a water bath for 10 min, and then adjusted its pH to ~7.4 by using 1.0 M HCl. The cooled and pH adjusted solution was pipetted in a cylindrical Teflon mould (Ø = 12 mm) at a volume of 250 µL and irradiated by a 15 W UV lamp with 365 nm wavelength for 5 min. Afterwards, the crosslinked GelMA hydrogels were washed with PBS 3x to remove traces of the photoinitiator and then immersed in 3 mL DMEM containing antibiotic/antimycotic solution in an incubator at 37ºC and 5% CO_2 for 24 hours to ensure full hydration of the sample.

3.2.4 GelMA hydrogel characterisation

3.2.4.1 Compressive modulus determination

For compressive modulus determination of swollen hydrogels, the samples were removed from the culture media, blotted with tissue paper to remove the residual liquid, and the dimensions were measured using a calliper (Mitutoyo, 0.01 mm resolution). The hydrogels were then loaded in a texture analyser (Stable Microsystems) with a 32-mm probe diameter

and a 5 kg-load cell. A ramp displacement speed of 0.05mm/s and 100% strain were used for the mechanical testing, and the compressive modulus was computed on the linear region within 0-10% strain. From a batch of synthesised GelMA, two independent experiments in triplicate were performed.

3.2.4.2 Rheological analysis

Rheological measurements for GelMA hydrogels were done using Physica MCR 301 rheometer (Anton Paar, UK). A 5-mm cylindrical hydrated GelMA hydrogel sample was cut using a biopsy punch and mounted on the rheometer with a gap distance of 1 mm and a plate diameter of 7 mm. For the strain sweeping test, storage (G') and loss moduli (G'') were analysed at a constant frequency of 1 Hz and temperature of T = 37°C from 0.1-100%; time sweeping test was performed for 300 s at a constant frequency rate of 1 Hz, 0.5% strain, and T = 37°C. Temperature sweep test range was from 25-50°C at a heating rate of 2°C/min at a constant frequency rate of 1 Hz and 0.5% strain. From a batch of synthesized GelMA, two independent experiments in triplicate were performed.

3.2.4.3 Swelling ratio evaluation

Similar to the preparation of hydrogels from the compressive modulus determination, crosslinked GelMA hydrogels were submerged in 3 mL DMEM in a 6-well plate at an incubator for 24 h. Afterwards, swollen hydrogels were harvested, excess water removed and weighed in a bijou. The hydrogels were then snap-frozen by immersion in liquid nitrogen and subsequently freeze-dried at -50°C for 3 days to ensure complete removal of

water. The weight of freeze-dried hydrogel was recorded in triplicate, and the swelling ratio was computed as follows:

$$Swelling\ ratio = \frac{weight\ of\ hydrated\ GelMA\ hydrogel}{weight\ of\ freeze\ dried\ GelMA\ hydrogel} \quad (3.2)$$

3.2.4.4 Cell culture

An established lab cell line of NIH 3T3s was cultured using DMEM containing 10% foetal bovine serum (FBS), 1% L-glutamine, and 1% antibiotic/antimycotic stock solution in a T75 flask. Cells were passaged every 3 days at 80-90% confluence, where the flasks are aspirated, washed with PBS, trypsinized for 5 mins, added culture media in a 1:5 ratio (one part of trypsin in 5 parts of culture media) to stop the reaction, centrifuged at 200g for 5 mins, and suspended in 1 mL volume of media. The split ratio was maintained at 1:4, and the passage number used in the experiments were 44-46.

3.2.4.5 Cell viability assay

A 5-10% wt/vol of GelMA was mixed in DMEM containing 0.5% wt/vol Irgacure 2959 and stored in an incubator for 5 h while stirring using a tube roller. After complete dissolution, the solution was filter sterilised in a cell culture hood using a 0.2 µm syringe filter and then stored overnight in an incubator. NIH 3T3 cells were then trypsinised and then suspended in GelMA solution at a concentration of approximately 2 x 10^6 cells/mL, and 10 µL of cell suspension was pipetted into a 24-well plate. The solution was then exposed to an Omnicure S2000 UV lamp with 320-500 nm wavelength for 15s at an

intensity of 6.9 mW/cm^2, and the crosslinked GelMA hydrogels were maintained in DMEM supplemented with 10% FBS and 5% antibiotic/antimycotic stock solution for 4 days. Cell viability was quantified at day 1 and day 4 using Calcein-AM/ethidium homodimer Live-Dead stain kit (Invitrogen) according to the manufacturer's instructions.

3.2.5 Statistical analysis

Results from experiments were statistically analysed using One-way ANOVA at a statistical significance criterion of $p<0.05$ To determine differences of the mean values, Tukey's post-hoc test was performed. At least triplicate samples and 50 or more cells were analysed per sample, and all error bars represent standard deviations. GraphPad Prism 7.0.3 was used to perform all statistical calculations.

3.3 Results

3.3.1 Morphology of GelMA prepared by dialysis and precipitation

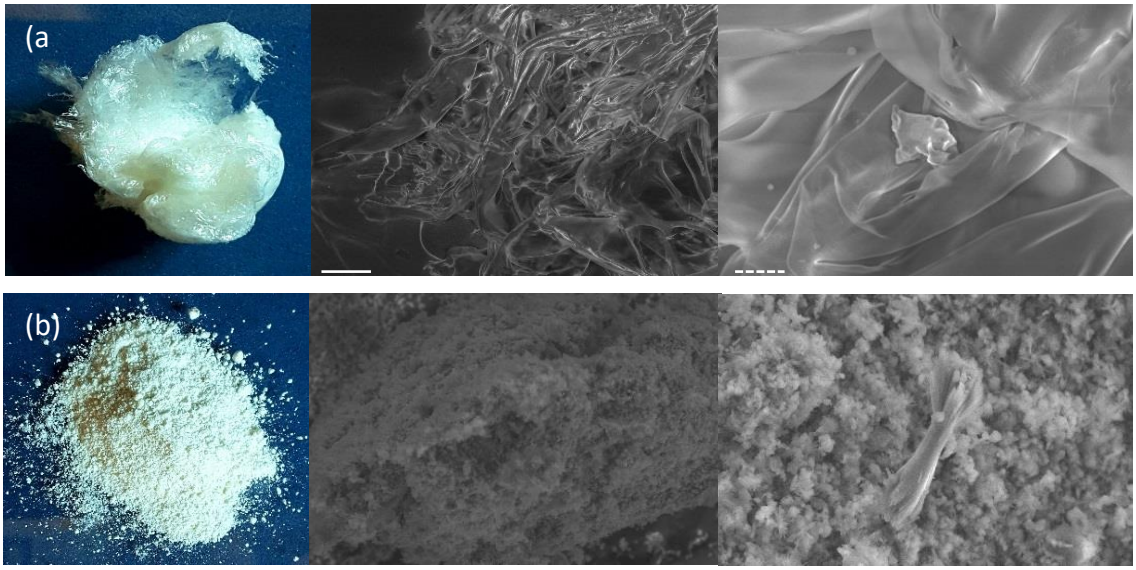


Figure 3.2. Photomicrographs and scanning electron micrographs of (a) dialysed and (b) precipitated GelMA. Scale bar: solid = 50 µm, dashed = 5 µm.

The morphology of the product of dialysis and precipitation methods varies, from a sheet-like structure to a powdered form. High-density product can be obtained upon precipitation and therefore be stored easily in low-volume containers, while dialysed GelMA requires spacious storage requirements. After the reaction process, a conventional way of purifying GelMA is using dialysis, where the reaction products are poured onto a membrane and suspended in water for several days at a constant temperature. The unwanted reaction products such as methacrylic acid and the unreacted methacrylic anhydride with the buffer salts used will start to diffuse out of the membrane upon suspension with water while GelMA is retained in the membrane; constant replacement of water daily would purify the samples inside the membrane, with only GelMA dissolved in water remaining. The water

will be eventually removed by freeze-drying the solution, leaving a foamy structure after processing (Fig. 3.2a). Dialysis usually lasts for 7 days, and freeze-drying for 4-7 days (Nichol *et al.*, 2010a) depending on the water content of the post-dialysis product, having the total purification time of about 11-14 days. On this process, large volumes with low content of solids are processed, making the purification limited to a few grams of freeze-dried GelMA.

In the precipitation method, separation of unwanted reaction products and GelMA instantaneously happens due to phase separation. The reaction products are slowly poured to a large volume of alcohol, either IMS or ethanol: methacrylic acid and methacrylic anhydride diffuse to the alcohol because of their large solubility, while GelMA, being insoluble to alcohol, precipitates. Buffer salts used in the reaction are likely to have been removed (via suspension in the alcohol) as suggested by the assessment of solids content using thermogravimetric analysis (Fig. 3.3), wherein there were no significant difference between the salt content of dialyzed (7.07 ± 0.28%) and precipitated (7.18 ± 0.59%) GelMA ($p = 0.8328$, $n=2$). The unwanted reaction products could co-precipitate with precipitated GelMA, and so redissolution with water and subsequent precipitation can ensure significant removal of these by-products. Precipitated GelMA can be removed from the alcohol suspension through filtration and centrifugation, leaving a compact solid mass where the solvent remaining is easily removed by vacuum or freeze-drying (Fig. 3.2). Processing time for precipitation lasts only for a few hours, with solids drying occupying the majority of the processing time (12-24 h). Products produced are compact and powdered, requiring less volume for storage and increased ease of handling as compared

to dialysis product of GelMA purification with a significant fraction of time reduced on overall processing. The process can also be easily scaled

up, and the solvent (alcohol) can be recovered via distillation for re-use to increase overall economy. The degree of substitution of synthesized GelMA was 97.77±4.88% and 93.28±4.06% for dialysis and precipitated processes respectively (n=3); both degrees of substitution for DI and PR GelMA show no significant difference (t-test, p=0.0623).

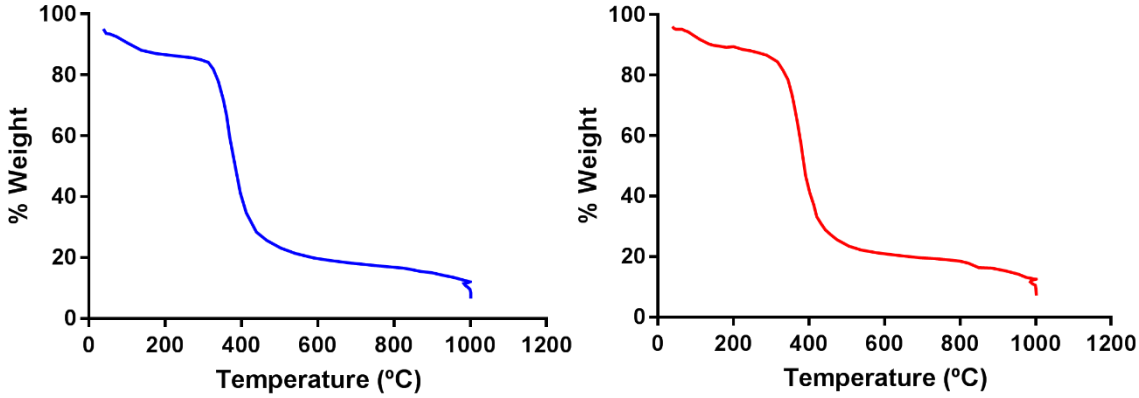


Figure 3.3 Representative thermogravimetric curves of (left) DI and (right) PR GelMA

3.3.2 Molecular weight of GelMA

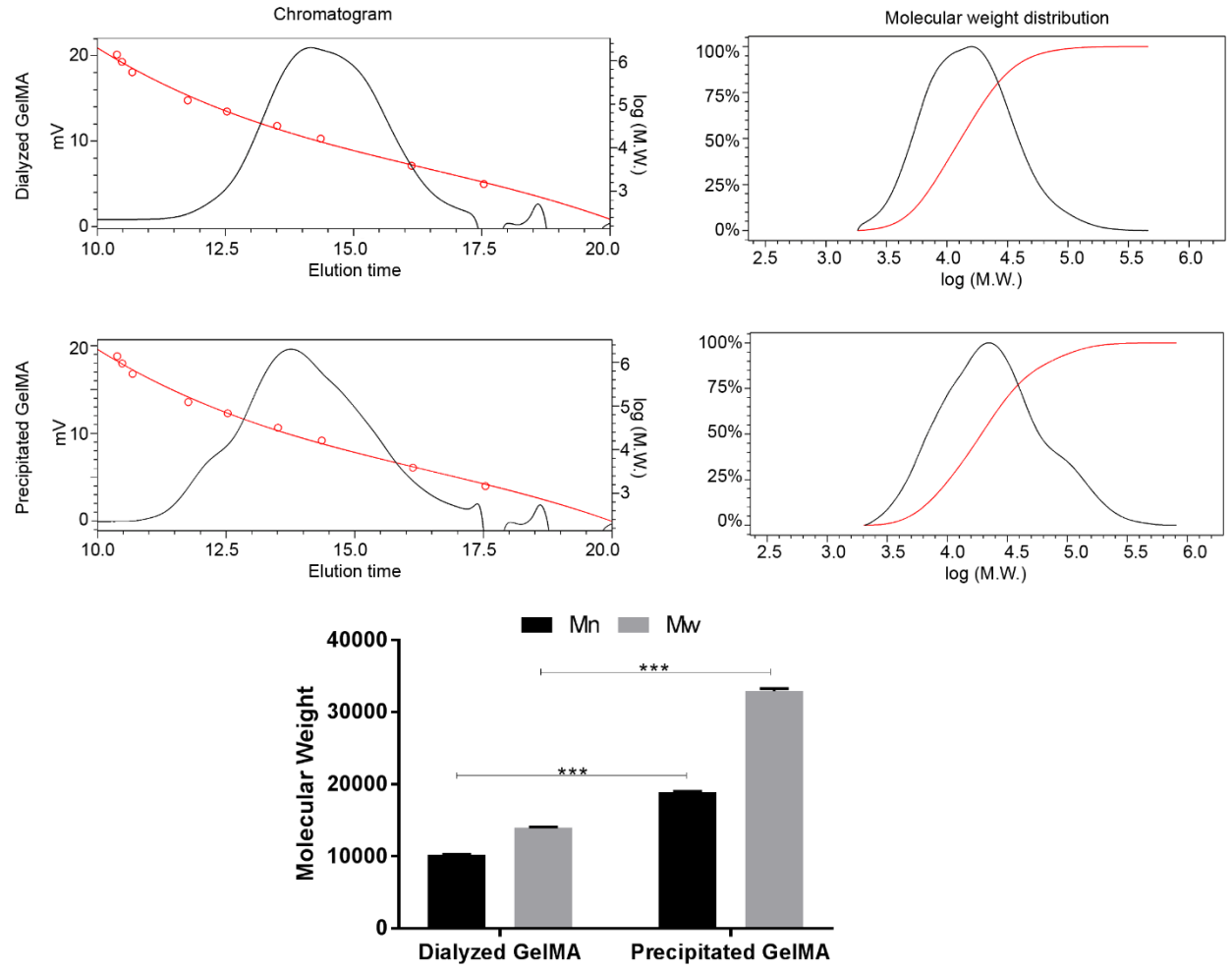


Figure 3.4 Chromatogram and molecular weight distribution of dialysed and precipitated GelMA using gel permeation chromatography. Student's t-test shows a significant difference between number averaged molecular weight (Mn) and weighted averaged molecular weight (Mw) (***p<0.0001, n=3). Calculated polydispersity for dialysed and precipitated GelMA was 1.85±0.024 and 2.35±0.016 respectively. Error bars represent SD.

The manufacturer's published molecular weight for porcine gelatin with 175-225 bloom ranges from 40,000-50,000, and so considerable reduction of molecular weight is observed after processing in dialysis in contrast with precipitation method (Fig. 3.4). Reduction of molecular weight is expected on the methacrylation of gelatin due to processing conditions, however considering also the prolonged suspension of GelMA in aqueous solution at elevated temperature, hydrolysis of gelatin occurs during dialysis, leading to cleavage of

peptide bonds that reduce the molecular weight further (van den Bosch & Gielens, 2003). The precipitation method removes the need for dialysis, and so molecular weight reduction is minimised, having the methacrylation the only main factor for molecular weight reduction. From the manufacturer's molecular weight specification (Sigma-Aldrich) of about 40 kDa on 175 bloom porcine gelatin, dialysis reduced GelMA weighted mean molecular weight to 18.90±0.13 kDa (52.76% reduction) as compared to precipitated GelMA weighted mean molecular weight of 32.93±0.35 (17.67% reduction). The molecular weight of GelMA affects the overall mechanical strength of the hydrogel, which is evidenced in the subsequent discussion.

3.4.3 Compressive mechanical strength and swelling ratio

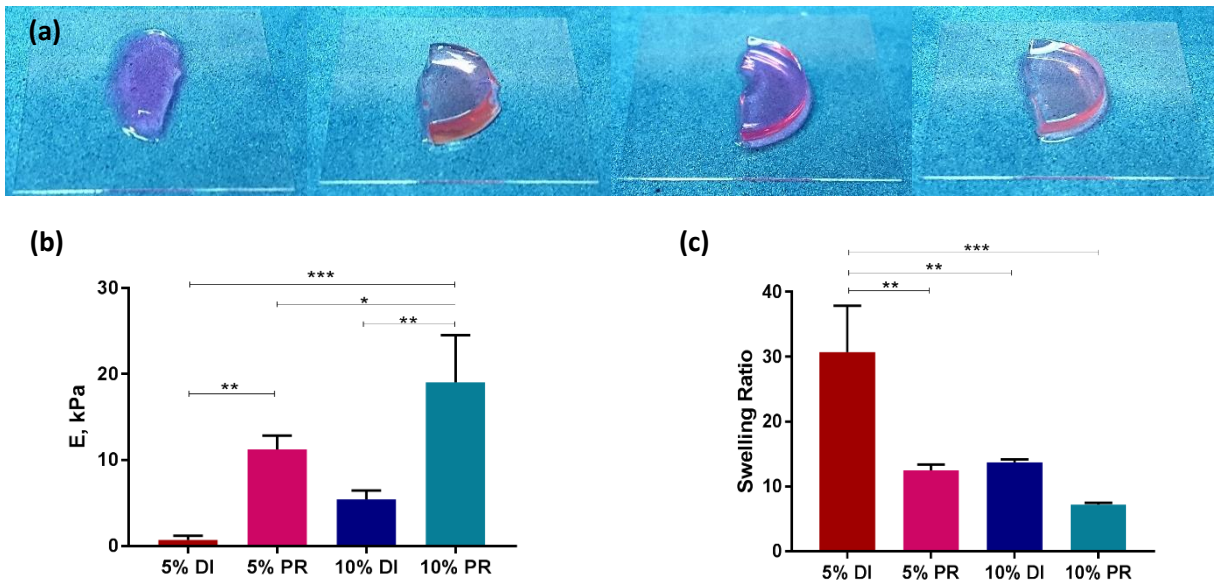


Figure 3.5 (a) GelMA hydrogels from left to right: 5% DI, 5% PR, 10% DI and 10% PR. (b) Compressive modulus and (c) swelling ratio of GelMA hydrogels; error bars as standard deviations. Different concentration and downstream processing techniques show statistically significant differences via ANOVA and Tukey's post hoc test (*p < 0.05, **p < 0.01, ***p < 0.001, n≥3). Error bars represent SD.

One of the inherent properties of polymers is that the mechanical strength is directly proportional to its molecular weight, where gelatin is graded in terms of bloom number (Bloom, 1925). The higher the bloom number, the larger its molecular weight and so the higher the stiffness of the gel (Bloom, 1925). Previous results show a considerable reduction of molecular weight due to processes involving its transformation into GelMA; effect of the molecular weight reduction is vividly seen in Fig. 3.5b. There is a sharp reduction of compressive moduli between DI and PR GelMA, which reflected the considerable molecular weight loss of dialysis as compared to precipitation. Measured values for 5% DI and PR were 0.7±0.5 and 11.23±1.59 kPa, and for 10% DI and PR were 5.43±1.02 and 19.03±5.5 kPa respectively; physical strength can be seen on the photomicrographs in Fig.3.5a. The swelling ratio, defined as the ratio of the mass of water absorbed to the gel dry mass, is highest in 5% DI, while there were no significant differences in 5% PR, 10% DI and PR (Fig. 3.2c). With precipitated GelMA, higher mechanical strength can, therefore, be obtained due to partial preservation of molecular weight of gelatin, and thus will be quite useful on tailoring range of compressive moduli for specific 3D culture conditions.

3.3.4 Rheological analysis of GelMA hydrogels

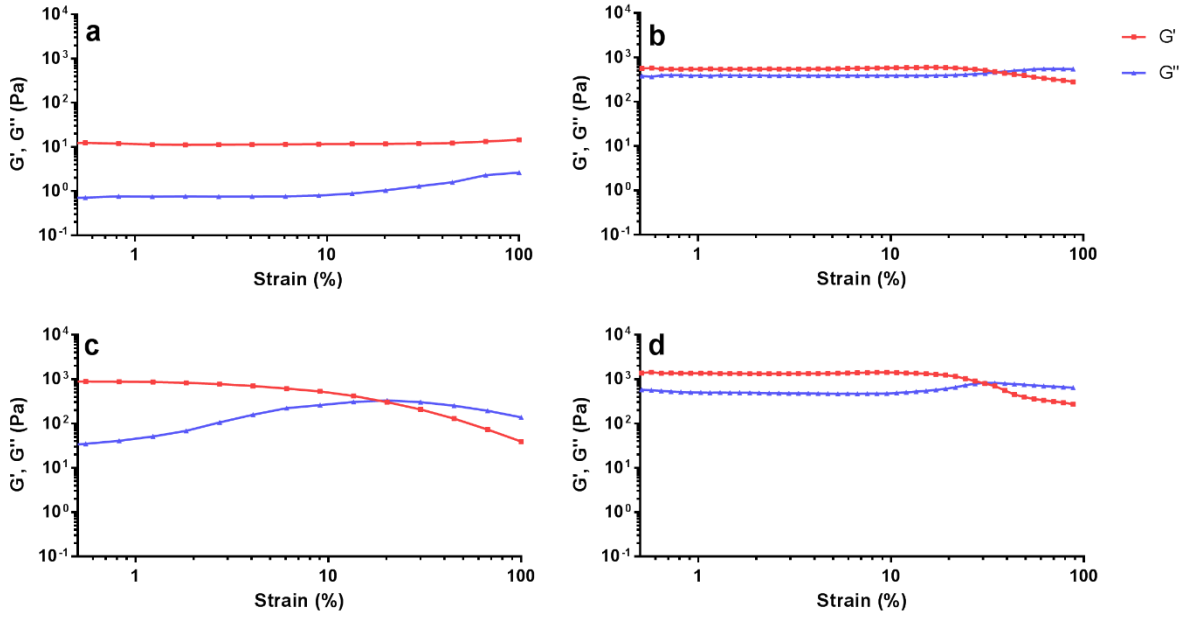


Figure 3.6 Strain sweep of (a) 5% Dialyzed, (b) 5% Precipitated, (c) 10% Dialyzed, and (d) 10% Precipitated gelatin methacryloyl at 1 Hz and T=37°C

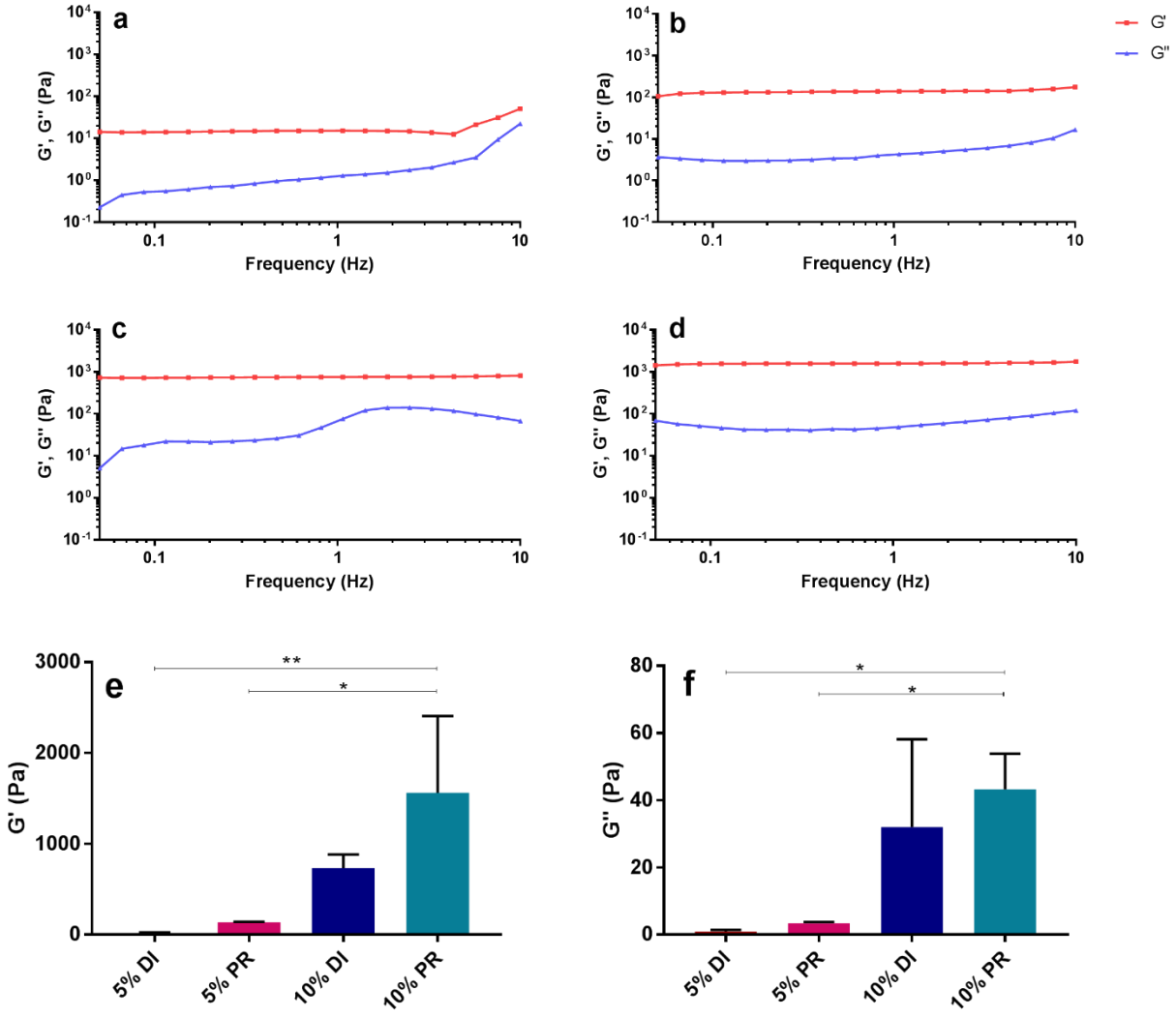


Figure 3.7 Frequency sweep of (a) 5% Dialyzed, (b) 5% Precipitated, (c) 10% Dialyzed, and (d) 10% Precipitated gelatin methacryloyl at 0.5% strain and T=37°C. Bar graphs of the determined storage (e) and loss (f) moduli on all samples. Statistically significant differences between 5% DI and PR to 10% PR at 95% CI via ANOVA and Tukey's post hoc test (*p < 0.05, **p < 0.01, n≥3). Error bars represent SD.

Strain sweeps were done to evaluate the linear viscoelastic region (LVE) of the synthesised GelMA, and all the samples behave linearly from 0.5% to 10% strain levels (Fig.3.6). Affirming the LVE, the storage and loss modulus of GelMA were determined via a frequency sweep (Fig.3.7). Experimental values for storage moduli obtained were: 5% DI

– 14.73±7 Pa, 5% PR – 135.04±5 Pa, 10% DI – 734.44±146 Pa, 10% PR – 1562.2±843 Pa; loss moduli: 5% DI – 0.87±0.6 Pa, 5% PR – 3.37±0.4 Pa, 10% DI – 32.04±26 Pa, 10% PR – 43.23±10 Pa. Storage and loss moduli are significantly higher at 10% PR as compared to 5 % PR and DI, indicating a higher crosslinking density which is attributed to the molecular weight and polymer concentration of the sample. Time and temperature sweep (Figs. 3.8 & 3.9) also show homogeneity and stability of the viscoelastic properties of the GelMA; the loss moduli fluctuations may be due to fluid transport gradients across the pores of the hydrogel albeit it is evident that it is in a pseudo-steady state trend. Stability at T = 37ºC is necessary for culture conditions, ensuring homogenous initial conditions throughout the timeframe of cell culture.

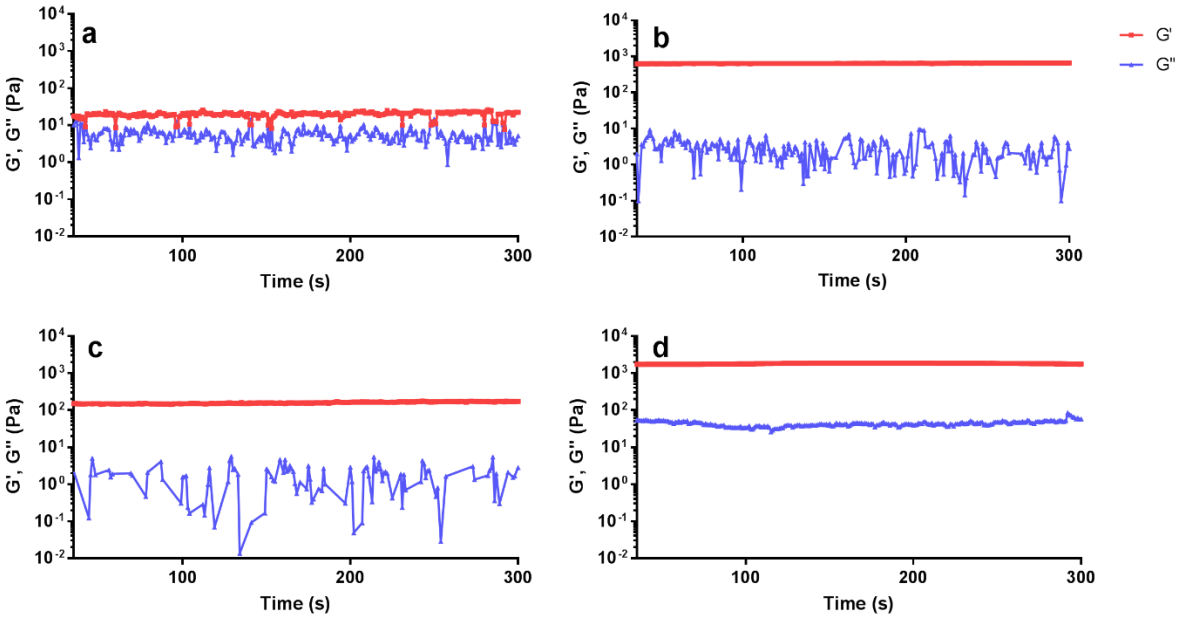


Figure 3.8 Time sweep of (a) 5% Dialyzed, (b) 5% Precipitated, (c) 10% Dialyzed, and (d) 10% Precipitated gelatin methacryloyl at 1 Hz, 0.5% Strain and T=37°C

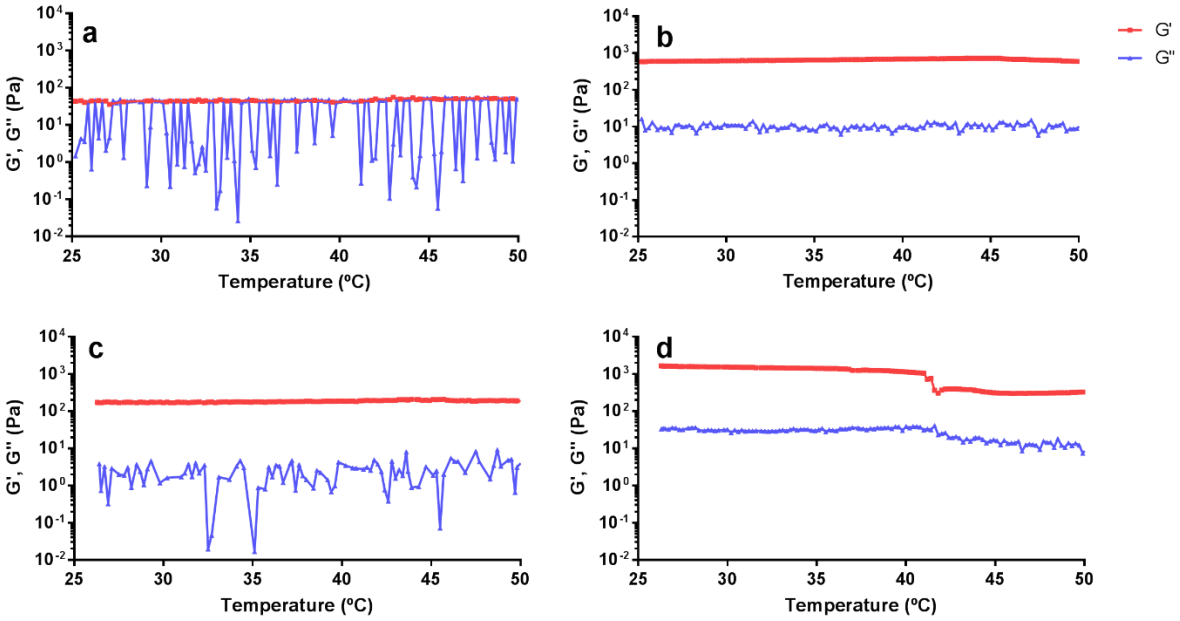


Figure 3.9 Temperature sweep of (a) 5% Dialyzed, (b) 5% Precipitated, (c) 10% Dialyzed, and (d) 10% Precipitated gelatin methacryloyl at 1 Hz, 0.5% Strain, and heating rate of 2°C/min

3.3.5 Cellular viability studies of GelMA hydrogels

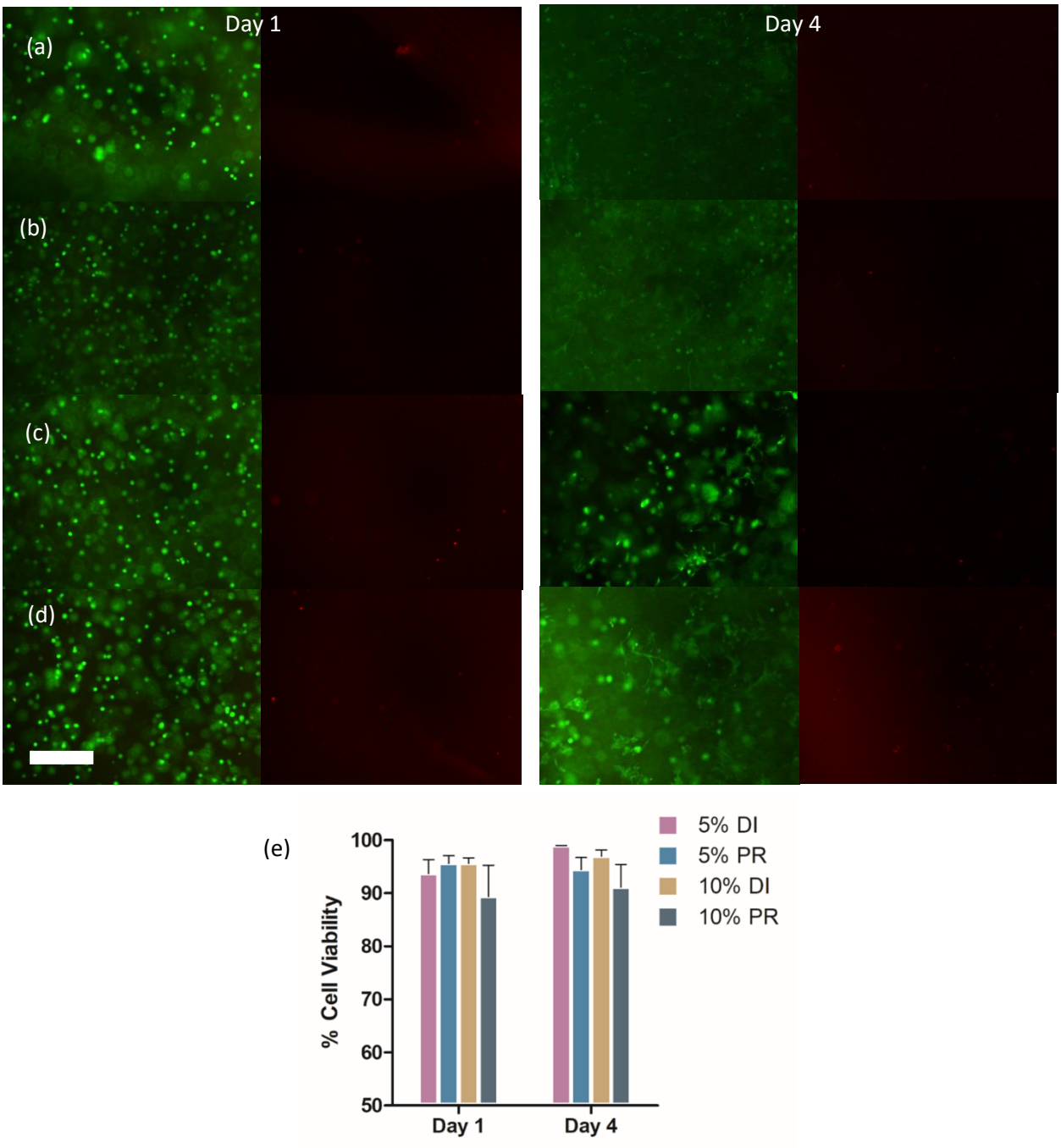


Figure 3.10 Cell viability assessment of NIH 3T3 fibroblasts encapsulated in 5% DI and PR (a & b), and 10% DI and PR (c & d) GelMA at Day 1 and 4, using Live (green, Calcein-AM)-Dead (red, Ethidium homodimer) stain. Bar graph (e) showing no significant difference in cellular viabilities between culture days (Repeated measures ANOVA, p=0.1114, at least 50 cells in each 3 different regions were analysed). Scale bar = 250 µm. Error bars represent SD.

Cellular viability on all scaffolds after encapsulation was higher than 85% after Day 1, indicating very low or no cytotoxicity upon contact with the scaffold. Focusing on the precipitated GelMA, this supports the earlier result that the by-products produced from the methacrylation of gelatin, i.e. methacrylic acid and unreacted methacrylic anhydride, had been substantially removed considering that there are no significant differences between cell viabilities of dialysed and precipitated GelMA (Fig. 3.10e). Rounded morphology of NIH 3T3s is seen on Day 1 of encapsulation, whereas on Day 4 cellular protrusions were evident indicating cell attachment and proliferation. Qualitatively, more protrusions are seen in lower concentrations of GelMA (5% DI and PR), which can be attributed to the mechanical strength of the scaffold as evidenced on several papers (Engler *et al.,* 2006; Rehfeldt *et al.,* 2007; Solon, *et al.,* 2007).

3.4 Discussion

The synthesis of GelMA was successfully achieved using dialysis and precipitation downstream processing techniques. Physical characterisation has been made on the products through environmental scanning electron microscopy and thermogravimetric analysis, where a clear difference in morphology is seen – precipitated GelMA in powder form and dialysis in foam; qualitatively the density was much higher in powdered form thereby allowing storage of bulk quantities in small space. The process also considerably reduced the amount of time for purification, with up to 86% as compared to the normal process. Thermogravimetric analysis showed that there had been no significant difference in the salt content of the sample, as well as also confirming that the purity in terms of the

presence of by-products within the product was comparable between the dialysed and precipitated GelMA. The degree of methacrylation via TNBS assay is unaffected by both processes, however the molecular weight is much reduced in dialysis versus precipitated method due to hydrolysis of peptide bonds in the duration of the dialysis, which highly affected the overall mechanical strength of the photopolymerized hydrogel; compressive, storage, and loss moduli confirmed the effect of the reduction of molecular weight via compressive and rheological analysis of the hydrogels. A higher range of mechanical strength could be attained on precipitated GelMA (up to 19 kPa, in contrast to dialysed GelMA with the same concentration [10%], only up to 6 kPa), thereby allowing tuning of mechanical strength for a larger range of values. Finally, cell viability was unaffected by the processes, with minimum viability of 85% on all of the encapsulated NIH 3T3s on both precipitated and dialysed GelMA, further affirming the removal of toxic by-products of the methacrylation of gelatin in precipitation process. At day 4, the cells in 5% GelMA (DI and PR) have more pronounced cellular protrusions, indicating motility and phenotype changes as compared to 10% GelMA. This cell response is likely due to the porosity and the mechanical strength of the hydrogels (Engler *et al.*, 2006; Rehfeldt *et al.*, 2007; Solon *et al.,* 2007), where less concentration of GelMA provides larger pores, and so does the ease of cellular movement. Overall, the studies confirmed that precipitated GelMA can be used as a platform for cell culture work, with a higher range of mechanical strength values as compared to the dialysed downstream processing technique.

The GelMA produced in this study was found to have wider range of mechanical stiffness, covering the range of stiffnesses of both physiological and pathological moduli in the airways. Since viability seen on GelMA hydrogels of the new downstream process is

comparable to the dialysis method, the material could now be used as a platform to observe the airway smooth muscle cells in response to the changing mechanical properties of the matrix. The next chapters discuss the effect of matrix stiffening and its consequences to the phenotype of airway smooth muscle cells.

Chapter 4

Airway smooth muscle cell recapitulates asthma-like phenotype by increasing substrate stiffness

4.1 Introduction

Airway smooth muscle is found in the airways, particularly in the dorsal side of the trachea and the inner layer of the bronchi (Mieczkowski, 2018). Airway smooth muscle cells (ASMCs) are capable of contracting the airway luminal diameter to modulate the air resistance as it travels in and out of the lungs (Amrani & Panettieri, 2003). The importance of airway smooth muscle can be seen in the developmental condition of the lungs.

Human airway development, was discussed in Chapter 1 by Pansky (Pansky, 1982b) . The distinctive order of differentiation of the mesenchymal cells in the developing organ highlights the role of airway smooth muscle for maturation of the airway, as it is differentiated earlier than the rest of the cells. ASMCs drive the layout structure of the airways via FGF-10 (Mailleux *et al.,* 2005) signalling which is required for lung morphogenesis (Bellusci *et al.,* 1997). Airway ASM peristalsis in the prenatal environment (Jesudason *et al.,* 2006), which increases in frequency towards birth (Parvez *et al.,* 2006), cues intermittent c-ring structure formation in the trachea as mechanical contraction is varied periodically across the tissue. The mechanotransducive function of the airway

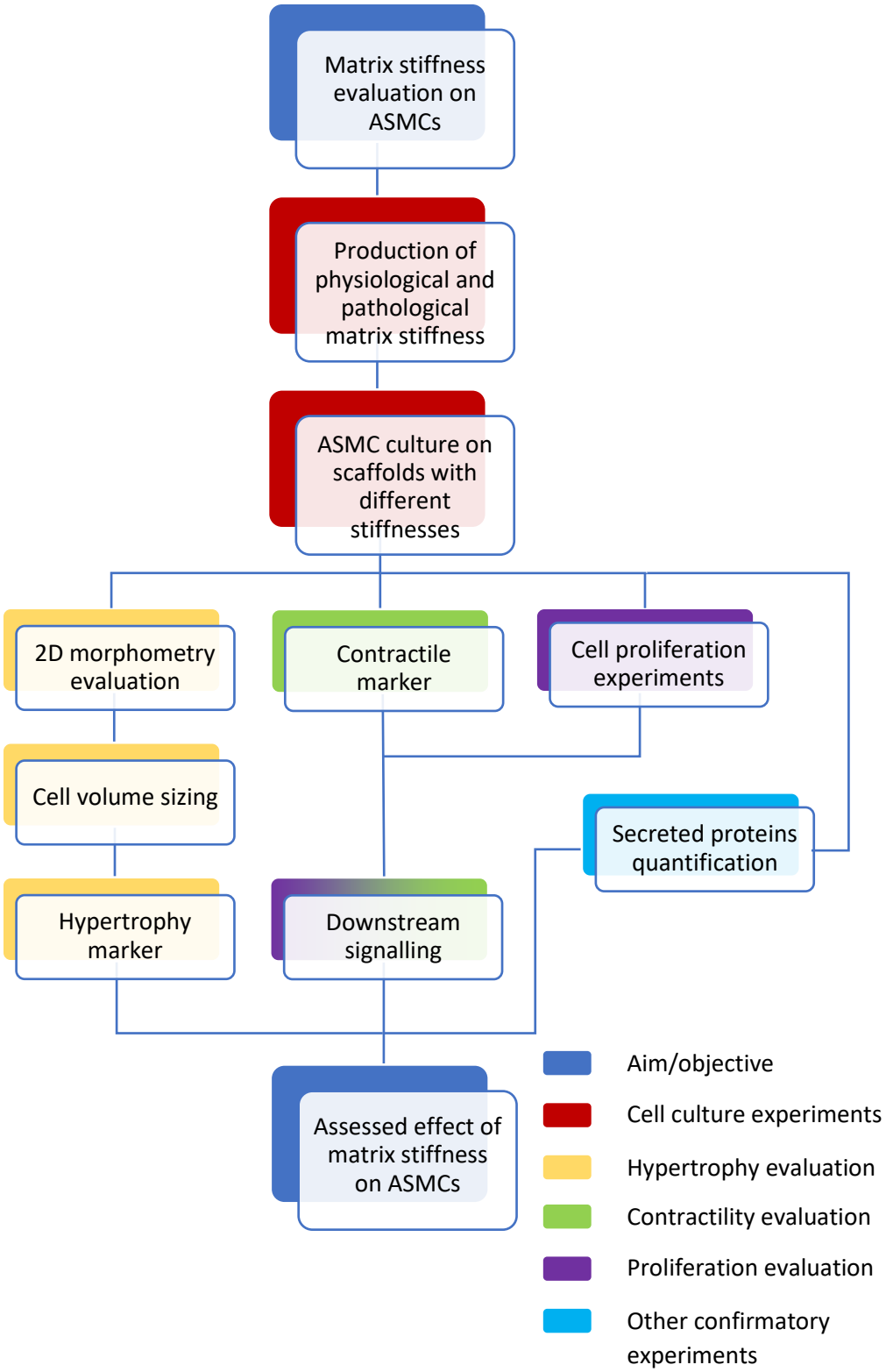
smooth muscle emphasizes its importance, and the absence of airway smooth muscle compromises the maturity of the lungs (Hines *et al.*, 2013).

Once developed, the airways, in response to an injury, recapitulate some of the developmental conditions: ASMCs in an onset of injury express FGF-10, a growth factor secreted from progenitor ASMCs (Mailleux *et al.*, 2005) in developing lungs, which promotes epithelial repair (Volckaert *et al.*, 2011). The crosstalk between cells helps maintain the integrity of the airways, following the same developmental pathways for whole organ homeostasis. However, in pathological conditions, signalling and biomechanics are compromised, resulting in unsynchronised overgrowth or degradation of tissues within the airways coupled with overlapping signals that perpetuate the condition.
In airway physiology, mechanical events such as the cycles of contraction and relaxation in the airways can affect the release of soluble factors. However, excessive mechanical activity and elevated soluble factors release can arise from pathologic conditions, such as asthma, which shifts the equilibrium so that cellular responses are aberrant. These events alter the microenvironment, specifically the ECM components, and can lead to perpetuation of pathologic conditions in the airways. For example in asthma, ASM mass is increased (Regamey *et al.*, 2008), and becomes hypercontractile (Ma *et al.*, 2002), with the airways getting stiffer (Brackel *et al.*, 2000). Understanding the effect of mechanical properties to the ASMCs can give insights on the behaviour of these cells under normal and pathological conditions.

In this study, a model scaffold was developed using GelMA with stiffnesses ranging from physiological equivalence to highly elevated levels representing pathological conditions

seen in asthma. GelMA was selected as the biomaterial since it has the RGD peptide adhesive motif (Davidenko *et al.,* 2016) to which cells attach similar to the collagen type I matrix that the ASMCs secrete. Here we assess whether matrix stiffness affects proliferation, contractility, and hypertrophy of ASMCs, and its repercussions on the biology of the airways.

Chapter experimental overview



4.2 Materials and methods

4.2.1 Synthesis of GelMA

The synthesis of GelMA was described in detail in the previous chapter. Briefly, gelatin (Bloom 175) wass dissolved in 0.25M carbonate-bicarbonate solution at 10% wt/vol, and 0.2 mL methacrylic anhydride per gram of gelatin was slowly added into the solution at 60ºC. After 2 hrs of reaction time, the reaction products were precipitated in industrial methylated solution and then the precipitate was collected and dissolved again in distilled H_2O. The precipitation-dissolution step was repeated 3x to further purify the product, and then snap-frozen using liquid nitrogen and placed overnight in a -80ºC freeze dryer. Product was collected and ground into a fine powder, and stored at -20ºC until use.

4.2.2 Cell culture

Primary human airway smooth muscle cells (hASMCs) were obtained from healthy non-asthmatic patients that had undergone bronchoscopy at Nottingham City Hospital. Primary hASMCs were cultured with DMEM (Gibco®, Thermofisher) containing 10% Fetal Bovine Serum (FBS, Invitrogen), supplemented with 1% L-glutamine (Invitrogen), 1% Penicilin/Streptomycin (P/S, Invitrogen) and 1% Antibiotic/Antimycotic stock solution(AB/AM, Invitrogen). Cells were expanded in a T-175 flask (Thermofisher) with an initial cell seeding of $5x10^5$ cells/plate, trypsinised at 90% confluence, and stored in a liquid nitrogen cryotank until further use. In all experiments, passage 5-6 were used.

4.2.3 Hydrogel-cultured hASMCs

A hydrogel disc 12 mm in diameter and 2 mm thickness was produced from a precursor GelMA solution containing 0.5% Irgacure 2959 in DMEM and crosslinked for 10 min. The hydrogels were washed with PBS 3 x 5 min to remove traces of photoinitiator as well as the unreacted GelMA. The scaffolds were then placed in a 12-well plate (non-treated, Nunc, Thermofisher) incubated at 37˚C overnight in DMEM containing 2% P/S and 2% AB/AM to ensure sterilisation and hydration. Cells from 3 different donors were cultured and expanded in a T-175 plate, trypsinised, and after the media was removed from the scaffold, cells were plated at a density of 2,000 cells/cm^2. The scaffold with cells was cultured with DMEM (Gibco®, Thermofisher) containing 10% FBS supplemented with 1% L-glutamine, 1% P/S and 1% AB/AM stock solution for 6 days. After the day 6, the scaffolds were washed with serum-free DMEM (supplemented only with 1% L-glutamine, 1% P/S and 1% AB/AM stock solution) and then incubated also with it for 24h to switch phenotype from proliferative to contractile. The cell-plated scaffold was then washed with PBS, fixed with 4% paraformaldehyde for 5 mins, and washed again with PBS.

4.2.4 Immunocytochemistry and morphometric analysis

Fixed samples incubated in PBS were immersed for 5mins in 0.3% Triton-X100 for permeabilisation of cells. The solution was then removed, washed 3 x 5 min with PBS, and blocked with 3% Goat Serum in PBS for 1 hr. The blocking solution was then removed, washed again in 1% BSA in PBS 3 x 5 min, and incubated with a primary antibody overnight at 4˚C. Below is the list of antibodies used for the experiment (Table 4.1):

Table 4.1. Antibodies used in the experiment

Antibody	Species	Dilution	Source
Primary			
α-SMA	Rabbit	1:200	Stratech
pGSK-3β	Mouse	1:250	Invitrogen
pSMAD2	Rabbit	1:100	Cell Signalling
Secondary			
Alexa Fluor™ 488 plus	Anti-Rabbit Goat	1:500	Invitrogen
Alexa Fluor™ 555 plus	Anti-Mouse Goat	1:500	Invitrogen

The next day, the antibody solution was removed, washed with 1% BSA in PBS 3 x 5 min, and incubated at dark with secondary antibody at room temperature for 2 hrs. The secondary antibody was removed, washed with 1% BSA in PBS 3 x 5 min, incubated with DAPI (4',6-Diamidino-2-Phenylindole, Dihydrochloride, Thermofisher) for 30 mins at 1:1000 dilution ratio, and then washed again with 1% BSA in PBS 3 x 5 min. Cells were imaged afterwards using a confocal microscope (Zeiss LSM 710) at constant gain, pinhole and laser power for all samples. The images were post processed using Cell Profiler™ (McQuin *et al.*, 2018).

4.2.5 Flow cytometry

ASMCs were cultured in a 6 well plate coated with GelMA of different stiffnesses, at a seeding density of 10,000 cells/cm^2 in DMEM containing 10% FBS, 1% L-glutamine, 1% Antibiotic/Antimycotic solution and 1% Penicillin/Streptomycin for up to 6 days at 37ºC

with 5% CO_2 and a humidified atmosphere. The samples were washed with PBS and subsequently cultured in a serum-free medium (DMEM with L-glutamine and antibiotics/antimycotics only) for 24 hrs. Cells were then detached with Accutase for 15 min at room temperature, centrifuged at 200g for 5 min, removed supernatant, and fixed with 4% paraformaldehyde for 15 mins. Samples were centrifuged to remove supernatant, washed with PBS, centrifuged again, and afterwards incubated for 15 mins with 0.5% Tween 20 in PBS over ice for permeabilization of cell membrane. The cells were centrifuged at 200g, washed again, treated for 5 mins with 100 µg/mL of 101 U/mg RNAse to prevent unwanted staining of RNA, washed again and incubated with 50 µg/mL Propidium iodide for 15 min on ice. Cells were then processed with a flow cytometer (Beckman Coulter FC500), measuring at least 10,000 cells for cell size and cell cycle analysis. Data were analysed using Kaluza Analysis™, where the scatter plot obtained from flow cytometer was gated to remove cell debris and doublets/triplets. To increase precision, analytical standard polystyrene beads of 10 and 20 µm size (Sigma) were run to serve as calibration to ascertain size of cells by gating them according to the forward scatter region. For the cell cycle analysis, PI histograms were processed using in-build cell cycle analyser with Michael H. Fox Algorithm to determine G1, S and G2 phases of the plot. All data presented were from 3 biological donors, used at passage 5-6.

4.2.6 Cell proliferation assay

Quantifying cellular proliferation was done via DNA Quantification and Rezasurin-based metabolic assays. ASMCs were plated on 60 mm GelMA coated glass petri dishes with a cell seeding density of 5,000 cells/cm^2 and cultured with DMEM without serum for 24 hrs

to synchronise cell cycle phases. After 24h, the cells were incubated with media containing serum, and after another 24 hrs, Presto Blue™ reagent was added and incubated for 1 hr and measured its fluorescence with a plate reader. This serves as a Day 0 measurement for data normalisation. Measurements were also done for Day 1 and Day 4, and metabolic fold change were assessed by dividing measurements from Day 0. For the DNA Quantification assay, the reagent PicoGreen™ from Sigma was used using the manufacturer's protocol. After culturing on pre-defined days, cells were detached using Accutase (Sigma) with incubation time of 15 min at room temperature, centrifuged at 200g, washed once with PBS, lysed, and treated with RNAse (50 U/mL) for DNA quantification. Day 0 was taken as well for the data normalisation, and the DNA was also quantified after Day 7. All data presented were from 3 biological donors, used at passage 4-6.

4.2.7 IL-6 and TIMP-1 quantification

The cell culture supernatants at -80°C were thawed at room temperature and centrifuged at 1000g for 15 min to remove cellular debris. The supernatant was removed and placed in a 1.5 mL Eppendorf under ice prior on quantification. To quantify IL-6 and TIMP-1, Enzyme-linked immunosorbent assay (ELISA) Duoset kit from R&D systems were used according to manufacturing instructions. The concentrations were normalised by cell number obtained from cell proliferation experiments.

4.2.8 Statistical analysis

Results from experiments were statistically analysed using Kruskal-Wallis for cell culture analysis and One-way ANOVA for the mechanical characterization of hydrogels at a statistical significance criterion of $p<0.05$ To determine differences of the mean values, Dunn/Tukey's post-hoc test was performed. Cells from 3 different donors were used in the experiment, with results showing the cumulative data for 2 independent experiments and all error bars represent standard deviations. GraphPad Prism 7.0.3 was used to perform all statistical calculations.

4.3 Results & Discussion

4.3.1 Preparation of scaffold with physiological and pathological matrix stiffness

The airway smooth muscle in relation to the tracheal mechanical compliance needs to be soft enough to elicit considerable contraction throughout the construct. Several papers had assessed the ASM mechanical strength, particularly Trabelsi *et al.,* (2010) determined the longitudinal and traversal mechanical properties of the tissue. Deriving the values from the graph we can obtain a longitudinal and traversal young's modulus of 5.84 and 6.79 kPa, the value in which the baseline modulus of the GelMA is produced. Increasing the polymer content of the solution raises the mechanical strength of the hydrogels, approximately 6x the physiological level for 10% wt/vol and 12x for the 15% wt/vol (Fig. 4.2). ASM has been observed to stiffen in pathological conditions including asthma and chronic obstructive pulmonary disorder, thus the scaffold can be used as a model on extracellular matrix stiffening of the airways.

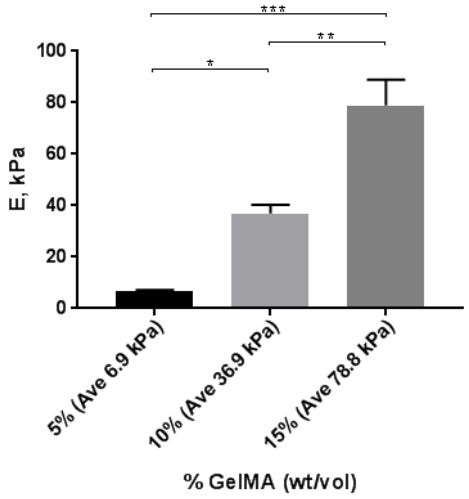


Figure 4.1 Young's modulus of GelMA hydrogels, with normal (= 1x, 5%), ≈5.5x (10%) and 11.4x (15% wt/vol GelMA) physiological stiffness levels as compared to native trachea.

4.3.2 Matrix stiffness affects the morphology and α-smooth muscle actin expression of ASMCs

Several parameters attributed to the morphology of hASMCs had a directly proportional effect dependent on the stiffness of the hydrogel. From a spindle-like structure similar to the native ASMC in the trachea and bronchi to spreaded phenotype with multiple processes extending from the cell (Fig. 4.3a) was observed as the stiffness was increased. Cellular area and perimeter, are all significantly increased from 1x to 12x scaffold stiffness (Fig. 4.3b-c). Additionally, the α-smooth muscle actin expression (Fig. 4.3d) is also upregulated as the modulus increased, indicating increased contractile activity of the cell. Cells cultured on a cover slip served as the control, although cells grew overlapping with each other and therefore single cell assessment could not be made. Instead, the control was included in the analysis of nuclei morphometry.

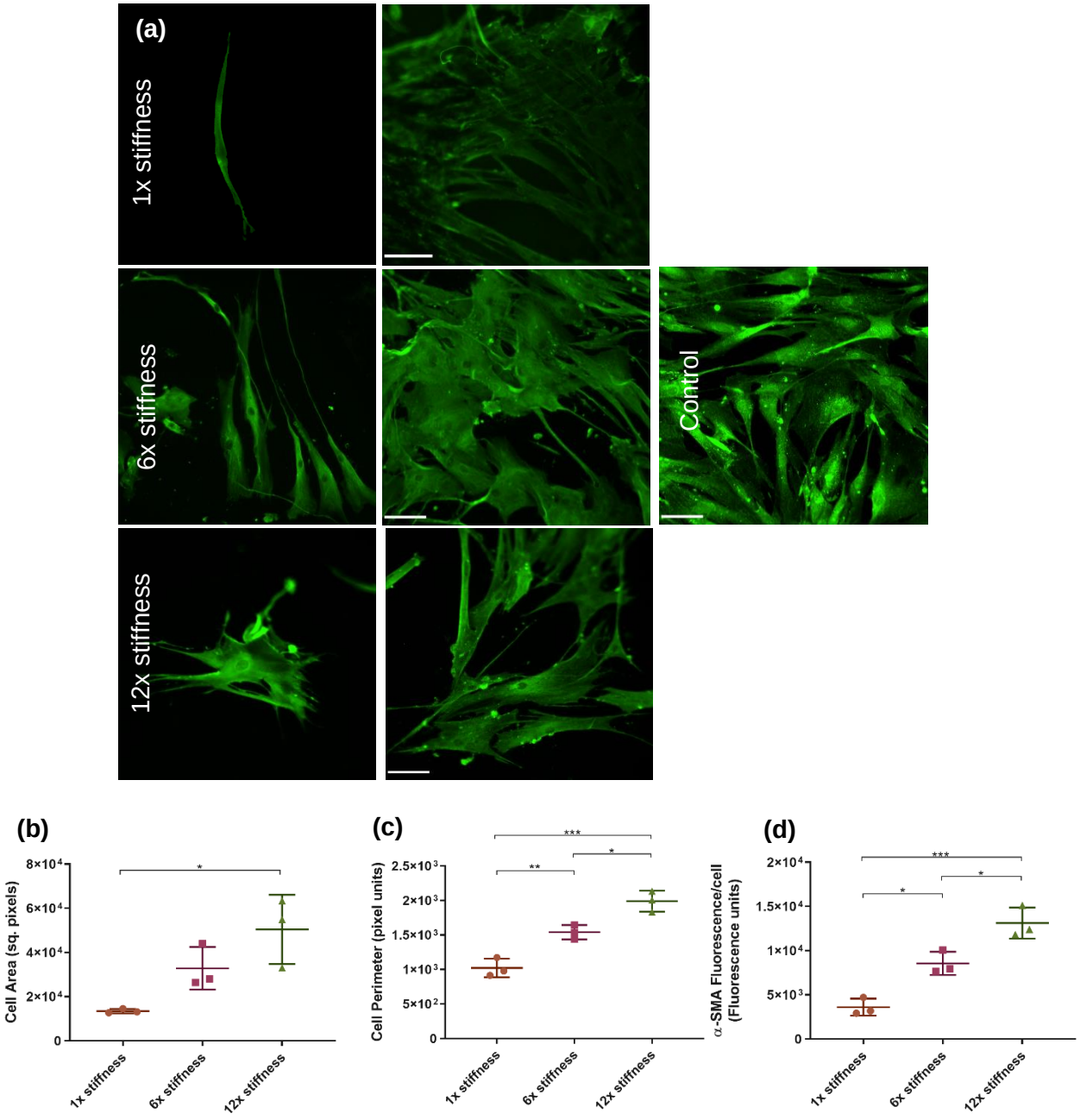


Figure 4.2 (a) Immunofluorescence staining of hASMCs cultured) under 1x, 6x and 12x physiological stiffness GelMA hydrogels, with control cultured on a cover slip. Cells were stained with α-smooth muscle actin (green, Alexa Fluor™ 488). Scale bar = 100 µm. Box-plot graph shown are morphometric measurement of cells: (b) Cell area (c) perimeter presented in pixel units. (d) Average fluorescence intensity of α-smooth muscle actin per cell presented as fluorescence units (integrated density). Box and whiskers plot show min to max range values obtained. No. of cells/donor analysed n ≥ 33, 3 donors, 3 technical replicates, 2 independent runs.

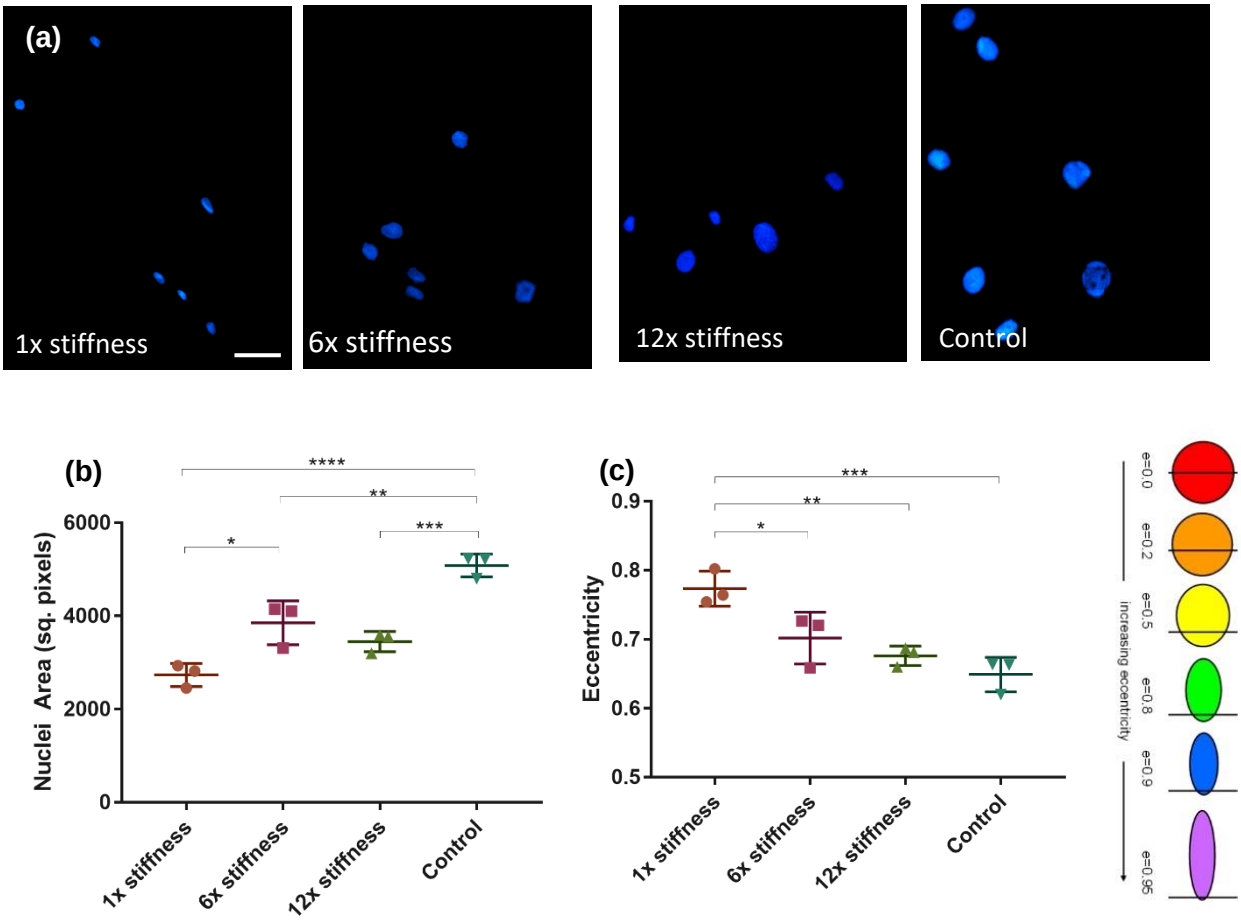


Figure 4.3 (a) Immunofluorescence staining of cell nuclei with DAPI. Scale bar = 50 µm. Nuclei morphometric analysis showing (b) Nuclei Area and (c) Nuclear Eccentricity. In nuclear eccentricity, the lower the number, the more circular the nucleus. No. of nuclei n ≥ 68, 3 donors, triplicate, 2 independent runs.

Coupling the previous cell morphometry result, the nuclei of ASMCs correlate as well on the stiffness of the substrate (Fig. 4.4a). Nuclei eccentricity (the degree of deviation from a circle) decreases (Fig. 4.4c) as the stiffness increases, while the area instead increases (Fig. 4.4b). Nuclei area increase can be attributed to the spreading of the cell on the substrate, as the cell is stretched in two dimensions, so does the area of the nuclei. Spindle shaped cells correspond to high nuclei eccentricity and low area, while the stiffer-substrate cultured cells have low nuclei eccentricity and high area.

4.3.3 Cell volume and TGF-β1 signalling is increased with matrix stiffness

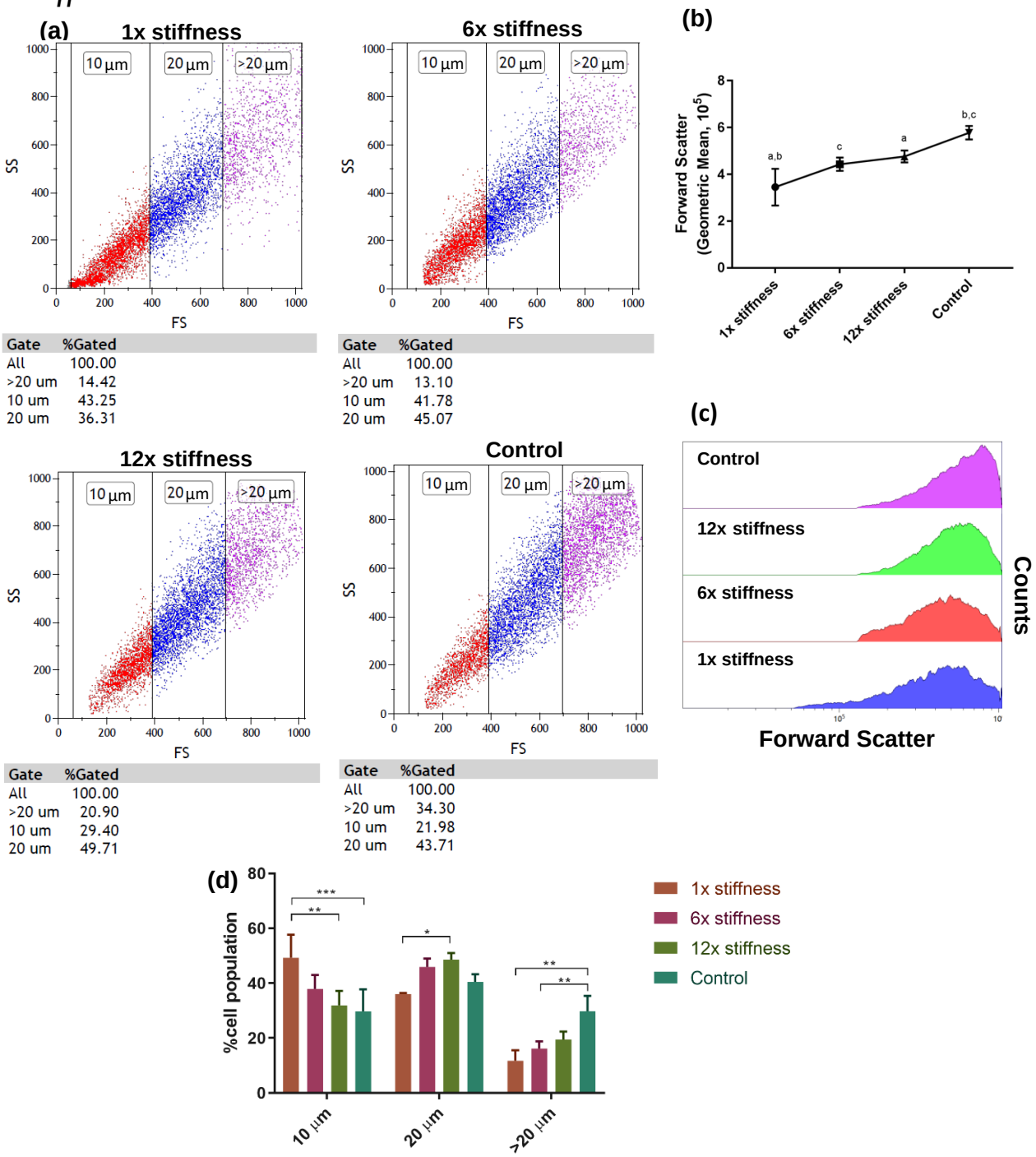


Figure 4.4 (a) Cell diameter increase as stiffness increases. (a) Scatter plots showing increasing density of cells in >20 µm region from 1x stiffness to control. b and c) forward scatter histogram and geometric mean line plot, showing an increasing trend (a & c, *p<0.05, b, **p<0.001). c) After gating with 10 µm and 20 µm calibration beads, cell population were classified into 10, 20 and >20um sizes, where a trend is seen that cell diameter increase as stiffness increase (*p<0.05, **p<0.001, ***p<0.0001). N=3 biological replicates, minimum of 10,000 cells analysed per sample and serum-starved for 24 hr before analysis.

Flow cytometry showed an increased cellular diameter as stiffness increases, as seen in the forward scatter measurements and scatter plots (Figs. 4.5a, b & c). Gating via calibration beads as shown in Fig. 4.5d beads allowed semi-quantification of cell diameters in a population, with the diameter decreasing in the 10-µm population and increasing in 20 and >20 µm population. The result correlates with the previous result that cell area also increases as stiffness increases.

The present molecular marker of hypertrophy, pGSK-3β, confirmed the effect of matrix stiffness on the hypertrophy of ASMCs (Deng *et al.*, 2008) (Fig 4.6a). Quantification of immunofluorescence showed increasing pGSK-3β expression along with increasing matrix stiffness (Fig. 4.6b). In addition, pSMAD2, a TGF-β1 downstream signalling transcription factor, is also elevated at increased matrix stiffness (Fig. 4.6c). This reflects the earlier observed increase in fluorescence of α-SMA, as it is known that TGF-β1 induces the upregulation of α-SMA which affects contractility (Caraci *et al.*, 2008).

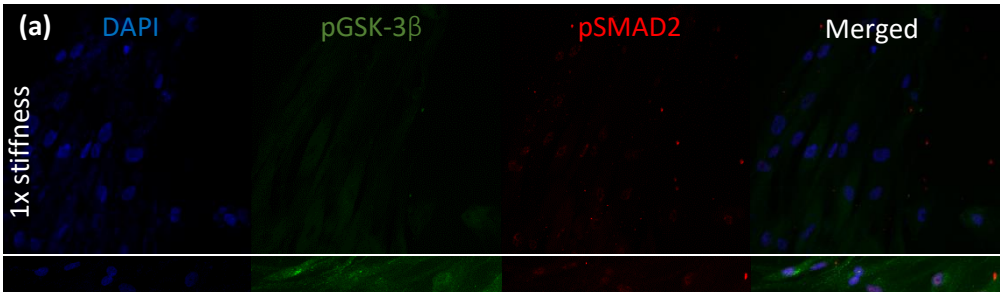


Figure 4.5 (a) Immunofluorescence staining of hASMCs cultured under 1x, 6x and 12x physiological stiffness GelMA hydrogels, with control cultured on a cover slip. Cells were stained with pSMAD2 (red, Alexa Fluor™ 555) and pGSK-3β (green, Alexa Fluor™ 488) (Scale bar = 100 µm). Box-plot shows average fluorescence intensity of (b) pSMAD2 and pGSK-3β (c) per cell presented as fluorescence units (integrated density). Box and whiskers plot show min to max range values obtained. No. of cells/donor analysed n ≥ 106, 3 donors, 3 technical replicates, 2 independent runs (*p<0.05, **p<0.001, ****p<0.00001)

4.3.4 Cell proliferation is increased with matrix stiffness

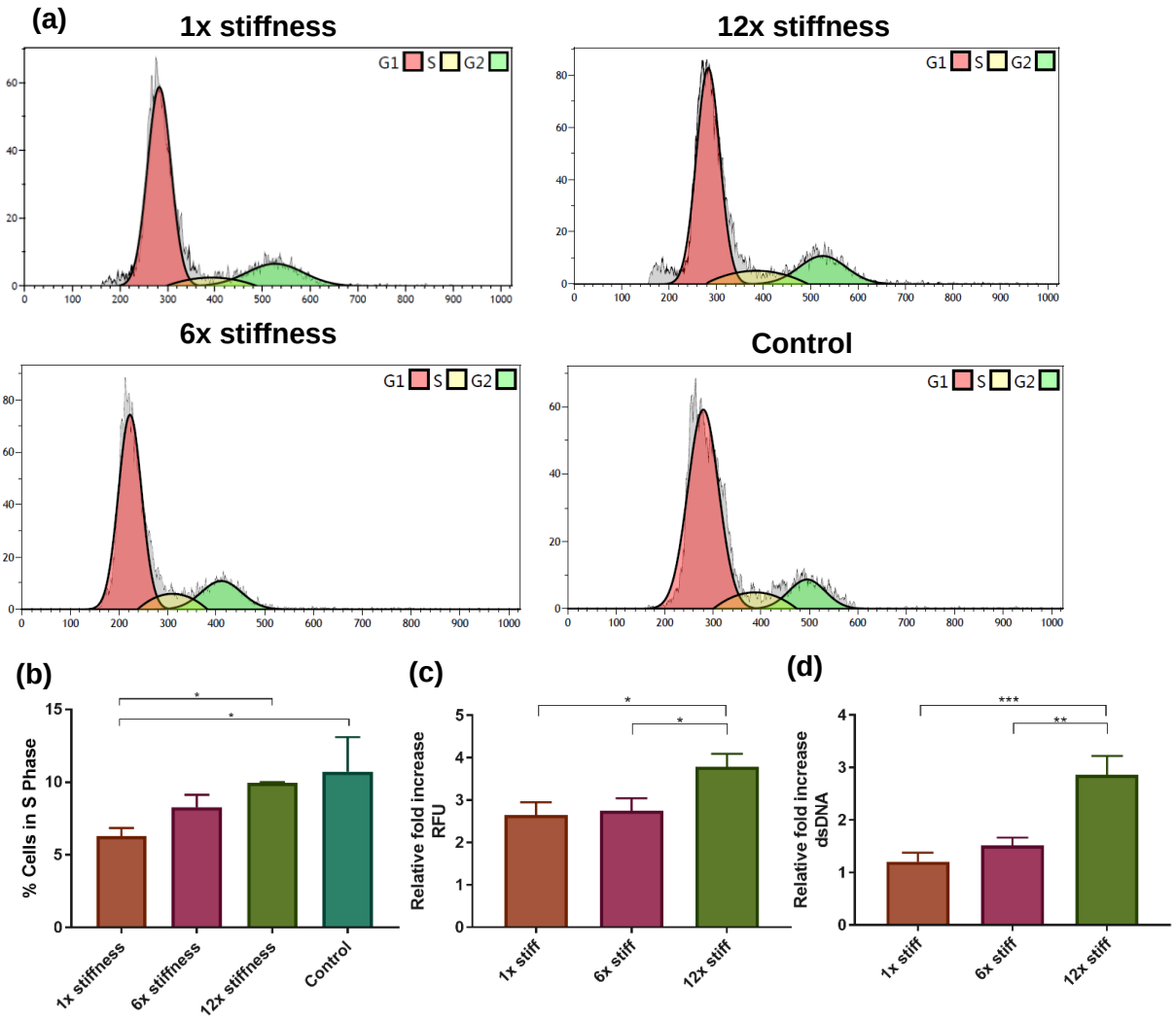


Figure 4.6 ASMCs proliferate more on stiffer matrix. a & b) Cell cycle analysis of cells, where % S phase of cells increases as the stiffness of gel increases. Minimum of 10,000 cells analysed per sample and serum-starved for 24 hr before analysis. c & d) Relative fold increase of relative fluorescence units (RFU) and DNA content of ASMC cultured with 10% FBS from Day 0, where there is a significant increase on the rate of proliferation on Day 7 among different matrix stiffness (*p<0.05, **p<0.001, ***p<0.0001). N=3 biological replicates, 3 technical replicates, 1 independent run for cell cycle analysis and 2 independent runs for Presto Blue and PicoGreen assay; cells are seeded at 5,000 cells/cm^2.

Cell cycle analysis reveal a significant difference in rates of proliferation on cells cultured in different stiffnesses. Percentage of cells in S phase is significantly increased as the matrix gets stiffer (Fig. 4.7a & b). Consequently, the resazurin-based metabolic assay (Fig.

4.7c) and PicoGreen DNA quantification (Fig. 4.7d) also proved to have an increasing trend, albeit significance is only seen in 12x stiffness levels. The trend shows similar response in fibroblasts (Hadjipanayi *et al.*, 2009), cancer cells (Huang & Ingber, 2005; Schrader *et al.*, 2011), and endothelial cells (Mason *et al.*, 2013), which may be attributed to the coordinated signalling pathways of focal adhesion proteins and Rho GTPase (Provenzano & Keely, 2011).

4.3.5 IL-6 and TIMP-1 is downregulated with increasing matrix stiffness

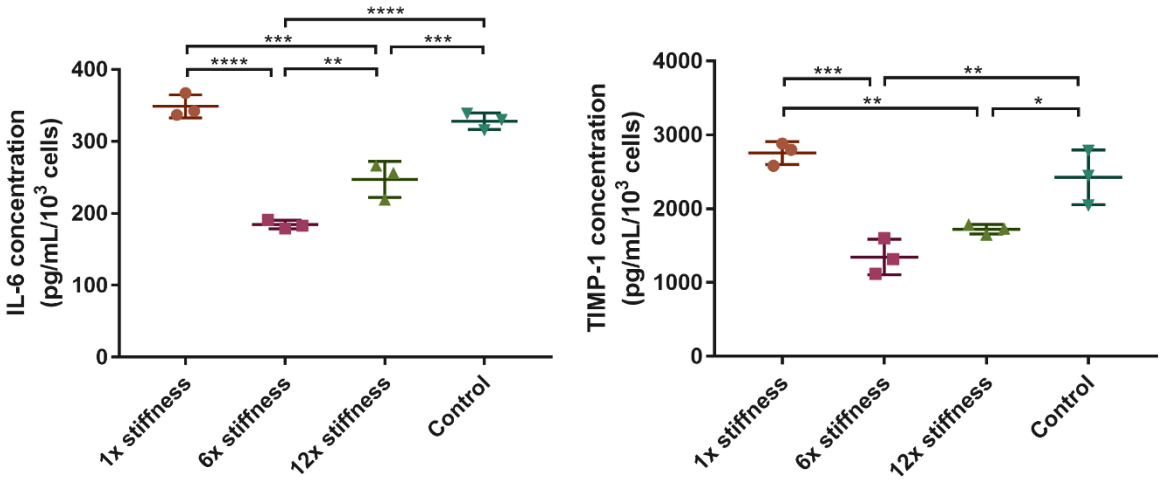


Figure 4.7 Quantification of IL-6 (left) and TIMP-1 (right) in cell culture supernatant via ELISA. Data is normalised with cell number, with 3 donors, 3 technical replicates, 2 independent runs. ANOVA shows statistically significant difference between stiffness levels, with **p < 0.001.

Secretion of functional molecules are also significantly affected by the change of matrix stiffness. For cells cultured on GelMA, increasing the stiffness decreases the secretion of IL-6 (Fig. 4.8, Left) and TIMP-1 (Fig. 4.8, Right). Both these molecules have been

associated with inflammatory response and matrix remodelling in the airways. Additional protein biomarkers MMP-9 and IL-1β were analysed as well but the concentrations in the supernatant were undetectable for all samples.

TIMP-1, a matrix metalloproteinase inhibitor, is secreted by cells to prevent proteolytic activity. Stiffening of the matrix reduced its expression, which it somewhat recapitulates the reduction of TIMP-1 in asthma. Usually, TIMP-1 is secreted in excess to modulate matrix remodelling, but alteration of TIMP-1/MMP-9 ratio inclines to a more pathological state of matrix remodelling (Vignola *et al.,* 1998).

The current results show the effect of young's modulus on the phenotype on the human airway smooth muscle. As the stiffness of the gel increases, the cytoplasmic and nuclear morphology characteristics increases as well (with the eccentricity inversely proportional to the stiffness). Increase in cell spreading area, as well as diameter, are seen in morphometry and flow cytometry analyses. Coupling the data with the increased immunofluorescence of phospho-GSK3β*,* a known marker of hypertrophy (Deng *et al.,* 2008), matrix stiffening strongly suggests induction of hypertrophy in ASMCs. Additional immunofluorescence analyses also showed elevated levels of α-SMA on matrix stiffening, and its upregulation could be explained by increased phosphorylation of SMAD2, a TGF-β1 downstream transcription factor (Caraci *et al.,* 2008). Upregulation of α-SMA indicates increased contractile activity, which is again a key marker in asthma. Increased TGF-β1 activity also increased phosphorylation of GSK-3β, and thus also promoting hypertrophy

(Caraci *et al.,* 2008). Elevated proliferation rates from cell cycle, metabolic, and DNA quantification assays is also in congruence with the phenotype seen in asthma.

Assessing the secretions of ASMCs to evaluate autocrine and paracrine effects, IL-6 and TIMP-1 are both downregulated as matrix stiffness increases. Interleukin-6 has could act both as a pro and anti-inflammatory cytokine, and so there is uncertainty to what its action could be on the cells. On the other hand, TIMP-1 is known to inhibit matrix remodelling, and IL-6 is known to induce TIMP-1 production (Silacci *et al.,* 1998). Downregulation of IL-6 would have caused downregulation of TIMP-1, and such cascade can cause promotion of matrix remodelling, another indication of the extracellular matrix changes in asthma. IL-6 also attenuates α-SMA production (An *et al.,* 2017), and so downregulation promotes increased contractile activity of ASMCs which supports the previous results. One plausible explanation on the inhibition of IL-6 production is the phosphorylation GSK-3β. GSK-3β promotes IL-6 production (Wang *et al.,* 2018), and therefore attenuation of its activity downregulates as well the production of IL-6, together with the aforementioned effect of cellular hypertrophy. Fig. 4.9 shows the possible signalling pathway involved in matrix stiffening:

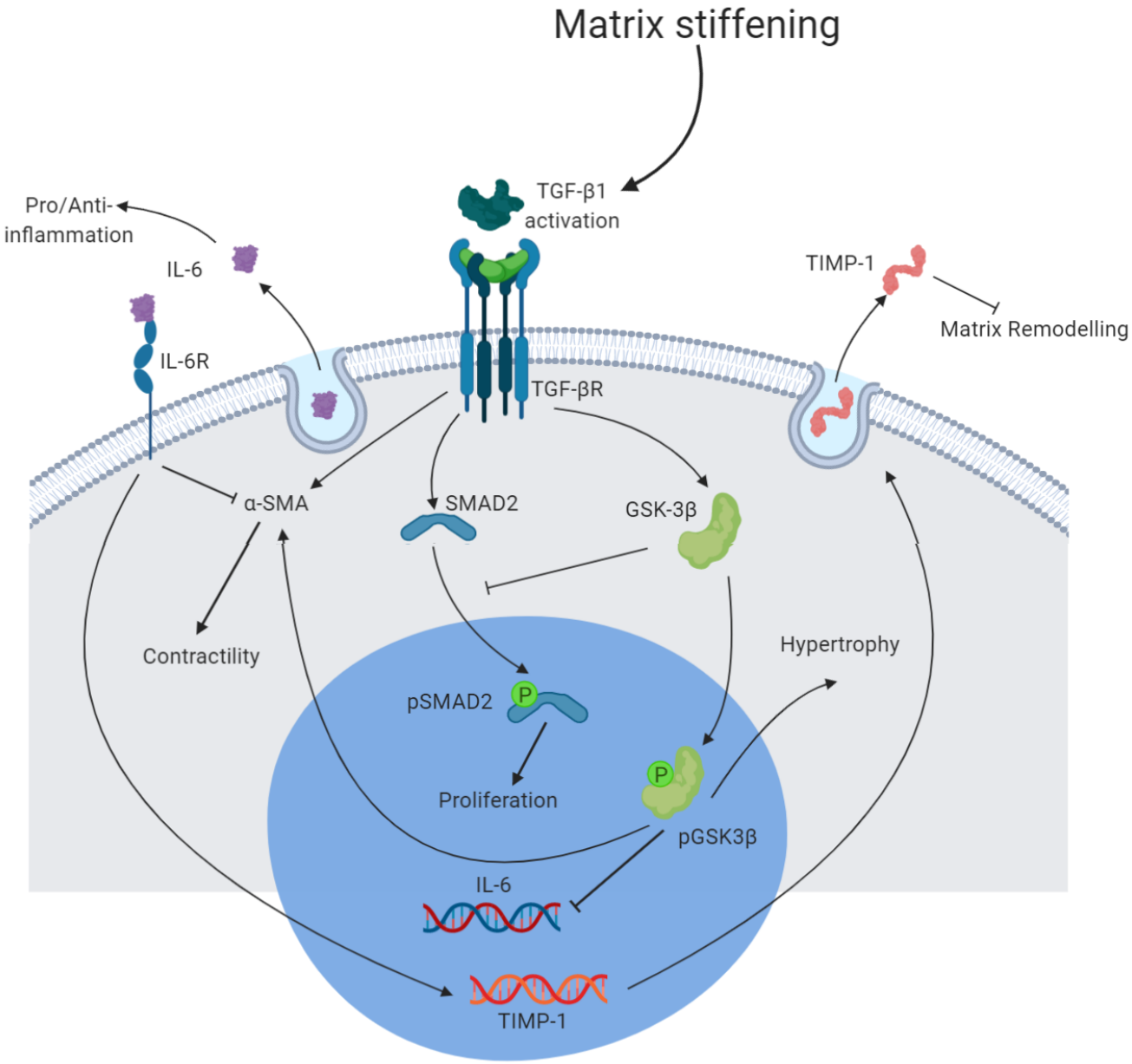


Figure 4.9 Hypothesised signalling pathways occurring in ASMCs in response to matrix stiffening. Increased ECM stiffness activates matrix-bound TGF-β1 which affects phosphorylation of pSMAD2 (contraction, proliferation) and increases α-SMA expression (contraction). Activity of GSK-3β is also affected, which its phosphorylation causes hypertrophy. In addition, matrix remodelling behaviour changes due to TIMP-1 downregulation, as well as inflammatory response of ASMCs via IL-6.

In the normal airways, the phenotype that hASMCs presented are elongated, spindle-like structure. The muscle cell shortens when contractile agonist is presented, either by the

neighbouring cells or from the inspired air. In pathological conditions such as asthma, the airway smooth muscle mass is significantly increased, and so the contraction is much more pronounced with a considerable reduction of airway diameter. Several researches also have discovered that the hASMCs became hypertrophic (Plant *et al.,* 2012), hyperproliferative (Johnson *et al.,* 2001), and hypercontractile (Berair *et al.,* 2013) as the phenotype becomes asthmatic. The results in this study may denote that it could be the stiffness of the airways that contributes to the phenotypic changes of hASMCs, since it is established that the stiffness of the airways is increased in pathologic conditions like asthma (Brackel *et al.,* 2000) and chronic obstructive pulmonary disease (Jones *et al.,* 2016). The increased stiffness of the airways can also be attributed to the elevated expression of crosslinking enzymes in the airways (data unpublished, Amanda Tatler et al.). As the pathological condition continues locally, the stiffening of the extracellular matrix components in the airways can drive the ASMCs to become hypertrophic, hyperproliferative and hypercontractile. The hypercontraction in the local environment can be propagated in the whole airways, thereby cascading the event to the tissue scale. ASM mass will be increased as a result, and with the pathological conditions maintained due to sustained expression of crosslinking proteins and contraction, a chronic condition develops. This hypothesized mechanism in terms of mechanotransduction pathways could be one of the underlying trails for chronic asthma development. If so, the inhibition of crosslinking enzymes may be a key to treat the asthmatic ASMCs, modifying the local microenvironment stiffness and afterwards reverting the phenotype to its normal state. Performing experiments on asthmatic ASMCs cultured on normal substrate stiffness could verify the hypothesis if the stiffness induces phenotypic changes from asthmatic to normal cells.

One caveat of the study is the method on increasing the stiffness of the material. As the stiffness of the gel increases, the availability of RGD peptides also increases since the polymer concentration is also increased. This could potentially confound the result on whether it is the stiffness or the adhesive motif availability that affects the phenotype. However, suppose that the pericellular matrix quantity is also increased in pathological conditions, then the material would fit as a model for airway stiffening.

In conclusion, the stiffness of the matrix affects the morphology and the α-SMA expression of the hASMCs. As the modulus increases, the cellular area, perimeter, and nuclei area increases. The relationship is inversely proportional to the eccentricity and aspect ratio, since elongation is prominent in lower stiff substrate. The cytoskeletal marker α-SMA is also increased as the modulus increases, indicating increased contractile activity. Cumulatively, the results suggest that the stiffening in the airways could contribute to the phenotypic change on the resident hASMCs, thereby propagating the diseased state of the airways.

Chapter 5

Basal membrane biomimicry with tuneable properties for human bronchial epithelial cell culture

5.1 Introduction

The luminal side of the airways is comprised of epithelium and is responsible for a multitude of functions in host defence, biochemical signalling, and inflammation (Hiemstra *et al.,* 2015). To accomplish its roles, epithelial cells use functional protein secretion such as mucous and growth factors to manipulate the microenvironment for maintenance of homeostasis. The airway epithelial cells sit in an extracellular matrix which has nanofibrous topography and contains a plethora of proteins that promote adhesion, remodelling, and migration of cells. Several authors have already developed *in vitro* models to replicate the airway niche, and several papers utilised electrospinning to mimic the cells' matrix.

Electrospinning is one of the most promising processes to fabricate fibres from a wide range of polymers. (Frenot, 2003) . Electrospinning, has recently attracted much attention not only because of its versatility with a variety of polymer materials but also its ability to produce fibres consistently within a submicron range that is otherwise cannot be achieved using standard fibre-generating technologies (Sun *et al.,* 2003). Over the years, almost 200

polymers had been electrospun and are characterised by its capabilities in use for membrane and substrates (Jiang *et al.,* 2004).

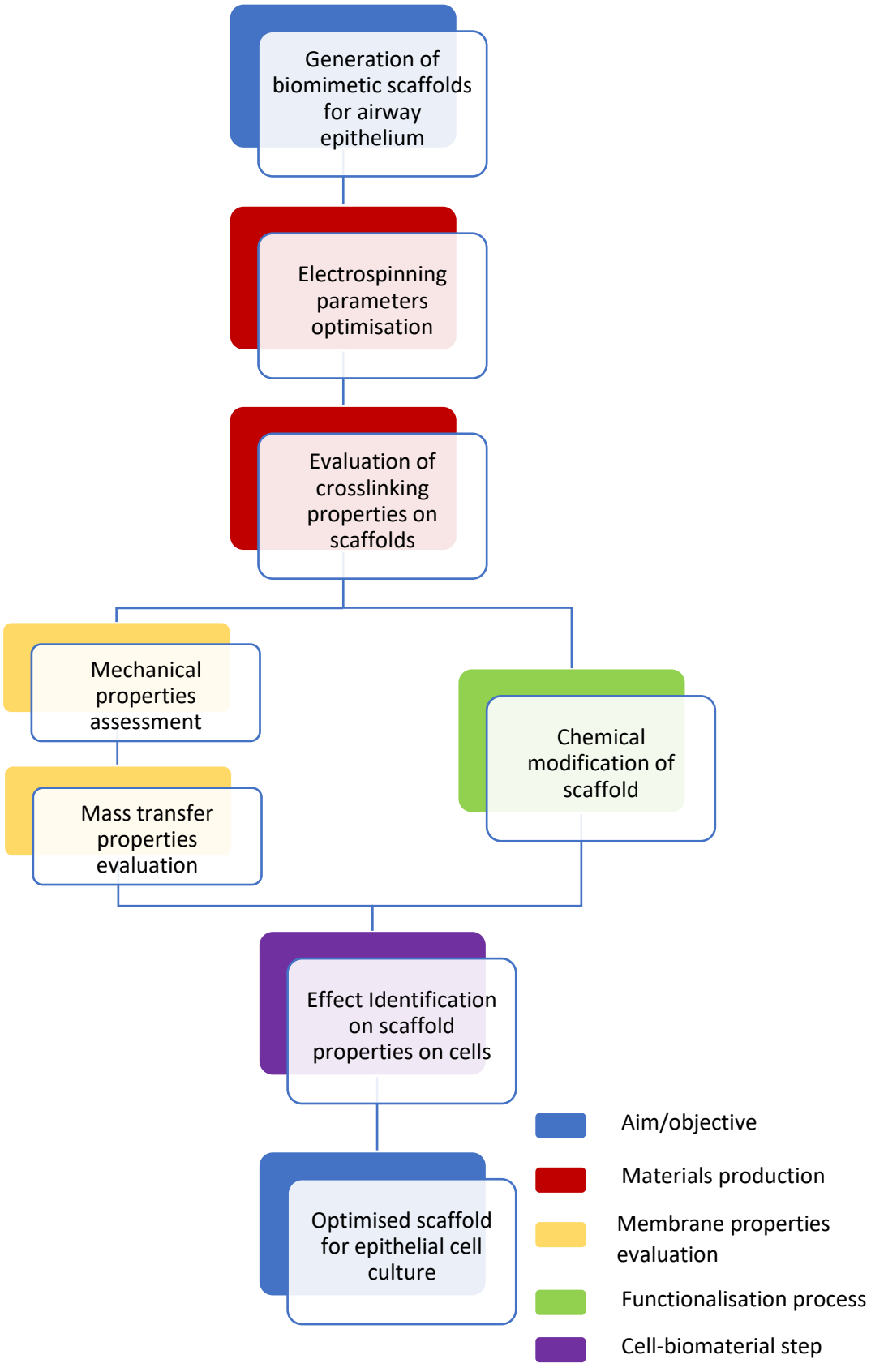
Of those who utilised electrospinning in projects to engineer the airway epithelium, most of the studies used synthetic polymers to culture airway respiratory epithelial cells (Morris *et al.*, 2014). However, to date, synthetic polymers have failed to renew the epithelium and integrate to the host (Cyranoski, 2016; Townsend *et al.,* 2018). A recent study summarised potential reasons of failure such as the incompatibility of the scaffold to support cellular migration and/or altered progenitor cell proliferation across the construct (Schwartz *et al.,* 2019); large animal models ended with stenosis and inadequate epithelialization, leading into failure of the graft (Schwartz *et al.,* 2019; Townsend *et al.,* 2018). Turning to natural polymers might offer opportunities for improved biological properties to successfully regenerate the airway epithelium and develop models to understand the dynamics occurring in the airways.

Several candidate materials of biological origin for epithelium extracellular matrix engineering are collagen, chitosan, and gelatin. Despite the tendency of biological-derived materials to have weak mechanical strength, chemical modifications can be performed on the backbone of the protein of interest to increase its strength. Recently, a few studies used electrospun gelatin methacryloyl and have proven it to be biocompatible. However, the tuneability of mechanical strength seemed to be limited to a narrow range (Aldana *et al.,* 2019). Also, numerous proteins that the airway epithelial cells secrete need to adhere on the surface so that the cells can remodel the matrix. Not only does the matrix need to be remodelled by the cells but antioxidant activity has also been identified as a critical function for the matrix to keep the integrity of the airway epithelium. These properties

cannot be recapitulated by one native biopolymer, and so developing a material that can mimic these complex properties would likely be the key to successful development of the airway epithelium.

In this study, we have used gelatin methacryloyl and the process of electrospinning to generate structurally similar fibres, in terms of diameter to the native extracellular matrix of the airways. We also have evaluated the tuneability of the mechanical strength of the scaffold, as well as analysing the effect of L-cysteine conjugation unto the surface of the scaffold on the overall bioactivity of the material. L-cysteine was chosen because of its thiol sidechain, to mimic some hypothesised function of laminin (as laminin is rich with cysteine residues) (Graf *et al.,* 1987) .

Chapter experimental overview



5.2 Methods

5.2.1 Electrospinning of GelMA

GelMA synthesised as described previously in Chapter 3 (precipitated) was dissolved in 2,2,2 – trifluoroethanol (Sigma) with a concentration of 20% wt/vol at 60°C. The resulting solution was transferred to a 10 mL syringe (BD Plastipak) and mounted in a syringe pump and the feed is attached to a plastic tubing with an end needle tip of 0.6 mm diameter. Using the electrospinning equipment (IME technologies), the temperature of the chamber was adjusted at 20°C and relative humidity of 70%. The collector used was a rotating mandrel of 10 cm in diameter and 20 cm in length with a rotation rate of 2000 rpm. To evenly distribute the material into the scaffold, a horizontal sweeping motion was utilised with a range of 15 cm and a sweeping velocity of 2 cm/s. The solution was pumped at a flow rate of 1 mL/h for 8 h, and the following factors are used to evaluate the alignment of nanofibers:

Table 5.1 Factors used in electrospinning

Run	Voltage (+, -)	Distance
A	+ 20 kV, -4 kV	20 cm
B	+ 25 kV, -4 kV	20 cm
C	+ 20 kV, -4 kV	12 cm
D	+ 25 kV, -4 kV	12 cm

5.2.2 Crosslinking of GelMA nanofibers

The GelMA nanofiber mat was removed from the collector, cut into 1x1 cm pieces, and then placed in a 60 mm petri dish. A crosslinking solution was made using a solution of IMS with varying amounts of distilled water (4-16% v/v), and 1% Irgacure 2959 (Sigma).

Four mL of the crosslinking solution was pipetted in the petri dish and irradiated in a 15W 365 nm UV bench lamp for 10 min. The solution was removed and the crosslinked scaffoldpeeled off the aluminium foil and washed with PBS 3x. The scaffolds were stored in PBS at 4°C prior on use.

5.2.3 Scaffold characterisation

5.2.3.1 Scanning electron microscopy

Wet crosslinked GelMA electrospun nanofibres were attached to a carbon tape mounted on an aluminium stub for electron microscope. The stubs were then placed in a vacuum oven overnight to dry the samples, and then sputtered with 10 nm of iridium to increase conductivity of the samples. The nanofibers were imaged at the Nanoscale and Microscale Research Centre at the University of Nottingham using a JEOL 7100F field emission gun – scanning electron microscopy at an accelerating working voltage of 5 kV and a working distance of 10 mm.

5.2.3.2 Surface elastic modulus determination

Crosslinked samples were mounted in a glass slide using a cyanoacrylate glue and left until the scaffold became immobile. The MFP-3D Standalone Atomic Force Microscope (AFM) (Oxford Instruments, Asylum Research Inc., CA) was used to obtain Force-displacement curves of GelMA for Young's modulus calculation. An AFM silicon nitride probe MLCT-C (Bruker Nano Inc., CA) with nominal tip radius of 30 nm, 2.5-8 μm tip length, 7 kHz Resonant Frequency and 0.01 N/m Spring Constant was used. The actual tip base radius, tip height and conical half-angle were calculated via SEM imaging of the probe, with values of 2.32 μm, 2.923 μm and 28.439°, respectively. The tip radius was characterised

by measurement of a standard sample, with a value of 32±4 nm. From the force-displacement, the Sneddon model was used to evaluate the surface modulus of the nanofibres.

5.2.3.3 Fourier Transform Infrared Spectroscopy

Samples were loaded into an ATR-FTIR spectrophotometer (Agilent Cary 630) with a wavelength resolution of 2 cm^{-1}. A Savitsky-Golay smoothing filter was employed using GraphPad Prism 7, and the spectra were overlaid to compare chemical changes in the scaffolds.

5.2.3.4 Protein diffusivity studies

A 1 cm x 1 cm scaffold was assembled with a cell-crown insert for 24 well plate. 100 µL of 1 mg/mL of bovine serum albumin conjugated with FITC (Sigma) in PBS was pipetted onto the apical side of the insert, and 1000 µL of PBS was pipetted at the basolateral side of the insert. The well plate was then placed in the plate reader (Tecan Infinite pro 200) and the fluorescence intensity was measured every 5 seconds in multiple points of the plate. To ensure homogeneity of the diffusing solution, a 3 mm orbital motion was added prior during measurement.

5.2.3.5 Porosity measurements

GelMA nanofiber scaffolds were soaked in 100% ethanol for 1 h and measured using a calliper for volume calculations. The scaffold was then transferred and weighed in a bijou, and then dried overnight in a vacuum oven at 20°C. Afterwards, the dried scaffold was weighed again and the mass of the bijou is subtracted to obtain the mass of the dried

scaffold. The porosity of the scaffold is calculated from the average of 3 samples as follows:

$$Porosity, \varepsilon = \frac{Mass_{wet\ scaffold} - Mass_{dry\ scaffold}}{Volume_{wet\ scaffold}\ \rho_{EtOH\ at\ 20℃}} \quad (5.1)$$

5.2.4 GelMA nanofiber functionalisation

5.2.4.1 L-cysteine conjugation via EDC-NHS coupling

Crosslinked scaffolds measuring 1 x 1 cm were incubated with a solution containing 0.5 mM of N-hydroxysuccinamide (NHS, Thermofisher) and 0.25 mM of L-cysteine hydrochloride monohydrate in a 2-(N-morpholino)ethanesulfonic acid (MES, Thermofisher) buffer at pH 6.4 for 10 minutes to allow permeation of molecules in the nanofiber matrix. To proceed with the conjugation, 0.25 mM of 1-ethyl-3-(-3-dimethylaminopropyl) carbodiimide hydrochloride (EDC, Thermofisher) in MES buffer at pH 6.4 was added to the solution for 1 hr. The solution is removed, and the scaffold is washed 3x and incubated in PBS overnight at 37°C. Prior to use on any experiments, scaffolds were washed again 3x in PBS and stored at 4°C.

5.2.4.2 Thiol content determination

The DTNB assay was used to determine free thiol groups as a measure of the scaffold conjugation. Briefly, the scaffolds were incubated with a 400 μL solution of 262 mM Tris-HCl and 13 mM EDTA (pH 8.9). For detection of sulfhydryl groups, 40 μL of 150 μM of

Ellman's reagent (5,5'-Dithio-bis (2-nitrobenzoic acid), Thermofisher) was added to the scaffold, pipetted several times for mixing the entire solution, and incubated for 20 minutes. To quantify the number L-cysteine conjugated, 100 μL of the resulting solution was pipetted in a 96-well plate, and the absorbance was measured at 412 nm. The absorbances were converted into concentrations using L-cysteine as a standard for calibration curve. For time-course experiments to evaluate the stability of conjugation, the concentration was divided to the initial mass of the scaffold prior on crosslinking to normalise the data.

5.2.4.3 H_2O_2 scavenging assay

The peroxide scavenging assay was performed to assess the antioxidant capacity of the scaffold. A 0.02% H_2O_2 solution was placed on the scaffold and incubated at 37°C for 5 min. 50 μL of the supernatant was mixed with 50 μL of TMB substrate solution (TMB) and 50 μL of 200 U/mL horseradish peroxidase. The resulting solution was incubated at dark for 5 minutes, and 10 μL of 2 N H_2SO_4 was added to stop the reaction. The absorbance was measured at 450 nm with correction values subtracted at 540 nm. The percentage of inhibition of free radicals is computed as follows:

$$\%\ Inhibition = \frac{A_{before\ incubation} - A_{after\ incubation}}{A_{before\ incubation}} \times 100 \qquad (5.2)$$

5.2.5 Biocompatibility studies

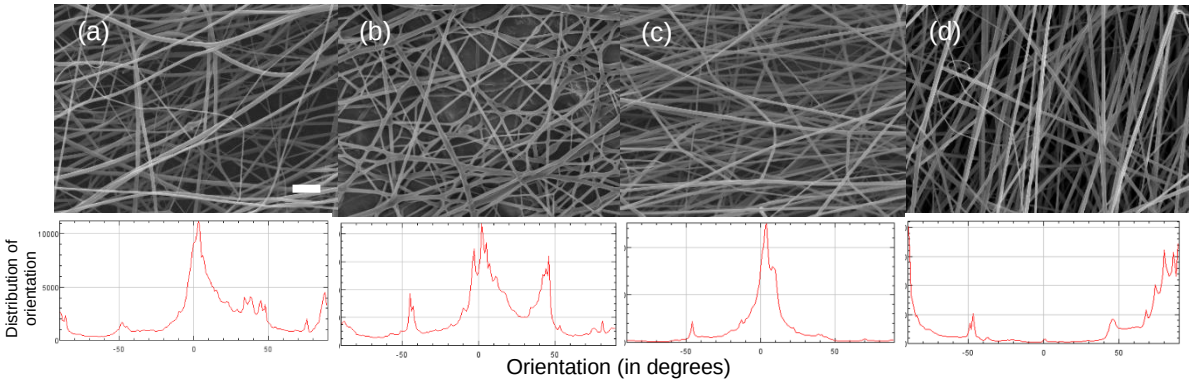
Calu-3 cells were used in the evaluation of biocompatibility of the electrospun scaffolds. Detailed culturing conditions and cellular viability assay was performed using Presto Blue are described in Chapter 2. Briefly, cells were plated at a concentration of 5,000 cells/cm^2 in α-MEM with 10% FBS, 1% Glutamax and 1% AB/AM stock solution. The cells were incubated with Presto Blue™ solution on Day 4 and fluorescence intensity was measured using a plate reader (Tecan).

5.2.5.1 Cell morphology evaluation

After 4 days of culture, scaffold-containing cells were fixed with 4% paraformaldehyde for 5 min. The fixing solution was removed and the scaffolds washed with 3x PBS. These samples were then dehydrated through increasing grades of ethanol and placed in a carbon tape mounted on an aluminium stub. Similar sample preparation and SEM imaging were performed as listed in section 5.2.3.1.

5.3 Results & Discussion

5.3.1 Nanofiber physical properties evaluation



Run	Average Diameter (nm)	Pore Area (μm^2)	Minimum Pore Area (μm^2)	% Porosity
a	319.9 ± 119.8	6.26 x 10^5	4.80 x10^3	49.01 ± 0.37
b	278.1 ± 101.1	5.52 x 10^5	4.12 x10^3	45.18 ± 6.63
c	336.2 ± 92.2	9.21 x 10^5	4.69 x10^3	52.99 ± 10.25
d	376.3 ± 119.8	7.01 x 10^5	4.34 x10^3	49.09 ± 0.10

Figure 5.1 Scanning electron micrograph of electrospun GelMA and the fibre alignment distribution. Scale bar = 1 µm with magnification of 10,000x. The table shows the mean morphological characteristics of the produced nanofiber.

Fibre diameter distributions of GelMA nanofibres ranged from 278-376 nm (Fig. 5.1., table), nearly the same diameter as the epithelial basement membrane extracellular matrix of the airways at 245 nm ± 83 (Harrington *et al.,* 2014). Observations on the effect of electrospinning parameters in on the characteristics of the fibres are seen, with fibre diameter decreasing as tip-to-collector distance increases. Other studies have made similar observations, and it has been deduced that increasing the tip-to-collector distance enables the fibre to be stretched further before attaching to the collector. The phenomenon, in turn, results in smaller fibre diameter. Thinner fibre diameter resulted in smaller pore area, albeit all scaffolds have comparable minimum pore area and porosity. On the alignment of the fibres into a rotating collector, only runs c & d (Fig. 5.1) achieved a degree of alignment

again likely due to tip-to-collector distance. Despite having a fast collector rotation speed, increasing the tip-to-collector distance can result in elevated turbulence of the whipping motion of the jet. This motion has an effect of increasing entropy as it attaches to the drum collector and not aligning to the directionality of the rotation. Of all the process evaluated, run (c) was chosen to be used for further analyses.

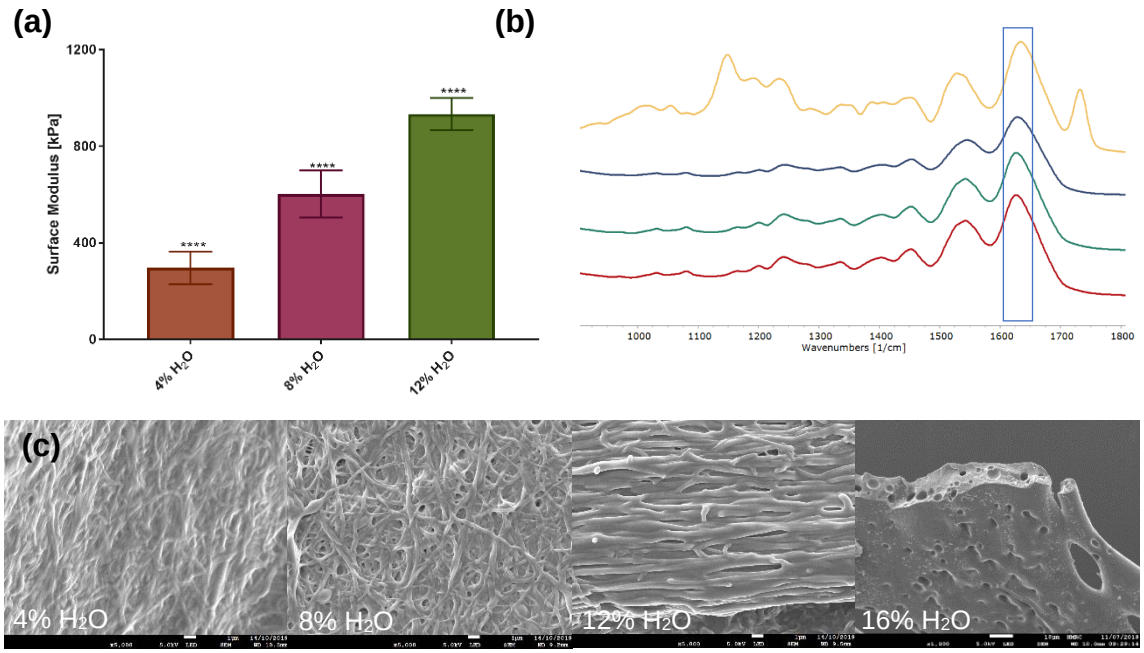


Figure 5.2 (a) Average from 36 force curves, triplicate samples. Two-way ANOVA shows a statistically significant difference between samples with $p<0.0001$. Stiffnesses recorded were as follows: 4% H_2O (296.9±67.4 kPa), 8% H_2O (602.5±97.7 kPa), 12% H_2O (933.3±66.56 kPa), with $p<0.0001$. (b) FTIR shows reduction of absorbance in 1670-1600 cm^{-1} spectra, confirming crosslinking of the methacrylate groups in electrospun GelMA. Legend: Yellow = uncrosslinked GelMA, Blue = 4% H_2O crosslinked, Green = 8% H_2O crosslinked, Red = 12% H_2O crosslinked. (c) Morphology of electrospun nanofibers after crosslinking in different water concentrations. AFM Measurements were performed by Francesco Pappalardo.

The modulus of electrospun nanofibers can be modulated by increasing the amount of water in the crosslinking solution. Young's modulus of the crosslinked nanofibers as seen in Fig. 5.2a is linearly related to the water content of the sample, averaging at approximately 75 kPa/1 % H_2O increase, independent of GelMA concentration and ranging

from ~296-933 kPa. The crosslinking is confirmed via FTIR in Fig. 5.2b, where the absorption of the methacrylate groups in the nanofibers decreased as compared to the uncrosslinked fibre. It is unclear how the modulus is increased as the water content in the crosslinking solution is increased, but one plausible reason is that the presence of water molecules enabled the penetration of the crosslinking agent throughout the fibres. Increasing the water content might have swollen the GelMA nanofibers temporarily, while alcohol retains its structural integrity prior to crosslinking, and after UV irradiation, the structure became permanent. Likely there is an increased degree of crosslinking as the water content is elevated, with more crosslinking agent permeated throughout the scaffold. SEM also showed morphological changes in the scaffold, where increased diameter is seen on the photomicrographs (Fig. 5.2c). The diameter increase is likely attributed to the swelling of the fibres due to the nature of the GelMA that behaves as hydrogel upon crosslinking; such nature supports the hypothesis stated earlier. Increasing further the water content in the crosslinking solution either resulted in the merging of the fibres (Fig. 5.2c, rightmost) and thus removing the nanostructure, or dissolving the nanofibers into the solution; the upper limit of which is 16% H_2O. The tuneability of the scaffolds in terms of mechanical strength can be furthered by modifying the methacrylate groups and increasing crosslinking time and crosslinker concentration, making the platform more versatile in culturing vast types of cells.

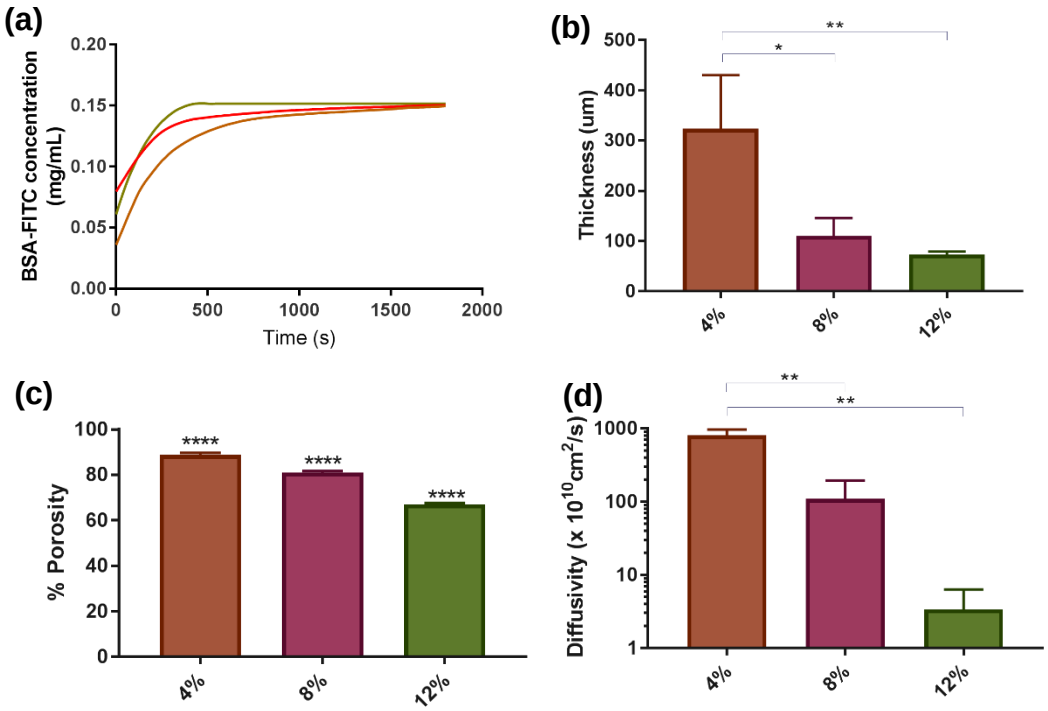


Figure 5.3 (a) Diffusion profile of crosslinked electrospun GelMA nanofibers. The profile shows a decreasing trend of (b) membrane thickness, (c) porosity and (d) diffusivity as stiffness increases (moderated by % H_2O in crosslinking). Legend: brown = 4% H_2O, magenta = 8% H_2O, and green = 12% H_2O. Used ANOVA with Tukey's post hoc test (p*<0.05, p**<0.01,p****<0.0001). Data shown here are from triplicate samples.

The rate of diffusion as a result of the changes in morphology is also affected. The diffusivity of BSA conjugated with FITC (MW = 68 kDa) varied highly across scaffolds (Fig. 5.3a), ranging from 1.39 x 10^{-10} to 9.18 x 10^{-8} cm^2/sec (Fig. 5.3c). As a basal membrane intended scaffold, the minimum diffusivity is similar to the native basal membrane extracellular matrix, thus mimicking the protein transport rate (Marlar *et al.*, 2014). The diffusivity is crucial to replicate the conditions in the airways to evaluate cell-cell communication via paracrine transport.

Observing the thickness of the scaffold and its diffusivity, one can deduce that the swelling of the nanofibers increased interstitial space across the scaffold (Fig. 5.3b). This property makes proteins diffuse faster in softer, swollen nanofiber hydrogels and decreases with less

swollen, more compacted and thus stiffer scaffold. The swelling of the nanofibers not only increases the inter-fibre spaces but also creates a more porous region inside individual fibres (Fig. 5.3d). With the unprecedented control of diffusivity, the property can be used to model pathological conditions, where the permeability of the airways are known to increase due to inflammation and obstruction (Goldie & Pedersen, 1995).

5.3.2 Nanofibre cysteine functionalization via EDC-NHS

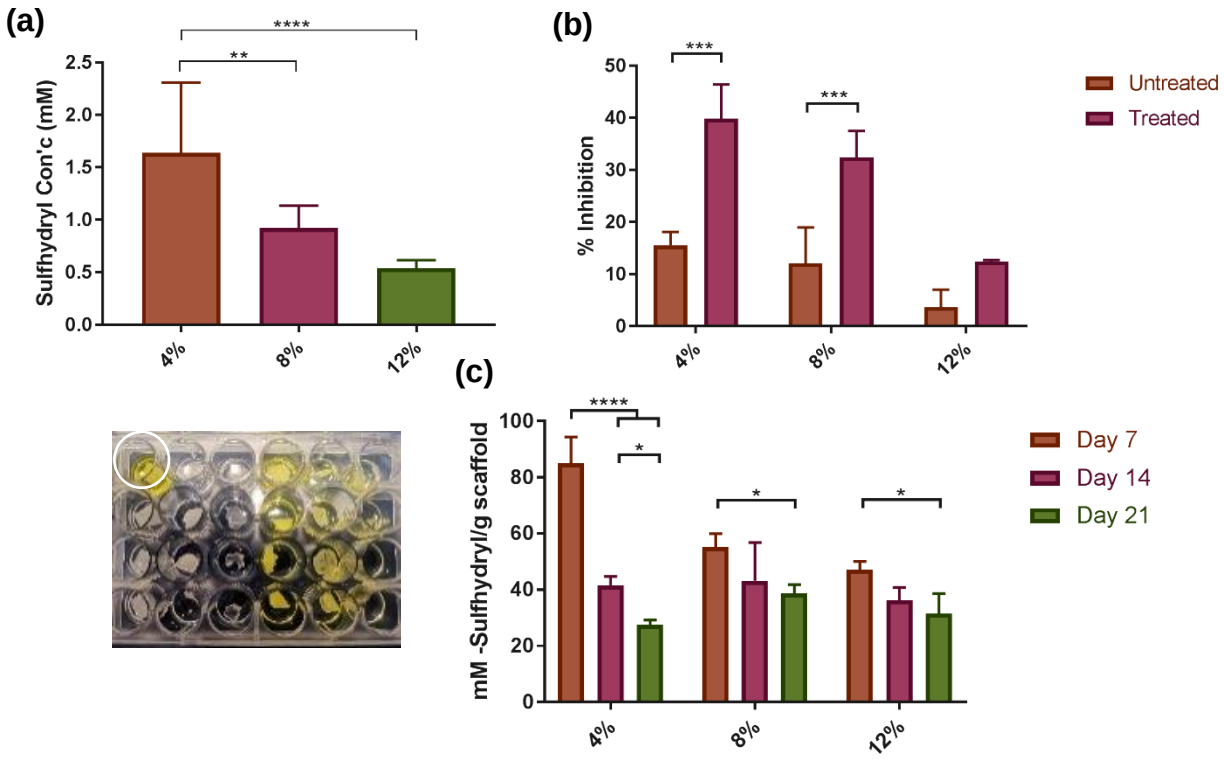


Figure 5.4 (a) DNTB assay for the determination of free thiol groups. Day 0 showed a significant difference in the number of thiols between samples. The figure below (a) showed positive sulfhydryl GelMA despite of EDC being absent in the reaction, which indicates absorption of L-cysteine that may lead to a false positive. (b) H_2O_2 scavenging assay, confirming the antioxidant properties of the sulfhydryl group. Time course determination of sulfhydryl compound is then performed (c) showing that GelMA nanofibers were indeed functionalised with thiol; samples without EDC did not show any reaction to DNTB, which shows desorption of L-cysteine residues. Used ANOVA with Tukey's post-hoc test (*p<0.05, **p<0.01, ***p<0.001, ****p<0.0001).

Conjugation of L-cysteine groups was successful via the EDC-NHS synthesis route. A maximum of ~1.6 mM cysteine (equivalent to ~82 mM cysteine/g of the scaffold) can be incorporated into the electrospun nanofibres, in which the soft (4% H_2O crosslinked) matrix has the highest value (Fig. 5.4a). This increased thiol content is likely due to less crosslinking density with a more swelled network, sequestering more L-cysteine and EDC-NHS into the fibres. Surface conjugation can therefore be tuned in with larger range for 4% H_2O crosslinked nanofibers as compared to the 8 and 12% H_2O crosslinked electrospun scaffolds. Confirmation of scaffold functionality was assessed using hydrogen peroxide scavenging assay. Scaffolds conjugated with sulfhydryl groups show increased inhibition of oxidation, with a decreasing percentage as the stiffness increases (Fig. 5.4b). Previous results showed higher thiolation in softer scaffolds, therefore, the degree of inhibition in can be attributed to the actual content of sulfhydryl on the scaffold.

Upon incubation of the scaffolds in PBS at 37°C at 5% CO_2 for 21 days, the sulfhydryl surface group concentration decreases significantly from Day 7 to 14 (Fig. 5.4, right). From Day 14 to 21, only 4% H_2O crosslinked nanofibres were significantly reduced. Two plausible reasons for surface thiol reduction could be deduced: first would be the scaffold's degradation, where surface hydrolysis can occur on the fibres and thereby removing the portion of the scaffold that contains the functionalisation. Second is the air-mediated oxidation of L-cysteine, wherein a freely available L-cysteine from the scaffold degradation reacts with the immobilised L-cysteine. The reaction forms a disulphide bridge between two sulfhydryl residues, forming the dipeptide L-cystine. It would be predicted that proteins from the culture media as well as cellular secretion will be binding unto the

surface as well, affecting matrix deposition and availability of functional molecules at the electrospun fibre.

5.3.3 Cell culture results

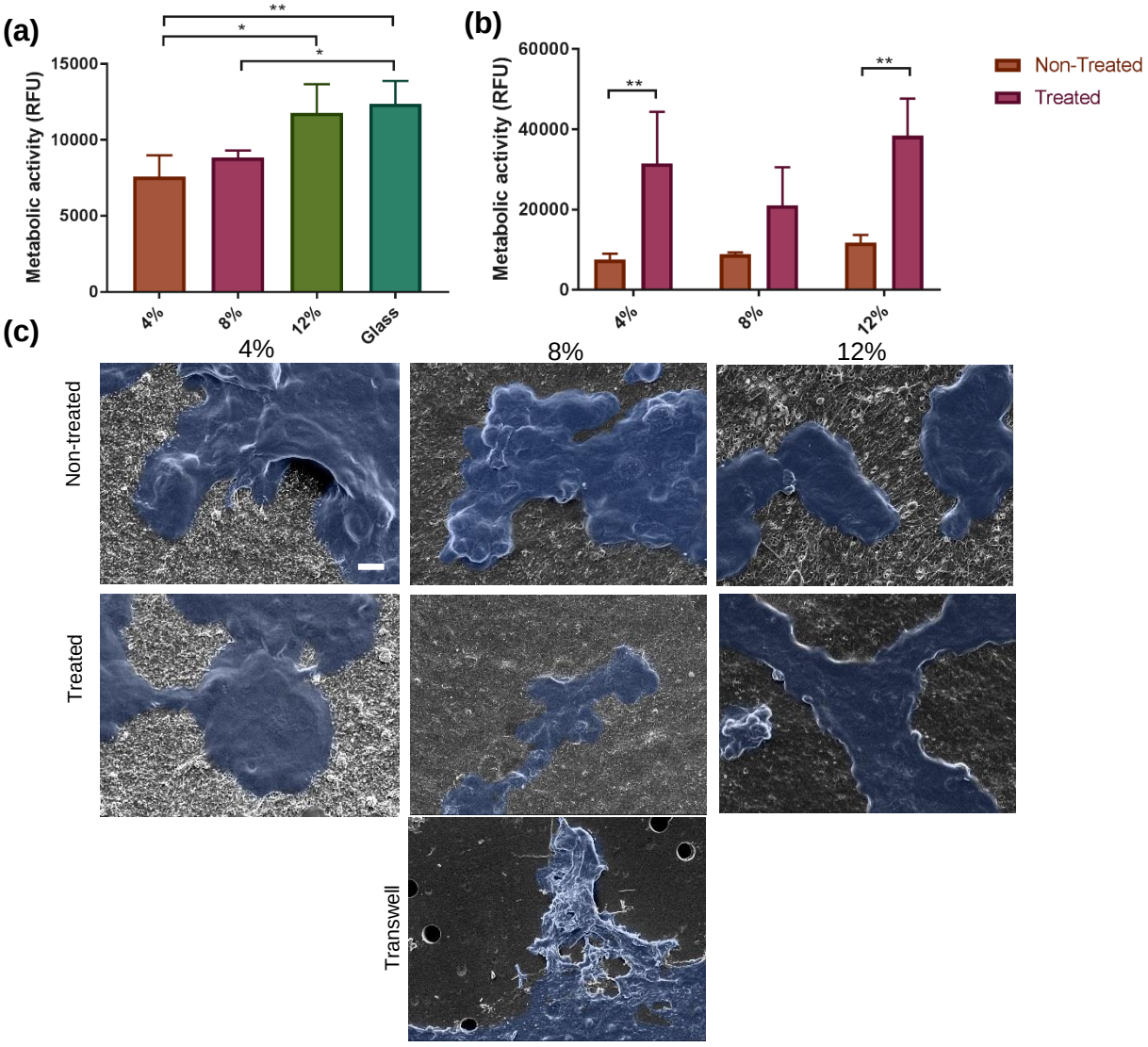


Figure 5.5 Presto Blue assay results after 4 days of culture of Calu-3 epithelial cells in electrospun scaffolds. (a) One-way ANOVA revealed higher metabolic activity in increasing scaffold stiffness (b) Two-way ANOVA showed significantly higher metabolic activity in the thiolated samples as compared to non-treated scaffolds, indicating an increased rate of proliferation (p*<0.01, p**<0.001, n=3 technical replicates). (c) FESEM false-coloured photomicrographs of calu-3 cells in different scaffold stiffnesses and treatment. Scale bar = 10 µm at 1,000x magnification.

The effect of matrix stiffness in epithelial cell proliferation was also investigated. The results show that stiffening increases the metabolic rate of cells, which could relate on the increased proliferation in Calu-3 cells, following the profile seen in ASMCs (Fig. 5.5a). Furthermore, cells cultured in thiol-containing scaffolds have a significantly increased rate of proliferation as compared to the non-treated ones, emphasizing the effect of conjugated cysteine on the scaffold (Fig. 5.5b). Structural elucidation using an electron microscope shows cells appear flatter as compared to non-thiolated scaffolds (Fig. 5.5c). This phenomenon usually indicates preferential cell spreading, in this case more spreading into the treated nanofibres in contrast with the non-treated ones. As discussed before, ECM secretions in the pericellular area could have attached more into the scaffold, making cellular proliferation and motility improve on the thiol-functionalised surfaces.

Electrospinning provides a process to generate sub-micron fibres using electric fields in a controlled chamber. The fibres produced are similar in general physical appearance to the basal lamina, where a nanofibrous structure is also observed in its extracellular matrix. The high surface to volume ratio creates a more conducive environment for the cells, allowing them to manipulate the matrix mechanically into a single fibre level. Porosity also allow cells to migrate inside the scaffold and create a complex microenvironment. The porous regions could possibly create an environment where cells populate inside the membrane and serve as the basal lamina, and the cells on the surface differentiate into specialised cells that recreate the stratified epithelium. By using GelMA, these nanofibrous scaffolds can be biodegraded by cells due to its collagen motifs, and cell adhesion with the RGD peptide in

its sequence. These characteristics of the electrospun GelMA nanofibres makes it a useful candidate for epithelial tissue engineering.

In this work, we varied the process elements to obtain different characteristics of the resulting mat. Overall, increasing tip-to-collector distance reduced the fibre diameter and the specificity of the orientation of the deposited fibres. This characteristic effect has also been observed in other studies, where empirical evidence shows that the higher the distance between the needle tip and collector, the more stretched the jet that results into thinner fibres (Doshi & Reneker, 1995). Orientation, however, is not maintained as the tip-to-collector distance is increased because of the elevated entropy caused by the whipping motion of the jet to the collector (Rajput, 2012). Aside from the fibre diameter and orientation, the resulting product can also be tuned mechanically by modifying the crosslinking conditions. By solely increasing the water content from 4-12% in the crosslinking bath solution, we managed to obtain a modulus range of approximately 300-900 kPa. The process maintained the topography of the scaffold, albeit fibre diameters increased considerably due to swelling, and a confirmation of the hydrogel characteristics of GelMA. On the other hand, increasing the water content further proved to be deleterious in the morphology of the fibres, removing the nanofibrous topography by having the fibres merged at 16% H_2O content.

The hydrogel characteristics of the scaffold was observed on the thickness profiling of the electrospun mats. The thickness varied largely across different crosslinking solutions as a consequence of varying swelling ratio interlinked with crosslinking density. This result also explains Young's modulus for each condition, where the higher the water content in crosslinking, the lesser the membrane thickness (which corresponds to swelling ratio) and

the stiffer the scaffold. Another consequence of membrane thickness is change in diffusivity of molecules and proteins. It can be deduced that the more swelled the polymer matrix is, the larger the porosity and the less compact the membrane is, thereby allowing molecules to diffuse faster. Diffusivities ranging from the scale of 10^{-8} to 10^{-10} cm^2/s were obtained from the scaffolds (Fig. 5.3). For future studies, this tuneability of diffusivity of the membranes could be further adjusted by co-spinning GelMA with a sacrificial polymer like polyvinyl alcohol, where immersion in a water bath will cause the dissolution of the sacrificial polymer and thereby increasing the permeability of the scaffold. This property is advantageous when simulating the effect of permeability of the epithelium on various cellular processes and drug delivery applications. Coupled with the mechanical strength tuning, the system can be effectively used to mimic changes in the airways for us to understand further the dynamics of cells and matrix in the airways.

Another aspect of this study is the functionalisation of the surface by L-cysteine. Conjugation of a sulfhydryl group in the scaffold could improve adhesion of secreted matrix by airway epithelial cells, as other studies have shown increased adhesion upon thiolation of surface (Yiu *et al.,* 2001). This can be mediated by the formation of disulphide bridges in the secreted proteins, where thiols augment the adhesion of extracellular matrix components from cellular secretion (Laragione *et al.*, 2003). Conjugation was higher in 4% H_2O crosslinked GelMA as compared to 8 and 12%, and this is likely due to larger accessible space for reaction in the more swelled network. Analysis of the conjugation stability in the nanofibres proved to have a decreasing trend over 3 weeks course, suggesting either oxidation of the sulfhydryl groups or surface degradation of the nanofibres, as hydrolysis can still partially degrade the scaffold. In addition, the sulfhydryl

groups conjugated at the surface showed antioxidant activity, where the thiol group in L-cysteine can undergo redox reactions to absorb free radicals and decrease overall ROS activity in the extracellular space (Chae *et al.*, 1994; Levonen *et al.*, 2004). The antioxidant property of the airway epithelium has been observed before (Wright *et al.*, 1994), and this property may be due to laminin, a thiol-containing ECM protein in the epithelium. The conjugation can protect the cells from free radicals, with the effect of improved proliferation and overall cell health in scaffold culture as observed in culturing Calu-3 airway epithelial cells. Fig. 5.6 shows the hypothesised mechanism occurring in the bespoke scaffold:

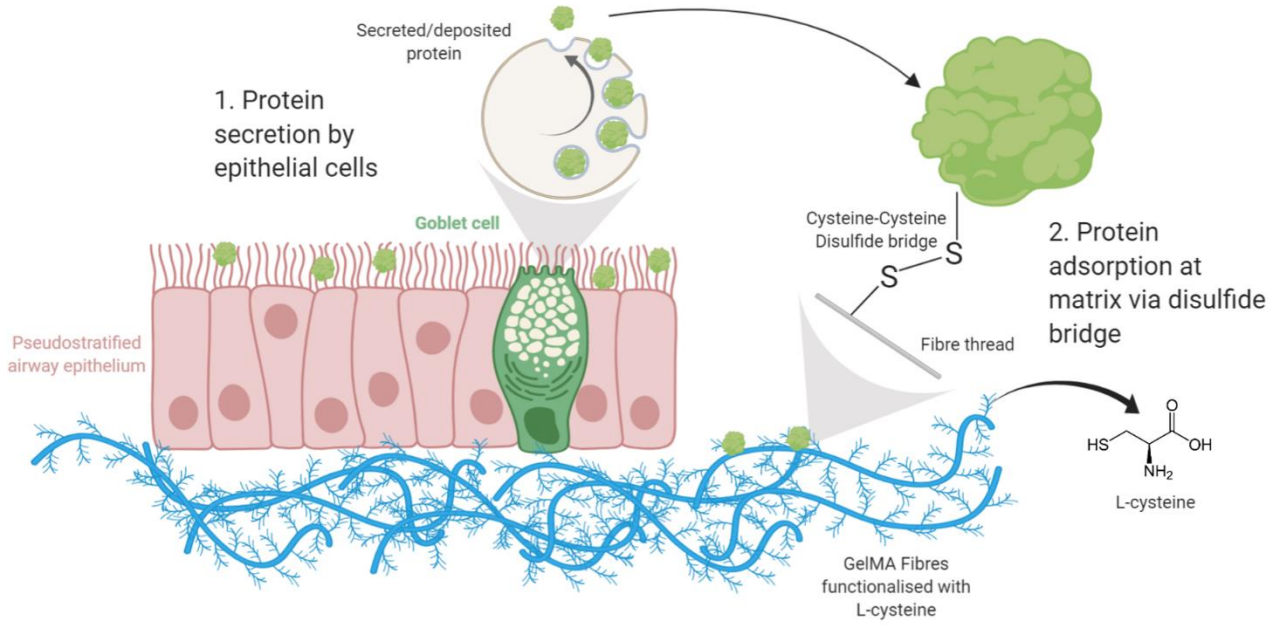


Figure 5.6 Schematic of protein adhesion in epithelial cell secretions through disulphide bonding in L-cysteine conjugated scaffolds. Proteins secreted by AECs through the apical and basal side (1) can be deposited in the electrospun matrix through physical adsorption by diffusion through the scaffold's pores, or by chemical adsorption via disulphide bridges in the conjugated nanofibres (2).

Overall, we have developed a material that mimics the morphology of basal lamina to engineer the airways epithelium. GelMA nanofibrous hydrogel scaffolds showed tuneable physical and membrane properties fit for understanding epithelium mechanodynamics. Conjugation with cysteine showed positive response with the cells, mimicking the antioxidative properties of the epithelium and increasing the rate of metabolism (which could translate into elevated proliferation) of airway epithelial cells. With the GelMA hydrogel platform previously used for ASMCs culture, an epithelium-smooth muscle junction could be successfully engineered to observe interactions between cells. This platform could be used to determine the effect of mechanical changes to the global cellular and signalling dynamics of the airway, leading to the causation of pathology.

Chapter 6

Tissue engineering of human airway cultured in a ‘novel’ Taylor-Couette-Poiseuille bi-perfusion bioreactor

6.1 Introduction

Tissue engineering offers an approach to understand mechanisms of the human body without the need of invasive procedures and availability of participants. The central dogma of tissue engineering revolves along cells, biomaterials, and bioreactors, to create a construct either for experimentation or potentially for transplantation. To be able to develop a model which recapitulates the dynamics inside our body and is iteratively and interactively tuned, would offer considerable advantage on observations of the physiology and pathology of the intended tissue of interest.

Of those organs that are in interest, the airways have piqued interest in the recent years of work on tissue engineering. On the perspective of transplantation, the airways necessitate immediate operation, usually in the form of resection and re-anastomosis when the damage is minimal. Extensive damage arising from airway cancer (Chao *et al.,* 1997), thyroid cancer (Cho *et al.,* 2010; Price *et al.,* 2008), smoking (Ziad, 2013; Thorley & Tetley, 2007), vehicular accidents (Karmy-Jones & Wood, 2007; Scaglione *et al.,* 2006) and

stenosis due to intubation (Andrews & Pearson, 1971; Cho *et al.*, 2013;Andrés *et al.*, 2004; Schultz *et al.*, 1991; Spittle & McCluskey, 2000)requires transplantation. Airway transplantation is very rare and is a difficult option due to the availability of the donors, short time required for intervention, and organ rejection (Beigel & Müller-Ruchholtz, 1984). For most of the patients, there are no option but only palliative treatment in point-of-care scenarios.

Understanding airway dynamics has been limited to non-invasive or minimally invasive procedures. Although we have advanced our knowledge on disease conditions of the airways, the observations on the interactions of cells and the effect of environmental factors has been limited. Use of *in vivo* models relies on allergen induced changes, where observation can mostly occur in endpoint assays (Aun *et al.*, 2017). The pathology propagation is also different, as mice for example do not have spontaneous asthma unlike humans (Aun *et al.*, 2017; Gelfand, 2002). Indeed, developing models with tuneable characteristics of the environment will let us understand further the pathogenesis of airway disease, and in turn develop strategies for intervention and treatment.

Recent work done by the team of Paolo Macchiarini gained considerable attention due to the use of the approach on the use of tissue engineering and regenerative medicine in creating the first ever human engineered airways (Bristol, 2008). Briefly, Macchiarini's approach used a patient's mesenchymal stem cells that is differentiated into chondrocytes and respiratory epithelial cells, seeded into a scaffold obtained from decellularized trachea or an electrospun polymer scaffold, grown using a bioreactor, and transplanted back into

the patient (Baiguera *et al.,* 2010). This process potentially beneficial, because the requirement of having a donor is removed, and risk of rejection is reduced due to the fact that the cells came from the patient themselves (Macchiarini *et al.,* 2008). However, after several surgeries were performed using , only one patient survived, with the the others dying because of the complications that arose after the surgery such as fatal airway (stent) occlusion, discontinuous epithelial coverage of the lumen of the trachea and trachea-esophageal/mediastinal fistula (Corbascio *et al.,* 2014).

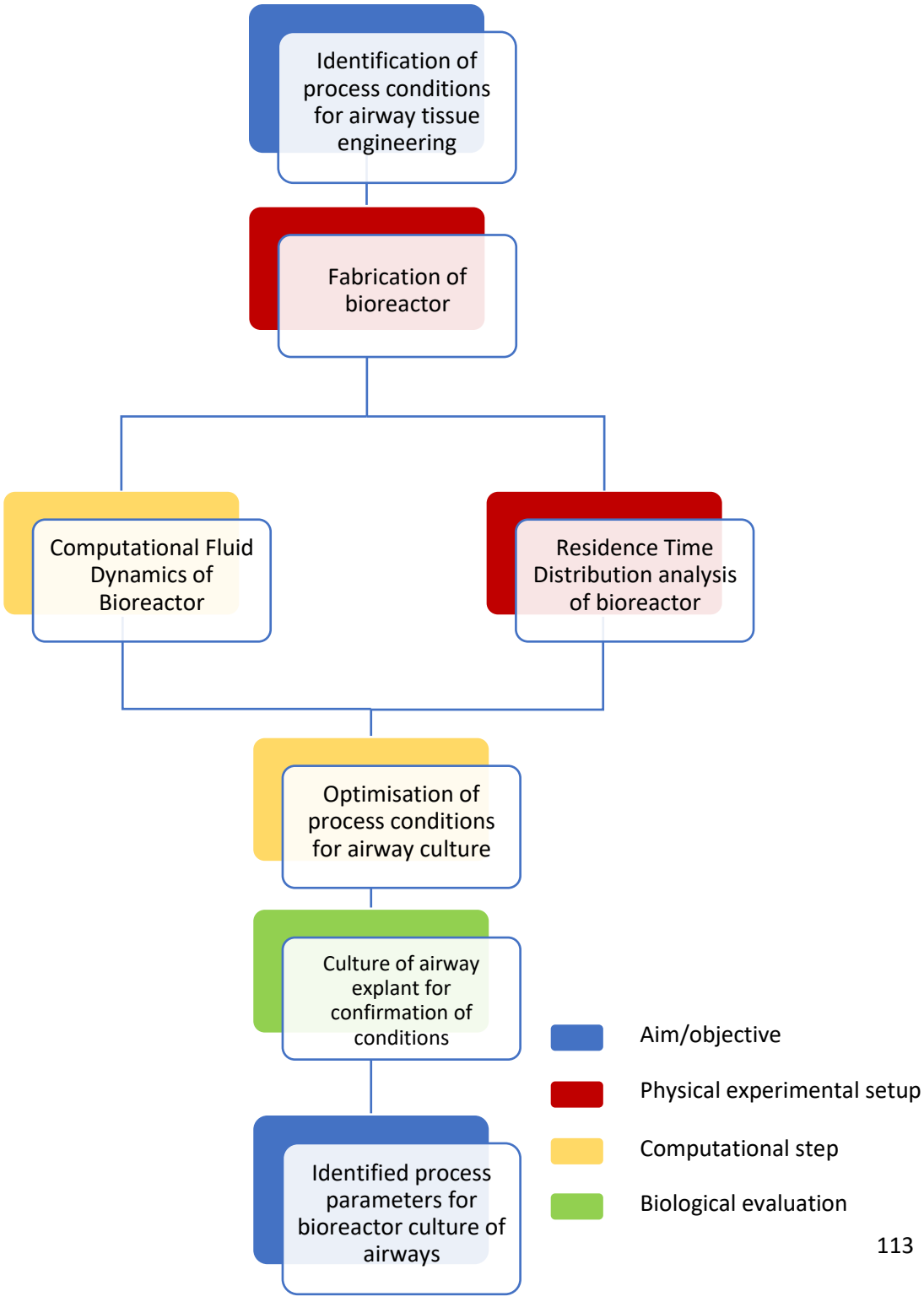
Noting these findings, we hypothesized on approaches to address the failure of the transplants. In particular, the finding that the transplanted trachea required stents because of the mechanical failure of the construct was either the material failure and/or the airway cells' immature phenotype due of the culturing conditions in the bioreactor. This could be addressed by modifying the culture conditions in the bioreactor, in which the flow regime and environment could be adjusted to increase proliferation of airway cells as well as differentiate them into ciliated and secretory cells types. In this chapter a new strategy for tissue engineering of human airways was designed, built and tested based on the use of a Taylor-Couette-Poiseuille (TCP) flow regime to increase the viability of the engineered trachea.

The TCP bioreactor system offers a cyclic shear stress induction to the outside layer of the airways via the TCP flow regime and an inner layer that is partially submerged with culture media, in which the space is saturated with oxygen and carbon dioxide. The configuration of the bioreactor permits a dual chamber for culture conditions where the outer layer of the

airways in the outer chamber is strengthened by the cyclic fluid environment; the inner chamber encourages growth of pseudostratified columnar epithelial cells by its air-liquid interface culture, which is the standard culture technique of differentiated primary airway epithelial cells.

With problems occurring on the current technology of airway tissue engineering, the TCP bioreactor system could provide the appropriate biomimicry of the physiological environment to engineer the airway combining biological and physical properties to drive and support its function. The TCP bioreactor system could deliver adjunct technology to the current biomaterials synthesis of scaffolds for the maturity of the tissue-engineered trachea, providing a possibility not just for understanding the biology of the airways, but also for patients that have terminal tracheal associated diseases to recover their quality of life.

Chapter experimental overview



6.2 Methods

6.2.1 Fabrication of the bioreactor

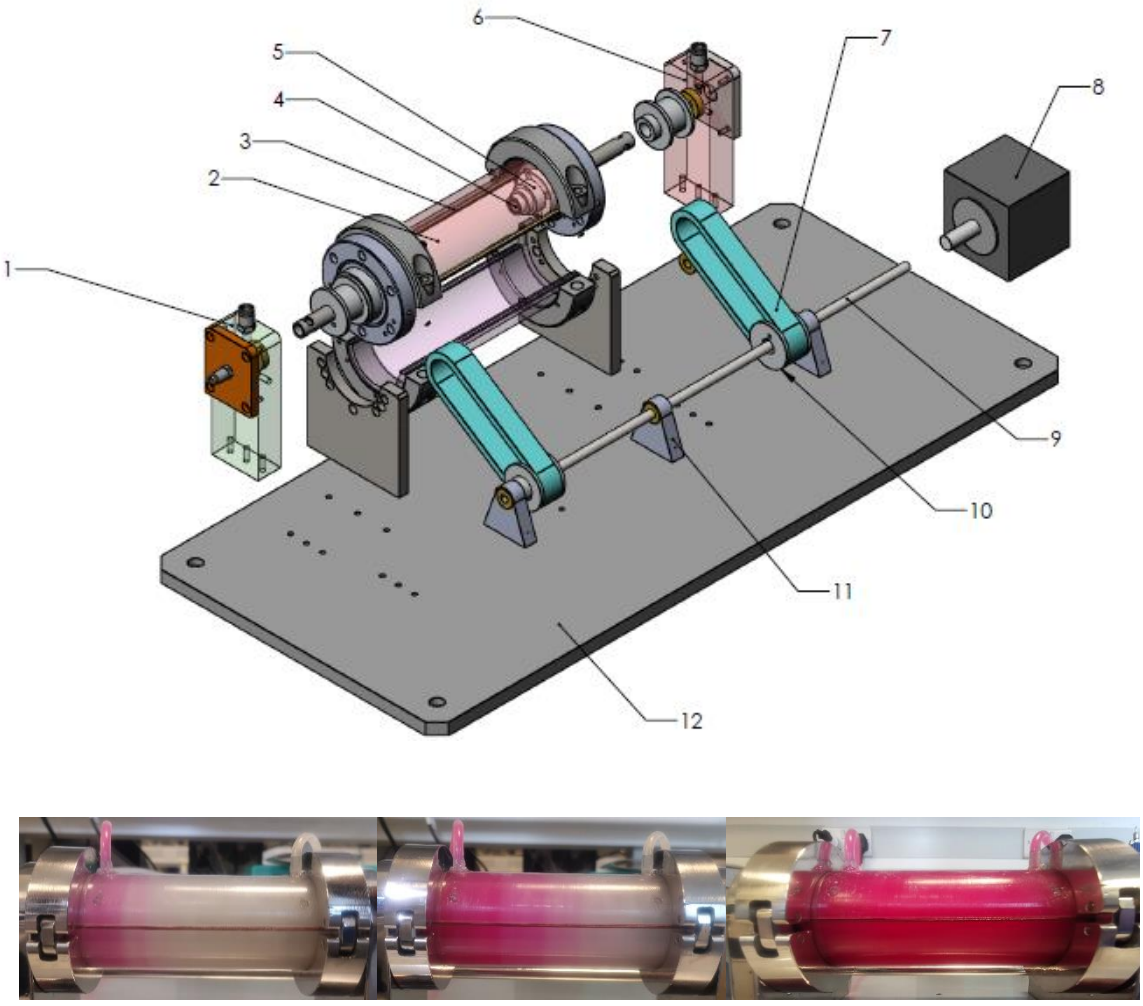


Figure 6.1 (Top) Numbered isometric exploded 3D assembly of the Taylor-Couette-Poiseuille bi-perfusion bioreactor. (Below) Flow imaging of the bespoke bioreactor, using aqueous solution of anisotropic stearic acid crystals perfused with phenol red after steady state conditions.

The bioreactor was designed to culture tubular organs with two chambers on the luminal and outer side. These chambers (named inner and outer chambers) are supported by

individual culture media for both the epithelium and the mesenchyme, while controlling the rate of shear across the scaffold/tissue. In our specific application the outer chamber culture medium supports the culture of chondrocytes, airway smooth muscles, and fibroblasts, while the inner chamber culture medium is an air-liquid interface with the media supporting the epithelium and basal cells.

The operation of the bioreactor is as follows (see Fig. 6.1 for reference): for the inner chamber, a fluid is fed into section (1), containing the culture medium for the epithelium. The nozzle in (1) is a specially designed rotary pneumatic fitting (FS Series 1/4" Straight Female Threaded BSPP ends and Nitrile Seals) for the capability to attach tubing while the construct is rotating and keeping the tube static. Section 1 can also have a T-junction, where a secondary fluid, air, is fed together with the medium for the inner chamber (2). The two-phase flow is recapitulated, controlling the liquid level and its velocity as it is being supplied in (2). A separate entrance of the media at the outer chamber (3) is supplied through small ø ID 2 mm nozzles. The outer chamber's enclosure is made up of a polycarbonate glass, where the nozzles are attached at both ends for the outer chamber media entrance and exit. The fluid enters/exits at (4), where a cylindrical knurled surface (5) is fitted for the construct to be mounted. Several diameters of (5) are fabricated to accommodate different diameters of the construct. The fluid from the inner chamber exits at (6), and both the media from inner and outer chamber is recycled to the reservoir. The inner chamber shaft where (5) is mounted is attached to a sprocket, with a timing belt (7) fitted from the bioreactor shaft to the motor (8) through a shaft extension (9) that is also fitted with a sprocket (10). The motor is designed to operate under humid conditions, with IP68 waterproof seal for continuous operation of the motor. The motor shaft assembly is

inserted into a base plate connector (11) that is screwed firmly at an aluminium base (12). All parts in which materials are not mentioned are made with medical grade stainless steel 316. O-rings for leakage prevention are food-grade silicone-based material. The bioreactor assembly can be disassembled and packed for autoclaving and reuse.

Now, considering the bespoke bioreactor is to be used for culturing tissues, characterisation is required for understanding the flow dynamics and its potential effect on the tissue engineered airways. The following shows both experimental and computational modelling presented when either trachea or primary bronchus would have been cultured.

6.2.2 Flow and shear-field simulation

The bioreactor was simulated using finite element method (FEM), performing computational fluid dynamics (CFD) to define the range of operating conditions for a TCP flow regime to occur. In performing the simulation, the following are the assumptions made for the model:

1. The fluid flow is laminar (low Reynolds number), incompressible, fully developed, and obeys Newtonian behaviour. Viscous heat dissipation is neglected and no-slip boundary condition is implemented on the scaffold.
2. The scaffold material is intact and does not degrade. Properties of the material are to be evaluated experimentally.

The governing equations for the mass and momentum balances are as follows:

$$\nabla \cdot (\rho \mathbf{u}) = 0 \tag{6.1}$$

$$\rho(\mathbf{u} \cdot \nabla)\mathbf{u} + 2\rho\boldsymbol{\omega} \times \mathbf{u} = \nabla \cdot [-p\mathbf{I} + \tau] + \mathbf{F} - \rho\boldsymbol{\omega} \times (\boldsymbol{\omega} \times \mathbf{r}) \tag{6.2}$$

where **u** is the vector velocity component in the rotational coordinate system, ρ is the density of the fluid, p is the pressure, **r** is the positional vector, and **ω**is the angular velocity vector. Equation 2 is the incompressible Navier-Stokes equation in rotational coordinates, and is used to simulate flow from the inner and outer chamber of the bioreactor. These coupled non-linear differential equations are to be evaluated using Finite Element Method. Contour plots of the scaffold's shear stress and fluid flow profile shall be generated and evaluated for optimization.

6.2.3 Residence time distribution analysis (RTD)

RTD is evaluated via stimulus-response technique. Sodium chloride at 2.5 M was used as a tracer and fed into the entrance outer chamber in a pulsed manner, and the output concentration of each outflow streams was determined using a conductivity meter; the salinity values obtained were converted into concentrations.

A plot of RTD Function $E(t)$versus time*t* will be generated, whereas variables for flow characteristics are:

$$E(t) = \frac{C_T(t)}{\int_0^\infty C_T(t)dt} \tag{6.3}$$

$$t_m = \int_0^\infty tE(t)dt \tag{6.4}$$

$$\sigma^2 = \int_0^\infty (t - t_m)^2 E(t)dt \tag{6.5}$$

Where C_T is the tracer exit concentration, t_m is the mean residence time, and σ^2 is the variance of the distribution. From these equations, the mass transfer evaluation in the reactor was quantified by solving for Peclet number:

$$\frac{\sigma^2}{{t_m}^2} = \frac{2}{N_{Pe}} - \left[\frac{2(1 - e^{-N_{Pe}})}{{N_{Pe}}^2}\right] \tag{6.6}$$

To evaluate the response of the bioreactor performance in conjunction with the aforementioned equations, a response surface methodology was used.

6.2.3 Response surface methodology – central composite design

Prior to RTD analysis, pre-determined sets of runs were evaluated using Response Surface Methodology, Central Composite Design for the simulation parameters. As the system is expected to have nonlinear behaviours, several central points shall be added to increase the curvature of the model as well as its accuracy. Process factors were considered in the RSM:

Table 6.1 Process factors used in RSM

Factors	Operation Values	Equivalent process factor
Flow rate (rotation rate of peristaltic pump)	60 rpm	3.6×10^{-5} mL/s
	85 rpm	5×10^{-5} mL/s
	110 rpm	6.4×10^{-5} mL/s
Inner cylinder rotation rate	30 rpm	π rad/s
	75 rpm	2.5 π rad/s
	120 rpm	4 π rad/s
Inner cylinder diameter	Trachea (Upper limit)	2.5 cm (Breatnach *et al.,* 1984)
	Bronchus (Upper limit)	2 cm (Lee *et al.,* 2014)

The aforementioned RTD parameters and the occurrence of bypassing and tailing are the measured responses. To further increase the accuracy of the model, a hierarchal model reduction will be used to eliminate factors and higher order interactions that has no significant contribution to the response. The Box-Cox plot for power transforms and Cook's Distance shall affirm the necessity of data transformation prior to model reduction. These methods shall be iterated until an acceptable value of Adjusted R^2 – Predicted $R^2 \leq$ 0.2 is obtained and therefore a representative empirical model for the process will be generated.

As RTD profiles of the bioreactor are determined, the variance of the resulting values can induce inconsistencies in the operation. To abate this effect, the standard deviations could be utilized for the minimization of Propagation of Error (PoE). This inherent experimental design of the bioreactor development is the so-called Design for Six Sigma approach, where the variance of the responses is to be minimized by adjusting the factors and its

variance that affects the process. The optimized results are determined with the objective of minimizing the standard deviations of the RTD parameters. Ranges of parameters will be screened depending on their desirability values and will be used for experimentation on the tissue engineering of airways, where the objective function will be maximisation of Peclet number and removal of bypassing and tailing.

6.2.4 Trachea bioreactor culture

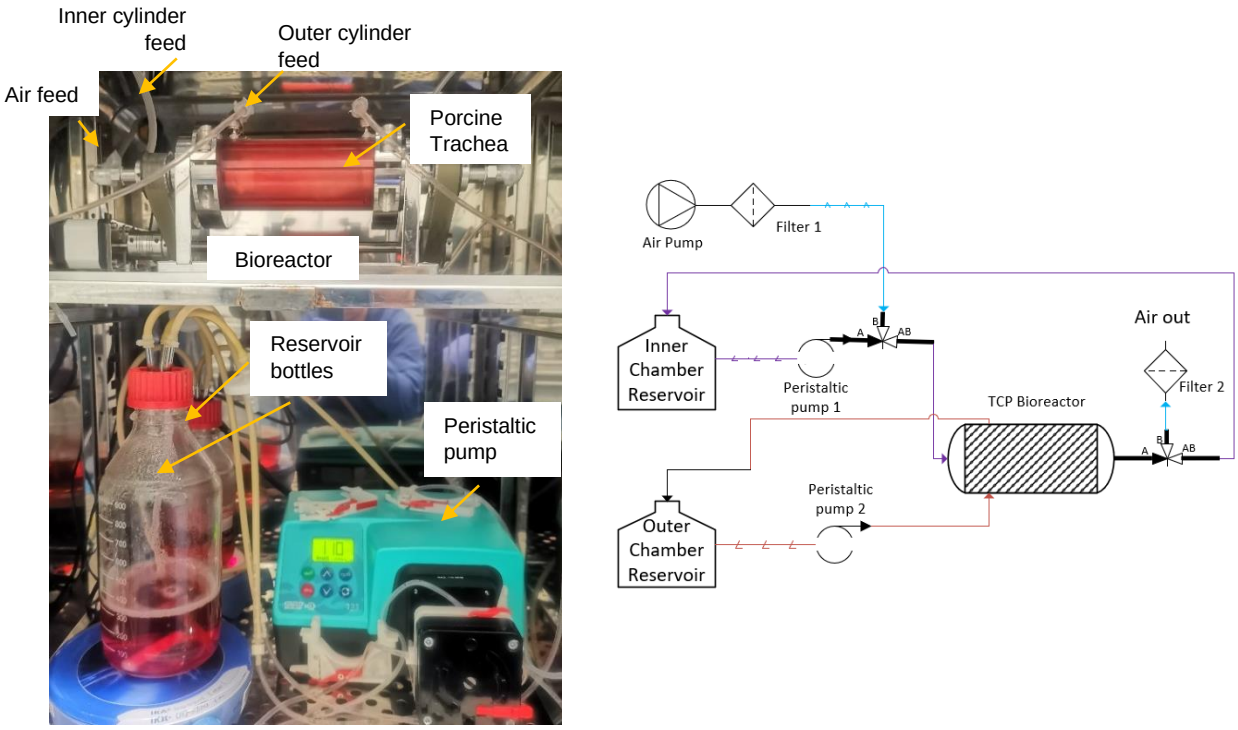


Figure 6.2 Photo on the operation of the bioreactor in the culture of trachea. The left diagram shows a process flow diagram on the operation during culture

To obtain a proof-of-concept in tissue engineering of the airways, a porcine trachea was cultured in the bioreactor. The trachea was obtained in a local abattoir in Nottingham, United Kingdom (Chettles, Stoke La, Nottingham), where after the local butchers sacrificed the animal, the trachea was excised and stored immediately in DMEM containing

4% Antibiotic/Antimycotic solution (Sigma) on wet ice. Upon arrival in the lab, the trachea was washed extensively with ice-cold PBS containing 2% Antibiotic/Antimycotic solution, and then cut with a sterile scalpel to accommodate the 10 cm upper length limit of the bioreactor. Excess connective tissue was manually removed with sterile scalpel and tweezers, and the cleaned trachea was then mounted in the bioreactor. The trachea outer region was cultured using DMEM with 20% FBS, 2% Glutamax (Invitrogen), and 2% Antibiotic/Antimycotic solution, while the luminal side of the airways was supplied by α-MEM (Lonza) with 20% FBS, 2% Sodium Pyruvate (Invitrogen), 2% Glutamax (Invitrogen), and 2% Antibiotic/Antimycotic solution. The bioreactor was placed in standard cell culture incubator maintained at 37°C and 5% CO_2.

6.2.5 Trachea histology

After 5 days of culture, the cultured trachea was removed from the bioreactor and washed thoroughly with PBS. It was then immersed in 4% buffered paraformaldehyde overnight and then processed using standard histological techniques: dehydrated with increasing grades of ethanol, paraffin embedded, and cut with 10 μm sections mounted on a glass slide for staining. Haematoxylin & Eosin, Masson's trichrome, and Periodic acid-Schiff base was used to evaluate temporal changes in the cellular and extracellular matrix of the porcine trachea. A pathologist (Dr. William Dalleywater, M.D.) at Queen's Medical Centre assessed the photomicrographs to confirm changes occurred in the trachea.

6.3 Results

6.3.1 Bioreactor flow-field simulation (velocity and vorticity)

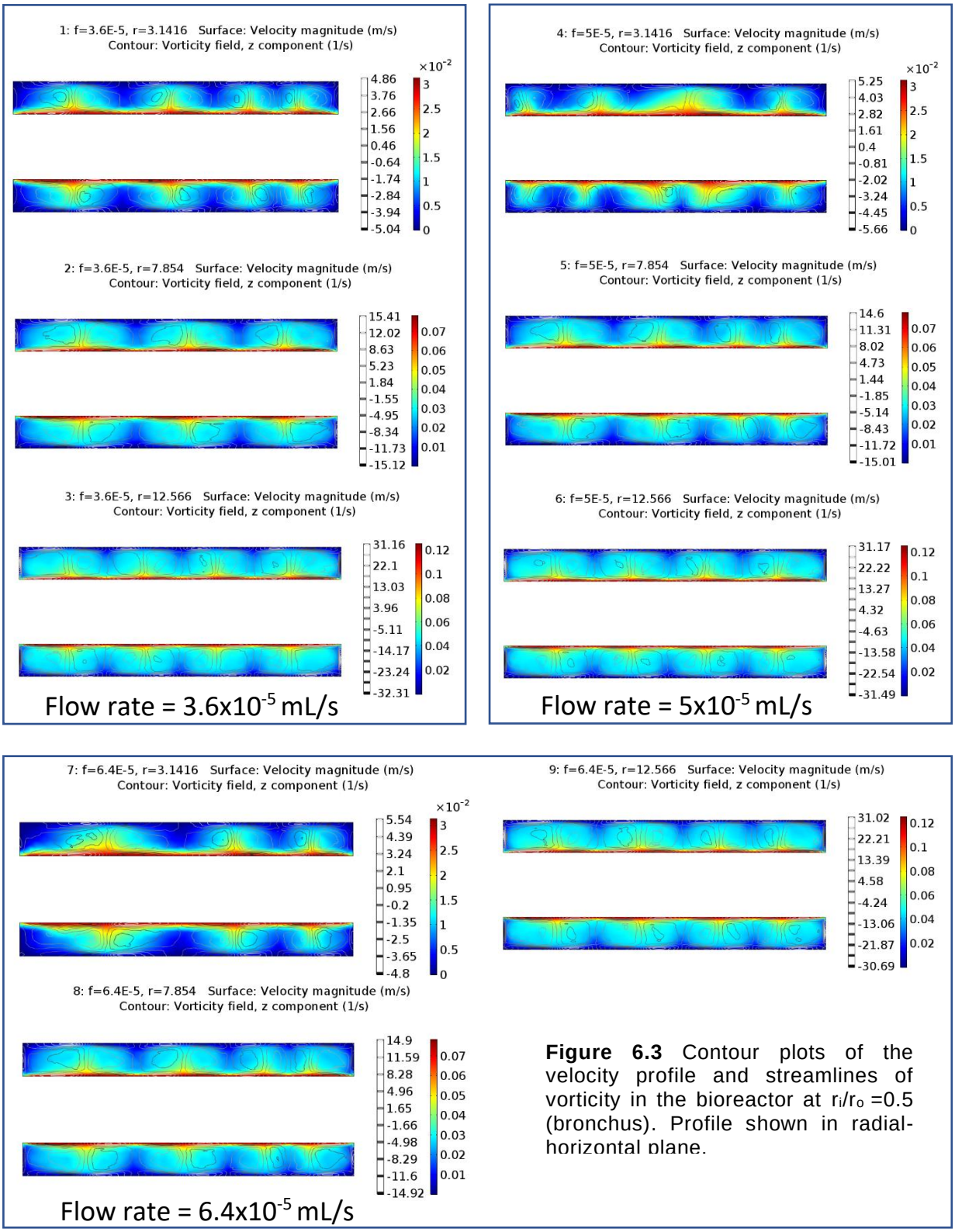


Figure 6.3 Contour plots of the velocity profile and streamlines of vorticity in the bioreactor at r_i/r_o =0.5 (bronchus). Profile shown in radial-horizontal plane.

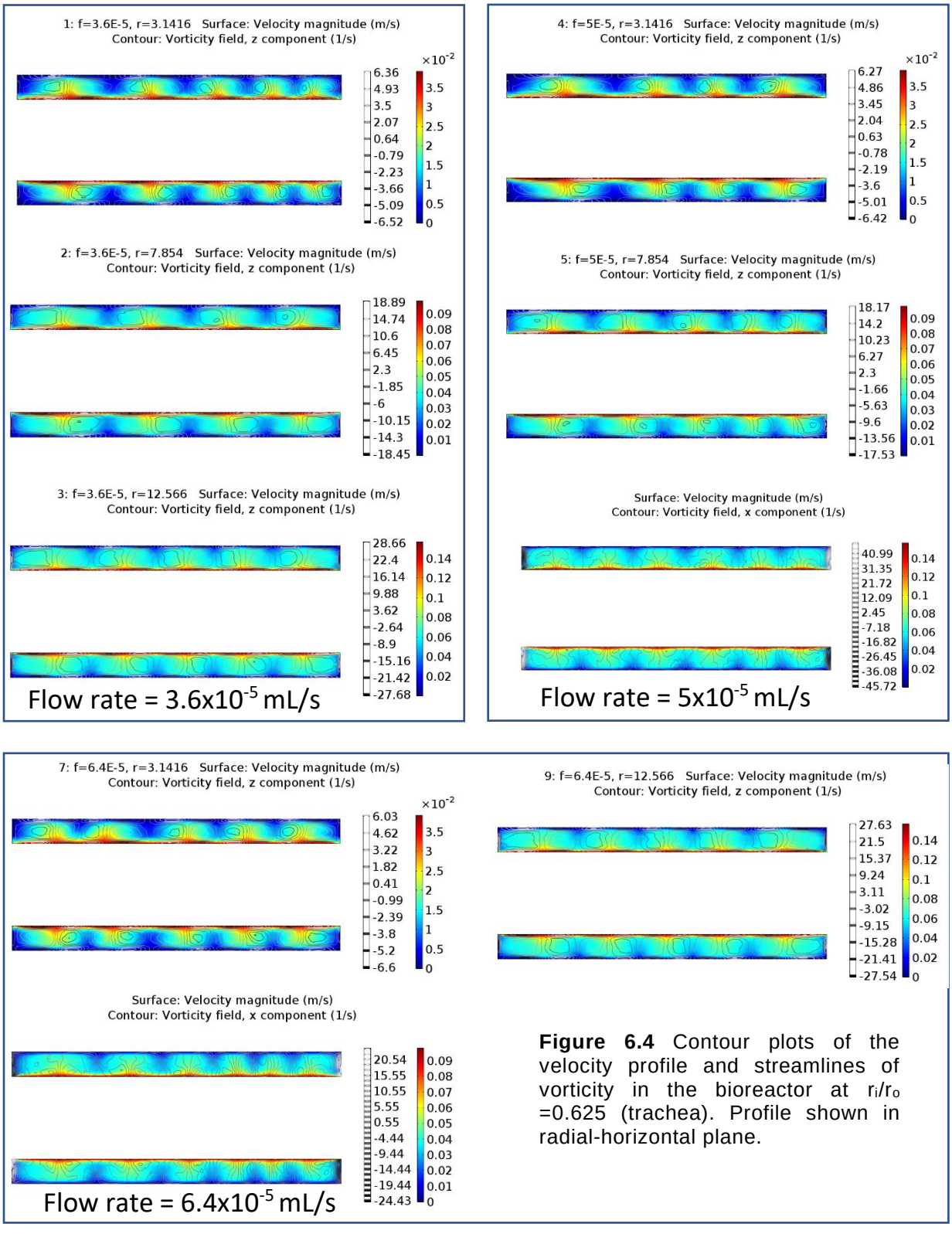


Figure 6.4 Contour plots of the velocity profile and streamlines of vorticity in the bioreactor at r_i/r_o =0.625 (trachea). Profile shown in radial-horizontal plane.

Simulation showed the confirmation of the TCP flow, with the inherent characteristics of formation of circular vortices (Figs. 6.3 & 6.4) and wavy velocity profiles (Marcus, 1984). Maximum velocities from each radii ratios range from ~3 x 10^{-2} to 0.12 m/s in bronchus (r_i/r_o =0.5), and 4 x 10^{-2} to 0.16 m/s in trachea (r_i/r_o =0.625). Overall, the rotation rate dictates the velocity of the fluid, as the flow coming from the incoming fluid is dampened by the inner cylinder walls and is dragged towards the rotational force generated inside the bioreactor. Vorticity, on the other hand, ranged from 4.86-31.17/s in bronchus and 6.36-40.99/s in trachea. These results show that the larger the radius ratio is, the higher the maximum velocity and vorticity that the reactor generates. Another significant difference is the number of taylor cells formed, where 6-8 taylor cells were formed in bronchus and 8-10 in the trachea. The number of taylor cells correlate well with the Peclet number values obtained from the experiment, as higher number of taylor cells generate higher convective mass transfer rates. This, in turn, lowers both the mean residence time and variance; the trachea has indeed lower residence time and variance in contrast to the bronchus, likely due to the flowfield difference between the two inner cylinder diameters.

Looking further at the effect of the process factors on the flowfield dynamics, generally the lowest rotation rate (π rad/s) produces axisymmetric vortices while increasing it further shifts the system into a more symmetric state. Radii ratio, on the other hand, affects the number of periods that the flowfield generates, from 3-4 periods in bronchus (Fig. 6.3) to 4-6 in trachea (Fig. 6.4). The vortices created within the reactor are in anti-parallel configuration, alternating clockwise-counterclockwise fluid rotations that makes mass transfer efficient by inter-vortex exchange. Consequenses of these flow profiles are

tuneability of oxygen, nutrient, and lactic acid distribution and elimination within the bioreactor. The flow regime has also a direct effect on the shear stress experienced at the surface of the inner cylinder, which we will look next.

6.3.2 Surface shear stress evaluation in inner cylinder

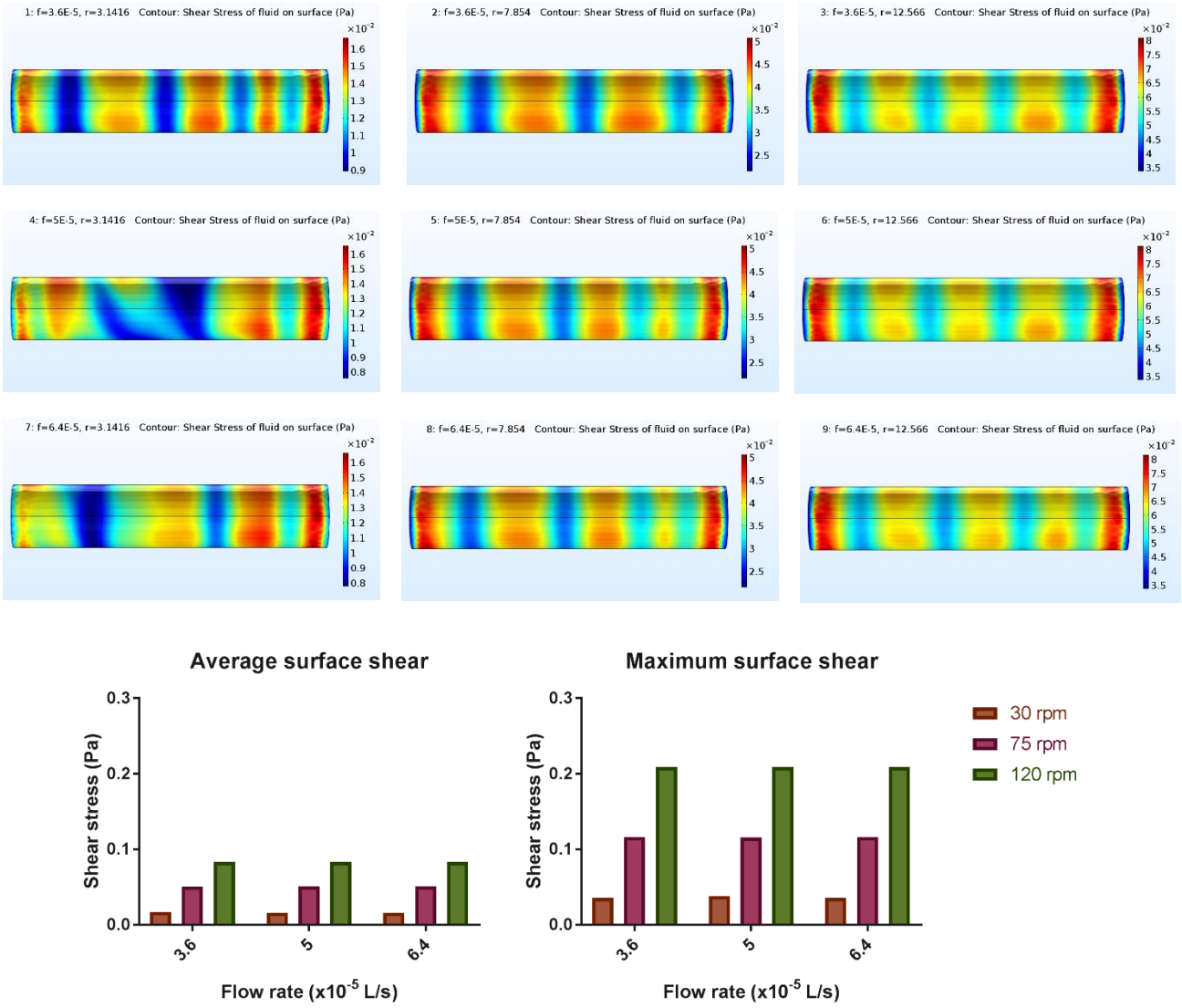


Figure 6.5 3D surface maps of the shear stress at the surface of the inner cylinder with r_i/r_o =0.5 (bronchus). Average and maximum surface shear values are plotted for comparison and evaluation of factor effects.

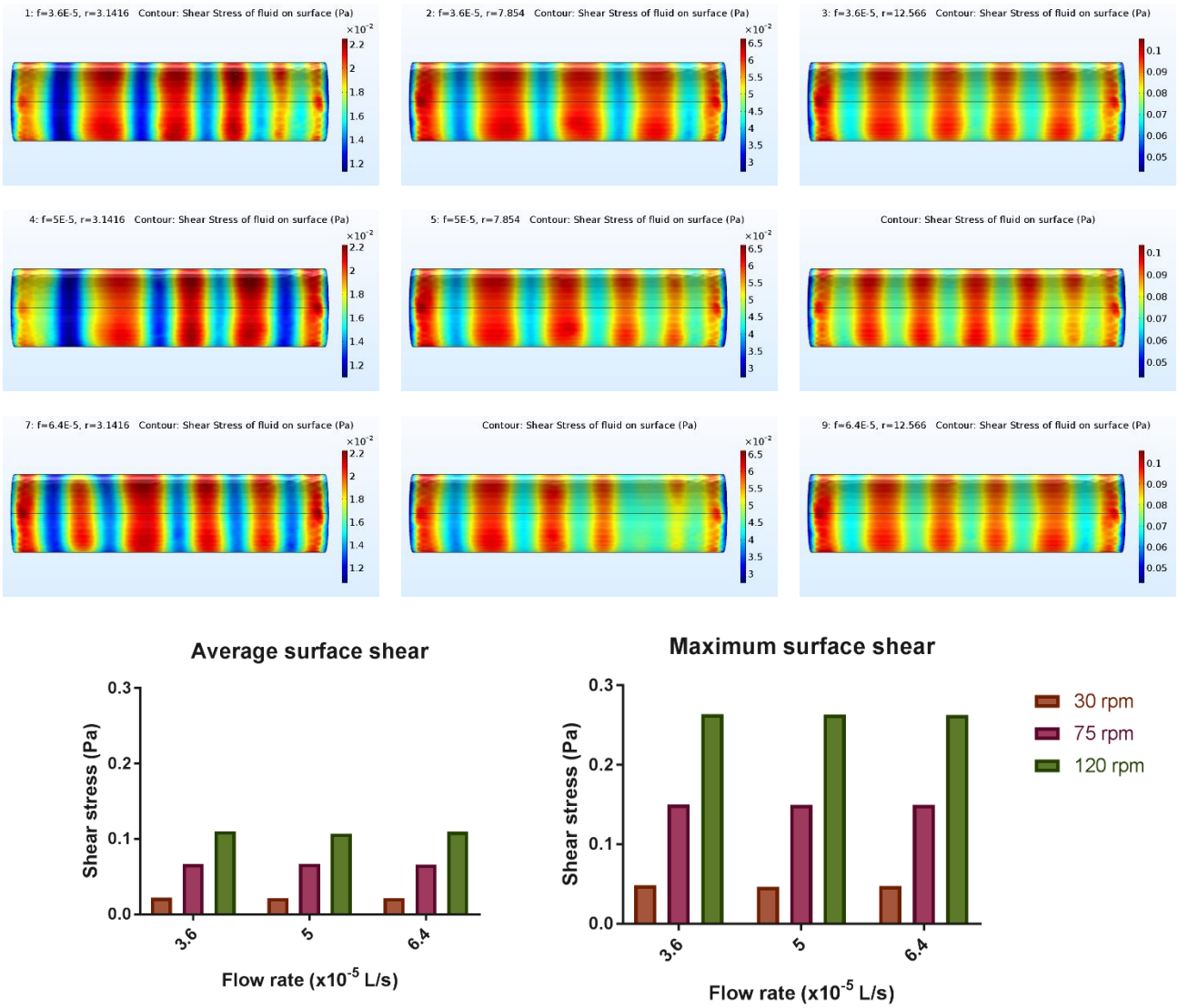


Figure 6.6 3D surface maps of the shear stress at the surface of the inner cylinder with r_i/r_o =0.625 (trachea). Average and maximum surface shear values are plotted for comparison and evaluation of factor effects.

The flow profiles observed in the previous result projected an intermittent pattern of shear stresses across the inner cylinder. Generally, the result shows that the higher the radius ratio, the larger the average and maximum shear stress experienced by the surface of the inner cylinder. The surface shear stress ranges obtained from bronchus (r_i/r_o =0.5) are from: average ~0.02-0.08 Pa, and maximum shear stress of ~0.04-0.21 Pa (Fig. 6.5, bar graphs). For trachea (r_i/r_o =0.625), the value goes up to the average shear stress of 0.02-0.11 Pa and

the maximum shear stress of 0.05-0.26 Pa (Figure 6.6, bar graphs). Considering the general formula of torque (τ)=$Fr\sin\theta$, where F is the force exterted, and r is the position vector (in this case, radius), the consequence of larger diameter results in a larger torque, and therefore higher shear stress experienced at the surface. Rotation rates of π and 2.5π rad/s has a axisymmetric periodicity along the surface, while at 4π rad/s has consistent maximam-minima locations along the length of the inner cylinder. Low rotation rates in bronchus, however, have more pronounced shear axisymmetry (Fig. 6.5, leftmost 3D plots), specially at higher flowrates. This behaviour might be that the transmission of energy from the inner cylinder to fluid is dissipated from the surface to the outer cylinder. The dissipated energy coming from the inner cylinder rotation coupled with the axial fluid movement can cause instabilities on the flow field, producing the shear stress distribution on the low rotation rates. The range, however, in which the values of shear stresses generated in the bioreactor are well below the limit of cell necrosis induction (Chisti, 2001). Simulation predicts well the flow profile of the bioreactor that would be otherwise difficult to observe experimentally. However, the reactors designed usually is deviating from the ideality, where the “real” reactor performance is actually observed using residence time distribution analysis. From these analysis, the average time of molecule inside the reactor, its variance, and the reactor performance in mass transfer is determined.

6.3.3 Residence time distribution analysis

6.3.3.1 First moment: Mean residence time

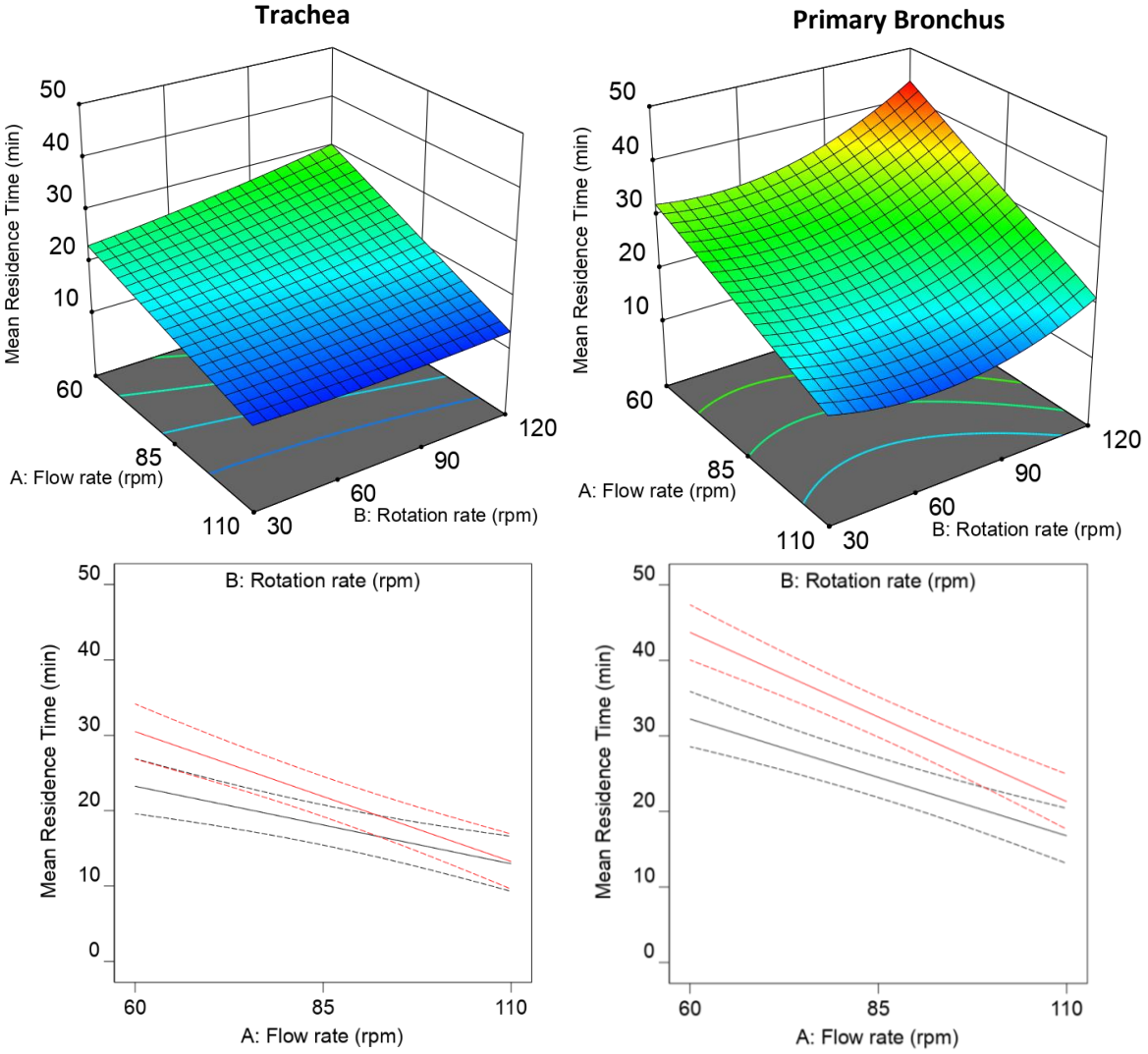


Figure 6.7 Top: 3D contour plot on the mean residence time of both trachea (r_i/r_o =0.625) and bronchus (r_i/r_o =0.5). Bottom: Interaction plots showing the coupled effect of rotation rate and flow rate to the mean residence time. Legend: black – 30 rpm, red - 120 rpm. Dashed line shows 95% confidence interval.

Our empirical model showed a very high model significance ($p<0.0001$), with an R^2 value of 0.9551, Adjusted R^2 of 0.9274, and Predicted R^2 of 0.8676 (Fig. 6.7). This reflects a very high predictability of the mean residence time and the confidence of tuneability is good. The mean residence time (t_m) of the bioreactor is highly affected by flowrate

($p<0.0001$), followed by rotation rate ($p=0.0004$) and airway size ($p=0.0075$). As the flowrate of the incoming fluid is increased in the outer chamber, the mean residence time decreases. However, as the rotation rate of the inner cylinder is increased, residence time is considerably increased as well, interacting with the volume flux coming inside of the bioreactor. Elevated flowrates increase the rate of liquid displacement in the bioreactor, thereby reducing residence time, but the higher the rotation rate would encourage vorticity that retains the tracer molecules in the taylor cells generated in the flow field. The effect of interaction parameter between flowrate and rotation rate is at a p-value of 0.0390.

The mean residence time of the bioreactor whether the trachea or bronchus is mounted differs significantly. Considering the reactor volume on cylinders with different radii ratios, a calculated difference of 18.75% in the outer chamber volume increased considerably the residence time in bronchus in contrast with the trachea. Additionally, the torque generated on the same rotation rate by the trachea is larger than the bronchus due to the difference in radius. The force generated upon rotation is then transmitted to the fluid that enhances the diffusion of molecules and mixing capacity of the bioreactor.

The mean residence time of the TCP bioreactor is modelled as:

$$t_m = 137.95 - 0.68A - 1.2B - 42.65C - 0.001543AB + 0.20693AC$$
$$0.534BC + 0.0107B^2 - 0.0042B^2C \qquad (6.7)$$

Where A = Fluid flowrate (in terms of peristaltic pump rotation rate, 60-110 rpm)

B = Inner cylinder rotation rate (30-120 rpm)

C = Airway size (2 cm for bronchus and 2.5 cm for trachea)

6.3.3.2 Second moment: variance

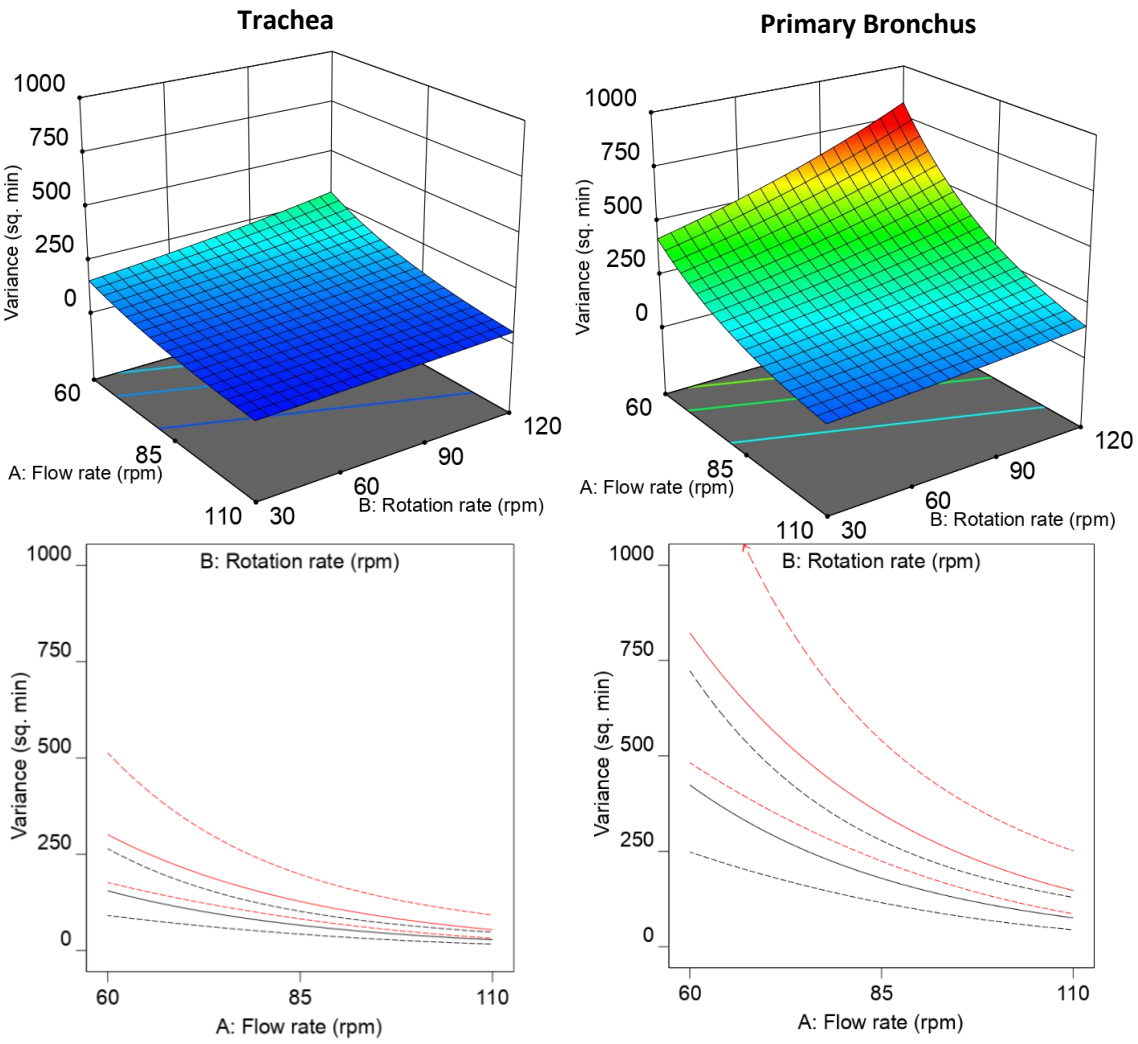


Figure 6.8 Top: 3D contour plot on the second moment of RTD (variance) of both trachea (r_i/r_o =0.625) and bronchus (r_i/r_o =0.5). Bottom: Interaction plots showing the coupled effect of rotation rate and flow rate to the resulting variance. Legend: black – 30 rpm, red - 120 rpm. Dashed line shows 95% confidence interval.

The above plot shows the bioreactor variance for both trachea and bronchus (Fig. 6.8). Variance of the bioreactor is highly attributed to the flowrate ($p<0.0001$). Higher flowrates tend to reduce the variance of the reactor, which actually correlates to the reduced mean residence time. Mixing is thereby improved on increasing the flowrate, but lower flowrates tend to spread more the RTD curve. The variance is further worsened if the inner cylinder

ratio is reduced, having the values reach as high as ~900 min^2 (p = 0.0002). Again, the larger outer chamber volume in relation to the decreased radii ratio will result in higher mean residence time and variance. This would likely result into much less mixing efficiency within the reactor. Rotation rate has the third significant effect on the variance (p=0.0341); higher rotation rates of the inner cylinder would shift the rotational Reynolds number higher. As the velocity distributions along the reactor is widened as the rotation rate is elevated, variance is then increased.

Fit statistics has an R^2 value of = 0.7770, Adjusted R^2 = 0.7399, and Predicted R^2 = 0.6719, which is still considered a good fit for empirical modelling. The variance can be expressed in a logarithmic response and linear factors:

$$\log \sigma^2 = 5.12 - 0.015A + 0.0032B - 0.874C \qquad (6.8)$$

Coupled with the mean residence time model, the empirical modelling is predicted to be well-behaved and confidence on simulated result is high for both RTD equations.

6.3.3.3 Peclet number

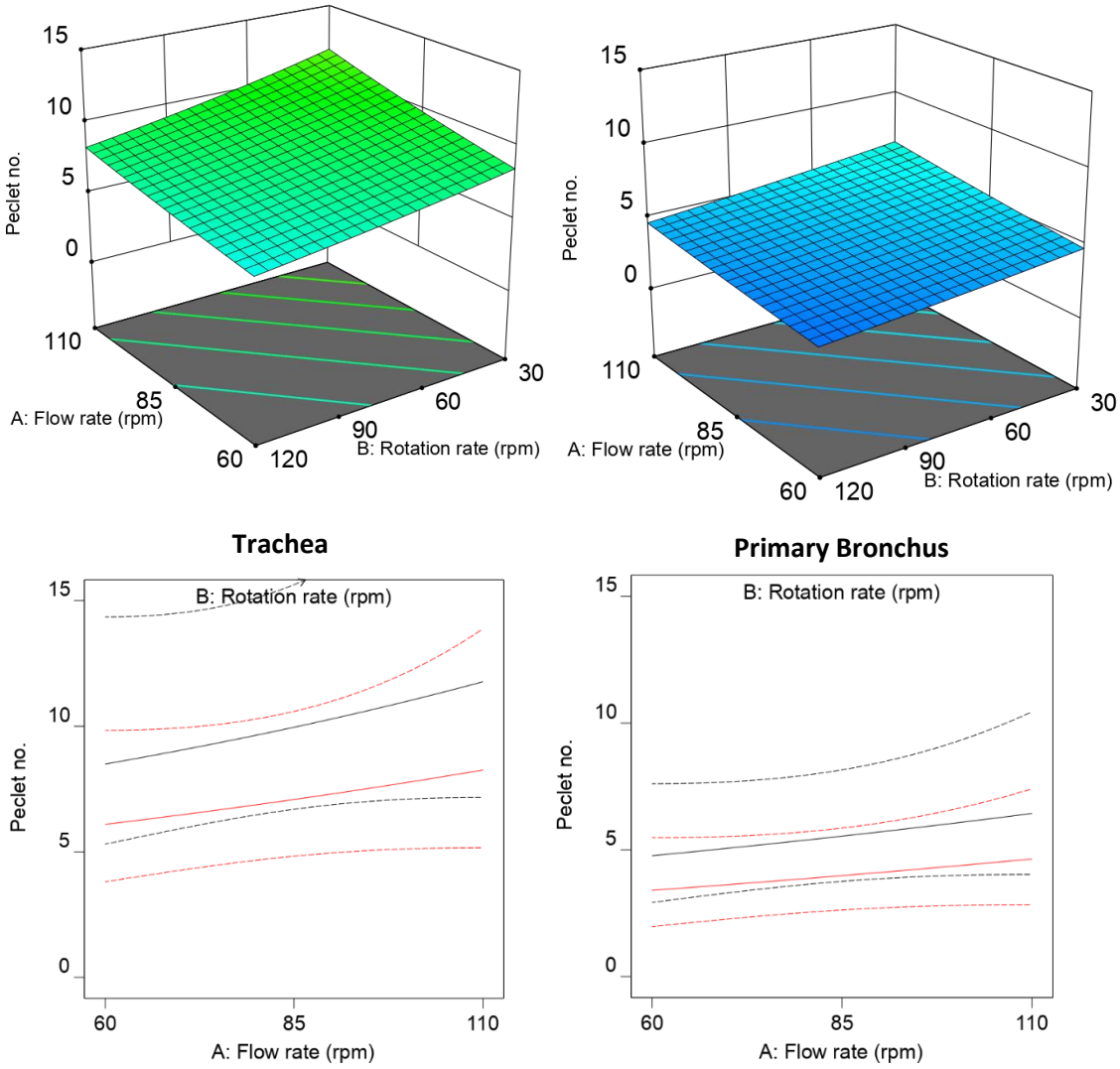


Figure 6.9 Top: 3D contour plot on the second moment of RTD (variance) of both trachea (r_i/r_o =0.625) and bronchus (r_i/r_o =0.5). Bottom: Interaction plots showing the coupled effect of rotation rate and flow rate to the resulting variance. Legend: black – 30 rpm, red - 120 rpm. Dashed line shows 95% confidence interval.

Although the fit for Peclet number is weakly correlating (Fig. 6.9, model R^2 = 0.4106), the results agree with the data obtained on the mean residence time and variance of the bioreactor. Going back to the definition of Peclet number, higher values reflect elevated convection rates for the tracer, and lower values denote that the main mass transport mechanism is by molecular diffusion. In reactor systems, continuous stirred tank reactors

(CSTR) display high Peclet numbers (N_{Pe}<100) because of the stirrer inducing convective mass transport, while plug flow reactors (PFR) have very low Peclet numbers due to mixing that relies only on fluid motion (N_{Pe}>100). The bioreactor designed can be considered an intermediate between the two general types, where the usual Peclet number is 1<N_{Pe}<100.

The inner cylinder size is the major factor that influences Peclet number (p=0.0066). As mentioned before, larger inner radius has more torque, and as it rotates, the force transmitted to the fluid is larger. This in turn increases the velocity and therefore changes the regime to a more convective type of mass transfer. The Peclet number can be modelled by the following equation:

$$\frac{1}{N_{Pe}+6} = 0.198057 - 0.000241A + 0.000146B - 0.045996C \qquad (6.9)$$

Where N_{Pe} is the Peclet number

6.3.3.4 Real reactor flow schemes: bypassing and tailing

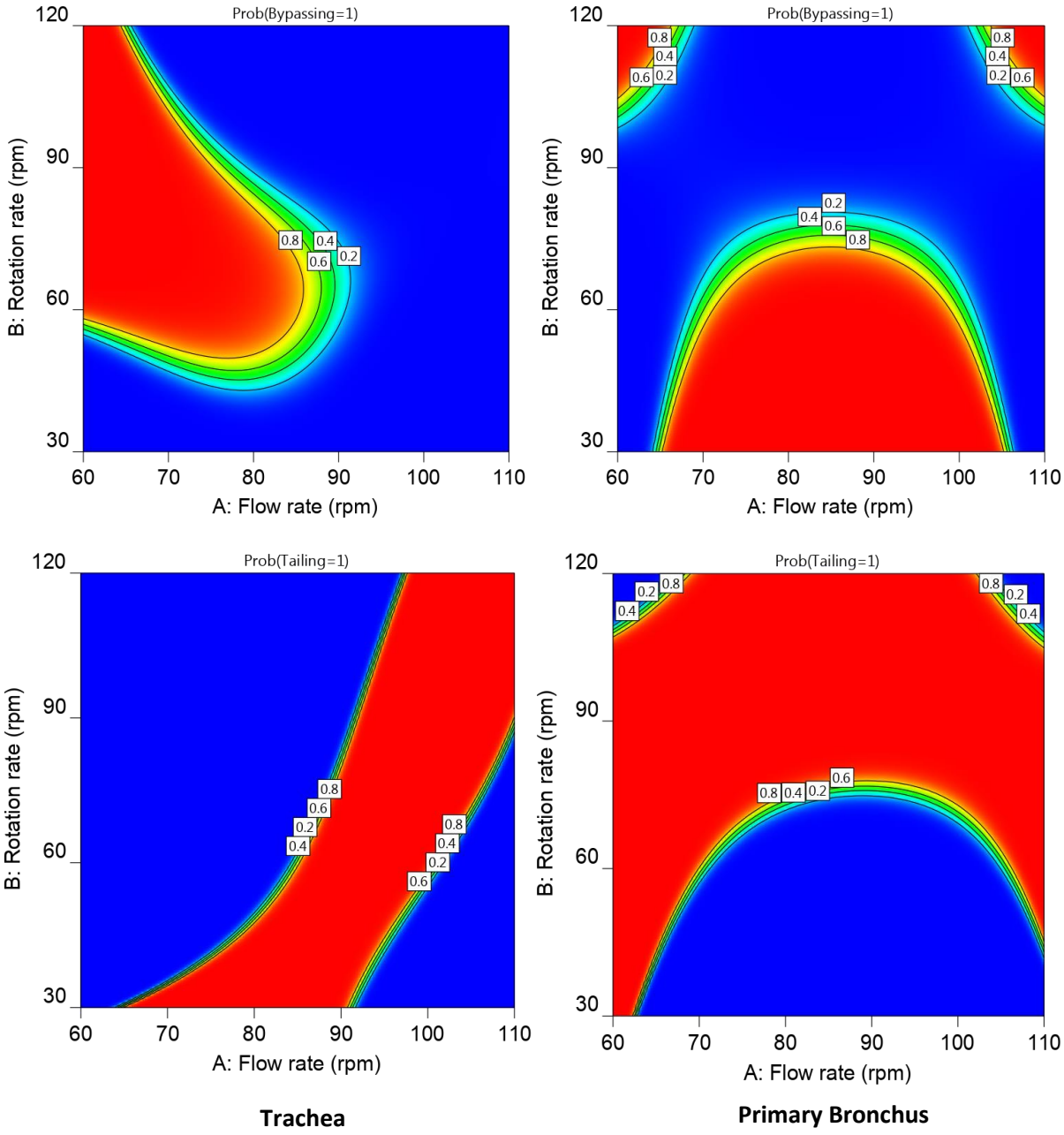


Figure 6.10 Reactor residence time distribution contour plots showing the probability of occurrence of bypassing (Top plots) and tailing (bottom plots) for trachea and bronchus mounted in the reactor. Blue region shows desired characteristics of the bioreactor, whereas the red region are the parameters which causes bypassing and tailing.

The result of the non-ideality in reactor systems produces either bypassing, tailing, or both. These two characteristics are undesirable and makes the efficiency of the reactor be reduced upon operation. On the operational factors in bioreactors, a relatively larger region in trachea is within the acceptable range in contrast to the bronchus (Fig. 6.10). In these graphs, it is obvious that the inner cylinder size affect largely the probability of occurrence of bypassing and tailing.

Bypassing, a phenomenon in reactors that is associated with a fluid stream going direcly from inlet to outlet ports, is likely to occur in smaller inner cylinder diameters. This phenomenon can be attributed with a dampened flow oscillation on the surface of the outer cylinder, as the torque generated by the inner cylinder could be dissipated by viscous effects of the fluid. The incoming fluid then can short-circuit into the outer cylinder surface to the effluent stream without being mixed into the taylor cells generated by the bioreactor. Tailing, on the other hand, is the result of delayed exit of molecules due to dead volume or molecules being “trapped” in the taylor vortices within the reactor. The higher the mixing efficiency, the less likelihood of tailing to occur. Citing the previous data on Peclet number, trachea has higher convection mass transfer regime and thereby increased mixing efficiency, in contrast with the bronchus. Larger areas of operation in bronchus would show tailing than in trachea, which has a higher inner diameter. Perhaps introduction of baffles within the outer cylinder could potenitally eliminate tailing and bypassing for a wide range of radii ratios.

With these results, an optimisation method has been performed to obtain a working process factors with the following criteria: maximise Peclet no., and remove bypassing and tailing in the process. By evaluating each criteria and factors and turning it into degrees of

desirability, we are able to obtain a process conditions of 60 rpm flow rate (3.6×10^{-5} mL/s) and rotation rate of 30 rpm (π rad/s) for the trachea (desirability = 0.745). For the bronchus, a flow rate of 110 rpm (6.4×10^{-5} mL/s) and a rotation rate of 30 rpm is the most optimal (desirability = 0.811).

To confirm experimentally on the maintenance of viability of the tissue, a trachea from porcine origin was mounted on the bioreactor and cultured for 5 days. We discuss further on the consequence of the flowfields unto the overall structure and viability of airways by histological methods.

6.3.4 Temporal changes in trachea culture using TCP bioreactor

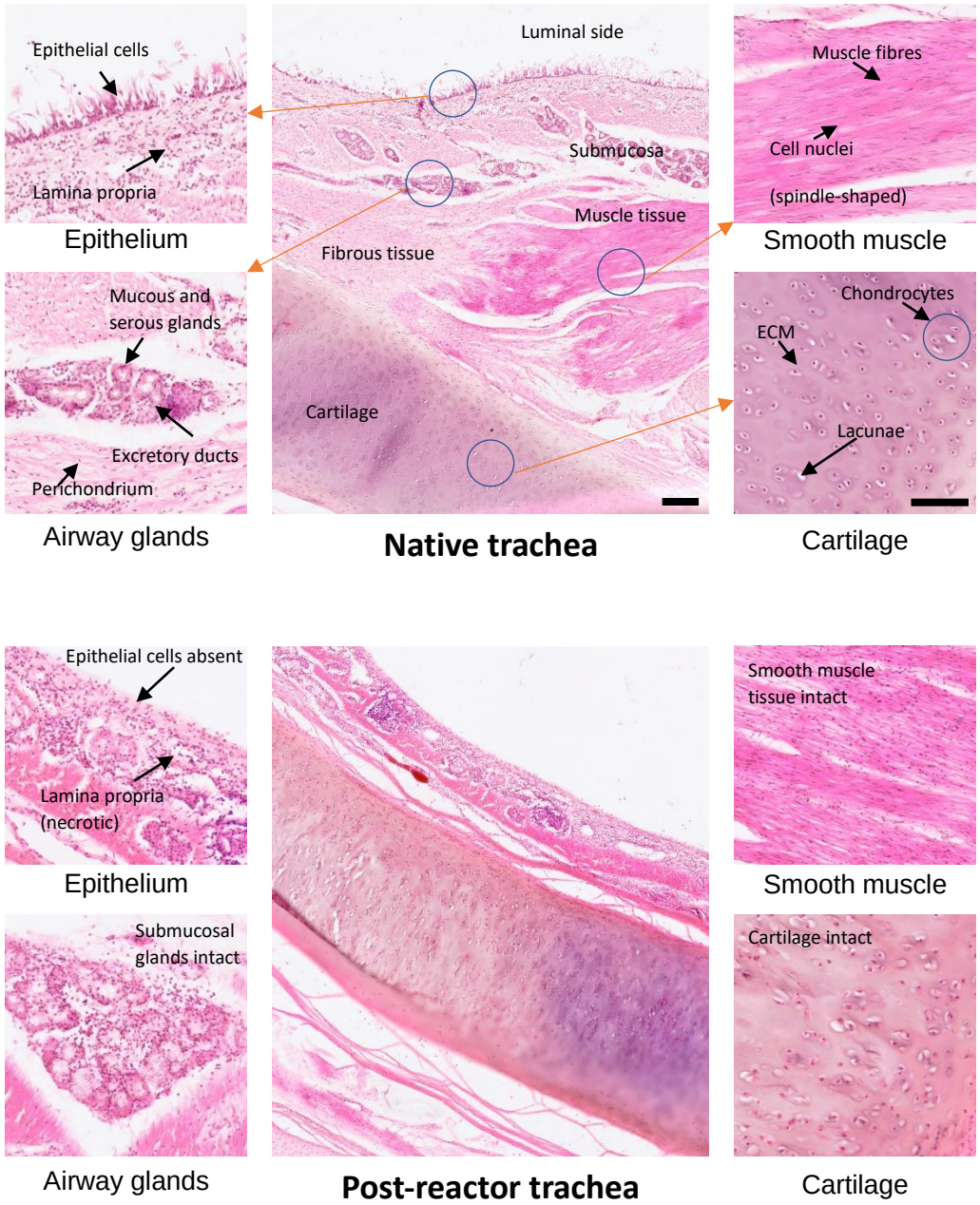


Figure 6.11 Hematoxylin and Eosin (H&E) sections of native trachea (top) and post-reactor trachea (bottom). Magnification: 4x and 20x. Scale bar = 100 µm

Comparative analyses of the pre- and post-bioreactor incubation of the trachea shows significant difference in the epithelial layer, but without major changes in the mesenchyme. The tracheal epithelium consists of a pseudostratified columnar phenotype in the native

trachea (Upper figure, upper right), where mucus and other vesicles are secreted upon the luminal side. After a 5-day incubation in the bioreactor, the epithelium has been denuded or lost and the lamina propria appeared to be necrotic (Fig. 6.11, bottom figure, upper left). Appearance of diffuse nucleus across the substructure can be seen, which is evident of necrosis. Two plausible reasons for this is as follows: that the shear forces delivered by the bioreactor over time caused denudation of the epithelium and necrosis of the substratum, or, an infection that may induce epithelial shedding and tissue necrosis. However, the submucosal glands remained intact as the terminal and collecting duct structures are well preserved(bottom figure, lower left). Smooth muscle fibres retained their orientation (bottom figure, upper right) and viability, and chondrocytes are still seen in the lacunae surrounded by its matrix (bottom figure, lower right). Overall, the airway structure from basal lamina to the chondrocytes retained their viability, but the epithelium was removed and the lamina propria became necrotic.

To observe changes in the extracellular matrix, Masson's trichrome was used for staining collagenous regions within the trachea (Fig. 6.12). Collagen distribution in the post-reactor trachea is comparable to the native trachea, where the degree of staining is qualitatively similar from the lamina propria to the cartilage. Airway smooth muscle fibres are kept intact with diffuse collagenous regions, indicating that the ECM secreted by smooth muscle cells have been well preserved in comparison to the native trachea. The tracheal cartilage deep blue staining corresponding to collagen type II is also similar to the native trachea, without any indication of ossification or tracheomalacia. These results complement the previous H&E staining on the preservation of integrity of the tissues and its extracellular matrix components.

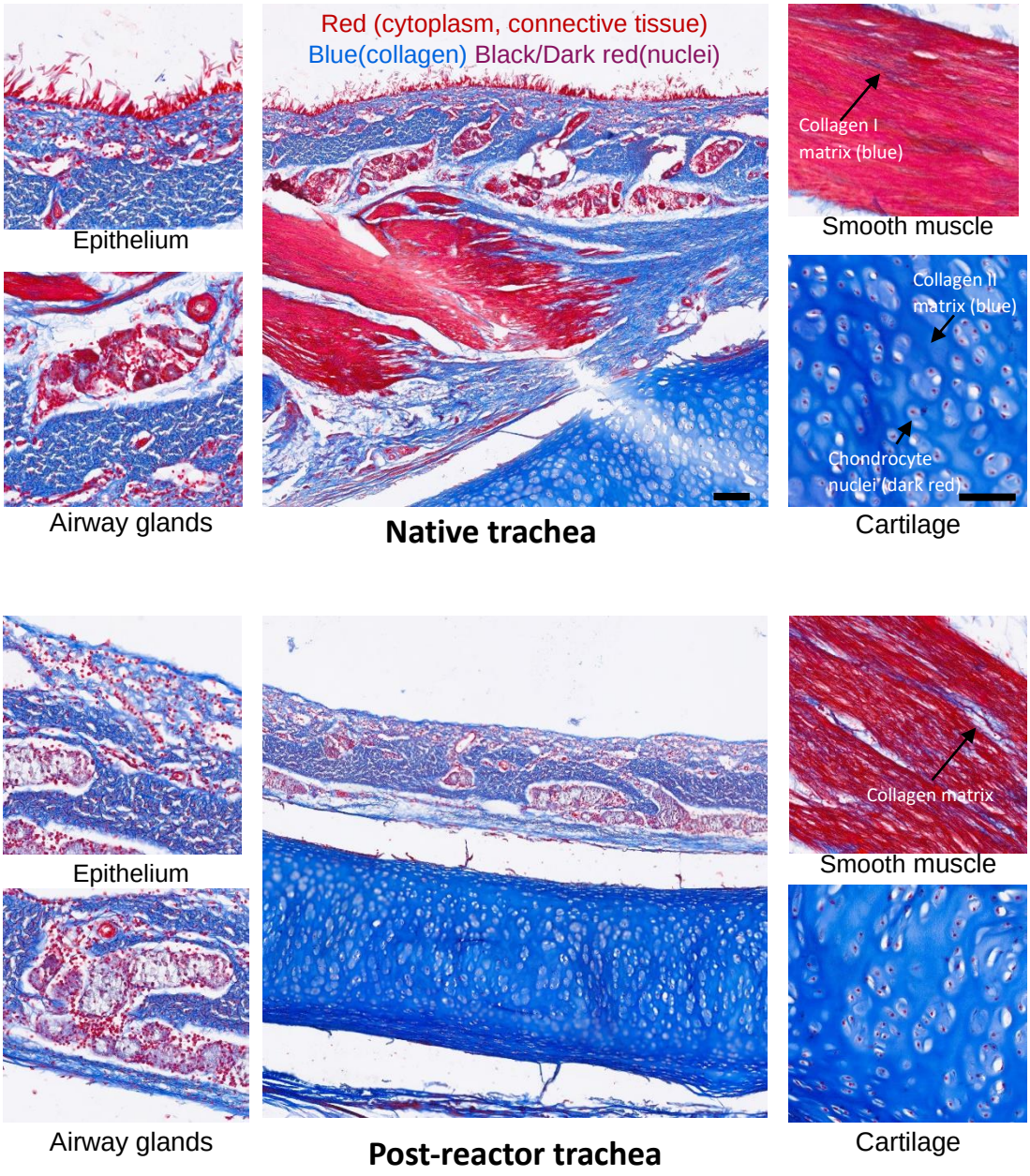


Figure 6.12 Masson's trichrome sections of trachea. Magnification: 4x and 20x. Scale bar = 100 µm. Blue staining shows collagen, red is cytoplasm and connective tissue, while black stains for nuclei

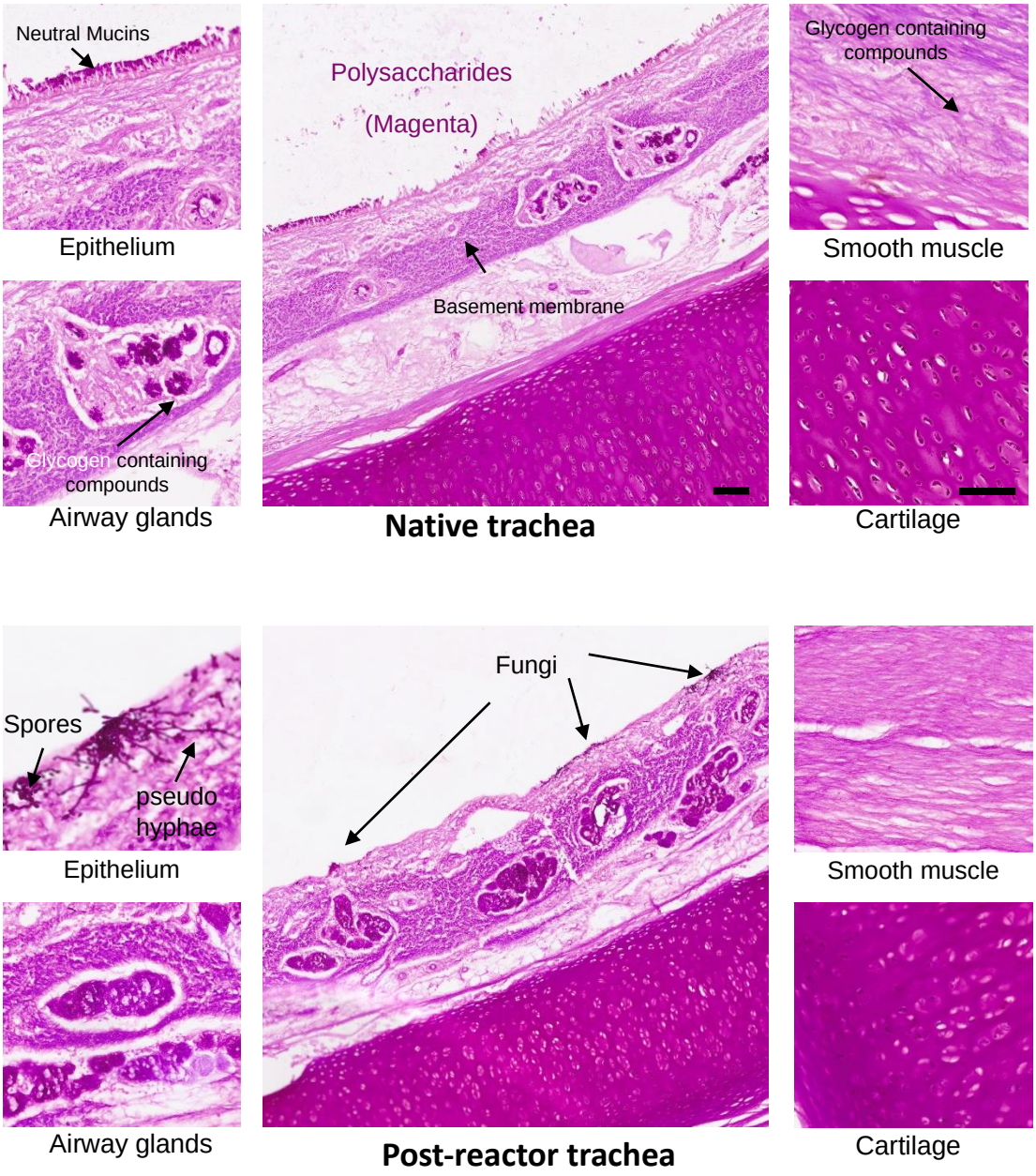


Figure 6.13 Periodic acid-Schiff base staining sections of trachea. Staining showed infiltration of fungi. Magnification: 4x and 20x. Scale bar = 100 µm

To evaluate the mucosa of the trachea, PAS staining was used. Dark magenta regions show neutral compounds containing polysaccharides, where the delineation of the basal lamina is clearly seen (Fig. 6.13). Epithelial cells in the native trachea is positive with mucins on its apical surface(top image, upper left), but the post-reactor trachea is seen instead with

fungal infection (bottom image, upper left). Vivid structures of the hyphae and spores are evident within the tracheal lumen, which can explain the epithelial shedding and the necrosis of the lamina propria. Based on the morphology and the location of the infection, the fungi is likely belonging to the genus *Candida*, where the budding cells and pseudohyphae are stained and is localised within the epithelium. Intensified colouration is also observed in the glands, potentially averting the fungal infection through mucus secretion and airway clearance (bottom image, lower left). Similar degrees of staining on both cartilage and smooth muscle are observed for both native and post-reactor trachea.

6.4 Discussion

The bioreactor was fabricated for culture of the airways in a bi-perfusion system. This is to mimic the conditions in the luminal layer, and stimulate mechanical forces in the airway mesenchyme. Looking at the flow profile generated by the bioreactor, a taylor-couette-poiseuille flow is produced at rotation rates of π to 4π radians/second (30-120 rpm). Increasing the rotation rate shifts the flow into turbulence, depicted by non-characteristic flow profile and absence of symmetric vortices (Ramis, 2020, data unpublished). The flow is characterised by formation of counter-current taylor cells and periodic velocity distributions. This is confirmed experimentally by employing a rheoscopic fluid and injecting a dye for flow visualisation.

The resulting shear profile across the surface of the inner cylinder appeared periodic as well, projecting on the velocity profile observed. The maximum shear stress experienced by the inner cylinder (i.e. the airway) is well below the threshold where necrosis is induced

(Chisti, 2001). As the structure of the airways in the outer layer is similarly intermittent with cartilage and smooth muscle tissue juxtaposed along its length, putting adjustable baffles in parallel with the cartilage will control the high and low shear regions. The synthesis of extracellular matrix by chondrocytes is known to be upregulated by cyclic shear (Jin *et al.,* 2001; Waldman *et al.,* 2003), while it hampers proliferation of smooth muscle cells (Kona *et al.,* 2009). Therefore, a spatial control within the reactor volume will enable maintenance of both tissues while enhancing the rate of mass transport of oxygen and nutrients to the whole thickness of the trachea.

By evaluating the residence time distribution analysis, we found out that the range of mean residence time and the corresponding variance and Peclet number can be tuned by adjusting the rotation rate and flow rate. The model predicted well the mean residence time response and variance, and the tuneability can be from 13.35-43.52 min in $r_o/r_i = 0.5$ (bronchus), and 13.13-30.75 in $r_o/r_i = 0.625$ (trachea). The means that if an agonist is perfused to the outer chamber, the time of delivery can be adjusted precisely depending on the application of interest. However, depending on the airway diameter, the response of the bioreactor changed drastically, having increased the mean residence time and variance, while reducing the Peclet number. This means that the lower the ratio of the outer to inner cylinder, the lesser the convective forces towards mass transfer is. As a result, oxygen and nutrient rates of diffusion will be reduced. Maintaining or increasing the ratio of outer to inner cyliner by an adjustable outer shell would be appropriate for the next iteration of the design. In addition, the undesired flow characteristics of the bioreactor, namely bypassing and tailing as a result of combination of the factors, have been eliminated by adjusting the

desirability function to avoid formation of bypass and tails. With this, the tuneability of the reactor and its performance can be assured for culturing the airways.

To assess the performance of the bioreactor, a porcine trachea was used as a model to evaluate the operating conditions. The first design iteration of the bioreactor proved to be difficult to use, as completely isolating the inner from the outer chamber by sealing the sides was tricky due to the slippery nature of the trachea. This might be resolved by using a wire clamp to firmly attach the ends to the rotating shaft of the inner chamber. Additional problems encountered were mounting the outer shell to the base plate and installing the fluid line inside the incubator. This user difficulty might have introduced contamination within the process, despite all parts have been autoclaved prior on use. A more pragmatic and ergonomic design will be used on the second design iteration for ease of use of the operator.

On evaluating the viability and structural preservation of the mounted trachea, histological stains were used to visualise tissue components. Overall, the mesenchyme was preserved after 5 days of culturing. Collagen and glycosaminoglycans content were qualitatively comparable for both the native and post-reactor trachea. Healthy tissues of muscular, glandular, and cartilaginous was observed and structural morphology was kept intact. On the other hand, the epithelium was completely removed and the lamina propria became necrotic after culture. PAS staining showed a positive fungal infection of genus *Candida*, which causes epithelial shedding and necrosis. Potential causes of infection could be user error, or the source where the trachea has been obtained. The trachea was also exposed briefly in open air upon transport from the abbatoir, which could also contribute to the

infection. With this, better tissue sterilisation methods should be used prior on culturing, as well as revising the current design to minimise movement that can ensue contamination. Overall, the bioreactor with the taylor-couette-poiseuille flow is designed for dynamic flow and shear profile that supports growth of the mesenchyme of the airways. Further investigations are needed to be done in a longer timescale to evaluate the effect of bioreactor operating conditions to the overall viability and structural integrity of the airways.

Chapter 7

General Discussion

The studies carried out in this work contributes to the development of the tissue-engineered airway, where scaffold stiffness, topography, and functional properties are tuned to mimic the niche of the airway cells. The initial groundwork developed is the production of the biomaterial, namely methacrylated gelatin, where the properties have been improved by making a new process for production. The GelMA produced using the precipitation method improved the properties of the material, increasing the range of tensile strength and yield it could have in contrast with the conventional dialysis method. In addition to the material properties, the process can be used as a platform for industrial production of GelMA. The dense powdered physical form of GelMA, and the alcohol-based precipitation method are both viable for upscale.

The material was used afterwards utilised to fabricate scaffolds that either mimic the native and pathological stiffness levels (in the case of ASMCs) or the topography and functionality of the native matrix (for the epithelium). To fully complement the material, a bioreactor system has been designed using a bi-perfusion system to allow the simultaneous luminal and basal culture of epithelium and the mesenchyme respectively.

Developing a tissue-engineered airway can elucidate pathways that cannot be seen readily *in vivo* systems. One aspect that was looked was the effect of matrix stiffening into the airway cells, in which significant changes in intracellular, secretory profile and rates of proliferation are observed. The advantage of the model is the ease of tuning of matrix properties and the availability of information in cellular response through the collection of

supernatant and intracellular contents. Animal *in vivo* models often fails to recapitulate several elements of the disease like asthma. Although airway can be induced in small animal models, the spontaneous development of asthma and even the disease itself can only be seen in humans. This poses another route for exploring the functionality of the tissue-engineered airway, as cells from human patients can be seeded unto the scaffolds and cultured into a reactor to mimic breathing while maintaining viability. Diseased states are also possible with the use of cells coming from diseased airways (i.e. asthma and COPD) and expanding them into the scaffolds for culture. Stimulus, environmental factors and drug responses can then be evaluated without the need for induction of disease phenotype in animals, as well as overcoming the difference of drug interactions between species.

7.1 Key findings

To develop the model for tissue-engineered airways, materials, cells and the microenvironment niche are studied to obtain relevant models for response evaluation. Starting at the materials development, the work developed the process to improve characteristics of GelMA so that a wider range of stiffness can be used for modelling studies. More than 300% increase in Young's modulus was observed in 10% wt/vol GelMA concentration, which is attributed to the preservation of molecular weight of gelatin in the precipitation than in dialysis downstream purification. Cellular viabilities on encapsulated NIH-3t3s are similar to both techniques with a minimum of 85% on both precipitated and dialysed GelMA, affirming removal of by-products and biocompatibility in the precipitated process.

Using the aforementioned GelMA, we produced scaffolds that are similar in the physiological and pathological range of stiffnesses. Morphological analysis showed that the cytoplasmic and nuclear area increased considerably as stiffness increases. The data is coupled with an increase in cellular diameter via flow cytometry, and elevated expression of pGSK-3β (marker of hypertrophy) confirming the increased volume of the cell. These phenomena are also accompanied by an elevated expression of α-SMA (which indicates increased contractility) and enhanced rate of proliferation. In addition, TGF-β1 downstream signalling pSMAD2 is increased as well, which indicates that TGF-b1 signalling is upregulated that also upregulates α-SMA and the rate of proliferation of ASMCs. Such cellular response is associated with the features of asthma: hypercontractility, hyperproliferation, and hypertrophy. A separate study whom we collaborate (Amanda Tatler) with have performed the inhibition of stiffening in a mouse model, and this has reverted the asthmatic airway into a normal-like phenotype. This confirms our hypothesis that the stiffness plays a significant role into the airway dynamics, and with the use of our GelMA hydrogel-based model of the airway stiffening, we can test primary human cells for possible treatment options in a diseased model of the airway.

Next is the development of the epithelium side of the airways. To mimic the nanofibrous topography of the ECM produced by the airway epithelial cells, electrospinning was used to create scaffolds. GelMA was still used as a substrate, and adjusting the stiffness was attained by controlling the crosslinking solution to alter the degree of crosslinking. By varying the amounts of water into the solution, the nanofibrous scaffolds stiffness levels were tuned to a degree of 75 kPa/1% H_2O at a maximum of 12% H_2O and a range of 300-900 kPa. The degree of crosslinking not only affected the modulus, but also the

permeability of the scaffold. Several studies in the airway epithelium involve the effect of the permeability, and so having another factor to control increases the flexibility of experiments that can be performed. Further, to mimic the functionality of the matrix, the surface was modified with L-cysteine. Thiolation of the scaffold resulted in its increased antioxidant capacity, an inherent property of the epithelium likely due to laminin- a thiol-containing ECM protein. In response to the cells being cultured on the scaffolds, increasing stiffness has also enhanced the rate of proliferation. Coupled with the scaffold thiolation, the proliferation effect has been more pronounced. Cysteine has also been known to have an anti-oxidative property, and with the molecule embedded into the matrix, it can protect the cells from free radicals and also increase the affinity of ECM secreted by cells through disulphide bonding. These synergistic mechanisms can be the reason of increased cellular proliferation in the thiolated scaffolds. With the biomimicked scaffold that has tuneable properties developed, the observation of the phenotypic changes occurring in the airways can be readily analysed with the tissue-engineered platform developed.

To fully complement the tissue-engineered airway smooth muscle and epithelial layer, a bioreactor system has been developed to enable simultaneous culture on the apical and basolateral side of the airways. A taylor-couette-poiseuille flow was adapted as the flow characteristics provide high mass transfer rates while minimising the shear stress to the surface. By varying the inner diameter (bronchus or trachea), the rotation rate of the inner cylinder, and the flow rate of the media, a simulation was performed to evaluate the flow profile and shear forces in the reactor. Mainly the inner cylinder rotation rate affected the flow regime and the shear, and the taylor-couette-poiseuille flow has been confirmed both computationally and experimentally. To assess the bioreactor performance in its deviation

from an ideal reactor, the mean residence time, variance, and the Peclet number was evaluated using response surface methodology. Increasing the flow rate and airway size decreased the mean residence time and variance, while increasing the rotation rate has a direct proportionality on the RTD parameters. In addition, Peclet number, which is a measure of convection or molecular diffusion, is mainly affected by the cylinder size. Undesired flow characteristics of bypassing and tailing are also seen in the bioreactor for some factor combination, and its elimination has been performed by utilising optimisation methods on the maximisation of desirability. The operating condition for the trachea is with a flow rate of 3.6×10^{-5} mL/s and π rad/s, and a flow rate of 6.4×10^{-5} mL/s and π rad/s for the primary bronchus. Using the optimised flow, we have mounted a 10 cm length porcine trachea into the bioreactor for a 5-day culture. Histological staining showed preservation of the basal lamina, glandular tissues, smooth muscle, and cartilage, while the epithelium was denuded and the lamina propria became necrotic. Periodic acid-Schiff base staining revealed that this was due to a fungal infection, specifically of the genus *Candida*, where spores and hyphae are seen extensively in the lamina propria. Despite the infection, the preservation of the extracellular matrix components in the mesenchyme were seen in the Masson's trichrome and Periodic acid-Schiff base staining. This indicates that the oxygenation and the shear stress was sufficient to maintain the trachea's viability for 5 days. The porcine trachea was obtained in a local abattoir in open air, and this might be the reason for the contamination. Procuring tissue in a large animal clean lab for testing as well as improving methods of sterilisation should be done in the next phase of work.

7.2 Current limitations

The scaffold work developed in this study is still in need of a method to form tubular structures, with a composite layer of GelMA hydrogel on the basolateral region, and electrospun nanofiber in the luminal layer. The current structure cannot support its own weight, and therefore inert supports are still necessary to be able to mount the construct into the bioreactor.

In addition, the work performed in Chapter 4 is with the caveat that the number of ligands is increased as we elevate the amount of GelMA into the solution to increase the Young's modulus of the material. This setting might have affected the cellular response, but it is also noteworthy to mention that collagen ECM is upregulated in asthma (Poon *et al.*, 2017) as with the crosslinking, and so the reflection of elevated integrin interacting ligands might be true in the tissue-engineered model. For the electrospun nanofibers, the stiffnesses used are only from the property of the resulting processes of crosslinking, as currently there are no published report on the modulus of human respiratory basal lamina and the epithelium. However, a study in chick basement membrane matrix reported values ranging from 0.95-3.30 MPa (Candiello *et al.*, 2007), and the lower limit was the modulus of the electrospun nanofiber crosslinked at 12% H_2O (0.93 MPa), which might be also the range for the human airway basal lamina. Further studies need to be done for the evaluation of the modulus of the human airway epithelium to be able to adjust the engineered scaffold to a physiological stiffness level.

7.3 Future work

The work to be carried out in the next phase of the project will be focused more on the disease modelling characteristics of the tissue-engineered airway. Initially, the response of human primary bronchial epithelial cells into the scaffold with different stiffnesses, permeability, and chemistry should be evaluated. After this, a co-culture system of airway smooth muscle and epithelial cells is recommended to be done by using a composite scaffold of GelMA hydrogel and nanofibers to capture the ECM characteristics in the native airway. An air-liquid interface should be utilised, and phenotypes of both cells should be assessed to understand further the interaction of cells and their response to the stiffening of the airway matrix. Diseased cells coming from asthmatic donors is recommended to be evaluated as well, where the reversal of phenotype is hypothesised for both asthmatic airway smooth muscle and epithelial cells if cultured on normal stiffness levels. From static culture conditions, a tubular construct should be fabricated. This construct is then mounted to a biodegradable 3D printed polycaprolactone for mechanical support, and then installed in the bi-perfusion bioreactor developed for dynamic culture conditions. The bioreactor is recommended to have a breathing apparatus module attached to the luminal side, where a programmable breathing mode can be employed for the reactor. The module would have consist of a negative pressure pneumatic pump controlled by an Arduino board, and this reflects breathing conditions in normal and pathological breathing mechanisms in human. The air line of the breathing system is also attached to temperature, humidity, and environmental chamber where particulates and pollutants (i.e. smoke) can be introduced to the luminal side of the engineered airway. With this model, shear stress and environmental conditions reflected in real conditions can be controlled in real time

situation. Both normal and asthmatic conditions will be simulated, and supernatant from the inner and outer chamber of the trachea can be collected to evaluate inflammatory response of the airways. A complex model can be further analysed by having a tri-culture platform with the immune cells cultured in the outer chamber of the bioreactor, since the reactor can also support suspension culture of cells. Additive complexity of experimental design can be performed in the modular design of the bioreactor to recapitulate real dynamics in the human airways, and potential treatment options can be tested using the delivery system included in the setup of the bioreactor.

7.4 Final conclusions

The main focus of the work is to develop a platform to engineer the human airways. GelMA process was modified to increase the range of mechanical stiffness, and this material was used as a scaffold for culturing airway cells. GelMA hydrogels were fabricated in different stiffnesses pertaining to the physiological and pathological conditions of the airway smooth muscle. Cultured primary airway smooth muscle cells in stiff GelMA hydrogels showed morphological and phenotypic behaviours similar to asthma. For the epithelial cells, an electrospun nanofiber scaffold functionalised with L-cysteine was produced to mimic the basal lamina of the epithelium ECM. Increased proliferation rates were observed in stiffer substrates, and the effect was amplified when cultured in conjugated scaffolds. To mimic the environment of the airways, a bi-perfusion bioreactor has been designed to support culture of the airways. A taylor-couette-poiseuille flow was utilised in the bioreactor, and the response was analysed using computational modelling and experimental

characterisation. A proof of concept study was made by culturing porcine trachea into the bioreactor, and after 5 days it showed that the mesenchyme was intact, indicating that the bioreactor can support the airway culture. Finally, the platform developed for culture of airway smooth muscle and epithelium will be used to further observe cellular and mechanotransduction mechanisms occurring in the airways. This will open new pathways for evaluating disease progressions in the airways and its treatment, helping the future researchers to aid the alleviation of airway diseases.

References

Aguirre, A., Planell, J. A., & Engel, E. (2010). Dynamics of bone marrow-derived endothelial progenitor cell/mesenchymal stem cell interaction in co-culture and its implications in angiogenesis. *Biochemical and Biophysical Research Communications, 400* (2), 284-291. doi:http://doi.org/10.1016/j.bbrc.2010.08.073

Aizawa, T., Kon, T., Einhorn, T., & Gerstenfeld, L. (2001). Induction of apoptosis in chondrocytes by tumor necrosis factor ‐ alpha. *Journal of Orthopaedic Research, 19* (5), 785-796.

Ajalloueian, F., Lim, M. L., Lemon, G., Haag, J. C., Gustafsson, Y., Sjoqvist, S., Macchiarini, P. (2014). Biomechanical and biocompatibility characteristics of electrospun polymeric tracheal scaffolds. *Biomaterials, 35* (20), 5307-5315. doi:10.1016/j.biomaterials.2014.03.015

Alagappan, V. K. T., Willems-Widyastuti, A., Seynhaeve, A. L. B., Garrelds, I. M., ten Hagen, T. L. M., Saxena, P. R., & Sharma, H. S. (2007). Vasoactive peptides upregulate mRNA expression and secretion of vascular endothelial growth factor in human airway smooth muscle cells. *Cell Biochemistry and Biophysics, 47* (1), 109-118. doi:10.1385/cbb:47:1:109

Aldana, A. A., Malatto, L., Rehman, M. A. U., Boccaccini, A. R., & Abraham, G. A. (2019). Fabrication of Gelatin Methacrylate (GelMA) Scaffolds with Nano- and Micro-Topographical and Morphological Features. *Nanomaterials (Basel, Switzerland), 9* (1), 120. doi:10.3390/nano9010120

Amrani, Y., & Panettieri, R. A. (2003). Airway smooth muscle: contraction and beyond. *The International Journal of Biochemistry & Cell Biology, 35* (3), 272-276. doi:http://doi.org/10.1016/S1357-2725 (02)00259-5

An, Z., Qiao, F., Lu, Q., Ma, Y., Liu, Y., Lu, F., & Xu, Z. (2017). Interleukin-6 downregulated vascular smooth muscle cell contractile proteins via ATG4B-mediated autophagy in thoracic aortic dissection. *Heart Vessels, 32* (12), 1523-1535. doi:10.1007/s00380-017-1054-8

Andrews, M. J., & Pearson, F. G. (1971). Incidence and pathogenesis of tracheal injury following cuffed tube tracheostomy with assisted ventilation: analysis of a two-year prospective study. *Annals of Surgery, 173* (2), 249-263.

Aragona, M., Panciera, T., Manfrin, A., Giulitti, S., Michielin, F., Elvassore, N., Piccolo, S. (2013). A Mechanical Checkpoint Controls Multicellular Growth through YAP/TAZ Regulation by Actin-Processing Factors. *Cell, 154* (5), 1047-1059. doi:https://doi.org/10.1016/j.cell.2013.07.042

Archer, C. W., & Francis-West, P. (2003). The chondrocyte. *The International Journal of Biochemistry & Cell Biology, 35* (4), 401-404. doi:https://doi.org/10.1016/S1357-2725 (02)00301-1

Arikawa, T., Omura, K., & Morita, I. (2004). Regulation of bone morphogenetic protein-2 expression by endogenous prostaglandin E2 in human mesenchymal stem cells. *Journal of Cellular Physiology, 200* (3), 400-406. doi:10.1002/jcp.20031

Asokananthan, N., Graham, P. T., Fink, J., Knight, D. A., Bakker, A. J., McWilliam, A. S., Stewart, G. A. (2002). Activation of Protease-Activated Receptor (PAR)-1, PAR-2, and PAR-4 Stimulates IL-6, IL-8, and Prostaglandin E_2 Release from Human Respiratory Epithelial Cells. *The Journal of Immunology, 168* (7), 3577-3585. doi:10.4049/jimmunol.168.7.3577

Aun, M. V., Bonamichi-Santos, R., Arantes-Costa, F. M., Kalil, J., & Giavina-Bianchi, P. (2017). Animal models of asthma: utility and limitations. *Journal of asthma and allergy, 10*, 293-301. doi:10.2147/JAA.S121092

Bae, S.-W., Lee, K.-W., Park, J.-H., Lee, J., Jung, C.-R., Yu, J., . . . Kim, D.-H. (2018). 3D bioprinted artificial trachea with epithelial cells and chondrogenic-differentiated bone marrow-derived mesenchymal stem cells. *International journal of molecular sciences, 19* (6), 1624.

Baiguera, S., Birchall, M. A., & Macchiarini, P. (2010). Tissue-engineered tracheal transplantation. *Transplantation, 89* (5), 485-491.

Baraniak, P. R., & McDevitt, T. C. (2010). Stem cell paracrine actions and tissue regeneration. *Regenerative medicine, 5* (1), 121-143. doi:10.2217/rme.09.74

Barnes, A., Corkhill, P. H., & Tighe, B. J. (1988). Synthetic hydrogels: 3. Hydroxyalkyl acrylate and methacrylate copolymers: surface and mechanical properties. *Polymer, 29* (12), 2191-2202. doi:https://doi.org/10.1016/0032-3861 (88)90111-5

Barnes, P. J., Cuss, F. M., & Palmer, J. B. (1985). The effect of airway epithelium on smooth muscle contractility in bovine trachea. *British Journal of Pharmacology, 86* (3), 685-691. doi:10.1111/j.1476-5381.1985.tb08946.x

Barnett, K., Jacoby, D. B., Nadel, J. A., & Lazarus, S. C. (1988). The effects of epithelial cell supernatant on contractions of isolated canine tracheal smooth muscle. *Am Rev Respir Dis, 138* (4), 780-783.

Barnett, K., Jacoby, D. B., Nadel, J. A., & Lazarus, S. C. (1988). The Effects of Epithelial Cell Supernatant on Contractions of Isolated Canine Tracheal Smooth Muscle. *American Review of Respiratory Disease, 138* (4), 780-783. doi:10.1164/ajrccm/138.4.780

Barrow, R. E., Wang, C. Z., Evans, M. J., & Herndon, D. N. (1993). Growth factors accelerate epithelial repair in sheep trachea. *Lung, 171* (6), 335-344.

Beigel, A., & Müller-Ruchholtz, W. (1984). Tracheal transplantation. *Archives of oto-rhino-laryngology, 240* (3), 217-225. doi:10.1007/BF00453374

Bellusci, S., Grindley, J., Emoto, H., Itoh, N., & Hogan, B. L. (1997). Fibroblast growth factor 10 (FGF10) and branching morphogenesis in the embryonic mouse lung. *Development, 124* (23), 4867-4878.

Benayoun, L., Druilhe, A., Dombret, M.-C., Aubier, M., & Pretolani, M. (2003). Airway Structural Alterations Selectively Associated with Severe Asthma. *American Journal of Respiratory and Critical Care Medicine, 167* (10), 1360-1368. doi:10.1164/rccm.200209-1030OC

Berair, R., Hollins, F., & Brightling, C. (2013). Airway smooth muscle hypercontractility in asthma. *J Allergy (Cairo), 2013*, 185971. doi:10.1155/2013/185971

Bloom, O. (1925). Machine for testing jelly strength of glues, gelatins, and the like: Google Patents.

Bonakdar, S., Emami, S., Shokrgozar, M., Farhadi, A., Hooshiar, A., & Amanzadeh, A. (2010). Preparation and characterization of polyvinyl alcohol hydrogels crosslinked by biodegradable polyurethane for tissue engineering of cartilage. *Materials Science and Engineering: C, 30*, 636-643. doi:10.1016/j.msec.2010.02.017

Bonvin, E., Le Rouzic, P., Bernaudin, J. F., Cottart, C. H., Vandebrouck, C., Crie, A., Bonora, M. (2008). Congenital tracheal malformation in cystic fibrosis transmembrane conductance regulator-deficient mice. *J Physiol, 586* (13), 3231-3243. doi:10.1113/jphysiol.2008.150763

Boussat, S., Eddahibi, S., Coste, A., Fataccioli, V., Gouge, M., Housset, B., Maitre, B. (2000). Expression and regulation of vascular endothelial growth factor in human pulmonary

epithelial cells. *American Journal of Physiology-Lung Cellular and Molecular Physiology, 279* (2), L371-L378.

Brackel, H. J., Pedersen, O. F., Mulder, P. G., Overbeek, S. E., Kerrebijn, K. F., & Bogaard, J. M. (2000). Central airways behave more stiffly during forced expiration in patients with asthma. *Am J Respir Crit Care Med, 162* (3 Pt 1), 896-904. doi:10.1164/ajrccm.162.3.9905034

Breatnach, E., Abbott, G. C., & Fraser, R. G. (1984). Dimensions of the normal human trachea. *American Journal of Roentgenology, 142* (5), 903-906. doi:10.2214/ajr.142.5.903

Bridge, J. C., Aylott, J. W., Brightling, C. E., Ghaemmaghami, A. M., Knox, A. J., Lewis, M. P., . . . Morris, G. E. (2015). Adapting the electrospinning process to provide three unique environments for a tri-layered in vitro model of the airway wall. *JoVE (Journal of Visualized Experiments)* (101), e52986.

Bristol, U. o. (2008). Adult Stem Cell Breakthrough: First Tissue-engineered Trachea Successfully Transplanted. Retrieved from http://www.sciencedaily.com/releases/2008/11/081119092939.htm

Bryce Mieczkowski, B. S. (2018). *Anatomy, Head and Neck, Trachea* Retrieved from https://www.ncbi.nlm.nih.gov/books/NBK448070/

Burdon, T. J., Paul, A., Noiseux, N., Prakash, S., & Shum-Tim, D. (2011). Bone Marrow Stem Cell Derived Paracrine Factors for Regenerative Medicine: Current Perspectives and Therapeutic Potential. *Bone Marrow Research, 2011*, 207326. doi:10.1155/2011/207326

Cairns, D. M., Lee, P. G., Uchimura, T., Seufert, C. R., Kwon, H., & Zeng, L. (2010). The role of muscle cells in regulating cartilage matrix production. *Journal of Orthopaedic Research, 28* (4), 529-536. doi:10.1002/jor.21014

Câmara, J., & Jarai, G. (2010). Epithelial-mesenchymal transition in primary human bronchial epithelial cells is Smad-dependent and enhanced by fibronectin and TNF-α. *Fibrogenesis & Tissue Repair, 3* (1), 2. doi:10.1186/1755-1536-3-2

Candiello, J., Balasubramani, M., Schreiber, E. M., Cole, G. J., Mayer, U., Halfter, W., & Lin, H. (2007). Biomechanical properties of native basement membranes. *Febs j, 274* (11), 2897-2908. doi:10.1111/j.1742-4658.2007.05823.x

Caraci, F., Gili, E., Calafiore, M., Failla, M., La Rosa, C., Crimi, N., Vancheri, C. (2008). TGF-beta1 targets the GSK-3beta/beta-catenin pathway via ERK activation in the transition of human lung fibroblasts into myofibroblasts. *Pharmacol Res, 57* (4), 274-282. doi:10.1016/j.phrs.2008.02.001

Caron, M. M. J., Emans, P. J., Coolsen, M. M. E., Voss, L., Surtel, D. A. M., Cremers, A., . . . Welting, T. J. M. (2012). Redifferentiation of dedifferentiated human articular chondrocytes: comparison of 2D and 3D cultures. *Osteoarthritis and Cartilage, 20* (10), 1170-1178. doi:https://doi.org/10.1016/j.joca.2012.06.016

Carroll, N., Elliot, J., Morton, A., & James, A. (1993). The Structure of Large and Small Airways in Nonfatal and Fatal Asthma. *American Review of Respiratory Disease, 147* (2), 405-410. doi:10.1164/ajrccm/147.2.405

Chae, H. Z., Uhm, T. B., & Rhee, S. G. (1994). Dimerization of thiol-specific antioxidant and the essential role of cysteine 47. *Proceedings of the National Academy of Sciences, 91* (15), 7022-7026.

Chao, M. W. T., Smith, J. G., Laidlaw, C., Joon, D. L., & Ball, D. (1989) Results of treating primary tumors of the trachea with radiotherapy. *International Journal of Radiation Oncology • Biology • Physics, 41* (4), 779-785. doi:10.1016/S0360-3016 (98)00120-5

Chen, L., Tredget, E. E., Wu, P. Y., & Wu, Y. (2008). Paracrine factors of mesenchymal stem cells recruit macrophages and endothelial lineage cells and enhance wound healing. *PLoS ONE, 3* (4), e1886.

Chetty, A., Andersson, S., Lassus, P., & Nielsen, H. C. (2004). Insulin-like growth factor-1 (IGF-1) and IGF-1 receptor (IGF-1R) expression in human lung in RDS and BPD. *Pediatric Pulmonology, 37* (2), 128-136. doi:10.1002/ppul.10415

Chevillard, M., Hinnrasky, J., Pierrot, D., Zahm, J. M., Klossek, J. M., & Puchelle, E. (1993). Differentiation of human surface upper airway epithelial cells in primary culture on a floating collagen gel. *Epithelial Cell Biol, 2* (1), 17-25.

Chien, S.-Y., Huang, C.-Y., Tsai, C.-H., Wang, S.-W., Lin, Y.-M., & Tang, C.-H. (2016). Interleukin-1β induces fibroblast growth factor 2 expression and subsequently promotes endothelial progenitor cell angiogenesis in chondrocytes. *Clinical Science (London, England : 1979), 130* (9), 667-681. doi:10.1042/CS20150622

Chisti, Y. (2001). Hydrodynamic damage to animal cells. *Critical reviews in biotechnology, 21* (2), 67-110.

Cho, E.-J., Kim, C. J., Lee, M. N., & Chung, M. Y. (2013). Tracheal granuloma after thyroidectomy with difficult intubation. *Korean journal of anesthesiology, 65* (6 Suppl), S38-S40. doi:10.4097/kjae.2013.65.6S.S38

Cho, J. W., Jeong, M. A., Choi, J. H., Cho, J. W., Lee, H. J., Kim, D. W., Seo, J. K. (2010). Anesthetic consideration for patients with severe tracheal obstruction caused by thyroid cancer -A report of 2 cases. *Korean journal of anesthesiology, 58* (4), 396-400. doi:10.4097/kjae.2010.58.4.396

Chosa, E., Hamada, H., Kitamura, K., Kuwasako, K., Yanagita, T., Eto, T., & Tajima, N. (2003). Expression of adrenomedullin and its receptor by chondrocyte phenotype cells. *Biochemical and Biophysical Research Communications, 303* (1), 379-386. doi:https://doi.org/10.1016/S0006-291X (03)00347-4

Chung, K. F. (2005). The Role of Airway Smooth Muscle in the Pathogenesis of Airway Wall Remodeling in Chronic Obstructive Pulmonary Disease. *Proceedings of the American Thoracic Society, 2* (4), 347-354. doi:10.1513/pats.200504-028SR

Clark, C. A., Li, T.-F., Kim, K.-O., Drissi, H., Zuscik, M. J., Zhang, X., & O'Keefe, R. J. (2009). Prostaglandin E2 inhibits BMP signaling and delays chondrocyte maturation. *Journal of Orthopaedic Research, 27* (6), 785-792. doi:10.1002/jor.20805

Coffey, E., Newman, D. R., & Sannes, P. L. (2013). Expression of Fibroblast Growth Factor 9 in Normal Human Lung and Idiopathic Pulmonary Fibrosis. *Journal of Histochemistry and Cytochemistry, 61* (9), 671-679. doi:10.1369/0022155413497366

Corbascio, M., Fux, T., Grinnemo, K.-H., & Simonsson, O. (2014). Analysis of Clinical Outcome of Synthetic Tracheal Transplantation Compared to Results Published in 6 Articles by Macchiarini et al. Retrieved from http://www.svt.se/svts/article2971361.svt/binary/Analys%20av%20transplantationer.pdf

Crisostomo, P. R., Wang, Y., Markel, T. A., Wang, M., Lahm, T., & Meldrum, D. R. (2008). Human mesenchymal stem cells stimulated by TNF-α, LPS, or hypoxia produce growth factors by an NFκB-but not JNK-dependent mechanism. *American Journal of Physiology-Cell Physiology, 294* (3), C675-C682.

Cyranoski, D. (2016). Artificial-windpipe pioneer under scrutiny again. Retrieved from https://www.nature.com/news/artificial-windpipe-pioneer-under-scrutiny-again-1.19272

Davidenko, N., Schuster, C. F., Bax, D. V., Farndale, R. W., Hamaia, S., Best, S. M., & Cameron, R. E. (2016). Evaluation of cell binding to collagen and gelatin: a study of the effect of 2D and 3D architecture and surface chemistry. *Journal of materials science. Materials in medicine, 27* (10), 148-148. doi:10.1007/s10856-016-5763-9

Deacon, K., & Knox, A. J. (2015). Human airway smooth muscle cells secrete amphiregulin via bradykinin/COX-2/PGE (2), inducing COX-2, CXCL8, and VEGF expression in airway epithelial cells. *American Journal of Physiology - Lung Cellular and Molecular Physiology, 309* (3), L237-L249. doi:10.1152/ajplung.00390.2014

Deng, H., Dokshin, G. A., Lei, J., Goldsmith, A. M., Bitar, K. N., Fingar, D. C., Bentley, J. K. (2008). Inhibition of glycogen synthase kinase-3beta is sufficient for airway smooth muscle hypertrophy. *J Biol Chem, 283* (15), 10198-10207. doi:10.1074/jbc.M800624200

Denisin, A. K., & Pruitt, B. L. (2016). Tuning the Range of Polyacrylamide Gel Stiffness for Mechanobiology Applications. *ACS Appl Mater Interfaces, 8* (34), 21893-21902. doi:10.1021/acsami.5b09344

Djouad, F., Jackson, W. M., Bobick, B. E., Janjanin, S., Song, Y., Huang, G. T., & Tuan, R. S. (2010). Activin A expression regulates multipotency of mesenchymal progenitor cells. *Stem Cell Research & Therapy, 1* (2), 11. doi:10.1186/scrt11

Doshi, J., & Reneker, D. H. (1995). Electrospinning process and applications of electrospun fibers. *Journal of electrostatics, 35* (2-3), 151-160.

Driver, J., Weber, C. E., Callaci, J. J., Kothari, A. N., Zapf, M. A., Roper, P. M., . . . Wai, P. Y. (2015). Alcohol Inhibits Osteopontin-dependent Transforming Growth Factor-β1 Expression in Human Mesenchymal Stem Cells. *Journal of Biological Chemistry, 290* (16), 9959-9973.

Duval, K., Grover, H., Han, L.-H., Mou, Y., Pegoraro, A. F., Fredberg, J., & Chen, Z. (2017). Modeling Physiological Events in 2D vs. 3D Cell Culture. *Physiology (Bethesda, Md.), 32* (4), 266-277. doi:10.1152/physiol.00036.2016

Engler, A. J., Sen, S., Sweeney, H. L., & Discher, D. E. (2006). Matrix Elasticity Directs Stem Cell Lineage Specification. *Cell, 126* (4), 677-689. doi:https://doi.org/10.1016/j.cell.2006.06.044

Fagan, K. A., McMurtry, I. F., & Rodman, D. M. (2001). Role of endothelin-1 in lung disease. *Respiratory Research, 2* (2), 90. doi:10.1186/rr44

Fan, Y., Wang, Y., & Wang, K. (2015). Prostaglandin E (2) stimulates normal bronchial epithelial cell growth through induction of c-Jun and PDK1, a kinase implicated in oncogenesis. *Respiratory Research, 16*, 149. doi:10.1186/s12931-015-0309-0

Fang, X., Neyrinck, A. P., Matthay, M. A., & Lee, J. W. (2010). Allogeneic human mesenchymal stem cells restore epithelial protein permeability in cultured human alveolar type II cells by secretion of angiopoietin-1. *Journal of Biological Chemistry, 285* (34), 26211-26222.

Featherstone, N. C., Jesudason, E. C., Connell, M. G., Fernig, D. G., Wray, S., Losty, P. D., & Burdyga, T. V. (2005). Spontaneous propagating calcium waves underpin airway peristalsis in embryonic rat lung. *Am J Respir Cell Mol Biol, 33* (2), 153-160. doi:10.1165/rcmb.2005-0137OC

Frenot, A. (2003). Polymer Nanofibers Assembled by Electrospinning. *Curr. Opin. Colloid. In. 8*, 64-75.

Freund, V., Pons, F., Joly, V., Mathieu, E., Martinet, N., & Frossard, N. (2002). Upregulation of nerve growth factor expression by human airway smooth muscle cells in inflammatory conditions. *European Respiratory Journal, 20* (2), 458-463.

Fukunaga, T., Yamashiro, T., Oya, S., Takeshita, N., Takigawa, M., & Takano-Yamamoto, T. (2003). Connective tissue growth factor mRNA expression pattern in cartilages is

associated with their type I collagen expression. *Bone, 33* (6), 911-918. doi:https://doi.org/10.1016/j.bone.2003.07.010

Gao, M., Zhang, H., Dong, W., Bai, J., Gao, B., Xia, D., Zheng, J. (2017). Tissue-engineered trachea from a 3D-printed scaffold enhances whole-segment tracheal repair. *Scientific Reports, 7* (1), 5246-5246. doi:10.1038/s41598-017-05518-3

Gardner, O., Fahy, N., Alini, M., & Stoddart, M. (2016). Differences in human mesenchymal stem cell secretomes during chondrogenic induction. *European cells & materials, 30*, 221-235.

Gaudet, I. D., & Shreiber, D. I. (2012). Characterization of methacrylated type-I collagen as a dynamic, photoactive hydrogel. *Biointerphases, 7* (1-4), 25-25. doi:10.1007/s13758-012-0025-y

Gelfand, E. W. (2002). Mice Are a Good Model of Human Airway Disease. *American Journal of Respiratory and Critical Care Medicine, 166* (1), 5-6. doi:10.1164/rccm.2204023

Goldie, R. G., & Pedersen, K. E. (1995). Mechanisms of increased airway microvascular permeability: role in airway inflammation and obstruction. *Clin Exp Pharmacol Physiol, 22* (6-7), 387-396. doi:10.1111/j.1440-1681.1995.tb02028.x

Goldsmith, A. M., Bentley, J. K., Zhou, L., Jia, Y., Bitar, K. N., Fingar, D. C., & Hershenson, M. B. (2006). Transforming growth factor-beta induces airway smooth muscle hypertrophy. *American Journal of Respiratory Cell and Molecular Biology, 34* (2), 247-254. doi:10.1165/rcmb.2005-0166OC

Gómez-Caro Andrés, A., Moradiellos Díez, F. J., Ausín Herrero, P., Díaz-Hellín Gude, V., Larrú Cabrero, E., de Miguel Porch, E., & Martín De Nicolás, J. L. (2004) Successful Conservative Management in Iatrogenic Tracheobronchial Injury. *The Annals of Thoracic Surgery, 79* (6), 1872-1878. doi:10.1016/j.athoracsur.2004.10.006

Gonfiotti, A., Jaus, M. O., Barale, D., Baiguera, S., Comin, C., Lavorini, F., (2014)Macchiarini, P. The first tissue-engineered airway transplantation: 5-year follow-up results. *The Lancet, 383* (9913), 238-244. doi:http://doi.org/10.1016/S0140-6736 (13)62033-4

Gospodarowicz, D., & Moran, J. S. (1975). Mitogenic effect of fibroblast growth factor on early passage cultures of human and murine fibroblasts. *The Journal of cell biology, 66* (2), 451-457.

Govindaraju, V., Michoud, M.-C., Ferraro, P., Arkinson, J., Safka, K., Valderrama-Carvajal, H., & Martin, J. G. (2008). The effects of interleukin-8 on airway smooth muscle contraction in cystic fibrosis. *Respiratory Research, 9* (1), 76-76. doi:10.1186/1465-9921-9-76

Graf, J., Iwamoto, Y., Sasaki, M., Martin, G. R., Kleinman, H. K., Robey, F. A., & Yamada, Y. (1987). Identification of an amino acid sequence in laminin mediating cell attachment, chemotaxis, and receptor binding. *Cell, 48* (6), 989-996. doi:10.1016/0092-8674 (87)90707-0

Guo, F. H., De Raeve, H. R., Rice, T. W., Stuehr, D. J., Thunnissen, F., & Erzurum, S. C. (1995). Continuous nitric oxide synthesis by inducible nitric oxide synthase in normal human airway epithelium in vivo. *Proceedings of the National Academy of Sciences, 92* (17), 7809-7813.

Gupta, P., Markham, A., & Morgan, R. M. (1991). Ca2+ion sequestration by guinea‐pig tracheal cartilage: its influence on trachealis reactivity to KCl. *British Journal of Pharmacology, 104* (1), 123-127. doi:10.1111/j.1476-5381.1991.tb12395.x

Guzy, R. D., Stoilov, I., Elton, T. J., Mecham, R. P., & Ornitz, D. M. (2015). Fibroblast Growth Factor 2 Is Required for Epithelial Recovery, but Not for Pulmonary Fibrosis, in Response to Bleomycin. *American Journal of Respiratory Cell and Molecular Biology, 52* (1), 116-128. doi:10.1165/rcmb.2014-0184OC

Hackett, N. R., Shaykhiev, R., Walters, M. S., Wang, R., Zwick, R. K., Ferris, B., Crystal, R. G. (2011). The Human Airway Epithelial Basal Cell Transcriptome. *PLoS ONE, 6* (5), e18378. doi:10.1371/journal.pone.0018378

Hadjipanayi, E., Mudera, V., & Brown, R. (2009). Close dependence of fibroblast proliferation on collagen scaffold matrix stiffness. *Journal of tissue engineering and regenerative medicine, 3* (2), 77-84.

Halayko, A. J., Salari, H., MA, X., & Stephens, N. L. (1996). Markers of airway smooth muscle cell phenotype. *American Journal of Physiology-Lung Cellular and Molecular Physiology, 270* (6), L1040-L1051.

Haraguchi, M., Shimura, S., & Shirato, K. (1999a). Morphometric Analysis of Bronchial Cartilage in Chronic Obstructive Pulmonary Disease and Bronchial Asthma. *159* (3), 1005-1013. doi:10.1164/ajrccm.159.3.9712144

Haraguchi, M., Shimura, S., & Shirato, K. (1999b). Morphometric Analysis of Bronchial Cartilage in Chronic Obstructive Pulmonary Disease and Bronchial Asthma. *American Journal of Respiratory and Critical Care Medicine, 159* (3), 1005-1013. doi:10.1164/ajrccm.159.3.9712144

Harrington, H., Cato, P., Salazar, F., Wilkinson, M., Knox, A., Haycock, J. W., Ghaemmaghami, A. M. (2014). Immunocompetent 3D model of human upper airway for disease modeling and in vitro drug evaluation. *Mol Pharm, 11* (7), 2082-2091. doi:10.1021/mp5000295

Hatachi, G., Machino, R., Tsuchiya, T., Taura, Y., Elgalad, A., Taniguchi, D., Nakayama, K. (2018). Scaffold-free trachea regeneration by tissue engineering with bio-3D printing†. *Interactive CardioVascular and Thoracic Surgery, 26* (5), 745-752. doi:10.1093/icvts/ivx444

Hay, D. W., Farmer, S. G., Raeburn, D., Robinson, V. A., Fleming, W. W., & Fedan, J. S. (1986). Airway epithelium modulates the reactivity of guinea-pig respiratory smooth muscle. *Eur J Pharmacol, 129* (1-2), 11-18.

Hayashi, K., Saga, H., Chimori, Y., Kimura, K., Yamanaka, Y., & Sobue, K. (1998). Differentiated phenotype of smooth muscle cells depends on signaling pathways through insulin-like growth factors and phosphatidylinositol 3-kinase. *J Biol Chem, 273* (44), 28860-28867. doi:10.1074/jbc.273.44.28860

Hiemstra, P. S., McCray, P. B., & Bals, R. (2015). The innate immune function of airway epithelial cells in inflammatory lung disease. *European Respiratory Journal, 45* (4), 1150-1162. doi:10.1183/09031936.00141514

Hines, E. A., Jones, M.-K. N., Verheyden, J. M., Harvey, J. F., & Sun, X. (2013). Establishment of smooth muscle and cartilage juxtaposition in the developing mouse upper airways. *Proceedings of the National Academy of Sciences, 110* (48), 19444-19449. doi:10.1073/pnas.1313223110

Hu, B., Trinh, K., Figueira, W. F., & Price, P. A. (1996). Isolation and sequence of a novel human chondrocyte protein related to mammalian members of the chitinase protein family. *Journal of Biological Chemistry, 271* (32), 19415-19420.

Hu, J., Hou, Y., Park, H., Choi, B., Hou, S., Chung, A., & Lee, M. (2012). Visible light crosslinkable chitosan hydrogels for tissue engineering. *Acta Biomaterialia, 8* (5), 1730-1738. doi:https://doi.org/10.1016/j.actbio.2012.01.029

Huang, B.-L., Brugger, S. M., & Lyons, K. M. (2010). Stage-specific control of connective tissue growth factor (CTGF/CCN2) expression in chondrocytes by Sox9 and β-catenin. *Journal of Biological Chemistry, 285* (36), 27702-27712.

Huang, S., & Ingber, D. E. (2005). Cell tension, matrix mechanics, and cancer development. *Cancer cell, 8* (3), 175-176.

Huether, S. E., & McCance, K. L. (1994). Pathophysiology: The biologic basis for disease in adults and children. *Dimensions of Critical Care Nursing, 13* (6), 315.

Huh, Y.-H., Kim, S.-H., Kim, S.-J., & Chun, J.-S. (2003). Differentiation status-dependent regulation of cyclooxygenase-2 expression and prostaglandin E2 production by epidermal growth factor via mitogen-activated protein kinase in articular chondrocytes. *Journal of Biological Chemistry, 278* (11), 9691-9697.

Ivkovic, S., Yoon, B. S., Popoff, S. N., Safadi, F. F., Libuda, D. E., Stephenson, R. C., Lyons, K. M. (2003). Connective tissue growth factor coordinates chondrogenesis and angiogenesis during skeletal development. *Development (Cambridge, England), 130* (12), 2779-2791.

Jang, J.-H., Chand, H. S., Bruse, S., Doyle-Eisele, M., Royer, C., McDonald, J., Nyunoya, T. (2017). Connective Tissue Growth Factor Promotes Pulmonary Epithelial Cell Senescence and Is Associated with COPD Severity. *COPD: Journal of Chronic Obstructive Pulmonary Disease, 14* (2), 228-237. doi:10.1080/15412555.2016.1262340

Jenkins, R. G., Su, X., Su, G., Scotton, C. J., Camerer, E., Laurent, G. J., Sheppard, D. (2006). Ligation of protease-activated receptor 1 enhances α v β 6 integrin–dependent TGF-β activation and promotes acute lung injury. *J Clin Invest, 116* (6), 1606-1614.

Jeon, O., Song, S. J., Lee, K.-J., Park, M. H., Lee, S.-H., Hahn, S. K., Kim, B.-S. (2007). Mechanical properties and degradation behaviors of hyaluronic acid hydrogels cross-linked at various cross-linking densities. *Carbohydrate Polymers, 70* (3), 251-257. doi:https://doi.org/10.1016/j.carbpol.2007.04.002

Jesudason, E. C. (2009). Airway smooth muscle: an architect of the lung? *Thorax, 64* (6), 541-545. doi:10.1136/thx.2008.107094

Jesudason, E. C., Smith, N. P., Connell, M. G., Spiller, D. G., White, M. R., Fernig, D. G., & Losty, P. D. (2006). Peristalsis of airway smooth muscle is developmentally regulated and uncoupled from hypoplastic lung growth. *Am J Physiol Lung Cell Mol Physiol, 291* (4), L559-565. doi:10.1152/ajplung.00498.2005

Jiang, H. L., Fance, G. F., Hsiao, B. S., Chu, B., & Chen, W. L. (2004). Optimization and Characterization of Dextran Membranes Prepared by Electrospinning. *Biomacromolecules 5*, 326-333.

Jikko, A., Wakisaka, T., Iwamoto, M., Hiranuma, H., Kato, Y., Maeda, T., Fuchihata, H. (1998). Effects of interleukin-6 on proliferation and proteoglycan metabolism in articular chondrocyte cultures. *Cell Biol Int, 22* (9-10), 615-621. doi:10.1006/cbir.1998.0304

Jin, M., Frank, E. H., Quinn, T. M., Hunziker, E. B., & Grodzinsky, A. J. (2001). Tissue shear deformation stimulates proteoglycan and protein biosynthesis in bovine cartilage explants. *Archives of biochemistry and biophysics, 395* (1), 41-48.

Jin, T., Siow, R. C., Li, L., & Liu, K.-K. (2016) Collagen matrix stiffness influencing on fibroblast contraction force. *Frontiers in Bioengineering and Biotechnology*. doi:10.3389/conf.FBIOE.2016.01.01917

John, A. E., Wilson, M. R., Habgood, A., Porte, J., Tatler, A. L., Stavrou, A., Jenkins, R. G. (2016). Loss of epithelial G_q and G₁₁ signaling inhibits TGFβ production but promotes IL-33–mediated macrophage polarization and emphysema. *Science Signaling, 9* (451), ra104-ra104. doi:10.1126/scisignal.aad5568

John, A. E., Wilson, M. R., Habgood, A., Porte, J., Tatler, A. L., Stavrou, A., Jenkins, R. G. (2016). Loss of epithelial Gq and G11 signaling inhibits TGFbeta production but promotes IL-33-mediated macrophage polarization and emphysema. *Sci Signal, 9* (451), ra104. doi:10.1126/scisignal.aad5568

John, M., Au, B.-T., Jose, P. J., Lim, S., Saunders, M., Barnes, P. J., Fan Chung, K. (1998). Expression and release of interleukin-8 by human airway smooth muscle cells: inhibition

by Th-2 cytokines and corticosteroids. *American Journal of Respiratory Cell and Molecular Biology, 18* (1), 84-90.

Johnson, P. R., Roth, M., Tamm, M., Hughes, M., Ge, Q., King, G., Black, J. L. (2001). Airway smooth muscle cell proliferation is increased in asthma. *Am J Respir Crit Care Med, 164* (3), 474-477. doi:10.1164/ajrccm.164.3.2010109

Johnson, P. R. A., Burgess, J. K., Ge, Q., Poniris, M., Boustany, S., Twigg, S. M., & Black, J. L. (2006). Connective Tissue Growth Factor Induces Extracellular Matrix in Asthmatic Airway Smooth Muscle. *173* (1), 32-41. doi:10.1164/rccm.200406-703OC

Johnson, S. R., & Knox, A. J. (1997). Synthetic functions of airway smooth muscle in asthma. *Trends in Pharmacological Sciences, 18* (8), 288-292. doi:https://doi.org/10.1016/S0165-6147 (97)01092-4

Jolly, L., Stavrou, A., Vanderstoken, G., Meliopoulos, V. A., Habgood, A., Tatler, A. L., Violette, S. (2014). Influenza Promotes Collagen Deposition via αvβ6-integrin Mediated Transforming Growth Factor β Activation. *Journal of Biological Chemistry*, jbc. M114. 582262.

Jones, R. L., Noble, P. B., Elliot, J. G., & James, A. L. (2016). Airway remodelling in COPD: It's not asthma! *Respirology, 21* (8), 1347-1356. doi:10.1111/resp.12841

Karmy-Jones, R., & Wood, D. E. Traumatic Injury to the Trachea and Bronchus. *Thoracic Surgery Clinics, 17* (1), 35-46. doi:10.1016/j.thorsurg.2007.03.005

Kaye, R., Goldstein, T., Grande, D. A., Zeltsman, D., & Smith, L. P. (2019). A 3-dimensional bioprinted tracheal segment implant pilot study: Rabbit tracheal resection with graft implantation. *International journal of pediatric otorhinolaryngology, 117*, 175-178.

Khan, M. A. (2013). Inflammation signals airway smooth muscle cell proliferation in asthma pathogenesis. *Multidiscip Respir Med, 8* (1), 11. doi:10.1186/2049-6958-8-11

Kim, J., Suh, S. W., Shin, J. Y., Kim, J. H., Choi, Y. S., & Kim, H. (2004). Replacement of a tracheal defect with a tissue-engineered prosthesis: Early results from animal experiments. *The Journal of Thoracic and Cardiovascular Surgery, 128* (1), 124-129. doi:http://doi.org/10.1016/j.jtcvs.2003.09.045

Kim, K. W., Jee, H. M., Park, Y. H., Choi, B. S., Sohn, M. H., & Kim, K. E. (2009). Relationship between amphiregulin and airway inflammation in children with asthma and eosinophilic bronchitis. *Chest, 136* (3), 805-810. doi:10.1378/chest.08-2972

Kinner, B., & Spector, M. (2001). Smooth muscle actin expression by human articular chondrocytes and their contraction of a collagen—glycosaminoglycan matrix in vitro. *Journal of Orthopaedic Research, 19* (2), 233-241. doi:10.1016/S0736-0266 (00)00081-4

Knox, A. J., Corbett, L., Stocks, J., Holland, E., Zhu, Y. M., & Pang, L. (2001). Human airway smooth muscle cells secrete vascular endothelial growth factor: up-regulation by bradykinin via a protein kinase C and prostanoid-dependent mechanism. *The FASEB Journal, 15* (13), 2480-2488.

Kojima, K., Bonassar, L. J., Roy, A. K., Mizuno, H., Cortiella, J., & Vacanti, C. A. (2003). A composite tissue-engineered trachea using sheep nasal chondrocyte and epithelial cells. *The FASEB Journal, 17* (8), 823-828. doi:10.1096/fj.02-0462com

Kojima, K., Bonassar, L. J., Roy, A. K., Vacanti, C. A., & Cortiella, J. (2002). Autologous tissue-engineered trachea with sheep nasal chondrocytes. *The Journal of Thoracic and Cardiovascular Surgery, 123* (6), 1177-1184. doi:http://doi.org/10.1067/mtc.2002.121161

Kona, S., Chellamuthu, P., Xu, H., Hills, S. R., & Nguyen, K. T. (2009). Effects of cyclic strain and growth factors on vascular smooth muscle cell responses. *The open biomedical engineering journal, 3*, 28.

Kuperman, D. A., Huang, X., Koth, L. L., Chang, G. H., Dolganov, G. M., Zhu, Z., Erle, D. J. (2002). Direct effects of interleukin-13 on epithelial cells cause airway hyperreactivity and mucus overproduction in asthma. *Nature Medicine, 8*, 885. doi:10.1038/nm734

Lan, B., Mitchel, J. A., O'Sullivan, M. J., Park, C. Y., Kim, J. H., Cole, W. C., Park, J.-A. (2018). Airway epithelial compression promotes airway smooth muscle proliferation and contraction. *American Journal of Physiology-Lung Cellular and Molecular Physiology, 315* (5), L645-L652. doi:10.1152/ajplung.00261.2018

Lan, R. S., Knight, D. A., Stewart, G. A., & Henry, P. J. (2001). Role of PGE2 in protease‐activated receptor‐1, −2 and −4 mediated relaxation in the mouse isolated trachea. *British Journal of Pharmacology, 132* (1), 93-100. doi:doi:10.1038/sj.bjp.0703776

Laragione, T., Bonetto, V., Casoni, F., Massignan, T., Bianchi, G., Gianazza, E., & Ghezzi, P. (2003). Redox regulation of surface protein thiols: Identification of integrin α-4 as a molecular target by using redox proteomics. *Proceedings of the National Academy of Sciences, 100* (25), 14737-14741. doi:10.1073/pnas.2434516100

Le, A. V., Cho, J. Y., Miller, M., McElwain, S., Golgotiu, K., & Broide, D. H. (2007). Inhibition of Allergen-Induced Airway Remodeling in Smad 3-Deficient Mice. *The Journal of Immunology, 178* (11), 7310-7316. doi:10.4049/jimmunol.178.11.7310

Lee, J. W., Son, J.-S., Choi, J.-W., Han, Y.-J., & Lee, J.-R. (2014). The comparison of the lengths and diameters of main bronchi measured from two-dimensional and three-dimensional images in the same patients. *Korean journal of anesthesiology, 66* (3), 189-194. doi:10.4097/kjae.2014.66.3.189

Lee, J. W., Son, J. S., Choi, J. W., Han, Y. J., & Lee, J. R. (2014). The comparison of the lengths and diameters of main bronchi measured from two-dimensional and three-dimensional images in the same patients. *Korean J Anesthesiol, 66* (3), 189-194. doi:10.4097/kjae.2014.66.3.189

Lee, K.-Y., Ho, S.-C., Lin, H.-C., Lin, S.-M., Liu, C.-Y., Huang, C.-D., Kuo, H.-P. (2006). Neutrophil-derived elastase induces TGF-β1 secretion in human airway smooth muscle via NF-κB pathway. *American Journal of Respiratory Cell and Molecular Biology, 35* (4), 407-414.

LeRoux, M. A., Guilak, F., & Setton, L. A. (1999). Compressive and shear properties of alginate gel: Effects of sodium ions and alginate concentration. *Journal of Biomedical Materials Research, 47* (1), 46-53. doi:10.1002/ (sici)1097-4636 (199910)47:1<46::aid-jbm6>3.0.co;2-n

Levonen, A.-L., Landar, A., Ramachandran, A., Ceaser, E. K., Dickinson, D. A., Zanoni, G., Darley-Usmar, V. M. (2004). Cellular mechanisms of redox cell signalling: role of cysteine modification in controlling antioxidant defences in response to electrophilic lipid oxidation products. *Biochemical Journal, 378* (Pt 2), 373.

Li, F., Armstrong, G. B., Tombran-Tink, J., & Niyibizi, C. (2016). Pigment epithelium derived factor upregulates expression of vascular endothelial growth factor by human mesenchymal stem cells: Possible role in PEDF regulated matrix mineralization. *Biochemical and Biophysical Research Communications, 478* (3), 1106-1110. doi:https://doi.org/10.1016/j.bbrc.2016.08.076

Lin, C., Yao, E., Zhang, K., Jiang, X., Croll, S., Thompson-Peer, K., & Chuang, P.-T. (2017). YAP is essential for mechanical force production and epithelial cell proliferation during lung branching morphogenesis. *eLife, 6*, e21130. doi:10.7554/eLife.21130

Lin, S., & Gu, L. (2015). Influence of crosslink density and stiffness on mechanical properties of type I collagen gel. *Materials, 8* (2), 551-560.

Lingaraj, K., Poh, C. K., & Wang, W. (2010). Vascular endothelial growth factor (VEGF) is expressed during articular cartilage growth and re-expressed in osteoarthritis. *Annals Academy of Medicine Singapore, 39* (5), 399.

Lotz, M. (2001). Cytokines in Cartilage Injury and Repair. *Clinical Orthopaedics and Related Research, 391*, S108-S115.

Ma, X., Cheng, Z., Kong, H., Wang, Y., Unruh, H., Stephens, N. L., & Laviolette, M. (2002). Changes in biophysical and biochemical properties of single bronchial smooth muscle cells from asthmatic subjects. *Am J Physiol Lung Cell Mol Physiol, 283* (6), L1181-1189. doi:10.1152/ajplung.00389.2001

Macchiarini, P., Jungebluth, P., Go, T., Asnaghi, M. A., Rees, L. E., Cogan, T. A., Parnigotto, P. P. (2008). Clinical transplantation of a tissue-engineered airway. *The Lancet, 372* (9655), 2023-2030.

Macchiarini, P., Jungebluth, P., Go, T., Asnaghi, M. A., Rees, L. E., Cogan, T. A., Birchall, M. A. (2008). Clinical transplantation of a tissue-engineered airway. *Lancet, 372* (9655), 2023-2030. doi:10.1016/s0140-6736 (08)61598-6

Mahoney, C., Conklin, D., Waterman, J., Sankar, J., & Bhattarai, N. (2016). Electrospun nanofibers of poly (ε-caprolactone)/depolymerized chitosan for respiratory tissue engineering applications. *Journal of Biomaterials science, Polymer edition, 27* (7), 611-625.

Mailleux, A. A., Kelly, R., Veltmaat, J. M., De Langhe, S. P., Zaffran, S., Thiery, J. P., & Bellusci, S. (2005). Fgf10 expression identifies parabronchial smooth muscle cell progenitors and is required for their entry into the smooth muscle cell lineage. *Development, 132* (9), 2157-2166. doi:10.1242/dev.01795

Malavia, N. K., Raub, C. B., Mahon, S. B., Brenner, M., Jr, R. A. P., & George, S. C. (2009). Airway Epithelium Stimulates Smooth Muscle Proliferation. *41* (3), 297-304. doi:10.1165/rcmb.2008-0358OC

Mann, B. K., Gobin, A. S., Tsai, A. T., Schmedlen, R. H., & West, J. L. (2001). Smooth muscle cell growth in photopolymerized hydrogels with cell adhesive and proteolytically degradable domains: synthetic ECM analogs for tissue engineering. *Biomaterials, 22* (22), 3045-3051. doi:10.1016/s0142-9612 (01)00051-5

Marcus, P. S. (1984). Simulation of Taylor-Couette flow. Part 1. Numerical methods and comparison with experiment. *Journal of Fluid Mechanics, 146*, 45-64.

Marlar, S., Arnspang, E. C., Pedersen, G. A., Koffman, J. S., & Nejsum, L. N. (2014). Measuring localization and diffusion coefficients of basolateral proteins in lateral versus basal membranes using functionalized substrates and kICS analysis. *Biochimica et Biophysica Acta (BBA) - Biomembranes, 1838* (10), 2404-2411. doi:https://doi.org/10.1016/j.bbamem.2014.06.005

Marlovits, S., Hombauer, M., Truppe, M., Vecsei, V., & Schlegel, W. (2004). Changes in the ratio of type-I and type-II collagen expression during monolayer culture of human chondrocytes. *Bone & Joint Journal, 86* (2), 286-295.

Martinez, A., Miller, M., Unsworth, E. J., Siegfried, J. M., & Cuttitta, F. (1995). Expression of adrenomedullin in normal human lung and in pulmonary tumors. *Endocrinology, 136* (9), 4099-4105.

Mason, B. N., Starchenko, A., Williams, R. M., Bonassar, L. J., & Reinhart-King, C. A. (2013). Tuning three-dimensional collagen matrix stiffness independently of collagen concentration modulates endothelial cell behavior. *Acta Biomaterialia, 9* (1), 4635-4644. doi:https://doi.org/10.1016/j.actbio.2012.08.007

Matsumoto, H., Moir, L. M., Oliver, B. G., Burgess, J. K., Roth, M., Black, J. L., & McParland, B. E. (2007). Comparison of gel contraction mediated by airway smooth muscle cells from patients with and without asthma. *Thorax, 62* (10), 848-854. doi:10.1136/thx.2006.070474

Matsumoto, H., Moir, L. M., Oliver, B. G. G., Burgess, J. K., Roth, M., Black, J. L., & McParland, B. E. (2007). Comparison of gel contraction mediated by airway smooth muscle cells from patients with and without asthma. *Thorax, 62* (10), 848-854. doi:10.1136/thx.2006.070474

Mauck, R. L., Soltz, M. A., Wang, C. C. B., Wong, D. D., Chao, P.-H. G., Valhmu, W. B., Ateshian, G. A. (2000). Functional Tissue Engineering of Articular Cartilage Through Dynamic Loading of Chondrocyte-Seeded Agarose Gels. *Journal of Biomechanical Engineering, 122* (3), 252-260. doi:10.1115/1.429656

Maunders, H., Patwardhan, S., Phillips, J., Clack, A., & Richter, A. (2007). Human bronchial epithelial cell transcriptome: gene expression changes following acute exposure to whole cigarette smoke in vitro. *Am J Physiol Lung Cell Mol Physiol, 292* (5), L1248-1256. doi:10.1152/ajplung.00290.2006

McKay, S., De Jongste, J. C., Saxena, P. R., & Sharma, H. S. (1998). Angiotensin II induces hypertrophy of human airway smooth muscle cells: expression of transcription factors and transforming growth factor-β1. *American Journal of Respiratory Cell and Molecular Biology, 18* (6), 823-833.

McKay, S., Hirst, S. J., Haas, M. B.-d., De Jongste, J. C., Hoogsteden, H. C., Saxena, P. R., & Sharma, H. S. (2000). Tumor necrosis factor-α enhances mRNA expression and secretion of interleukin-6 in cultured human airway smooth muscle cells. *American Journal of Respiratory Cell and Molecular Biology, 23* (1), 103-111.

McMillan, S. J., Xanthou, G., & Lloyd, C. M. (2005). Manipulation of Allergen-Induced Airway Remodeling by Treatment with Anti-TGF-β Antibody: Effect on the Smad Signaling Pathway. *The Journal of Immunology, 174* (9), 5774-5780. doi:10.4049/jimmunol.174.9.5774

McQuin, C., Goodman, A., Chernyshev, V., Kamentsky, L., Cimini, B. A., Karhohs, K. W., Carpenter, A. E. (2018). CellProfiler 3.0: Next-generation image processing for biology. *PLOS Biology, 16* (7), e2005970. doi:10.1371/journal.pbio.2005970

Meyerholz, D. K., Stoltz, D. A., Namati, E., Ramachandran, S., Pezzulo, A. A., Smith, A. R., Welsh, M. J. (2010). Loss of cystic fibrosis transmembrane conductance regulator function produces abnormalities in tracheal development in neonatal pigs and young children. *Am J Respir Crit Care Med, 182* (10), 1251-1261. doi:10.1164/rccm.201004-0643OC

Mills, P. R., Davies, R. J., & Devalia, J. L. (1999). Airway Epithelial Cells, Cytokines, and Pollutants. *160* (supplement_1), S38-S43. doi:10.1164/ajrccm.160.supplement_1.11

Mohri, Z., Del Rio Hernandez, A., & Krams, R. (2017). The emerging role of YAP/TAZ in mechanotransduction. *Journal of thoracic disease, 9* (5), E507-E509. doi:10.21037/jtd.2017.03.179

Mohtai, M., Gupta, M. K., Donlon, B., Ellison, B., Cooke, J., Gibbons, G., Smith, R. L. (1996). Expression of interleukin-6 in osteoarthritic chondrocytes and effects of fluid-induced shear on this expression in normal human chondrocytes in vitro. *Journal of Orthopaedic Research, 14* (1), 67-73. doi:10.1002/jor.1100140112

Morris, G. E., Bridge, J. C., Brace, L. A., Knox, A. J., Aylott, J. W., Brightling, C. E., Rose, F. R. (2014). A novel electrospun biphasic scaffold provides optimal three-dimensional topography for in vitro co-culture of airway epithelial and fibroblast cells. *Biofabrication, 6* (3), 035014. doi:10.1088/1758-5082/6/3/035014

Murata, M., Yudo, K., Nakamura, H., Chiba, J., Okamoto, K., Suematsu, N., Masuko, K. (2009). Hypoxia upregulates the expression of angiopoietin-like-4 in human articular chondrocytes: Role of angiopoietin-like-4 in the expression of matrix metalloproteinases and cartilage degradation. *Journal of Orthopaedic Research, 27* (1), 50-57. doi:10.1002/jor.20703

Naylor, B. (1962). The Shedding of the Mucosa of the Bronchial Tree in Asthma. *Thorax, 17* (1), 69-72.

Nemoto, Y., Kanai, T., Takahara, M., Oshima, S., Nakamura, T., Okamoto, R., Watanabe, M. (2013). Bone marrow-mesenchymal stem cells are a major source of interleukin-7 and sustain colitis by forming the niche for colitogenic CD4 memory T cells. *Gut, 62* (8), 1142-1152. doi:10.1136/gutjnl-2012-302029

Nguyen, Q. T., Hwang, Y., Chen, A. C., Varghese, S., & Sah, R. L. (2012). Cartilage-like mechanical properties of poly (ethylene glycol)-diacrylate hydrogels. *Biomaterials, 33* (28), 6682-6690. doi:https://doi.org/10.1016/j.biomaterials.2012.06.005

Nichol, J. W., Koshy, S., Bae, H., Hwang, C. M., Yamanlar, S., & Khademhosseini, A. (2010a). Cell-laden microengineered gelatin methacrylate hydrogels. *Biomaterials, 31* (21), 5536-5544. doi:10.1016/j.biomaterials.2010.03.064

Nichol, J. W., Koshy, S. T., Bae, H., Hwang, C. M., Yamanlar, S., & Khademhosseini, A. (2010b). Cell-laden microengineered gelatin methacrylate hydrogels. *Biomaterials, 31* (21), 5536-5544. doi:https://doi.org/10.1016/j.biomaterials.2010.03.064

Nishida, T., Kubota, S., Nakanishi, T., Kuboki, T., Yosimichi, G., Kondo, S., & Takigawa, M. (2002). CTGF/Hcs24, a hypertrophic chondrocyte-specific gene product, stimulates proliferation and differentiation, but not hypertrophy of cultured articular chondrocytes. *J Cell Physiol, 192* (1), 55-63. doi:10.1002/jcp.10113

Oliveira, L. C., Danilucci, T. M., Chaves-Neto, A. H., Campanelli, A. P., Silva, T. C., & Oliveira, S. H. (2016). Tracheal Smooth Muscle Cells Stimulated by Stem Cell Factor-c-Kit Coordinate the Production of Transforming Growth Factor-beta1 and Fibroblast Growth Factor-2 Mediated by Chemokine (C-C Motif) Ligand 3. *J Interferon Cytokine Res, 36* (6), 401-411. doi:10.1089/jir.2015.0102

Olze, H., Kaschke, O., & Müller, W. D. (1997). Investigations to improve the design of an alloplastic epithelialized tracheal replacement. *HNO, 45* (6), 453-459. doi:10.1007/s001060050123

Omoto, S., Nishida, K., Yamaai, Y., Shibahara, M., Nishida, T., Doi, T., Takigawa, M. (2004). Expression and localization of connective tissue growth factor (CTGF/Hcs24/CCN2) in osteoarthritic cartilage. *Osteoarthritis and Cartilage, 12* (10), 771-778. doi:https://doi.org/10.1016/j.joca.2004.06.009

Pan, J., Luk, C., Kent, G., Cutz, E., & Yeger, H. (2006). Pulmonary Neuroendocrine Cells, Airway Innervation, and Smooth Muscle Are Altered in Cftr Null Mice. *American Journal of Respiratory Cell and Molecular Biology, 35* (3), 320-326. doi:10.1165/rcmb.2005-0468OC

Panitch, H. B., Wolfson, M. R., & Shaffer, T. H. (1993). Epithelial modulation of preterm airway smooth muscle contraction. *Journal of Applied Physiology, 74* (3), 1437.

Pansky, B. (1982a). Development Of The Lower Respiratory System: Larynx And Trachea *Review of Medical Embryology*: McGraw-Hill.

Pansky, B. (1982b). Development Of The Lower Respiratory System: The Bronchi And Surrounding Structures *Review of Medical Embryology* (Vol. 59): McGraw-Hill.

Parreno, J., Raju, S., Wu, P.-h., & Kandel, R. A. (2016) MRTF-A signaling regulates the acquisition of the contractile phenotype in dedifferentiated chondrocytes. *Matrix Biology*. doi:https://doi.org/10.1016/j.matbio.2016.10.004

Parvez, O., Voss, A.-M., de Kok, M., Roth-Kleiner, M., & Belik, J. (2006). Bronchial Muscle Peristaltic Activity in the Fetal Rat. *Pediatric Research, 59*, 756. doi:10.1203/01.pdr.0000219121.15634.d1

Perez-Zoghbi, J. F., Bai, Y., & Sanderson, M. J. (2010). Nitric oxide induces airway smooth muscle cell relaxation by decreasing the frequency of agonist-induced Ca²⁺ oscillations. *The Journal of General Physiology, 135* (3), 247-259. doi:10.1085/jgp.200910365

Pierce, R. J., & Worsnop, C. J. (1999). Upper Airway function and dysfunction in respiration. *Clinical and Experimental Pharmacology and Physiology, 26* (1), 1-10. doi:10.1046/j.1440-1681.1999.02988.x

Plant, P. J., North, M. L., Ward, A., Ward, M., Khanna, N., Correa, J., Batt, J. (2012). Hypertrophic airway smooth muscle mass correlates with increased airway responsiveness in a murine model of asthma. *Am J Respir Cell Mol Biol, 46* (4), 532-540. doi:10.1165/rcmb.2011-0293OC

Polacek, M., Bruun, J.-A., Elvenes, J., Figenschau, Y., & Martinez, I. (2011). The secretory profiles of cultured human articular chondrocytes and mesenchymal stem cells: implications for autologous cell transplantation strategies. *Cell transplantation, 20* (9), 1381-1393.

Polacek, M., Bruun, J. A., Johansen, O., & Martinez, I. (2010). Differences in the secretome of cartilage explants and cultured chondrocytes unveiled by SILAC technology. *Journal of Orthopaedic Research, 28* (8), 1040-1049. doi:10.1002/jor.21067

Poon, A. H., Choy, D. F., Chouiali, F., Ramakrishnan, R. K., Mahboub, B., Audusseau, S., Hamid, Q. (2017). Increased Autophagy-Related 5 Gene Expression Is Associated with Collagen Expression in the Airways of Refractory Asthmatics. *Frontiers in Immunology, 8* (355). doi:10.3389/fimmu.2017.00355

Postma, D. S., & Timens, W. (2006). Remodeling in asthma and chronic obstructive pulmonary disease. *Proc Am Thorac Soc, 3* (5), 434-439. doi:10.1513/pats.200601-006AW

Price, D. L., Wong, R. J., & Randolph, G. W. (2008). Invasive thyroid cancer: management of the trachea and esophagus. *Otolaryngologic clinics of North America, 41* (6), 1155-x. doi:10.1016/j.otc.2008.08.002

Provenzano, P. P., & Keely, P. J. (2011). Mechanical signaling through the cytoskeleton regulates cell proliferation by coordinated focal adhesion and Rho GTPase signaling. *Journal of Cell Science, 124* (8), 1195-1205. doi:10.1242/jcs.067009

Pufe, T., Harde, V., Petersen, W., Goldring, M. B., Tillmann, B., & Mentlein, R. (2004). Vascular endothelial growth factor (VEGF) induces matrix metalloproteinase expression in immortalized chondrocytes. *The Journal of pathology, 202* (3), 367-374.

Raeburn, D., Rodger, I. W., Hay, D. W. P., & Fedan, J. S. (1986). The dependence of airway smooth muscle on extracellular Ca2+ for contraction is influenced by the presence of cartilage. *Life Sciences, 38* (16), 1499-1505. doi:https://doi.org/10.1016/0024-3205(86)90563-1

Rains, J. K., Bert, J. L., Roberts, C. R., & Pare, P. D. (1992). Mechanical properties of human tracheal cartilage. *J Appl Physiol (1985), 72* (1), 219-225. doi:10.1152/jappl.1992.72.1.219

Rajput, M. (2012). *Optimization of Electrospinning Parameters to Fabricate Aligned Nanofibers for Neural Tissue Engineering.* National Institute Of Technology Rourkela.

Ramchandani, R., Shen, X., Elmsley, C. L., Ambrosius, W. T., Gunst, S. J., & Tepper, R. S. (2000). Differences in airway structure in immature and mature rabbits. *Journal of Applied Physiology, 89* (4), 1310-1316. doi:10.1152/jappl.2000.89.4.1310

Recklies, A. D., White, C., & Hua, L. (2002). The chitinase 3-like protein human cartilage glycoprotein 39 (HC-gp39) stimulates proliferation of human connective-tissue cells and activates both extracellular signal-regulated kinase-and protein kinase B-mediated signalling pathways. *Biochemical Journal, 365* (1), 119-126.

Regamey, N., Ochs, M., Hilliard, T. N., Mühlfeld, C., Cornish, N., Fleming, L., Davies, J. C. (2008). Increased Airway Smooth Muscle Mass in Children with Asthma, Cystic Fibrosis, and Non-Cystic Fibrosis Bronchiectasis. *American Journal of Respiratory and Critical Care Medicine, 177* (8), 837-843. doi:10.1164/rccm.200707-977OC

Rehfeldt, F., Engler, A. J., Eckhardt, A., Ahmed, F., & Discher, D. E. (2007). Cell responses to the mechanochemical microenvironment—Implications for regenerative medicine and drug delivery. *Advanced Drug Delivery Reviews, 59* (13), 1329-1339. doi:https://doi.org/10.1016/j.addr.2007.08.007

Retsch-Bogart, G. Z., Stiles, A. D., Moats-Staats, B. M., Van Scott, M. R., Boucher, R. C., & D'Ercole, A. J. (1990). Canine tracheal epithelial cells express the type 1 insulin-like growth factor receptor and proliferate in response to insulin-like growth factor I. *Am J Respir Cell Mol Biol, 3* (3), 227-234. doi:10.1165/ajrcmb/3.3.227

Rojas, M., Xu, J., Woods, C. R., Mora, A. L., Spears, W., Roman, J., & Brigham, K. L. (2005). Bone marrow–derived mesenchymal stem cells in repair of the injured lung. *American Journal of Respiratory Cell and Molecular Biology, 33* (2), 145-152.

Rosenthal, A. K., Gohr, C. M., Ninomiya, J., & Wakim, B. T. (2011). Proteomic analysis of articular cartilage vesicles from normal and osteoarthritic cartilage. *Arthritis & Rheumatism, 63* (2), 401-411. doi:10.1002/art.30120

Rossios, C., Pavlidis, S., Gibeon, D., Mumby, S., Durham, A., Ojo, O., Adcock, I. M. (2017). Impaired innate immune gene profiling in airway smooth muscle cells from chronic cough patients. *Biosci Rep, 37* (6). doi:10.1042/bsr20171090

Ruocco, S., Lallemand, A., Tournier, J. M., & Gaillard, D. (1996). Expression and localization of epidermal growth factor, transforming growth factor-α, and localization of their common receptor in fetal human lung development. *Pediatric Research, 39* (3), 448-455.

Sanchez-Adams, J., Leddy, H. A., McNulty, A. L., O'Conor, C. J., & Guilak, F. (2014). The Mechanobiology of Articular Cartilage: Bearing the Burden of Osteoarthritis. *Current rheumatology reports, 16* (10), 451-451. doi:10.1007/s11926-014-0451-6

Sanchez-Esteban, J., Tsai, S.-W., Sang, J., Qin, J., Torday, J. S., & Rubin, L. P. (1998). Effects of Mechanical Forces on Lung-Specific Gene Expression. *The American Journal of the Medical Sciences, 316* (3), 200-204. doi:https://doi.org/10.1016/S0002-9629 (15)40402-1

Scaglione, M., Romano, S., Pinto, A., Sparano, A., Scialpi, M., & Rotondo, A. (2006) Acute tracheobronchial injuries: Impact of imaging on diagnosis and management implications. *European Journal of Radiology, 59* (3), 336-343. doi:10.1016/j.ejrad.2006.04.026

Schittny, J. C., Miserocchi, G., & Sparrow, M. P. (2000). Spontaneous Peristaltic Airway Contractions Propel Lung Liquid through the Bronchial Tree of Intact and Fetal Lung Explants. *American Journal of Respiratory Cell and Molecular Biology, 23* (1), 11-18. doi:10.1165/ajrcmb.23.1.3926

Schrader, J., Gordon-Walker, T. T., Aucott, R. L., van Deemter, M., Quaas, A., Walsh, S., Iredale, J. P. (2011). Matrix stiffness modulates proliferation, chemotherapeutic response, and dormancy in hepatocellular carcinoma cells. *Hepatology (Baltimore, Md.), 53* (4), 1192-1205. doi:10.1002/hep.24108

Schrader, J., Gordon‐Walker, T. T., Aucott, R. L., van Deemter, M., Quaas, A., Walsh, S., Iredale, J. P. (2011). Matrix stiffness modulates proliferation, chemotherapeutic response, and dormancy in hepatocellular carcinoma cells. *Hepatology, 53* (4), 1192-1205.

Schultz, S. C., Hammon, J. W., Jr., Turner, C. S., McGuirt, W. F., Jr., & Nelson, J. M. (1999) Surgical management and follow-up of a complex tracheobronchial injury. *The Annals of Thoracic Surgery, 67* (3), 834-836. doi:10.1016/S0003-4975 (98)01206-5

Schwartz, C. M., Stack, J., Hill, C. L., Lallier, S. W., Chiang, T., Johnson, J., & Reynolds, S. D. (2019). Electrospun scaffolds limit the regenerative potential of the airway epithelium. *Laryngoscope Investigative Otolaryngology, 4* (4), 446-454. doi:10.1002/lio2.289

Shannon, J. M., Nielsen, L. D., Gebb, S. A., & Randell, S. H. (1998). Mesenchyme specifies epithelial differentiation in reciprocal recombinants of embryonic lung and trachea. *Dev Dyn, 212* (4), 482-494. doi:10.1002/ (sici)1097-0177 (199808)212:4<482::aid-aja2>3.0.co;2-d

Sherman, T. S., Chen, Z., Yuhanna, I. S., Lau, K. S., Margraf, L. R., & Shaul, P. W. (1999). Nitric oxide synthase isoform expression in the developing lung epithelium. *Am J Physiol, 276* (2 Pt 1), L383-390.

Shirahama, H., Lee, B. H., Tan, L. P., & Cho, N.-J. (2016). Precise Tuning of Facile One-Pot gelatin Methacryloyl (GelMA) Synthesis. *6*, 31036. doi:10.1038/srep31036

Shraideh Ziad, A.-A. W., Badran Darwish. (2013). Effects of cigarette smoking on histology of trachea and lungs of albino rat. *RESEARCH OPINIONS IN ANIMAL & VETERINARY SCIENCES*, 356-362.

Silacci, P., Dayer, J. M., Desgeorges, A., Peter, R., Manueddu, C., & Guerne, P. A. (1998). Interleukin (IL)-6 and its soluble receptor induce TIMP-1 expression in synoviocytes and chondrocytes, and block IL-1-induced collagenolytic activity. *J Biol Chem, 273* (22), 13625-13629. doi:10.1074/jbc.273.22.13625

Solon, J., Levental, I., Sengupta, K., Georges, P. C., & Janmey, P. A. (2007). Fibroblast Adaptation and Stiffness Matching to Soft Elastic Substrates. *Biophysical Journal, 93* (12), 4453-4461. doi:https://doi.org/10.1529/biophysj.106.101386

Sonnylal, S., Xu, S., Jones, H., Tam, A., Sreeram, V. R., Ponticos, M., de Crombrugghe, B. (2013). Connective tissue growth factor causes EMT-like cell fate changes in vivo and in vitro. *Journal of Cell Science, 126* (10), 2164-2175. doi:10.1242/jcs.111302

Sophia Fox, A. J., Bedi, A., & Rodeo, S. A. (2009). The basic science of articular cartilage: structure, composition, and function. *Sports health, 1* (6), 461-468.

Spees, J. L., Lee, R. H., & Gregory, C. A. (2016). Mechanisms of mesenchymal stem/stromal cell function. *Stem Cell Research & Therapy, 7* (1), 125. doi:10.1186/s13287-016-0363-7

Spittle, N., & McCluskey, A. (2000). Tracheal stenosis after intubation. *BMJ : British Medical Journal, 321* (7267), 1000-1002.

Stadler, J., Stefanovic-Racic, M., Billiar, T. R., Curran, R. D., Mcintyre, L. A., Georgescu, H. I., Evans, C. H. (1991). Articular chondrocytes synthesize nitric oxide in response to cytokines and lipopolysaccharide. *The Journal of Immunology, 147* (11), 3915-3920.

Stamatiou, R., Paraskeva, E., Gourgoulianis, K., Molyvdas, P.-A., & Hatziefthimiou, A. (2012a). Cytokines and Growth Factors Promote Airway Smooth Muscle Cell Proliferation. *ISRN Inflammation, 2012*, 13. doi:10.5402/2012/731472

Stamatiou, R., Paraskeva, E., Gourgoulianis, K., Molyvdas, P. A., & Hatziefthimiou, A. (2012b). Cytokines and Growth Factors Promote Airway Smooth Muscle Cell Proliferation. *ISRN Inflammation, 2012*, 731472. doi:10.5402/2012/731472

Standring, S. (2016). *Gray's anatomy : the anatomical basis of clinical practice* (41 ed.). New York: Elsevier.

Sumanasinghe, R. D., Bernacki, S. H., & Loboa, E. G. (2006). Osteogenic differentiation of human mesenchymal stem cells in collagen matrices: effect of uniaxial cyclic tensile strain on bone morphogenetic protein (BMP-2) mRNA expression. *Tissue Engineering, 12* (12), 3459-3465.

Sumanasinghe, R. D., Pfeiler, T. W., Monteiro-Riviere, N. A., & Loboa, E. G. (2009). Expression of proinflammatory cytokines by human mesenchymal stem cells in response to cyclic tensile strain. *Journal of Cellular Physiology, 219* (1), 77-83. doi:10.1002/jcp.21653

Sun, Z. C., Zussman, E., Yarin, A., Wendorff, J. H., & Greiner, A. (2003). Compound Core-shell Polymer Nanofibers by Co-electrospinning. *Advanced Materials*, 1929-1932.

Takahashi, M., Li, T. S., Suzuki, R., Kobayashi, T., Ito, H., Ikeda, Y., Hamano, K. (2006). Cytokines produced by bone marrow cells can contribute to functional improvement of the infarcted heart by protecting cardiomyocytes from ischemic injury. *Am J Physiol Heart Circ Physiol, 291* (2), H886-893. doi:10.1152/ajpheart.00142.2006

Takeda, N., Sumi, Y., Préfontaine, D., Abri, J. A., Heialy, N. A., Al‐Ramli, W., Hamid, Q. (2009). Epithelium‐derived chemokines induce airway smooth muscle cell migration. *Clinical & Experimental Allergy, 39* (7), 1018-1026. doi:10.1111/j.1365-2222.2009.03238.x

Tatler, A. L., John, A. E., Jolly, L., Habgood, A., Porte, J., Brightling, C., Jenkins, G. (2011). Integrin αvβ5-Mediated TGF-β Activation by Airway Smooth Muscle Cells in Asthma. *The Journal of Immunology, 187* (11), 6094-6107. doi:10.4049/jimmunol.1003507

ten Hallers, E. J. O., Rakhorst, G., Marres, H. A. M., Jansen, J. A., van Kooten, T. G., Schutte, H. K., Verkerke, G. J. (2004). Animal models for tracheal research. *Biomaterials, 25* (9), 1533-1543. doi:http://doi.org/10.1016/S0142-9612 (03)00500-3

Thorley, A. J., & Tetley, T. D. (2007). Pulmonary epithelium, cigarette smoke, and chronic obstructive pulmonary disease. *International Journal of Chronic Obstructive Pulmonary Disease, 2* (4), 409-428.

Townsend, J. M., Ott, L. M., Salash, J. R., Fung, K.-M., Easley, J. T., Seim, H. B., Detamore, M. S. (2018). Reinforced Electrospun Polycaprolactone Nanofibers for Tracheal Repair in an In Vivo Ovine Model. *Tissue engineering. Part A, 24* (17-18), 1301-1308. doi:10.1089/ten.tea.2017.0437

Tschumperlin, D. J., Boudreault, F., & Liu, F. (2010). Recent advances and new opportunities in lung mechanobiology. *Journal of biomechanics, 43* (1), 99-107.

Upton, P. D., Wharton, J., Davie, N., Ghatei, M. A., Smith, D. M., & Morrell, N. W. (2001). Differential adrenomedullin release and endothelin receptor expression in distinct subpopulations of human airway smooth-muscle cells. *American Journal of Respiratory Cell and Molecular Biology, 25* (3), 316-325.

Vacanti, C. A., Paige, K. T., Kim, W. S., Sakata, J., Upton, J., & Vacanti, J. P. (1994). Experimental tracheal replacement using tissue-engineered cartilage. *Journal of Pediatric Surgery, 29* (2), 201-205. doi:http://dx.doi.org/10.1016/0022-3468 (94)90318-2

van den Bosch, E., & Gielens, C. (2003). gelatin degradation at elevated temperature. *International Journal of Biological Macromolecules, 32* (3), 129-138. doi:https://doi.org/10.1016/S0141-8130 (03)00046-1

van Susante, J. L., Buma, P., van Osch, G. J., Versleyen, D., van der Kraan, P. M., van der Berg, W. B., & Homminga, G. N. (1995). Culture of chondrocytes in alginate and collagen carrier gels. *Acta Orthop Scand, 66* (6), 549-556. doi:10.3109/17453679509002314

Vignola, A. M., Riccobono, L., Mirabella, A., Profita, M., Chanez, P., Bellia, V., Bonsignore, G. (1998). Sputum metalloproteinase-9/tissue inhibitor of metalloproteinase-1 ratio

correlates with airflow obstruction in asthma and chronic bronchitis. *Am J Respir Crit Care Med, 158* (6), 1945-1950. doi:10.1164/ajrccm.158.6.9803014

Vogel, G. (2015). Report finds trachea surgeon committed misconduct. Retrieved from http://www.sciencemag.org/news/2015/05/report-finds-trachea-surgeon-committed-misconduct

Volckaert, T., Dill, E., Campbell, A., Tiozzo, C., Majka, S., Bellusci, S., & De Langhe, S. P. (2011). Parabronchial smooth muscle constitutes an airway epithelial stem cell niche in the mouse lung after injury. *J Clin Invest, 121* (11), 4409-4419. doi:10.1172/jci58097

Waldman, S. D., Spiteri, C. G., Grynpas, M. D., Pilliar, R. M., & Kandel, R. A. (2003). Long‐term intermittent shear deformation improves the quality of cartilaginous tissue formed in vitro. *Journal of orthopaedic research, 21* (4), 590-596.

Walker, F., Kato, A., Gonez, L. J., Hibbs, M. L., Pouliot, N., Levitzki, A., & Burgess, A. W. (1998). Activation of the Ras/mitogen-activated protein kinase pathway by kinase-defective epidermal growth factor receptors results in cell survival but not proliferation. *Molecular and cellular biology, 18* (12), 7192-7204.

Wang, L., Li, X., & Wang, Y. (2018). GSK3β inhibition attenuates LPS-induced IL-6 expression in porcine adipocytes. *Scientific Reports, 8* (1), 15967. doi:10.1038/s41598-018-34186-0

Wang, Y., & Lou, S. (2001). Direct protective effect of interleukin-10 on articular chondrocytes in vitro. *Chin Med J (Engl), 114* (7), 723-725.

Webb, B. D., Walsh, G. L., Roberts, D. B., & Sturgis, E. M. (2005) Primary Tracheal Malignant Neoplasms: The University of Texas MD Anderson Cancer Center Experience. *Journal of the American College of Surgeons, 202* (2), 237-246. doi:10.1016/j.jamcollsurg.2005.09.016

Wechselberger, G., Russell, R. C., Neumeister, M. W., Schoeller, T., Piza-Katzer, H., & Rainer, C. (2002). Successful transplantation of three tissue-engineered cell types using capsule induction technique and fibrin glue as a delivery vehicle. *Plastic and reconstructive surgery, 110* (1), 123-129.

Weidenbecher, M., Tucker, H. M., Gilpin, D. A., & Dennis, J. E. (2009). Tissue-engineered trachea for airway reconstruction. *The Laryngoscope, 119* (11), 2118-2123. doi:10.1002/lary.20700

Weksler, N. B., Lunstrum, G. P., Reid, E. S., & Horton, W. A. (1999). Differential effects of fibroblast growth factor (FGF) 9 and FGF2 on proliferation, differentiation and terminal differentiation of chondrocytic cells in vitro. *Biochemical Journal, 342* (Pt 3), 677-682.

Wells, R. G. (2005). The role of matrix stiffness in hepatic stellate cell activation and liver fibrosis. *Journal of clinical gastroenterology, 39* (4), S158-S161.

Wen, F.-Q., Liu, X., Manda, W., Terasaki, Y., Kobayashi, T., Abe, S., Rennard, S. I. (2003). T H 2 cytokine-enhanced and TGF-β-enhanced vascular endothelial growth factor production by cultured human airway smooth muscle cells is attenuated by IFN-γ and corticosteroids. *Journal of allergy and clinical immunology, 111* (6), 1307-1318.

Windmolders, S., De Boeck, A., Koninckx, R., Daniëls, A., De Wever, O., Bracke, M., Rummens, J.-L. (2014). Mesenchymal stem cell secreted platelet derived growth factor exerts a pro-migratory effect on resident Cardiac Atrial appendage Stem Cells. *Journal of Molecular and Cellular Cardiology, 66*, 177-188. doi:https://doi.org/10.1016/j.yjmcc.2013.11.016

Wislet-Gendebien, S., Bruyere, F., Hans, G., Leprince, P., Moonen, G., & Rogister, B. (2004). Nestin-positive mesenchymal stem cells favour the astroglial lineage in neural progenitors and stem cells by releasing active BMP4. *BMC Neurosci, 5*, 33. doi:10.1186/1471-2202-5-33

Wright, D. B., Trian, T., Siddiqui, S., Pascoe, C. D., Johnson, J. R., Dekkers, B. G., Ojo, O. O. (2013). Phenotype modulation of airway smooth muscle in asthma. *Pulm Pharmacol Ther, 26* (1), 42-49. doi:10.1016/j.pupt.2012.08.005

Wright, D. T., Cohn, L. A., Li, H., Fischer, B., Li, C. M., & Adler, K. B. (1994). Interactions of oxygen radicals with airway epithelium. *Environ Health Perspect, 102 Suppl 10*, 85-90. doi:10.1289/ehp.94102s1085

Xie, S., Sukkar, M. B., Issa, R., Oltmanns, U., Nicholson, A. G., & Chung, K. F. (2005). Regulation of TGF-β1-induced connective tissue growth factor expression in airway smooth muscle cells. *American Journal of Physiology-Lung Cellular and Molecular Physiology, 288* (1), L68-L76.

Yang, K.-Y., Chen, Y.-M., Huang, M.-H., & Perng, R.-P. (1997). Revisit of Primary Malignant Neoplasms of the Trachea: Clinical Characteristics and Survival Analysis. *Japanese Journal of Clinical Oncology, 27* (5), 305-309. doi:10.1093/jjco/27.5.305

Yiu, H. H. P., Botting, C. H., Botting, N. P., & Wright, P. A. (2001). Size selective protein adsorption on thiol-functionalised SBA-15 mesoporous molecular sieve. *Physical Chemistry Chemical Physics, 3* (15), 2983-2985. doi:10.1039/B104729A

Yu, X., Feng, L., Han, Z., Wu, B., Wang, S., Xiao, Y., Cheng, S. (2016). Crosstalk of dynamic functional modules in lung development of rhesus macaques. *Molecular BioSystems, 12* (4), 1342-1349. doi:10.1039/C5MB00881F

Zaleskas, J. M., Kinner, B., Freyman, T. M., Yannas, I. V., Gibson, L. J., & Spector, M. (2001). Growth factor regulation of smooth muscle actin expression and contraction of human articular chondrocytes and meniscal cells in a collagen-GAG matrix. *Exp Cell Res, 270* (1), 21-31. doi:10.1006/excr.2001.5325

Zang, M., Zhang, Q., Chang, E. I., Mathur, A. B., & Yu, P. (2012). Decellularized tracheal matrix scaffold for tissue engineering. *Plastic and reconstructive surgery, 130* (3), 532-540.